Quantum Cascade Laser Spectroscopy: Applications and Developments

A thesis submitted for the degree of Doctor of Philosophy
by

Richard Walker

Balliol College, University of Oxford

Trinity Term 2011

Declaration of Authorship

I, Richard Walker, declare that this thesis titled, 'Quantum Cascade Laser Spectroscopy: Applications and Developments' and the work presented in it are my own. I confirm that:

- This work was done wholly or mainly while in candidature for a research degree at this University.
- Where any part of this thesis has previously been submitted for a degree or any other qualification at this University or any other institution, this has been clearly stated.
- Where I have consulted the published work of others, this is always clearly attributed.
- Where I have quoted from the work of others, the source is always given. With the exception of such quotations, this thesis is entirely my own work.
- I have acknowledged all main sources of help.
- Where the thesis is based on work done by myself jointly with others, I have made clear exactly what was done by others and what I have contributed myself.

Signed: _____

Date: _____

"How many hertz are there in a gigahertz?"

James Kenny (2008)

University of Oxford

Abstract

Physical and Theoretical Chemistry Laboratory
Department of Chemistry

Doctor of Philosophy

by Richard Walker

This thesis presents work examining the characteristics and applicability of quantum cascade lasers. An introduction is given explaining both the desire for a widely tunable, narrow bandwidth device working in the midinfrared, as well as detailing the ways in which quantum cascade lasers (QCLs) fulfill these requirements. The development and manufacture of QCLs are then discussed. The experimental section of this thesis is then split into three parts.

Chapter 2 concerns the characterisation and application of several pulsed QCLs. The intrapulse mode of operation is employed and the effect of the resulting rapid frequency chirp upon molecular spectra is investigated in the form of rapid passage signals. The evolution of said rapid passage signals is then investigated as a function of chromophore pressure and identity, with different QCLs, chirp rates, and optical path lengths. The prospect of producing population transfer with chirped lasers is discussed.

Chapters 3, 4, and 5 are then concerned with the application and characterisation of continuous wave QCLs. In these chapters a widely tunable commercially produced EC-QCL is utilised as well as two DFB QCLs, one of which is used in tandem with a home-made mount and temperature controller. In Chapter 3 a number of sensitive detection techniques are compared with the employment of wavelength modulation spectroscopy, long path cells and optical cavities, and the narrow bandwidth of QCLs utilised to determine a previously unknown spectral constant of DBr. Chapters 4 and 5 then utilise the high power of an external cavity quantum cascade laser in sub-Doppler Lamb-dip and polarisation spectroscopy measurements and then a pump-probe experiment. The laser linewidth is investigated on a millisecond timescale returning a current noise limited value of c.a. 2 MHz and the fundamental linewidth of the device investigated by altering the injection current. Chapter 5 is concerned with the pump-probe experiment, directly measuring the hot band absorption in a ladder like transition ($\mathrm{R}(6.5)_{\frac{1}{2}}$ $v = 1 \leftarrow 0$ and $\mathrm{P}(7.5)_{\frac{1}{2}}$ $v = 1 \leftarrow 0$). The Bennett peak in the hot band is observed with a DFB-QCL

swept at ~ 0.15 MHz ns^{-1} and is seen not just as a pump bandwidth limited lineshape, but as a highly velocity selected rapid passage signal. The effect of pressure, pump and probe scan rate and power upon this rapid passage signal is also studied. It is further noted that rapid thermalisation occurs within $v = 1$ such that at pressures above c.a. 30 mTorr a broad NO doublet absorption is observed beneath the Bennett peak from which a total population transfer of c.a. 16% can be estimated. Finally an experiment is discussed in which this population transfer could be increased for use in secondary applications.

Chapter 6 then presents initial measurements with two prototype pulsed 3.3 µm QCLs considering the prospects of such devices. A Fabry-Pérot device is first studied using a Fourier transform spectrometer and temperature tuning used to produce a spectrum of the Q-branch of CH_4 around 3025 cm^{-1}. Experiments are then performed using a DFB QCL investigating the chirp rate of the system as an indicator of the rate of heat accumulation within the system. Heat management is of particular consideration when the sea-change is made from pulsed to continuous devices. For this device absorption spectra of two CH_4 transitions at 2971 cm^{-1} are used to determine the chirp rate, which is found to be c.a. 1.8 GHz ns^{-1}, at least an order of magnitude higher than that of the longer wavelength pulsed devices considered in Chapter 2.

Acknowledgements

There are a great many people without whom this thesis would not have been produced, or more critically perhaps, without whom the making of this thesis would have been nowhere near as fun. I would like to thank Grant for rescuing me from the solemn depths of NMR, giving me the opportunity to work on such an exciting project, and being a constant source of enthusiasm throughout these last four years.

JP took me under his wing early on in my DPhil, and whilst I could never hope to aspire to his historic prowess, it was his mentoring (along with some aquatic engineering from Howard) that spurred me on to win the prestigious Hepwood prize. He has lead me through conferences, explained spectroscopy, and taught me not to worry when there's a gas leak "It's just a point source".

Damien has been an indispensable help for the last couple of years, with his micrometric fingers, and a lab seemingly filled with infinite pieces of useful equipment and no one to use them. I also owe him a debt for introducing me to the wonders of the Brompton, though I think everyone else may take issue with this, perhaps enjoying conversations about folding mechanisms less than me.

I have never seen anyone smile as much as Elin does. She has been consistently upbeat, even under the weight of the Maxwell-Bloch equations, thank you. In the year since James arrived I have already felt dwarfed by his ability to deal with matrices in the n^{th} dimension, I wish him all the best in the next few years. Just remember: QCLs are wicked.

Part IIs and Masters students, Tim Belcher, Henry Northern and Erwin Smakman are of particular note for their experimental contributions over the last few years; having patience where I wouldn't have, and putting up with my somewhat ad-hoc managerial style. Nick Zani too, digital squadron and Kissy Klub member, I'm glad that you had the run of the computer, even if Henry and Erwin weren't.

Gilly, Rich Dear, Lee and Martin are to be thanked for their (almost) unwavering support of Pub Mondays, try as we might we may have failed to not talk about work, but at least it was only complaining, which is fun. Each of you deserves individual thanks for your friendship over the years, but for now this is all you're getting.

Beth has been a friend, and a sympathiser over the years, we're nearly there, I hope this time isn't as bad as Part II hand in... Graham deserves thanks for uncountable LabView programs, innumerable rounds at the club, and that most measureable of events, his gigasecond (though the less said about that the better). Luca, or Mr Zugspitze Tractor

2009, Ann, Julian, Tom, and other less diligent lunch attenders for their appreciation (or not) of Neale Harvey. Katy, I don't care much for Cheryl, and your music taste is worse than Lee's, but you are almost as cheerful as Elin and that's always kept me smiling. Sophie was an inspiration, especially when it comes to graph design, and I think the only other person to quite understand the special joy of a visiting academic.

Even if I've never had the opportunity to wear the t-shirt I'd like to take this opportunity to say that 'I like Gus', for his good humour, his wisdom, and his unending tales of PTCL bureaucracy.

Outside of work, countless biere blondes and bottles of port shared with Andrew, Lucy, Ab, Tom, Laurence, James, Charlotte over the last 8 years have cemented friendships that have been of regular solace, and can only continue to grow. My surrogate girlfriend, Greg, too deserves thanks, for keeping me cool, and i trust he shall continue to do so now we once again live in the same city.

I want to thank my parents, all four of them, for supporting me for the last four years. I have been frequently absent, but knowing that I have two homes to flee to has kept me grounded in this strange period of homelessness. I may not say it but I love you all, and the same goes of my siblings (sometimes more than others...).

There are more, and I don't have room for you all, but I would be remiss if I didn't thank Crystal as well. Thanks to you I have a new home. Hopefully it will be tidy sometimes.

Hindrances

These acknowledgements cannot go by without the inclusion of hindrances, to which I can really only put my name, though I had some help:

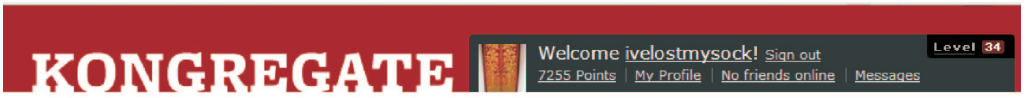

Contents

List of Figures

Chapter 1

Introduction

1.1 Absorption Spectroscopy

As monochromatic radiation is passed through an absorbing homogenous medium the transmitted intensity, I, is determined by the incident intensity, I_0, the frequency dependent absorption cross-section, σ, the path length, l, and the number density of absorbing particles, N, in a manner described by the Beer-Lambert Law.

$$I = I_0 e^{-\sigma l N} \tag{1.1}$$

The degree to which light is absorbed is thus quantified, and from the magnitude of absorption the concentration of a system can be determined.

$$A = -ln(I/I_0) = \sigma l N \tag{1.2}$$

This, most simply, can be referred to as absorption spectroscopy, an absolute technique. The sensitivity achieved in an absorption spectroscopy can be characterised by the ratio of signal to noise (S/N). Signal here corresponds to the absorbance, A, a measure of the fractional change of intensity through a sample, and noise, N, a single standard deviation of the baseline signal. In this case it is evident that in order to increase the signal magnitude and thus the sensitivity of absorption spectroscopy, there are three relevant variables. A larger number density will increase the degree of absorption, and whilst this is not always possible - particularly when real time measurements are required- it is a technique applied to trace gas analysis in the form of 'preconcentration'. The path length may be increased, whether by a multipass cell or through the use of an optical cavity, and both of these techniques are discussed in detail in Chapter 3. Finally, the absorption cross section, a measure of how strongly a molecule interacts with light,

whilst not initially appearing to be mutable is in fact variable; a given molecule will absorb at a wide range of wavelengths corresponding to transitions between different forms of energy level (rotational, vibrational and electronic) with cross sections varying by many orders of magnitude.

Industrial development of near-infrared (NIR) (0.8 µm – 2.7 µm) semiconductor diode lasers for telecom based applications has led to a wide variety of cheap and reliable radiation sources based on elements from the III and V groups of the periodic table (III-V). These devices were easily applicable to the interrogation of ro-vibrational transitions and indeed are still widely used for tunable diode laser absorption spectroscopy (TDLAS). The ro-vibrational transitions in the NIR are however relatively weak (integrated cross sections of the order 10^{-23} $cm^2\,cm^{-1}molecule^{-1}$) as they typically correspond to either combination bands which are formally disallowed in the harmonic approximation or hot bands. In contrast, between 3 µm and 12 µm, termed the mid-infrared (MIR), bands are several orders of magnitude stronger, corresponding as they do to the fundamental vibrational transitions (Figure 1.1) which are strongly allowed, and generally access pairs of states with a large population of molecules in the ground state at room temperature.

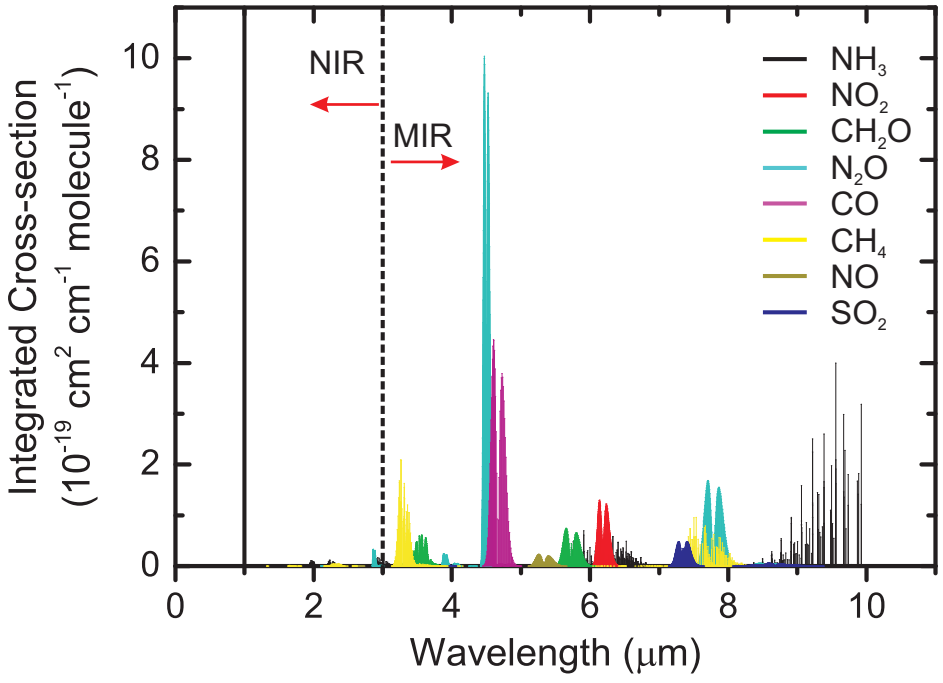

FIGURE 1.1: Integrated absorption cross-sections of a selection of atmospherically important molecules for their near and mid-infrared transitions [1]. Transitions in the near infrared are several orders of magnitude smaller than those in the near infrared.

The prevalence of these strong transitions presents an ideal spectral range for a number of applications; from trace gas sensing in its many guises (atmospheric studies, medical

diagnostics, engine performance studies etc); to reaction kinetics and dynamics studies, and pertinently in the case of this thesis, population transfer studies. It is however, not possible to design efficient traditional semiconductor diode lasers with appropriate band gaps to operate in the MIR and consequently alternative radiation sources had to be considered. The following section presents some of these alternatives, and discusses their strengths and weaknesses.

1.1.1 Midinfrared Radiation Sources

Carbon dioxide and carbon monoxide lasers have long been in use for MIR spectroscopic studies. They are typically high power (up to kW), devices capable of operating in both pulsed and cw modes, and with output wavelengths determined by the position of the vibrational transitions of the corresponding carbon oxide (9.4 & 10.6 µm for CO_2 and 5.3 µm for CO). When operating in cw mode these devices often have narrow linewidths, and their high powers allow their use for multiphoton dissociations [2]. Unfortunately however, these transition wavelengths are not tunable and as a consequence neither are the lasers. Consequently spectroscopic application is limited to molecules with transitions coincident or near-coincident with CO/CO_2 transitions, restricting their applicability.

An alternative to direct MIR sources is the production of radiation through a non-linear optical process utilising widely available sources in the NIR: Difference Frequency Generation (DFG). Here, two lasers at frequencies ω_1 and ω_2 are combined, and passed through a crystal with a high second order electromagnetic susceptibility (typically $LiNbO_3$). In general there would be several non-linear processes in operation, but by manipulating the phases of the radiation within the crystal it is possible to favour DFG such that a third photon is produced with a frequency $\omega_3 = \omega_2 - \omega_1$. This methodology can be used to produce continuous, narrow bandwidth light (< 20 MHz), tunable through scanning the frequency of either of the incident lasers. However, even with near perfect phase-matching using a periodically poled $LiNbO_3$ crystal, conversion efficiency is poor (c.a. 0.04 % $W^{-1}\,cm^{-1}$ [3]) meaning that typical output powers are in the µW range, even with relatively high input powers. Furthermore, the continuous tuning range is somewhat limited by the need to maintain phase-matching for optimum output efficiency. The efficiency of these devices can be improved by the addition of waveguides, but typically only by the order of 10× [4] and as such DFG is rarely used outside the 3 µm region where there is little alternative.

Another non-linear technique used to produce MIR light is that employed in Optical Parametric Oscillators (OPOs). Here, a single pump beam at ω_3 is applied to a non-linear crystal (again $LiNbO_3$ is commonly used), and two photons are created at ω_2 and ω_1, such that $\omega_3 = \omega_2 + \omega_1$ [5]. The exact wavelengths are determined by angle or temperature tuning of the crystal much like DFG, and several Watts of power can be achieved with the help of a resonant cavity. OPOs work in either continuous wave or pulsed mode, and can be tuned over a very wide spectral range. However, light is typically produced with a bandwidth in excess of 0.1 cm^{-1} [6] so is not applicable to high resolution studies, and though stabilisation methods do exist, the methodology is non-trivial.

The most popular devices for TDLAS in the mid-infrared have, until recently, been Pb-Salt diode lasers [7]. These are effectively normal semiconductor diode lasers, manufactured from lead chalcogenides with band gaps between 2 and 20 µm. As these devices are merely a different mode of diode lasers they have a lot of positive qualities, including tunability, narrow bandwidth and cw output. However, output powers tend to be fairly low (sub-mW), and more importantly, cryogenic cooling is required for operation - adding extra layers of complexity, and effectively barring the devices from tertiary use for instance by a medical professional.

Figure 1.2 shows the operating wavelength ranges of some of these radiation sources, alongside that of a completely different device: the quantum cascade laser, a semiconductor based device which has been shown to operate between 2 and 120 µm and is described in detail in the next section.

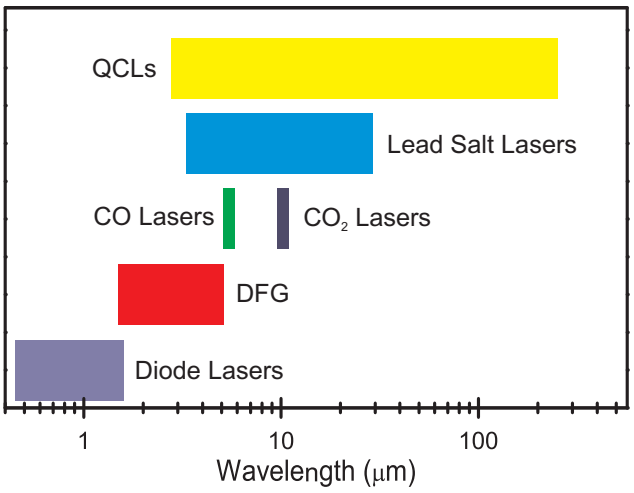

FIGURE 1.2: Wavelength regions accessible with a selection of radiation sources across the infrared.

1.2 Quantum Cascade Lasers

Traditional semiconductor diode lasers operate upon a fairly simple principle whereby a population inversion is created between energy levels. Electrons in the conduction band combine with holes in the valence band and photons are produced as is shown schematically in Figure 1.3. As the energy gap gets smaller however, and emission frequencies move from the NIR to the MIR, Auger recombination becomes the main loss mechanism of III-V devices [8], drastically reducing their efficiency and making this design unsuitable for use at longer wavelengths.

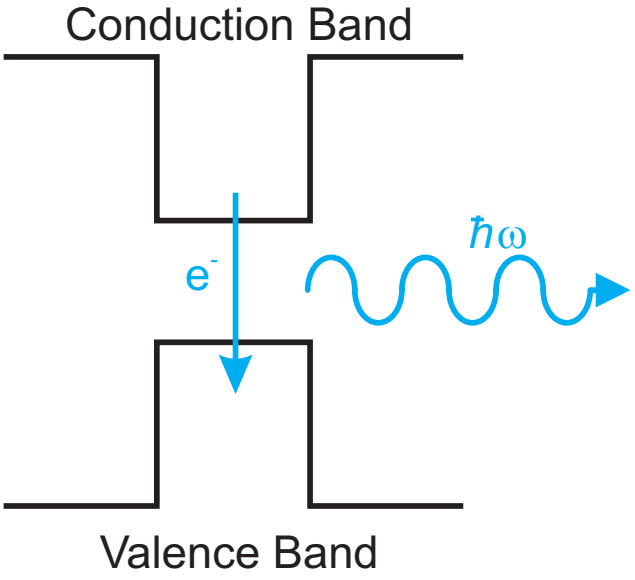

FIGURE 1.3: A schematic of an example diode laser active region. An electron relaxes from the conduction band into the valence band releasing a single photon.

In 1970, Esaki and Tsu [9] introduced the concept of semiconductor superlattices made up of barriers and wells thin enough to exhibit resonant tunnelling, and the following year Kazarinov and Sunis [10] built upon this concept, proposing a laser gain medium composed of such a superlattice. Material engineering techniques of the age however, were unable to fabricate such a device, and it was not until 1994 that an experimental demonstratration was realised by Faist et al. [11] in the quantum cascade laser (QCL).

A typical active region of a QCL is depicted in Figure 1.4. Nanometre thick, monocrystalline layers of semiconductor of alternating band gap are deposited using an epitaxial technique (e.g. molecular beam epitaxy (MBE)). If the thickness of the layers approaches the de Broglie wavelength of the material ($\sim$ 25 nm in GaAs) then a quantum well is created analogous to the simple particle in a box system with energy levels determined by the layer thickness. Furthermore, if these wells are layered upon each other with barrier thicknesses less than 5 nm then electron tunnelling between wells becomes an

efficient process and a four level laser system can be created. This principle is shown in Figure 1.4: electrons are injected from an upper state (level 4) into level 3, a radiative transition then occurs to level 2, from which electrons rapidly depart into level 1 and then into digitally graded alloy, continuously maintaining the population inversion over levels 2 and 3. Finally, by applying a voltage gradient to the gain medium the system tilts in energy and a single electron can continually 'cascade' though a concatenated series (typically 30-100 [12]) of discrete active regions, producing a photon at each.

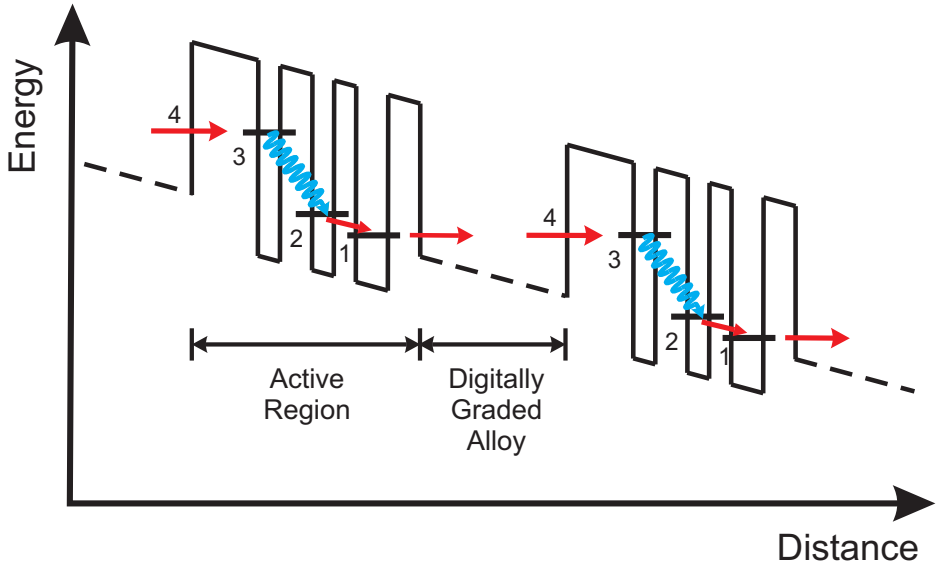

FIGURE 1.4: The active region of a QCL. Electrons are pumped from the continuum (level 4) into the top level of the lasing transition (level 3) before radiatively relaxing to level 2. Electrons then flow rapidly from level 2 to level 1 before tunnelling into the continuum and eventually into the next active region. Adapted from [11].

As all transitions in this design are intra-band, and there is no annihilation of charge carriers, a single electron can produce a large number of photons during the cascade, leading to high wall plug efficiency (< 53 %) [13], and allowing output powers of several Watts to be achieved from a single chip [14, 15]. Further, as the energy levels within the wells are determined by quantum confinement, the energy of the lasing transition is determined entirely by the thickness of the layers, and there is no need for exotic materials with specially designed band gaps. Instead mature semiconductor technology can be employed, and well known materials utilised (e.g. InGaAs/AlInAs or GaAs/Al(Ga)As).

The layers deposited to create the gain medium are so small that the active part of the chip is of the order of millimetres deep and micrometres wide, whilst the bulk resonator (including cladding, etc.) has a length of the order of a centimetre. Figure 1.5(a) shows a QCL chip on its mount alongside a penny for scale, whilst Figure 1.5(b) shows a zoom upon the chip itself. The laser is grown upon a wafer and then this wafer is placed on a copper mount for thermal dissipation. Gold contacts are then adhered to the top of the

chip and connected to a contact on the mount via gold wires for inclusion into a circuit.

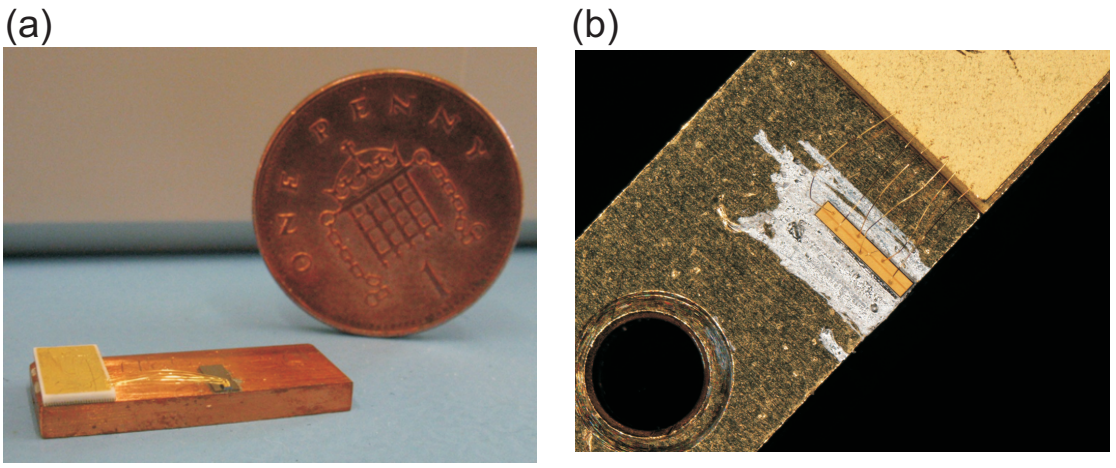

FIGURE 1.5: (a) A mounted QCL chip shown alongside a penny for scale and (b) a zoom upon a mounted QCL chip. Seen here is the laser on a copper block for thermal dissipation with an electric contact on the left hand side, gold wires extend from the copper contact to the top of the narrow QCL chip on top of the much broader substrate.

Unlike conventional diode lasers, because of the very efficient phonon scattering rate, the non-radiative lifetime of level 3 is much higher than that of spontaneous emission (ns vs ps). As a result, noise due to spontaneous emission is suppressed and the linewidth of the emission can inherently be very narrow [16] (a topic which shall be discussed in more detail in Chapter 4).

In the first instance QCLs were produced only in pulsed form with the need for cryogenic cooling. Huge volumes of heat can be produced during lasing, as Joule's first law states:

$$Q = I^2Rt \tag{1.3}$$

where Q is heat, I is current, R is resistance and t is time. At threshold of the first reported QCL at 10 K, 850 mA of current were flowing through the laser with a resultant voltage of 8 V [11], meaning that 7 W of heat would need to be dissipated for continuous operation. As the temperature of operation increases for a QCL chip, the threshold of operation increases also, meaning that there was no prospect at all of these initial devices operating continuously at room temperature. However, changes in waveguide and improvements in bandgap design for efficiency such as the bound-to-continuum modification [17] have improved matters. A further improvement is so called 'epi-down' mounting when the laser is mounted such that the gain medium itself is in direct contact with the thermal contact, leading to much improved heat dissipation over the more typical substrate down designs.

These improvements mean that whilst in 1994 operation was only possible in pulsed mode at cryogenic temperatures ($< 90K$), currently pulsed mode QCLs are operable with air cooling only and cw devices operate at room temperature - though most commonly with water cooling in order to dissipate the heat produced during operation.

There are a number of variations upon this basic structure that have been developed in order to change the properties and improve the performance of the QCL gain medium. Some of these are discussed in the next section.

1.3 Gain Medium Variations

There are two basic forms of lasing transition within QCLs, referred to as vertical and diagonal depending upon whether the radiative transition occurs within a single quantum well or between adjacent wells, respectively.

For gain media with a vertical lasing transition the separation of the two relevant energy levels is reasonably independent of applied electric field and consequently also of temperature [18, 19]. This can be of particular use when building a stable, fixed frequency QCL, but can also limit the tuning range of these devices. In contrast the first QCL gain medium design was based upon a diagonal lasing transition [11], as is shown in Figure 1.4, a structure producing devices which are typically less stable with respect to applied field, as it is this field which controls the gradient and so in part the energy gap for the transition.

More drastic variations to the gain medium occur with the introduction of so called 'superlattice' or 'bound-to-continuum' devices. In these systems the lasing transition occurs not between single energy levels but instead involves transitions between 'minibands'. This behaviour is demonstrated in Figure 1.6 for a bound-to-continuum structure where the lower state of the lasing transition is in fact the continuum between the individual laser systems. These devices have been of particular interest as coupling the electrons directly into this state not only guarantees a rapid removal of electrons from the system, helping to maintain population inversion, but also blurring the resonance frequency such that a wide range of wavelengths may be produced by a single chip (c.a. 150 cm^{-1} vs 80 cm^{-1}) [20].

A further development widening the tuning range of QCLs is the development of so called monolitihic devices whereby a series of different cascades are coupled together, a methodology that has allowed laser tuning ranges up to 432 cm^{-1} (7.6 – 11.4 µm) [21].

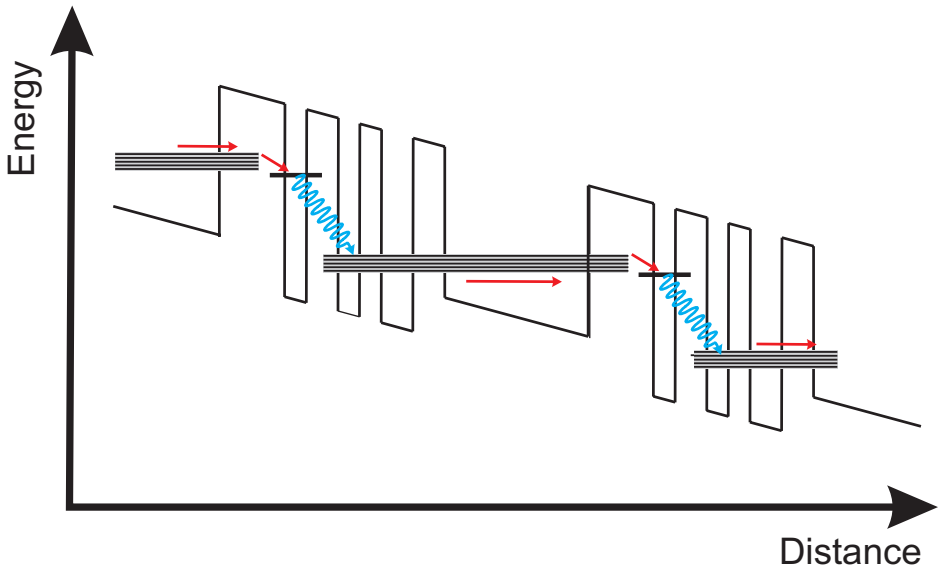

FIGURE 1.6: The active region of a bound-to-continuum QCL. In contrast to the traditional structure in Figure 1.4, the radiative transition occurs between an upper bound state and a lower continuum of levels, which then feed into the top level of the next radiative transition.

1.3.1 Wavelength Range

Typical QCLs are designed with a combination of III-V materials, with GaAs-Al(Ga)As and InGaAs-AlInAs being common material combinations. The primary determination of the wavelength produced by a laser is the depth of the well, determined by the energy of the barrier conduction band. This in turn is constrained by the materials used, as the alternating layers are required to have similar lattice constants for the formation of a congruous gain material. This design principle works well in the wavelength range 4–12 µm however, outside this region, as the wavelength is pushed towards either the NIR through the highly desirable 3 µm range or the THz range at long wavelength, there are a range of problems.

Towards the THz the energy gaps within the wells become increasingly small, and one of the largest issues becomes the efficiency of optical phonon relaxation over small energy gaps, which significantly increases the rate of non-radiative relaxation. There has been a degree of success in circumventing this limit [22–24], but as this thesis is not concerned with such long wavelength devices these developments will not be discussed here.

Short wavelength QCLs are of particular interest as the 3 µm wavelength range contains many strong transitions corresponding to the fundamental stretching vibrations of C-H, O-H and N-H bonds in atmospherically important molecules. The production of these devices however requires very deep wells, and there are a number of technological barriers to the production of such a system. For one, the very thin layers required for high

upper energy levels within the quantum wells can be difficult to manufacture with some materials, and further it is often difficult to ensure a good interface between these thin layers and the high conduction band offset barriers [25]. Even with relatively high barriers there can still remain a problem as the high energy levels involved in the lasing transition can approach the top of the well, at which point escape of electrons from the well substructure can begin to compete with radiative decay, as is shown in Figure 1.7.

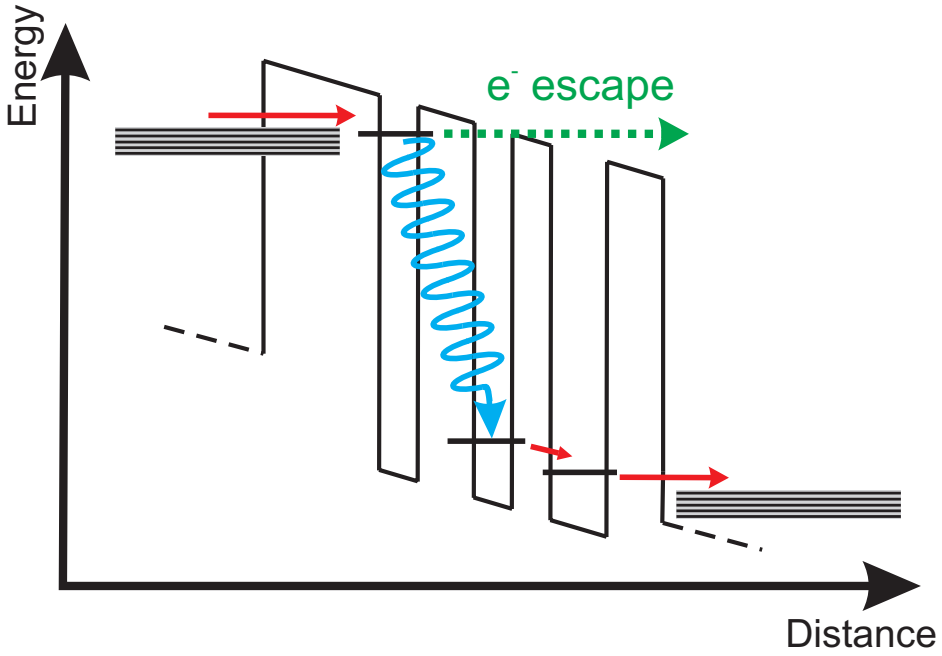

FIGURE 1.7: The active region of a deep well QCL. Often the need for a large energy gap for low wavelength operation requires bound energy levels high up in wells. At high energy however large losses can occur due to loss of electrons tunnelling from the quantum well system.

Work is being done in order to circumvent these problems, and some of the latest results are shown in Chapter 6. In particular 'strain compensation' by which layers are physically compressed by neighbouring layers in order to alter the lattice constant and improve interfaces have been used with reasonable success. In this manner QCLs operating down to 3.5 µm have been produced with InGaAs material, down to 3.3 µm using AlAs barriers, and doping these layers with Sb has even produced systems lasing down to 3.1 µm [25–28]. There has even been one paper published in the last year demonstrating a QCL operating near 2.6 µm produced by reducing the coupling between adjacent quantum wells [29] though with the result of very large threshold current (> 4 A at 170 K).

Further work is currently in progress in an attempt to use II-IV materials in order to stretch the possibilities for QCL fabrication. Devices based upon ZnCdSe/ZnCdMgSe grown upon an InP substrate are expected to have a lower limit of operation of c.a. 2

µm, and as II-IV materials have higher melting points than those composed of III-V elements, better thermal management and a higher temperature stability is anticipated [30–32]. However these materials have their own problems as II-IV technology is nowhere near as mature as III-V, and devices made with these materials are still very much in their infancy.

1.3.2 Interband Cascade Lasers

Interband cascade lasers (ICLs) are an interesting variation upon QCL technology designed in order to provide a suitable replacement for QCLs in the 3 µm range. In these devices, thin layers of semiconductor are deposited together much as they are in QCLs. However, in contrast with a QCL active region where the lasing transition occurs between two levels in the conduction band (intraband), in an ICL the lasing transition sees electrons recombine with holes in the valence band before tunnelling back into the conduction band. This behaviour is shown in Figure 1.8 for a 'W-shaped' active region. There has been a fair degree of success in the development of these devices [33–37], and they are beginning to become commercially available [38, 39]. However the complex gain medium design combined with a high temperature sensitivity caused by large non-radiative losses mean that their usefulness is significantly limited for the time being.

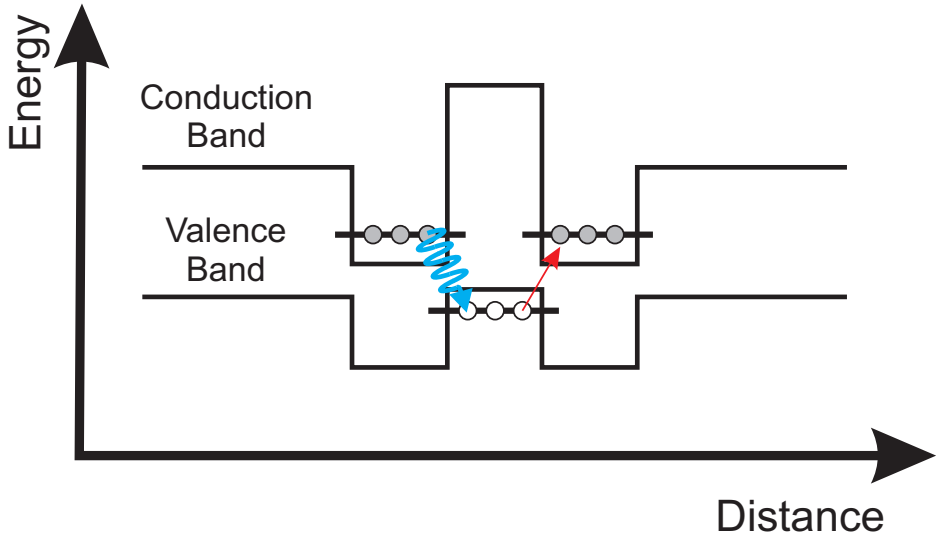

FIGURE 1.8: Lasing action in a W-shaped quantum well system, adapted from [36]. Electrons in the conduction band are trapped in a well, and then radiatively combine with holes in the valence band. With the addition of a field gradient tunnelling back into the valence band can become a competitive process such that the electron can cascade through the system much like in a QCL.

1.4 Wavelength Selection Mechanism

Wavelength selection for QCLs is performed using essentially the same processes as are used for traditional semiconductor lasers.

The core gain material is cleaved such that a semiconductor-air interface is produced, and as the refractive index of air is significantly smaller than that of the gain medium a resonator is formed and light is able to build up at selective frequencies determined by the resonator's free spectral range (FSR):

$$\Delta\nu_{FSR} = \frac{c}{2 * n_{reson}\, l}, \tag{1.4}$$

where n_{reson} is the refractive index and l is the length of the resonator. For a QCL built from InGaAs and AlGaAs the stack of layers has a refractive index of 3.35 (a linear interpolation between the two values $n_{InGaAs} \sim 3.49$ and $n_{AlInAs} \sim 3.2$) and cladding of either AlInAs or InP (n_{InP}=3.1) is used. This leads to a Fabry-Pérot resonator (FP), and the output of the laser is observed as a comb of frequencies separated by the FSR (Figure 1.9). With a standard FP resonator light is lost from both facets, however if the back facet is coated such that it becomes highly reflective (HR) then the efficiency of the resonator can be further improved.

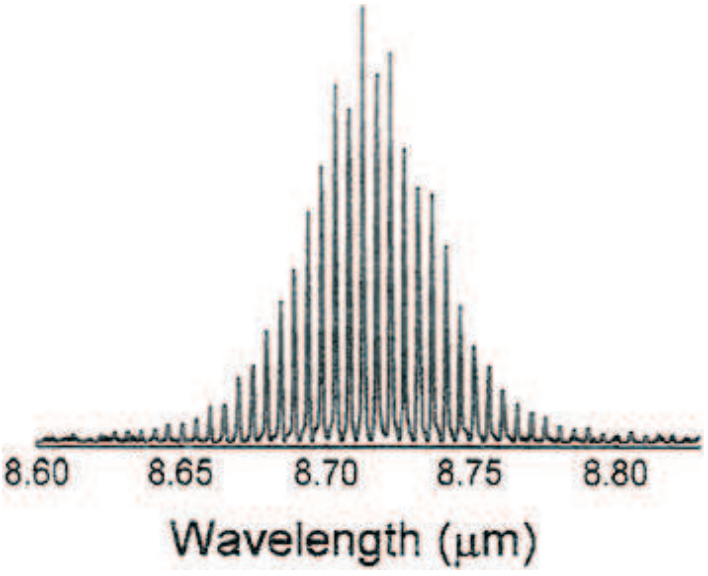

FIGURE 1.9: Radiation output from a Fabry-Pérot QCL centred at 8.7 μm with a FSR of ~ 0.7 cm^{-1}. From [18]

If a series of peaks and troughs are now etched into the waveguide along the dimension of resonance then the refractive index of the system will also periodically vary with these

perturbations. Such a structure is called a Bragg grating and is shown integrated to a QCL chip in Figure 1.10.

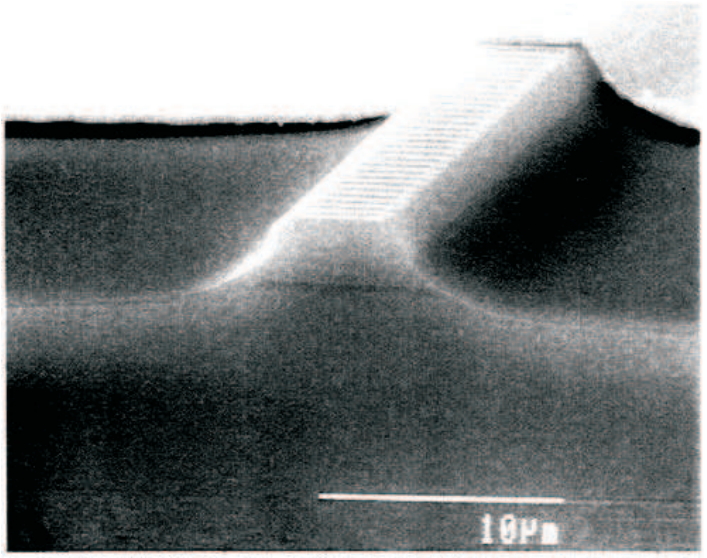

FIGURE 1.10: Scanning electron microscope image of a DFB QCL. The dark fringes here show the grating etched into the top of the chip. From [18]

The Bragg grating here will support only certain modes within the resonator, which in turns feeds back to the gain material, meaning that only a narrow range of frequencies will be produced. The laser frequency can then be tuned by changing the temperature of the laser chip - either directly or through the addition of current - as this then changes the pitch of the grating and in turn the supported modes. These gratings are widely used as frequency selective devices for semiconductor lasers which are referred to as distributed feedback (DFB) lasers [40]. One of the major advantages of such a device is the robust nature of a fully integrated laser circuit; as there are no moving parts it is highly inert to mechanical vibration.

A second method of wavelength selection, applicable beyond semiconductor lasers, is to place the gain material within a cavity to form an external cavity (EC) system. In an EC-QCL the radiation needs to satisfy the conditions of resonance within the FP system and the cavity simultaneously. There are two basic mechanisms utilised for the construction of EC systems, the Littrow and Littman-Metcalf [41] arrangements as shown in Figure 1.11 (a) and (b), respectively.

Each of these setups has their own advantages, the Littman-Metcalf laser for example typically produces a narrower linewidth as the radiation is passed over the diffraction grating twice, but is of lower power as of the light reflected from the mirror a small percentage is lost at the grating. The EC-QCL systems used in this thesis are both

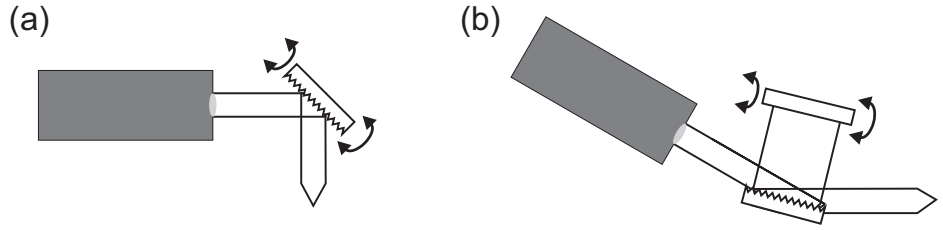

FIGURE 1.11: External cavity laser configurations showing (a) Littrow and (b) Littman-Metcalf arrangements. In the Littrow configuration the wavelength of the radiation is controlled by changing the angle of the diffraction grating, whilst in the Littman-Metcalf arrangement an extra mirror is utilised.

arranged in the Littrow configuration however and so this design is shown in more detail in Figure 1.12.

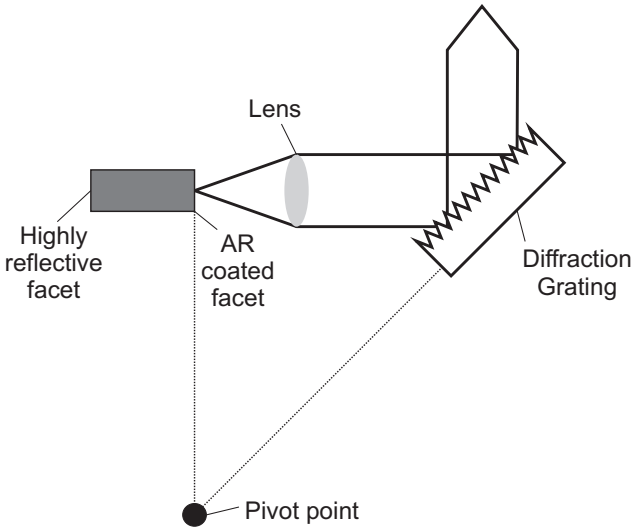

FIGURE 1.12: Schematic diagram of a Littrow Configuration EC-QCL.

In this design the optical cavity is formed between the highly reflective back facet of the QCL chip and a diffraction grating. A lens is placed within the cavity in order to collimate the output from the laser which is highly divergent (typically $\sim 60°$). The grating can be thought of as a series of microreflectors, each reflecting the same wavelength of light at phase steps of 2π. If it is then mounted such that its pivot is in line with the front facet of the QCL then tuning can be performed by a simple rotation whereby the wavelength is changed and every micromirror is kept at $m\lambda/2$ away. External cavities are typically capable of tuning over larger wavelength ranges than DFB QCLs as they are not constrained by the tuning afforded by thermal effects upon a Bragg grating. They also tend to produce higher power devices as the higher reflectivity within the system allows losses to be reduced. External cavity systems have a number of disadvantages however. For one, they are built from a series of mechanical parts, each of which can individually fail. This limits their robustness, and as the whole system is necessarily

small, the PZT controlling the grating must be brought very close to the cavity, meaning that frequency tuning of the system itself introduces mechanical instability. A high quality broadband anti-reflection coating is required on the gain medium facet in order to prevent any contribution from FP structure and finally the back-coupling of the light into this facet can produce problems, as the size of the laser facet means that the beam must be focused below the diffraction limit.

The additional manufacturing processes involved in the production of a DFB structure did not require a large degree of specialisation for their application to QCLs and as such the first DFB-QCL was produced as early as 1997 [42, 43]. External cavity systems are far more complex, and production of a working EC-QCL was not achieved until 2001 [44], and until recently there was only one company providing commercial devices c.f. dozens for DFB QCLs. One of the largest problems has been the production of effective anti-reflection coatings for the front facet of the QCL chip. In the MIR coatings are necessarily thicker than in the NIR and finding a coating material with both the correct refractive index and coefficients of thermal expansion matching that of the gain medium proved difficult. The issue of thermal expansion in particular was pertinent when QCL operation required cryogenic cooling, as the coatings would often flake and degrade [8]. In fact, the solution to this problem was found not through improvement of antireflection coating, but instead through the development of low thermal load, room temperature QCLs.

1.5 Overview of Thesis

The desire to work in the frequency ranges afforded by QCLs as well as their high power and narrow bandwidth have lead to their rapid development and widespread application in a large number of fields. To date work has been performed not only in spectroscopy [45–47] but also in atmospheric sensing [48, 49], kinetics [50–52], medical diagnosis [45, 53–57] and explosives detection [58, 59]. QCLs in essence are touted to be the MIR anaolgue of NIR diodes, with the main limitation to this aim being cost, which can only decrease as these devices become more widely used, and manufacturing methodologies improve. This thesis presents work demonstrating the potential and applicability of QCLs with an eye to their utilisation as devices for inducing population transfer in a low pressure gaseous medium to be implemented in reaction dynamics.

Specifically, Chapter 2 demonstrates work performed with pulsed QCLs, comparing both DFB and EC systems, and investigating the effects produced when the lasers are run in intrapulse mode. Chapter 3 is concerned with application of cw QCLs to a range of 'normal' spectroscopic applications. DFB and EC systems are utilised in a number

of sensitive detection techniques, and the narrow bandwidth of an EC-QCL is used to determine previously unknown hyperfine coupling constants of DBr.

Chapter 4 is concerned with the application of an EC-QCL to non-linear spectroscopic techniques. The high power of an EC-QCL is used to perform saturation spectroscopy, and the linewidth of the laser is investigated through Lamb-dip spectroscopy. Sub-Doppler polarisation spectroscopy is then performed, applying the high power of the EC-QCL to the production of an anisotropic system which is then probed through its polarisation changing effect upon a weak probe beam.

Chapter 5 demonstrates studies of the saturation produced by the high powered EC-QCL with the direct detection of the population pumped into the first vibrationally excited state with a second weak DFB QCL. The degree of population is investigated by study of a rapidly thermalised excited state absorption signal, and an unexpected rapid passage signal upon the instantaneously pumped and detected Bennett peak is investigated.

Chapter 6 then presents initial studies with two research grade pulsed QCLs working in the 3.3 μm range. A multi-mode FP device is investigated with the use of a Fourier transform infrared spectrometer, and a spectrum taken of the CH_4 transitions around this region. A single mode DFB device is then investigated with spectra of a low pressure sample of CH_4 used to determine the approximate chirp rate. This information in turn applied to consider the feasibility of such devices for general use and the prospect of cw operation.

Chapter 2

Pulsed Quantum Cascade Lasers

2.1 Operation Modes

Initially, due to the large volume of heat produced during operation, single-mode QCLs were available only as pulsed DFB systems with very low duty cycles (c.a. 5 %). In these lasers gross wavelength tuning is achieved through a slow alteration of the temperature of the gain medium, but in order to record a spectrum one of two faster methodologies in employed, both of which are demonstrated is Figure 2.1.

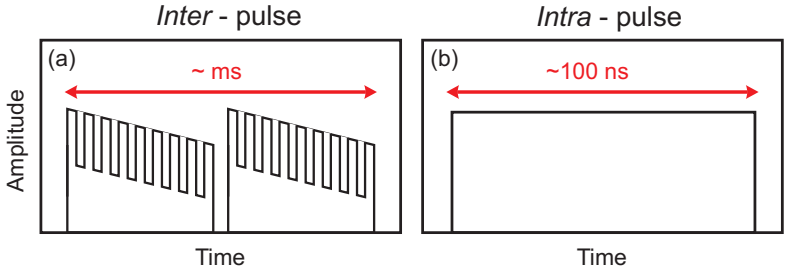

FIGURE 2.1: The current pulse shapes applied to a QCL for operation in (a) inter-pulse or (b) intra-pulse mode.

In the so called interpulse operation scheme (Figure 2.1(a)), a sub-threshold current ramp is applied to the laser, superimposed with a series of short (c.a. nanosecond) pulses. The current ramp here provides a wavelength tuning then realised by the pulses, during which the wavelength is in principle stationary. These individual points can then be reassembled to form a spectrum over the course of ms.

Intrapulse operation (Figure 2.1(b)), in contrast, is performed by the application of a comparatively long (100's of nanoseconds) square pulse. This applied current pulse induces Joule heating in the gain medium, which in turn leads to a change in refractive

index, and consequently the wavelength of the emitted radiation. Thus, a fast change from high to low frequency (termed a down-chirp) occurs throughout the duration of the pulse, with a frequency change typically on the order of 100 MHz ns^{-1}. In this manner spectral ranges of the order of a wavenumber can be covered within a single sub-microsecond pulse. This is a property of use for rapid spectral analysis, as a wide spectral area containing features from many distinct gases can be observed in a single time slice. Examples of particular interest include the application of pulsed QCLs to atmospheric analysis, whereby the atmosphere can be considered essentially 'frozen' within the pulse length, and any turbulence induced lineshape effects neglected, and the study of reaction kinetics, when fast time resolution of a spectral region is required in order to gain insight into reaction processes [52].

The work presented in this chapter has been performed using the intrapulse methodology, in part due to the time resolution gained as well as the ease of application, but also as it allowed the investigation of some interesting optical effects, as outlined in Section 2.3.

2.2 Spectroscopy

When interrogating the absorption characteristics of a gas in a high pressure mixture, as one does when investigating a gas in the atmosphere, or in a breath sample, spectra produced by the intrapulse method are near-enough identical to those that would be expected from a continuous wave experiment using for example a diode laser: i.e. a smooth, symmetrical Voigt or Lorentzian absorption is returned and high accuracy pressure broadening parameters can be determined from the lineshape. However, as the pressure of the sample, and hence number of collisions, is reduced the lineshape starts to change, and a degree of asymmetry becomes apparent in the absorption spectra. When the collisional rate is further reduced such that the laser frequency sweeps through a transition faster than the relaxation period of the system then the asymmetry becomes further pronounced and a series of oscillations around the baseline is observed later in time than (and consequently on the low frequency side of) the absorption. This behaviour is demonstrated in Figure 2.2 and is described as rapid passage (RP). It is an effect which has been observed in a number of optical systems - most notably Stark spectroscopy performed with a CO_2 laser [60–62], and in the microwave region [63], but was first observed in continuous wave nuclear magnetic resonance (NMR) experiments [64, 65].

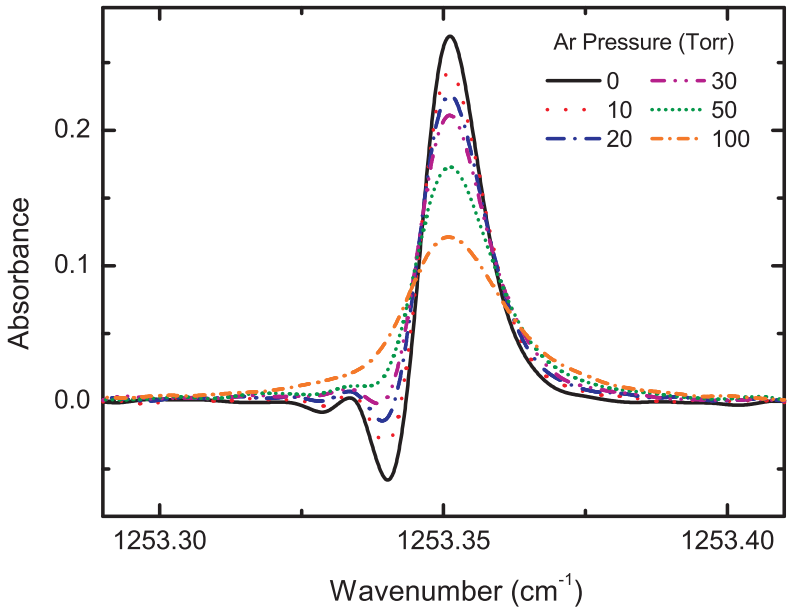

FIGURE 2.2: Spectra of 140 mTorr of CH_4 with varying pressures of buffering Ar gas, showing a symmetric Voigt line profile at high total pressure and the asymmetric rapid passage affected lineshape at low pressure. From [66]

In brief, as the laser sweeps through the transition, a polarisation is induced within the sample, and the beating of this induced polarisation with the incident chirped electromagnetic field manifests as the oscillations in this characteristic rapid passage signal. This transient signal can be seen to decay at a rate determined by a combination of collisional dephasing, and broadening produced by interference between both the array of signals produced by the individual oscillators present in the sample and the bandwidth of the detection system. A fair degree of investigation has been performed upon these effects in pulsed QCLs [67–70] and a fuller theoretical description is given in the following section.

2.3 Rapid Passage

It is near impossible to calculate the full range of processes that occur when light interacts with a truly multi-levelled system. However, a degree of insight into the dominant interactions can be gained by considering the simplified model of the interaction of a near monochromatic radiation field with a so called non-degenerate two-level atom.

Here, the two levels are described by the Bloch formalism, commonly used in NMR, as the system is analogous to a spin-1/2 nucleus in a static magnetic field being interrogated by a radiofrequency (rf) field directed along the z axis. In NMR, this system is described

by the Bloch equations; under the rotating wave approximation [71] these are as follows:

$$\frac{\mathrm{d}u}{\mathrm{d}t} = -(\omega-\omega_0)v(t) - \frac{u(t)}{T_2'} \tag{2.1}$$

$$\frac{\mathrm{d}v}{\mathrm{d}t} = (\omega-\omega_0)u(t) + \frac{v(t)}{T_2'} - \gamma B_1 M_z \tag{2.2}$$

$$\frac{\mathrm{d}M_z}{\mathrm{d}t} = \frac{M_{eq}-M_z}{T_1} + \gamma B_1 v, \tag{2.3}$$

where B_1 is the applied rf field, $\omega-\omega_0$ is the frequency detuning of that rf field from resonance (ω_0), γ is the gyromagnetic ratio of the nucleus, T_1 and T_2 are relaxation times separated for reasons we will discuss later, M_z is the longitudinal magnetisation, M_{eq} is the equilibrium value of M_z in the absence of a field, and u and v are functions of the transverse magnetisations M_x and M_y in phase and in quadrature with respect to the rf field,

$$u = M_x\cos(\omega t) - M_y\sin(\omega t) \tag{2.4}$$

$$v = -M_x\sin(\omega t) - M_y\cos(\omega t). \tag{2.5}$$

The dynamical equations resulting from a spin-based Hamiltonian, are almost identical to those concerning our two-level atom, and as such we can draw the following analogies:

Static field Zeeman splitting	$\Leftrightarrow$	Energy level splitting
Oscillating applied rf field	$\Leftrightarrow$	Laser radiation
Longitudinal magnetisation	$\Leftrightarrow$	Population of excited state
Transverse magnetisation	$\Leftrightarrow$	Oscillating dipole moment

In this manner, the Bloch equations can be reformed to become the Optical-Bloch or Maxwell-Bloch equations:

$$\frac{\mathrm{d}u}{\mathrm{d}t} = -(\omega-\omega_0)v(t) - \frac{u(t)}{T_2} \tag{2.6}$$

$$\frac{\mathrm{d}v}{\mathrm{d}t} = (\omega-\omega_0)u(t) + \frac{v(t)}{T_2} + \kappa\mathcal{E}w \tag{2.7}$$

$$\frac{\mathrm{d}w}{\mathrm{d}t} = -\frac{w-w_{eq}}{T_1} - \kappa\mathcal{E}v. \tag{2.8}$$

Here the gyromagnetic ratio has been replaced by κ defined as $\frac{2\mu}{\hbar}$ with μ the transition dipole moment, the applied rf field has become the applied laser field, $\mathcal{E}$, and M_z becomes

a measure of population transfer, or specifically, population inversion, w. Also, by observing the behaviour of oscillations in the dipole moment in phase and quadrature with the incident radiation - u and v - we can gain some insight into the physical meaning of these terms. In particular, it is apparent that when the laser is turned on, the population inversion changes only due to v, thus as changes in w correspond to energy input to the system we can see v is a measure of absorption and u is a measure of dispersion. Specifically, u and v are the real and imaginary parts of the refractive index of the system.

Using the axes u, v and w we can now create a 'pseudospin vector' $\boldsymbol{\rho} = (u, v, w)$, which like the Bloch vector $\boldsymbol{M} = (M_x, M_y, M_z)$, holds to a conservation law such that $u^2 + v^2 + w^2 = 1$. This pseudospin vector can thus be envisioned as being restrained to a unit sphere, termed the Bloch sphere. Furthermore, in this treatment, neglecting the effects of relaxation, the incident laser field is described as a torque vector,

$$\frac{\mathrm{d}}{\mathrm{d}t}\boldsymbol{\rho} = \boldsymbol{\Omega} \times \boldsymbol{\rho} \qquad \text{where,} \qquad \boldsymbol{\Omega} = (-\kappa\mathcal{E},\, 0,\, \omega_0 - \omega), \tag{2.9}$$

acting upon and precessing about $\boldsymbol{\rho}$, as can be seen in Figure 2.3, with components $-\kappa\mathcal{E}$ and $\Delta = \omega_0 - \omega$ in the u and w directions respectively. At resonance, i.e. $\Delta = 0$ the torque vector $\boldsymbol{\Omega}$ has a magnitude $\kappa\mathcal{E}$ referred to as the Rabi frequency.

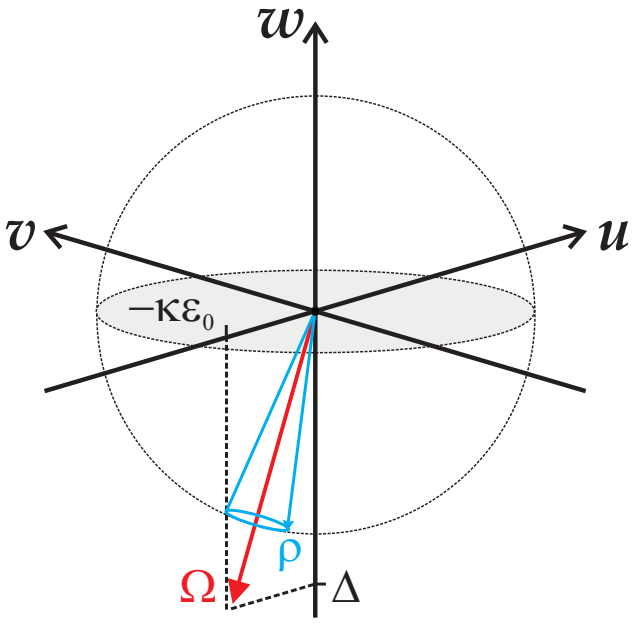

FIGURE 2.3: The effect of applying coherent radiation to the Bloch vector system. The pseudospin vector $\boldsymbol{\rho}$ precesses about the torque vector $\boldsymbol{\Omega}$.

If the applied radiation is of fixed frequency, or at a frequency changing slowly with respect to the rate of relaxation, then energy from $\mathcal{E}$ flows in and is dissipated into the

surroundings by relaxation and these formulae give solutions of the form expected in 'normal' spectroscopy as is shown in Figure 2.4 for the case of a chirp rate 1 kHz ms^{-1} versus a collisional lifetime of 2 ns.

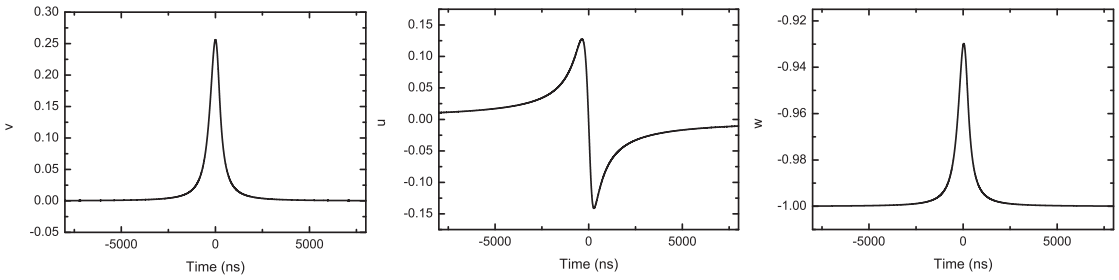

FIGURE 2.4: Absorption (v), dispersion (u), and population transfer (w) as a function of time for a slow sweep (1 kHz ms^{-1}) through a transition with a collisional lifetime of 2 ns.

However, if the relaxation rates are decreased/and or the rate of frequency change is increased, then the response of the coupled light-atom system alters, and the rapid passage oscillations observed in our experiments become apparent in the simulation shown in Figure 2.5 for a chirp rate of 100 MHz ns^{-1} and with collisional lifetime of 10µs.

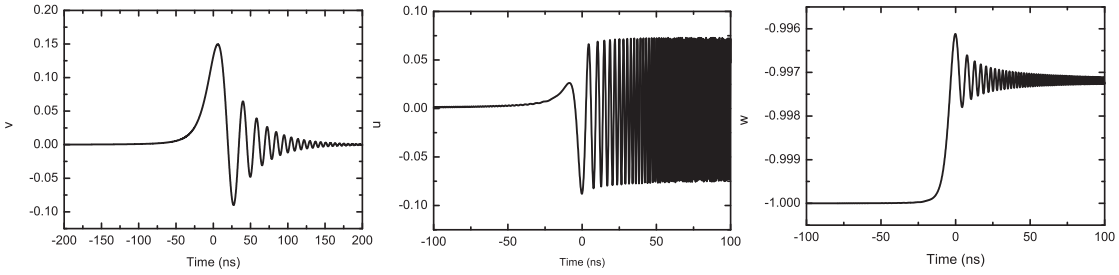

FIGURE 2.5: Absorption (v), dispersion (u), and population transfer (w) as a function of time for a fast sweep (100 MHz ns^{-1}) through a transition with a collisional lifetime of 10µs.

From the starting conditions $u = v = 0$, $w = -1$, i.e. radiation far from resonance and population entirely in the ground state, an intense, rapidly chirped laser source can cause the pseudospin vector to shift from equilibrium and progress through the u and v planes towards the top of the sphere ($w = 1$). Whilst it is possible in an idealised case to achieve so called 'adiabatic following' [72]- an effect discussed in section 2.7.2 - whereby complete population transfer is achieved in a single laser sweep, the lineshapes observed in a pulsed QCL experiment are due largely to changes in the absorptive and dispersive parts of the refractive index of the sample (u and v) and there is minimal population transfer.

The simulation of absorption in Figure 2.5 has far more structure than the experimental data in Figure 2.2 and this is because we have yet to consider the relaxation constants T_1 and T_2. In NMR, T_1 and T_2 correspond to relaxation of the magnetisation parallel and perpendicular to the direction of the applied static field, and are usually termed the 'spin-lattice' and 'spin-spin' relaxation times. In optical processes the exact processes occurring differ, but the distinction between population and polarisation changing relaxation times is still useful.

T_2 corresponds to dephasing of the system, and can be viewed as a depolarisation constant. T_2 originates from incoherent interactions affecting all components of the system homogeneously, such as collisions and radiative decay. These processes lead to a transition width of $\frac{1}{T_2}$, referred to as the homogenous linewidth, as it affects all oscillators in a bulk sample identically, and as the decay is exponential in time, it manifests as a Lorentzian lineshape.

As well as these homogeneous broadening effects, there are also inhomogeneous contributions to the linewidth which are caused by interactions affecting each species within a bulk sample differently. The most prominent of these broadening contributions is the Doppler effect whereby the resonant frequency of any single oscillator is shifted from the rest resonance frequency ω_0 by a factor dependent upon its velocity with respect to the direction of laser field propagation, v_E,

$$\omega_0' = \omega_0(1 \pm \frac{v_E}{c}). \tag{2.10}$$

If a Maxwell-Boltzmann distribution of velocities is presumed then a Gaussian lineshape is observed with a full width at half maximum (FWHM) of

$$\delta\omega_0 = \sqrt{\frac{8kT\ln 2}{m}}\left(\frac{\omega}{c}\right), \tag{2.11}$$

where k is Boltzmann's constant, T is the temperature, m is the mass of the molecule (or atom) in question, ω is the frequency of light, and c is the speed of light.

These two contributions to the linewidth mean that in a typical absorption experiment a composite lineshape called a Voigt will be observed, consisting of a continuum of Lorentzian peaks, linewidth $\frac{1}{T_2}$, distributed in a Gaussian manner as is shown in Figure 2.6.

This figure is demonstrative of a typical MIR spectroscopic study at low pressure where the natural and collisional lifetimes are long enough for the Lorentzian component to be at least an order of magnitude smaller than the Doppler width.

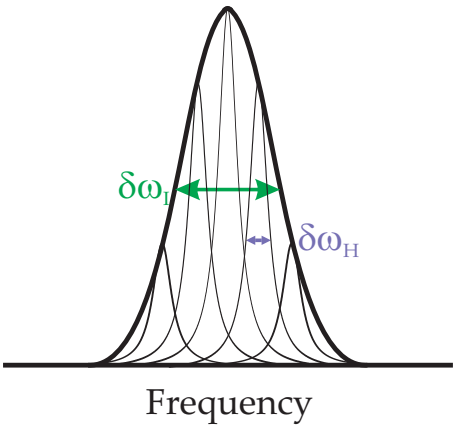

FIGURE 2.6: An array of homogenously broadened Lorentzian lineshapes, Doppler shifted to produce an overall inhomogenously broadened Doppler lineshape.

In much the same way that both the Lorentzian and Gaussian components contribute to an absorption profile, both the inhomogeneous and homogeneous linewidth components affect the observed, bulk polarisation of the system. When an array of dipoles are excited, each molecule acts as an individual emitter and the interference between this collection of oscillations, themselves excited at slightly different frequencies due to different velocity components along k, causes a dephasing, effectively damping out the macroscopic polarisation. The observed signal is thus a sum of all of these dipoles and as the E field is due to the bulk properties of the sample, a collection of molecules can cease to have an observable polarisation long before the individual oscillations disappear.

As T_1 solely affects w, it is best understood as the excited state lifetime - i.e. that $\frac{1}{T_1}$ is the rate constant for the decay of the system towards $w = -1$. Were there to be no collisions this rate would be fixed at the reciprocal of the natural lifetime of the excited state, also known as Einstein's A coefficient, but for the fundamental rovibrational transitions in the MIR this is typically of the order of seconds, and collisional de-excitation usually dominates. Furthermore, T_1 is usually of the order of T_2 [63, 73] and the two are typically set as equal.

The effect of these decay processes is perhaps best understood through considering the effect of applying a near resonant coherent light source to the two level atom. In this situation the system cycles from the ground to the excited state periodically over time. In the Bloch vector system: before light is applied the Bloch vector, $\boldsymbol{\rho}$ sits pointing vertically to $w = -1$. Upon application of the light field the $\boldsymbol{\Omega}$ torque vector manifests, inducing $\boldsymbol{\rho}$ to precess about it in a cone, with vertical component defined by the detuning $((\omega - \omega_0)(t))$, and with a component in the u direction of the on resonance Rabi frequency $\Omega(0)$. If the field is constant, precession rate stays constant, however this behaviour is subject to the damping processes already mentioned, and thus dephases from the driving field at a time T_2. That is to say that it relaxes at rate $\frac{1}{T_2}$ towards the vertical axis of the sphere. At the same time however, the system is relaxing towards $w = -1$ at a rate $\frac{1}{T_1}$, and thus damps these oscillations, leading to an observed free-induction decay

signal, reflecting the sum of these two processes. These processes are shown in Figure 2.7 for an exaggerated case.

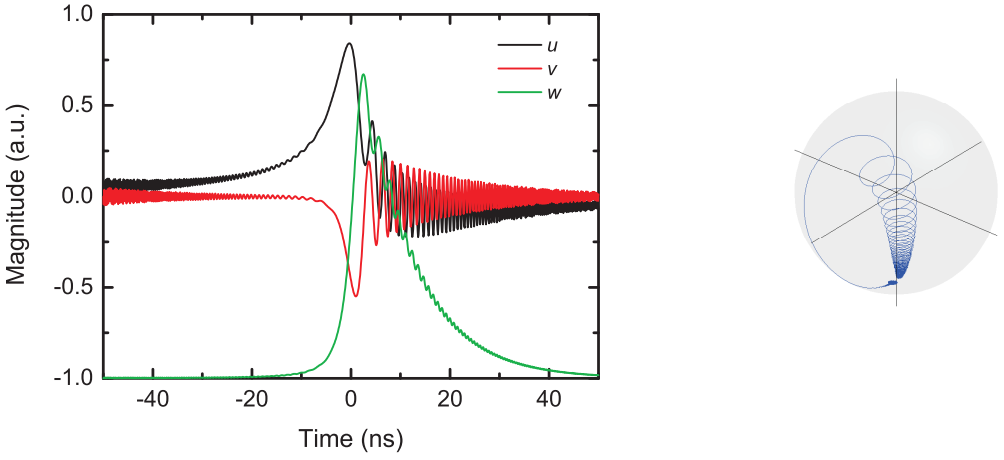

FIGURE 2.7: Absorption (v), dispersion (u), and population transfer (w) as a function of time for an exaggerated case. Population can be seen to move from the lower to the upper state, rotating through both the u and v directions before relaxing back to $w = -1$.

2.4 Experimental

The lasers, detectors and generic equipment used for the experiments presented in this chapter are described in this section. A water-cooled DFB QCL from Alpes Laser operating in the range 1248 – 1257 cm^{-1}, and giving a peak pulse power of 25 mW over this range was driven by a Q-MACS system from Neoplas Control. Coarse wavelength tuning was performed by altering the temperature in the range -20 to 20 °C via a Peltier thermoelectric cooler (TEC) using a programmable function generator [TTi, model TG1304], whilst tuning during spectroscopic experiments was performed through the intrapulse method discussed in Section 2.1. Figure 2.8 depicts the Q-MACS mounting system, showing the off-axis paraboloid used for collimation as well as the the red diode laser and beamsplitter assembly utilised for alignment. The beam width measurement is also shown in which the 'knife-edge' method employed by Kim et al [74] was used to determine a beam radius of 5 mm. During operation laser pulses of 190 ns were applied at 100 kHz giving a duty cycle of $< 2\%$.

Another system used was a tunable external cavity QCL (EC-QCL) from Daylight Solutions outputting radiation over 8 mW peak power from 1195 - 1280 cm^{-1} without the need for either cryogenic or water cooling. The laser and external cavity were driven

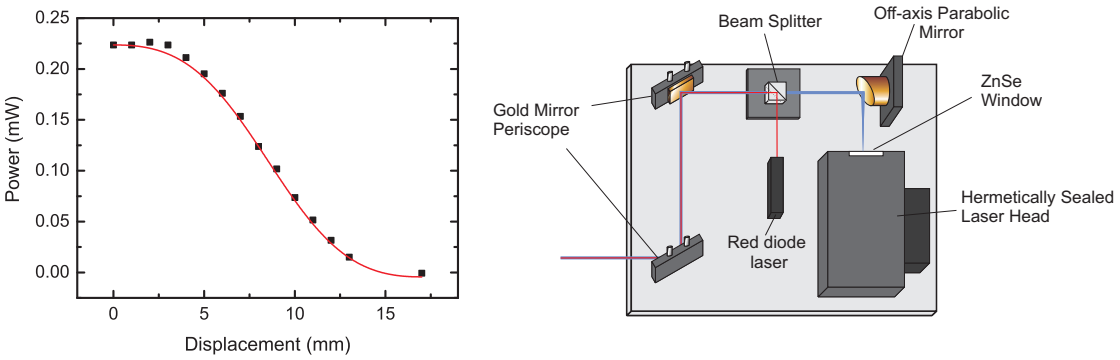

FIGURE 2.8: The measured beam width of the mounting, collimation and alignment system for the Q-MACS QCL

with the use of a proprietary driver, and intrapulse methodology was once again employed. Pulses of 500 ns were applied at a repetition rate of 90 kHz giving a duty cycle of 4.5% and peak pulsed powers of up to 250 mW were determined in the range 1210–1276 cm^{-1}. A beam waist of 1.8 mm was measured for this system.

Signals were detected on a thermoelectrically cooled MCT detector (VIGO PVI-2TE-10.6) with a 900 MHz bandwidth and then recorded using a 2 GS s^{-1} 350 MHz bandwidth digitising oscilloscope (LeCroy Wavesurfer 434).

2.5 Characterisation and Comparison

This section exhibits work done to investigate the base behaviour of both DFB and EC-QCLs comparing and contrasting their behaviour when interrogating a sample of N_2O.

Firstly, frequency calibration of the two lasers within a scan was performed by the insertion of a 75 mm Ge etalon with a 500 MHz free spectral range (FSR) into the beam path. Figure 2.9 shows the signal observed for the Q-MACS both through this etalon and through an empty 70 cm cell, as well as the chirp rate and minimum resolution implied by such a fast chirp [75]. As can be seen the laser produces a rapid frequency down chirp slowing over the course of the pulse from 225 to 160 MHz ns^{-1}. In this manner, just a little over 1 cm^{-1} is covered in 190 ns. The structure present at the beginning and end of the pulse is due to impedance mismatching between the laser and pulse source, and cuts down the usable frequency range of the pulse to ~ 0.8 cm^{-1}.

In contrast Figure 2.10 shows data produced as the output of the Daylight EC-QCL is passed through the same 70 cm cell and etalon, and notable differences are apparent. In particular the baseline structure on the empty cell data is far more structured than is

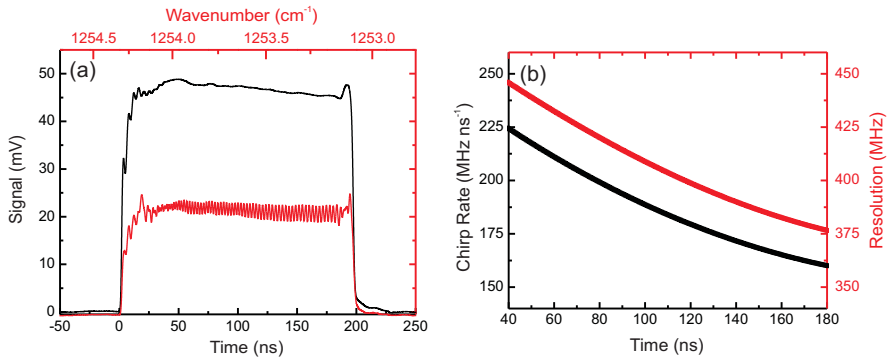

FIGURE 2.9: (a) A 190 ns laser pulse from the Q-MACS (black) and the signal detected through a 500 MHz Ge etalon (red). (b) Chirp rate (black) recorded in (a) alongside calculated system resolution (red) during the pulse.

observed for the DFB QCL, and these discontinuities are further emphasised in the etalon trace. The tuning range between these 'mode-hops' is c.a. 3 GHz, corresponding to a FSR of the order expected for the laser's external cavity, which is unable to respond on the timescale of the laser pulse. Despite the multiple mode hops during a single current pulse, the chirp rate still appears to decrease in a similar manner to that of the DFB QCL and the tuning range between the hops exhibit single mode behaviour. Finally, the mode hops are produced at fixed times within the pulses and as such variation in pulse structure is sufficiently small to allow rapid passage structures to be observed in averaged transmission spectra.

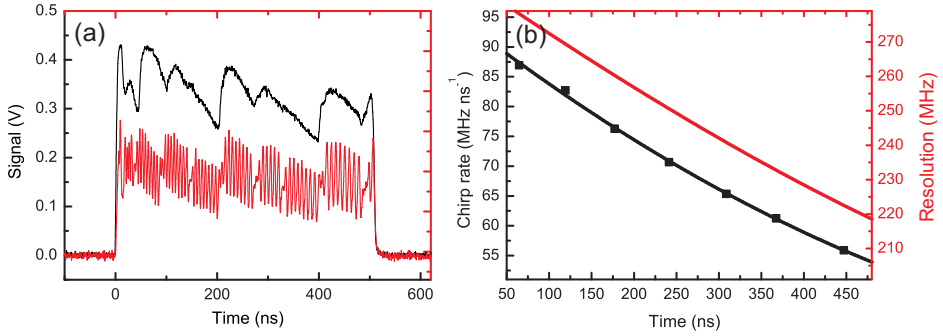

FIGURE 2.10: (a) A 500 ns laser pulse of the Daylight Solutions QCL (black) and the signal detected through a 500 MHz Ge etalon (red). (b) Chirp rate (black) recorded in (a) alongside implied system resolution (red) during the pulse.

The difference between the chirp rates of these two lasers is made most apparent in figure 2.11 where spectra of 20 mTorr of N_2O are exhibited as measured on the P(36)e transition in the ν_1 band. This data is a cumulation of 1000 averages and has been converted into absorbance $A = -\ln(I/I_0)$. The difference between the chirp rates is manifest both through the difference in line widths due to the chirp rate induced resolution change

$\Delta v_{\text{resolution}} = \sqrt{0.886\alpha}$, where α is the chirp rate of the laser, and also in the apparent oscillation periods on the low frequency side of the absorption.

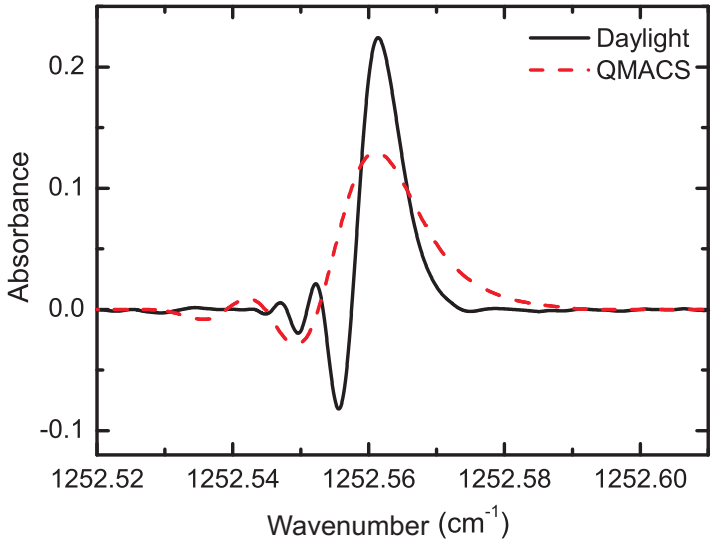

FIGURE 2.11: Spectra of 20 mTorr of N_2O as measured with both laser systems for the P(36)e rovibrational transition in the ν_1 band.

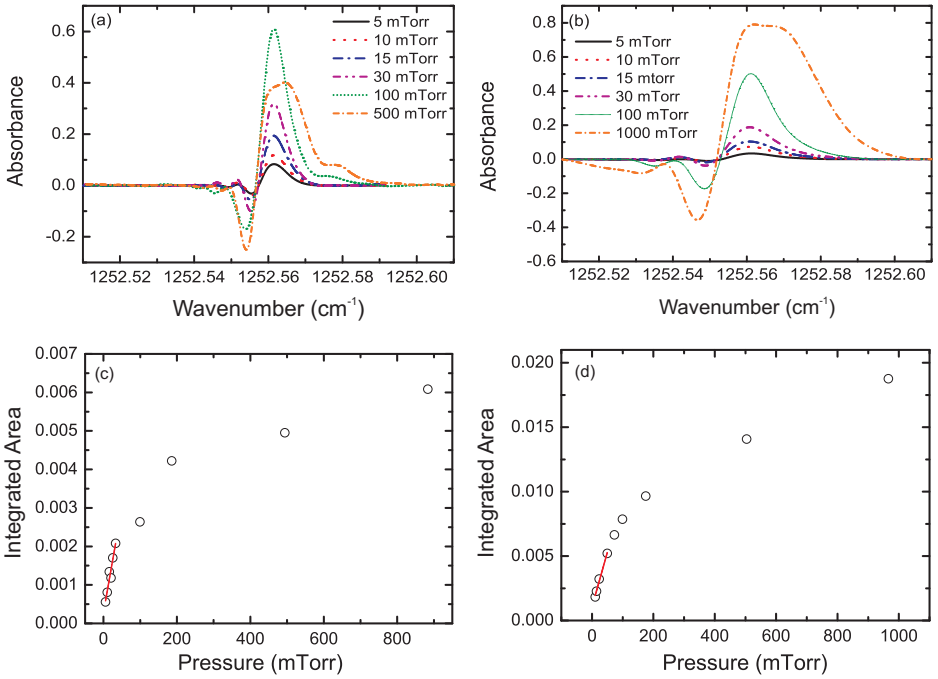

FIGURE 2.12: Spectra for varying pressures of N_2O gas measured using (a) the Daylight EC-QCL and (b) the Q-MACS QCL and compared with the observed integrated areas for(c) the Daylight and (d) the Q-MACS. The red lines correspond to a linear fit to the pressures below 50 mTorr, and correspond to integrated crosssection values of 2.14×10^{-20} and 3.32×10^{-20} cm^2 cm^{-1} molecule^{-1}, deviations of 46 % and 16 % respectively form the literature value of 3.98×10^{-20} cm^2 cm^{-1} molecule^{-1} [1].

Figure 2.12 shows the effect of varying the pressure of N_2O in a 70 cm cell between 5 and 500 mTorr for the EC-QCL and up to 1000 mTorr for the Q-MACS. The Daylight data is taken at a chirp rate of 75 MHz ns^{-1} and the Q-MACS data at 220 MHz ns^{-1}. Notably, neither system returns a peak absorbance in line with that expected from the Beer-Lambert Law, an effect characteristic of rapid passage [68]. For example, in the Daylight spectra the maximum absorbance shown in Figure 2.12(a) is ~ 0.23, whereas a value of 0.76 is expected from the Beer-Lambert Law. Also, as high pressures are reached a second absorption feature at 1252.579 cm^{-1} due to a P(34)f transition in the $(1,1,1,0) \leftarrow (0,1,1,0)$ band starts to become apparent for the Daylight spectra, whereas only a slight perturbation is observed for the Q-MACS system - an effect reflecting the difference in resolution of the two systems. Examining the integrated areas of the absorption section of the features, an approximately linear increase in the magnitude of the signal with pressure up to about 50 mTorr is seen for both lasers but with significantly different gradients. For the EC-QCL a gradient that is only 54% of that expected from the integrated absorption cross section is observed, implying a deviation between the measured and experimental number densities of 46%. For the Q-MACS system the corresponding deviation is only $\sim 16\%$, and this disparity reflects the non-equilibrium nature of the laser matter interaction and the larger driving provided by the high powered Daylight system. These observations reflect the increased driving in the system leading to complex and rapidly varying temporal behaviour of the refractive index.

2.6 Probing Optically Thick Minimally Damped Systems

Further to the reduced peak area, rapid passage signals are also seen to induce a more subtle pressure dependent effect in the observed spectra of low pressure, highly absorbing gases. This section investigates these effects with the application of a multipass White cell.

An experiment was set up, whereby light from either the Q-MACS or the Daylight QCL could be directed through a 5 m path length White cell (Specac Tornado) with CaF_2 windows and onto the VIGO detector. The cell was filled with a quantity of N_2O and the spectra of the P(36)e transition in the ν_1 bending mode at 1252.6 cm^{-1} observed with both lasers. Figure 2.13 shows the results of this study, and it is clear that as the number density of gas is increased, the initial spike in the RP signatures consistently shift to lower wavenumber at a rate of 100s MHz $Torr^{-1}$: an effect at least three orders of magnitude larger than would be expected from traditional pressure induced shifts (c.a. 0.1-1 MHz $Torr^{-1}$) [76].

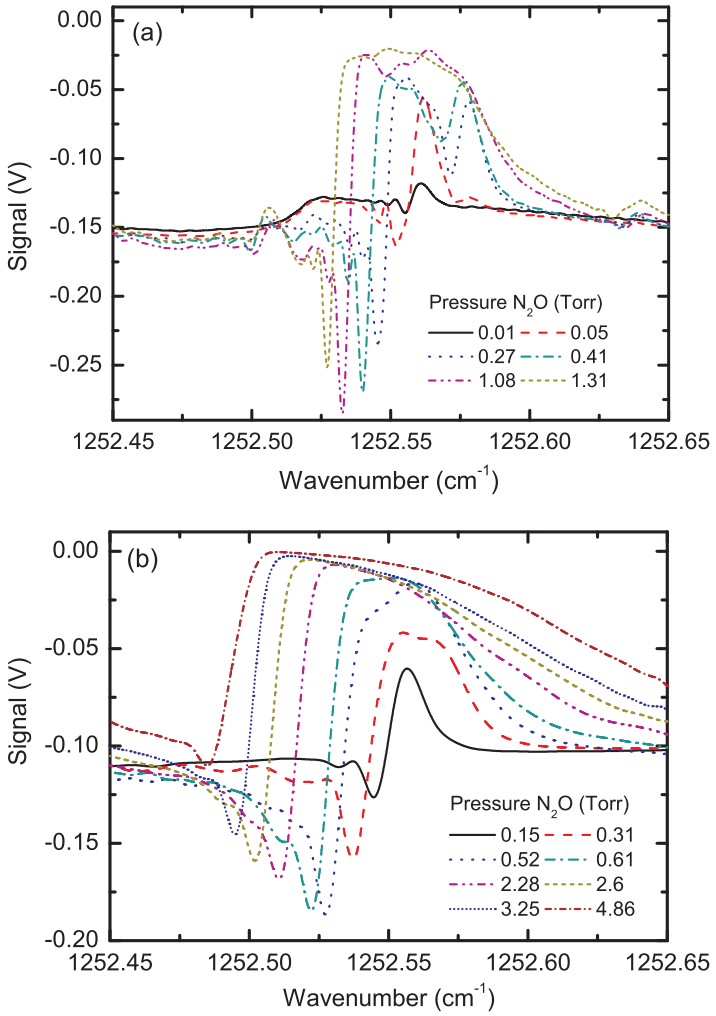

FIGURE 2.13: Rapid passage signals as a function of N_2O pressure for the P(36)e transition measured with (a) the Daylight and (b) the Q-MACS laser.

It is notable that the data shown in Figure 2.13(a), which were obtained using the Daylight laser, show more structure at higher wavenumber than that in Figure 2.13(b). This is the same structure present in Figure 2.12 due to the interference of a relatively weak (10^{-22} cm^2 cm^{-1} molecule^{-1}) transition much more apparent here due to the high pressures and long path length.

In order to verify that this pressure-induced shift was genuine, and not an experimental artefact induced by external factors, etalon traces were taken alongside the molecular spectra in order to show that the lasers were well-behaved. Unfortunately, the setup did not permit simultaneous spectra and etalon traces to be recorded, as the power output of the Q-MACS laser was too low for etalon contrast to be achieved from the split beam, but verification of the frequency stability was possible. Figure 2.14 shows spectra recorded with the Q-MACS laser at 15 mTorr and 380 mTorr of N_2O with a 10 minute interval, along with etalon traces taken immediately after the first measurement, and directly before the second. Whilst there is a clear shift in the emission peak between

TABLE 2.1: The spectroscopic data for the N_2O and CH_4 transitions investigated in this work [1].

Molecule	Line position cm^{-1}	Integrated linestrength $cm^2\ cm^{-1}\ molecule^{-1}$	Einstein A factor s^{-1}	Transition dipole moment D	Rotational assignment
N_2O	1252.5608	3.98×10^{-20}	5.60	7.62×10^{-2}	P(36)e
N_2O	1261.9874	10.4×10^{-20}	5.77	6.48×10^{-2}	P(26)e
CH_4	1253.3491	2.08×10^{-20}	2.04	1.22×10^{-2}	P(8)

these two spectra, the two etalon traces are completely in-phase, from which a high level of laser stability can be inferred.

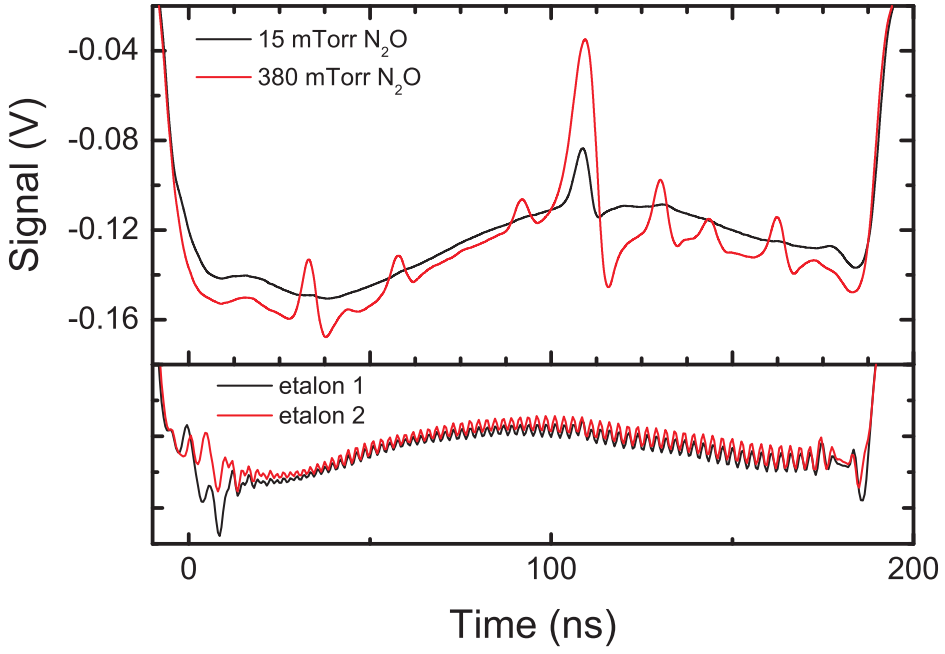

FIGURE 2.14: Spectra of the P36(e) transition for 15 mTorr and 380 mTorr of N_2O measured with the Q-MACS laser and taken with a 10 minute interval, alongside etalon traces taken following the first measurement (etalon 1) and immediately preceding the second (etalon 2). The spectrum at higher pressure exhibits a clear delay in RP signal.

Having determined the validity of our measurements it is now possible to further investigate this effect by comparing the pressure shifts of a number of transitions in different molecules; specifically the transitions P(26)e and P(36)e of the ν_1 symmetric stretch mode of N_2O and the P(8) transition of the ν_4 bending mode of CH_4. Due to the limited tuning range of the Q-MACS system the P(26)e transition was only accessible with the Daylight laser. The spectroscopic data pertinent to the probed transitions is

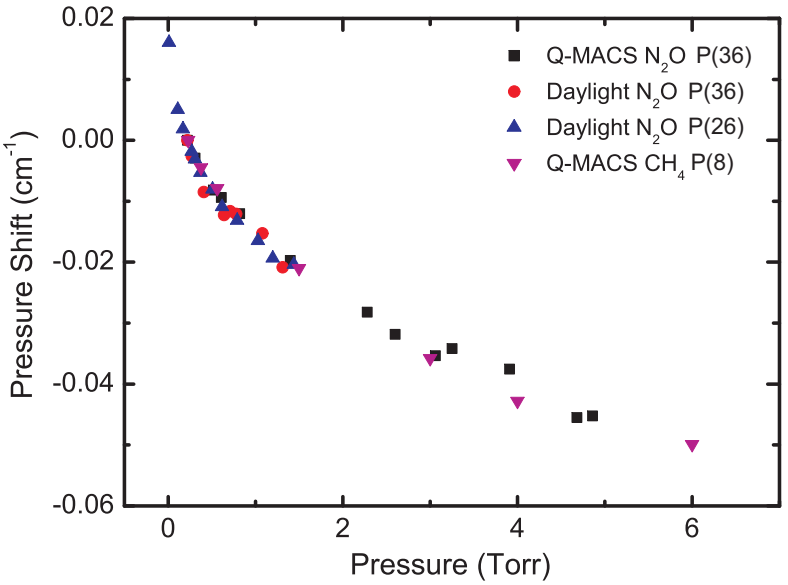

FIGURE 2.15: Pressure shifts for a selection of transitions measured with both the Q-MACS and Daylight Solutions Lasers.

given in Table 2.1. Figure 2.15 gives the frequency shift between the absorption and first emissive peaks relative to that at 20 mTorr, as a function of gas pressure.

As the delay increases as a function of pressure, pressures lower than 20 mTorr will give positive shifts in our reference frame, but this is only an effect caused by the normalisation procedure. From this data it is clear that for a given transition (within the conditions measured), the magnitude of shift is independent of the laser used, and hence the power, and chirp rate, and that it does not vary significantly between the N_2O transitions and the CH_4 transition despite a difference in transition dipole moment of a factor of 6. It is also of note that each of the tetrahedral splitting components of the P8 and P9 CH_4 transitions show the same behaviour, though this data has been omitted from the graph for clarity.

It therefore appears that the medium couples to the laser equally efficiently for these transitions, leading to an equivalent change in the refractive index of the gas at a given pressure and a similar pressure shift is observed.

Whilst this data would appear to show that the measured shift is transition dipole independent, other work investigating strong transitions ($\sigma \sim 10^{-19}$ cm^2 cm-1 molecule^{-1}, $\mu \sim 1$ D) ν_2 band of NH_3 around 10 µm has shown a measured shift directly related to the transition dipole moment [69], a conclusion that marks the similarity in shifts for N_2O and CH_4 as unexpected. However, the rapid passage structure is determined not only by the magnitude of the polarisation induced within the sample but also by the dephasing rates due to collisions, and it is here that T_1 and T_2 play a role. The measurements presented here are sensitive to the difference in the dephasing rates between

these two species, with the polarisation of the N_2O being more readily removed by self collisions than is the case for CH_4; a result in keeping with the longer range dipole-dipole interactions that operate between N_2O molecules compared with non-polar CH_4, and mirroring the collisional broadening rates [1].

This pressure shift in rapid passage signals of high absorbance but low pressure gas samples has been observed previously in studies by Duxbury et al [67]. They worked on the spectroscopy of N_2O in a long path Herriot cell (up to 110 m), at 7.8 µm, and later C_2H_2 at around the same wavelength [70]. In these papers, comparisons were made between this effect and that observed by Genack et al [77] whilst investigating the travelling wave amplification of short CO_2 laser pulses in a cell containing hot CO_2. In Genack's work the laser radiation had a phase shift externally applied to it using a CdTe phase shifter, and the constructive and destructive interference between this radiation and the field induced in the CO_2 cell observed. Although in neither Duxbury's work nor our own is an external phase shift employed, it is thought that one can be induced in the incident radiation during propagation through the cell. Thus, it is supposed that the long path length, and small degree of collisional relaxation in our experiments allows this pressure shift to be observed. In Duxbury's work the importance of this very extended path length is thus emphasised, and simulations have been published, solving the Maxwell-Bloch equations numerically for a closed two level system, incorporating a step-wise propagation of radiation through the sample [70]. This model however, whilst showing qualitative agreement between theory and experiment, returns a factor of 5 discrepancy between the modelled and experimental shift.

In order to gain further insight into the role played by pathlength, studies have also been carried out in a 40 cm cell where propagation effects should play a minimal role in the interaction of the radiation with the sample. The shifts previously measured over a 5 m path length for CH_4 P(8) and N_2O P(36)e transitions are plotted in Figure 2.16(a), and alongside these are the shifts measured for the same transitions in a 40 cm cell. It is apparent here that at shorter path lengths the shifts in the rapid passage signal still occur, and are still congruent but display a marked decrease due to the shorter path length. Figure 2.16 further shows the methane data plotted alongside simulations performed by E. McCormack solving the Maxwell-Bloch equations and propagating the results using the analytical expressions for a driven two-level system with relaxation, given by Torrey [78]. Reasonable agreement is seen between simulation and theory, and it is clear that there is no need for self-focusing to be invoked as suggested by Duxbury et al. [70].

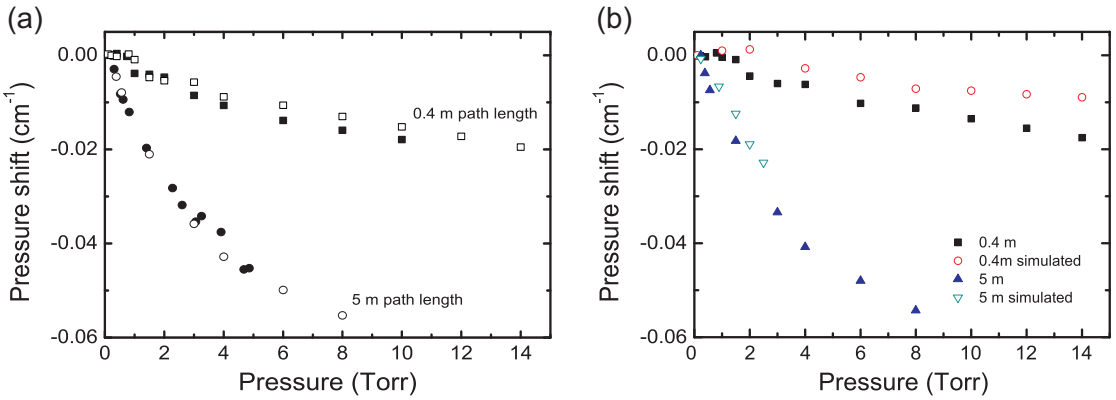

FIGURE 2.16: (a)Pressure shifts for the N_2O P(36)e (closed symbols) and CH_4 P(8) (open symbols) transitions as measured with the Q-MACS laser for an absorption path length of 0.4 m and 5 m. (b) The CH_4 results from (a) alongside simulations performed by E. McCormack, showing good agreement between theory and literature.

2.7 Population Transfer

The rapid passage signals observed in the case of pulsed QCL spectra are due almost entirely to a change in polarisation with very minimal population transfer. There is however great interest in the prospect of state preparation, particularly for use in reaction dynamics or kinetics - the ability to produce a sample of reagent in a specific excited quantum state would allow further insight into the potential energy surfaces of, say, the photolysis of ozone or N_2O.

This section discusses a variety of single photon methods used to prepare molecules into an excited state, and considers ways of increasing the population transfer produced by the rapid passage effect.

2.7.1 Incoherent and Coherent Light

We once again return to our two-level atom in the ground state, and now apply incoherent, near-resonance radiation. Using Einstein's treatment of excitation and emission within a system, and assuming that the radiation is intense enough that spontaneous emission has a negligible effect upon the population, the excited state population at time t is

$$P_e(t) = \frac{1}{2}[1 - e^{-BF(t)}], \tag{2.12}$$

where $F(t) = \int_{-\infty}^{t} I(t')\,\mathrm{d}t'$ is the pulse radiation fluence up to time t, with $I(t)$ the time-varying radiation intensity, and B the Einstein coefficient [79]. As time increases the excited state population monotonically increases towards 50%, the saturation value, and the maximum population transfer possible with incoherent light.

If we replace our incoherent light source with a coherent one, then the behaviour of the system changes, and instead of a monotonic increase we instead see the sinusoidal oscillations in the excited state population referenced in section 2.3,

$$P_e(t) = \tfrac{1}{2}(1 - \cos \Omega t), \tag{2.13}$$

where $\Omega = \frac{\mu\epsilon}{\hbar}$ is the previously discussed Rabi frequency. If the electric field is varying with time then Ω is replaced by the pulse area $\theta(t) = \int_{-\infty}^{t} \Omega(t')\,\mathrm{d}t'$. As can be seen from Figure 2.17, the excited state population now oscillates between 0 and 1, and given a pulse area equal to an odd multiple of π complete population transfer to the excited state can be achieved.

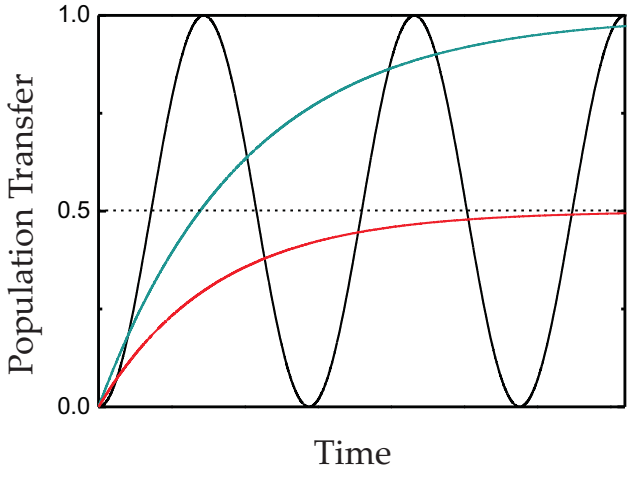

FIGURE 2.17: Schematic showing population transfer achievable using Incoherent (red) and Coherent (black) radiation versus adiabatic rapid passage (blue).

2.7.2 Adiabatic versus Linear Rapid Passage

Whilst complete population transfer can be achieved via a π-pulse in an idealised case, in practice it is not so simple. A real sample of molecules or atoms will always be in motion, and as such will exist with an array of velocities. Molecules with a velocity component in the direction of beam propagation will experience a Doppler shift such that that excitation is no longer exactly resonant and molecules moving transversely to the laser propagation will experience a pulse duration dependent upon their transit time across the beam. These velocity dependent effects, along with fluctuation in the electric field due to beam inhomogeneities result in a significant decrease in population transfer; in extreme cases down to the 50% observed in incoherent studies. In contrast,

adiabatic rapid passage (ARP) is relatively robust with respect to these effects. A thorough description of the optical phenomenon is given in the paper by Vitanov et al [79].

More generally Ernst,(in 'Sensitivity Enhancement in Magnetic Resonance vol. 2') [80] discusses the different regimes within which passage through resonance can occur, as shown in Figure 2.18. The behaviour observed in an experiment is here defined by the relationship between two parameters, the saturation parameter S, and the normalised chirp rate A where,

$$S = [\Omega_0]^2 T_1 T_2 \qquad \text{and} \qquad A = \alpha T_1 T_2, \tag{2.14}$$

with the chirp rate, α, defined as the radiation frequency change as a function of time in units of $(\mathrm{Hz})^2$, Ω_0 the on resonance Rabi frequency and T_1 and T_2 are again the depopulation and de-excitation time periods. For the pulsed QCL experiments discussed here the high chirp rate places us in the fast passage regimes to the right hand side of the diagram. Whether the rapid passage is linear or adiabatic is thus determined by the ratio, β,

$$\beta = \frac{A}{S} \quad = \quad \frac{\alpha}{[\Omega_0]^2}. \tag{2.15}$$

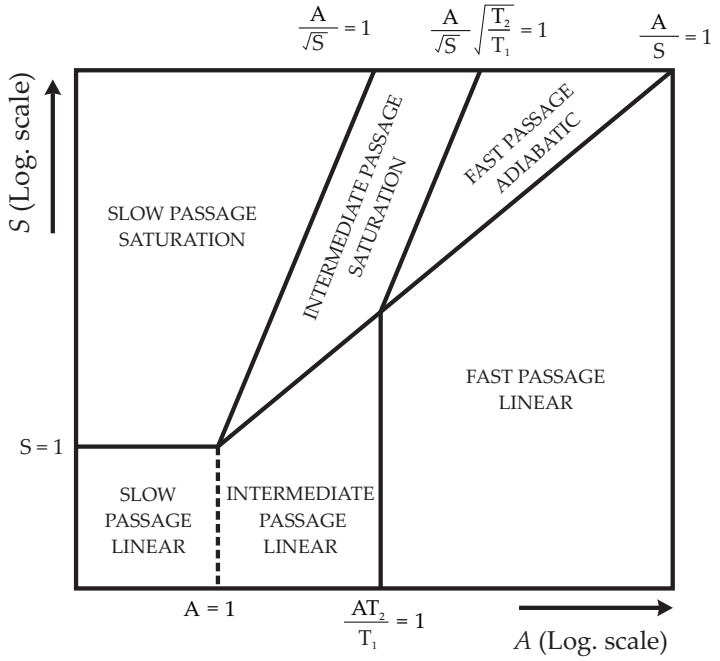

FIGURE 2.18: Passage regions as determined by the relaxation normalised chirp rate, A, and saturation parameter, S. Adapted from [80].

The principle of ARP can be understood best by considering the Bloch formalism, as although equations 2.7 - 2.8 are derived for a field at fixed frequency, this constraint can be relaxed under the condition that the field variation is slow enough

$$\frac{\mathrm{d}}{\mathrm{d}t}\left|\frac{\Delta}{\kappa\mathcal{E}}\right| << \kappa\mathcal{E}. \tag{2.16}$$

As for the constant field case, applying an electric field $\mathcal{E}$ to the system causes the Bloch vector to begin precessing around the applied torque vector at a frequency $\Omega(\Delta, t) = \sqrt{(\kappa\mathcal{E}(t))^2 + \Delta^2}$. Now, imagining an initial system with a field far from resonance (i.e. a large $|\Delta|$), we can consider the effect of sweeping $\mathcal{E}$ through the transition much faster than relaxation, but still satisfying Equation 2.16. Here, with a large transition dipole moment and/or a strong laser field the adiabatic condition can be met, and $\boldsymbol{\Omega}(t)$ will change direction very slowly compared to the rate of precession of $\boldsymbol{\rho}$ around it. In this manner the Bloch vector can be said to adiabatically follow $\boldsymbol{\Omega}(t)$. If $\boldsymbol{\rho}$ begins at the nadir of the Bloch sphere then this adiabatic following can lead to a complete inversion, as the w component evolves from -1 to +1. This effect, is demonstrated in Figure 2.17 and was first used experimentally to achieve population transfer in NMR [81]. It has however since been achieved optically through tuning of both the laser radiation [82], and also the transition frequency itself in Stark spectroscopy [62].

In these current pulsed experiments, whilst the chirp rate is large enough to ensure that passage is observed, the conditions required for the observation of ARP are not met. That is that whilst the rate of change of detuning must be much faster than relaxation,

$$\frac{\Omega(0)}{T_2} << \frac{\mathrm{d}\Delta}{\mathrm{d}t}, \tag{2.17}$$

the precession of the torque vector $\boldsymbol{\Omega}$ around $\boldsymbol{\rho}$ is too fast for the following condition to be met

$$\frac{\mathrm{d}\Delta}{\mathrm{d}t} << \Omega^2 \tag{2.18}$$

and thus allow adiabatic following. Figure 2.19 shows a simulation of the evolution of w as a typical pulsed QCL pulse is applied, chirping from positive to negative detuning at a chirp rate of 65 MHz ns^{-1}, over the P(36)e transition of N_2O (resonance at 0 ns).

Population transfer can be quantified from this graph as equal to $(w + 1)/2$, and it is instantly apparent that even in this simplified case insufficient excited state molecules (0.0015%) would be prepared for any secondary applications.

In order to sufficiently increase this transfer level we would need to move towards the adiabatic limit. As the boundary between linear and adiabatic rapid passage is defined by the $A/S = 1$ limit, if we consider only situations in which behaviour can be considered

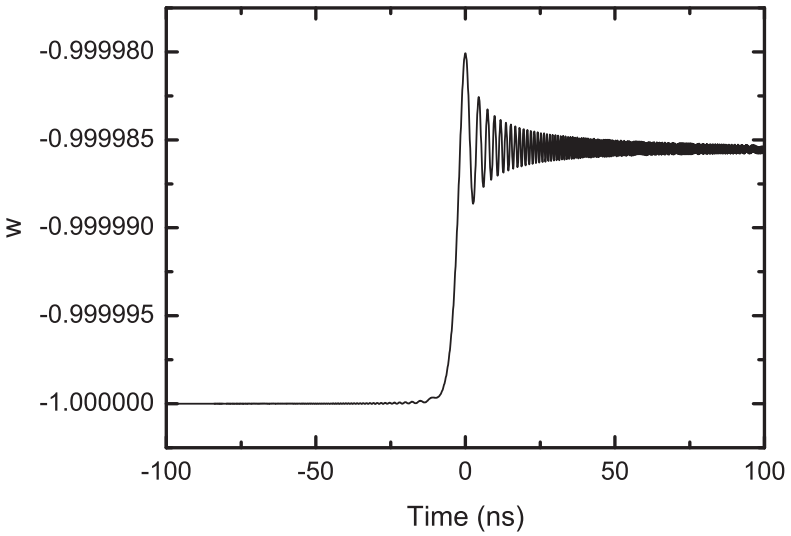

FIGURE 2.19: Simulation performed using the Maxwell-Bloch equations estimating the population inversion (w) induced during a Q-MACS pulse upon the CH_4.

as rapid then the aforementioned value $\beta = \alpha/[\Omega_0]^2$ may be used as a marker of passage form. Particularly we can consider $\beta = 0$ and $\beta = \infty$ as the limits towards which we wish to tend in order to reach either adiabatic or linear rapid passage respectively. In the present case we find ourselves firmly in the linear regime with a β of 1100, far from the ideal case as is shown in Figure 2.20.

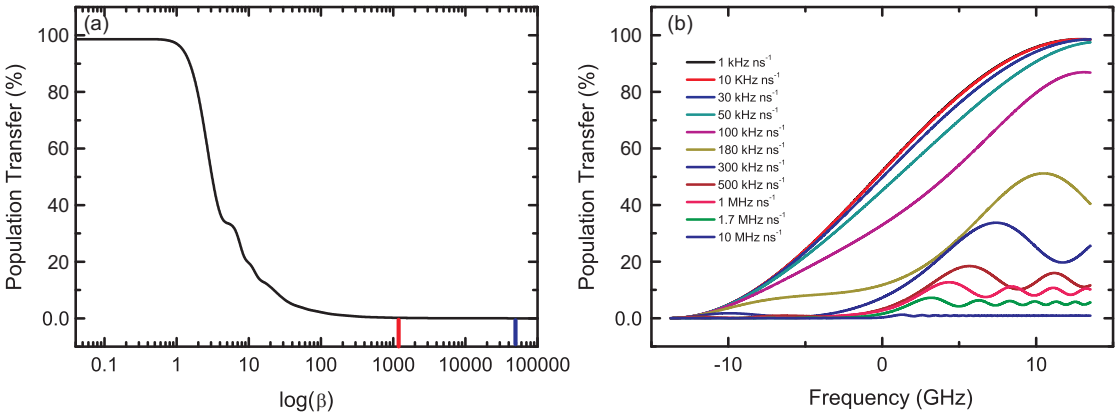

FIGURE 2.20: (a) Population Transfer as a function of β. Q-MACS and Daylight β's shown as blue and red (b) Population transfer as a function of frequency for a selection of chirp rates.

Thus, in order to increase the population transfer we shall need to either increase our Rabi frequency or decrease our chirp rate. The chirp rate of a pulsed QCL is however determined by the rate of heating and as such is invariable outside of narrow limits. Thus, with a typical chirp rate of 65 MHz ns^{-1} a Rabi frequency of 250 MHz would be required to meet the adiabatic condition $\beta = 1$. In order to achieve such a large Rabi frequency the electric field would have to be 40 times larger than present, demanding

the beam radius be reduced to c.a. 100 µm. Whilst it would be physically possible to reach this beam waist, such strong focusing would result in rapid divergence following the focal point and thus significantly decrease the useful interaction path length such that only a very small number of molecules would see anywhere near the maximum electric field.

In contrast, were we to have control over the rate of frequency change, then for the P(36)e transition, lowering the chirp rate to c.a. 50 kHz ns^{-1} would give us $\beta = 1$. For pulsed laser systems this is not possible, but Chapters 4 and 5 discuss population transfer options provided by the higher powers and control of chirp rate afforded by cw QCLs.

As the simulations shown in Figure 2.20 demonstrate, all of the experiments performed in this chapter are well within the linear passage regime. However, in order to further investigate this limit, work has been performed investigating the slower chirping Daylight QCL at a variety of powers. In Figure 2.21 data is shown for spectra of 30 mTorr of N_2O in a 70 cm cell for two different chirp rates (75 and 58 MHz ns^{-1}). In this experiment the

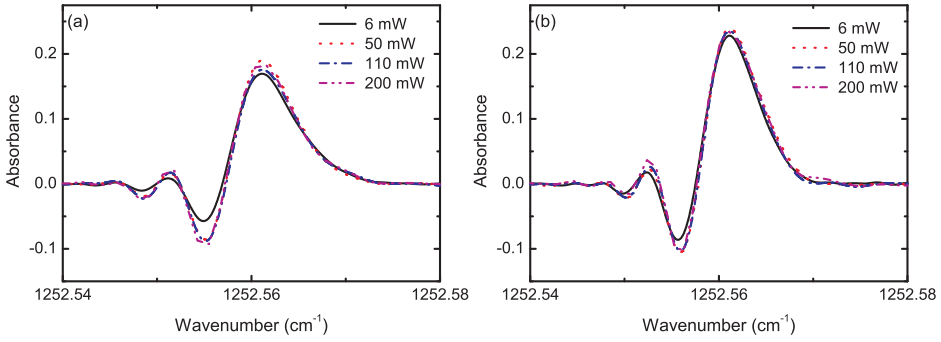

FIGURE 2.21: Spectra for varying powers in the Daylight EC-QCL (a) at a chirp rate of 75 MHz ns^{-1} and (b) at a chirp rate of 58 MHz ns^{-1}. The power levels correspond to the averaged power.

laser output power was maintained at its maximum output power, but then attenuated before the cell with the use of a wire grid polariser. The rapid passage structure is clearly observed over two decades of power at both chirp rates, demonstrating the relative insensitivity to power in this regime. This result is expected, and is demonstrable from the Bloch 'phase diagram' in Figure 2.18, as a change of power without a variation in chirp rate is merely a change in S and as such is a vertical transition on the diagram. It is there demonstrated that the linear rapid passage regime is maintained down to the horizontal axis from any point within that regime.

2.8 Conclusions

This chapter has seen discussion of two different QCLs, a DFB QCL and a higher power EC-QCL. The spectral output of both lasers has been compared, and the effects of the rapidly swept pulses have been examined. Rapid passage has been shown to disappear as a function of increased collision rate, and a simple model has been presented to explain the behaviour of this effect within a two-level atom. The effect of pressure and path length upon the form of rapid passage signal has been investigated, and the shift between positive and negative absorption described as a function of number density for a number of transitions in N_2O and CH_4. These delay measurements have provided some surprising results, both in the concordance in degree of shift between these molecules, and in the importance of path length. These measurements have thus indicated the insights that this form of coherent spectroscopy can provide into the relaxation processes within the molecular gas system, and the degree to which field propagation can play a part in the observed spectra. Finally, a discussion was presented of the various means of producing population transfer within a molecular system, with an eye upon the coherent processes occurring during a QCL pulse. The effect of power upon the observed spectra was observed, and it has been concluded that pulsed QCLs are not currently capable of the power and chirp rates required for utilisable population transfer.

Chapter 3

Continuous Wave Quantum Cascade Laser Absorption Spectroscopy

The first continuous wave (cw) QCL was demonstrated a year later than its pulsed analogue [19], a delay owing in large part to the thermal stress induced by the large amount of heat that builds up in the active region during operation. Thus, innovations in heat management were required, leading to the first room temperature cw QCL being demonstrated only in 2002 [83]. Indeed water cooling is typically still required for their operation, though convection based devices are starting to become available.

There are a number of advantages of cw QCLs over pulsed systems; for one, tuning schemes are much simpler, as a scan can be performed by applying a current ramp directly to the laser. Furthermore, as the current change can be made to be relatively slow and constant there is no observable frequency chirp as there is in *both* pulsed operating modes, meaning that there is negligible tuning-rate-induced broadening so that sub-Doppler resolution is achievable raising the prospect of the utilisation of sensitive detection schemes based upon optical cavities.

In this chapter work is presented using both DFB and external cavity cw QCLs. A variety of spectroscopic techniques are discussed and their sensitivities are compared. The high resolution afforded by these devices is then utilised to determine spectral constants of deuterium bromide, previously unknown due to the lack of versatile radiation sources in the mid-infrared.

3.1 Experimental

3.1.1 EC-QCLs

Most of the work presented in this chapter is performed using one of two EC-QCLs from Daylight solutions both based upon the 21052-MHF model: one operating over the range 1872–1958 cm^{-1} at a chip temperature of 15 °C, outputting powers in excess of 60 mW, and another covering a wider range (1776–1968 cm^{-1}) at a chip temperature of 17 °C with output powers in excess of 80 mW over the whole range. For this latter device there is a smaller internal region (1870–1920 cm^{-1}) free from mode-hops and over which the output power was in excess of 100 mW, but there is no such range for the former. In both cases where mode hops were present in a scan, alteration of either the injection current or chip temperature was often sufficient to provide a single mode scanning range of c.a. 0.5 cm^{-1}. The behaviour of these two systems is similar enough that distinguishing between models is not necessary except for where it is obvious (for instance in available tuning ranges, or higher output powers) but for clarity's sake, work performed with an EC-QCL in this chapter is largely performed using the narrower tuning device excepting that in Section 3.3 and all else in this thesis is performed with the wider tuning device.

Both devices are capable of being tuned through three mechanisms operating on different time scales; the length of the cavity may be stepped using the laser controller, a sine wave (up to 10 V) can be applied to the piezo (PZT) controlling the output grating, or a ramp applied directly to the injection current. The cavity length can be stepped with 6 different preset tuning rates for the grating inside the laser head, the fastest of which covers the entire tuning range of the laser in c.a. 10 s. This tuning mechanism is exhibited in Figure 3.1(a) whereby the laser beam from an EC-QCL is passed over 2 m of free space and collected onto a detector (VIGO PVI-2TE-6). The fast oscillation on the baseline (Figure 3.1 (c)) corresponds to an imperfect anti-reflection coating, which is optimised for operation at the high wavenumber end of the tuning range, but the larger sharp dips correspond to transitions due to aerial water ($\sim 1\%$), which are compared to the (black) HITRAN data [84]. An average tuning rate of 100 MHz ms^{-1} is observed, and over the entire range of the laser there are more than 40 mode hops, in the lower wavenumber region (Figure 3.1 (b)). These mode hops are largely due to manufacturing issues with the antireflective coating, and its sub-optimal performance in this region, although there is a further contribution from impedance mismatching as discussed in [85]. Using this method of scanning data was typically very noisy, and averaging made impossible due to hysteresis in the scan.

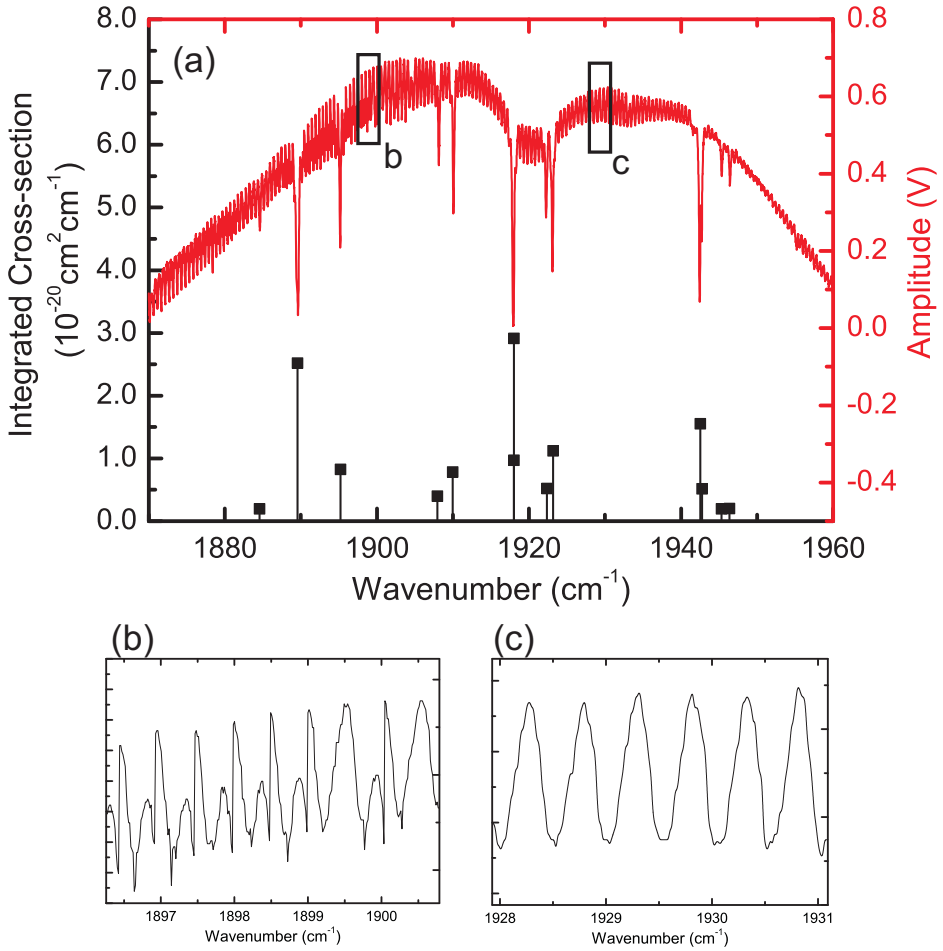

FIGURE 3.1: Transmitted intensity after a pathlength of 2 m in laboratory air ($\sim 1\%$ water in laboratory air) showing (a) the spectrum of the ν_2 band of water between 1872 and 1958 cm^{-1}as compared to the HITRAN water spectrum, (b) mode hops in baseline oscillation, (c) fast oscillation due to imperfect antireflection coating.

When tuning the system by applying a sine wave modulation to the PZT in the laser head, a spectral range of c.a. 1.2 cm^{-1} can be swept through at rates from 1 - 100 Hz. Figure 3.2 shows the effect of tuning the laser in this manner over the (14,2,13) ← (13,1,12) transition within the ν_2 band of water in 2 m of lab air. In this case a 70 V signal has been applied to the piezo at a frequency of 10 Hz, and a Voigt fit is shown on top of the data. The recorded transition has a full width at half maximum (FWHM) of 850 MHz, consistent with an air-broadening parameter of 0.51 MHz $Torr^{-1}$ as reported in the HITRAN 2004 database [84].

When modulating the injection current of the laser, a sine wave of 2 V peak to peak can be applied at rates between 10 kHz and 2 MHz, resulting in a maximum tuning range of c.a. 500 MHz. Unfortunately this limited tuning range is narrower than the full width of a typical transition in this tuning range (Doppler widths c.a. 200 MHz) and so is not generally applicable to direct spectroscopy (for an exception see section

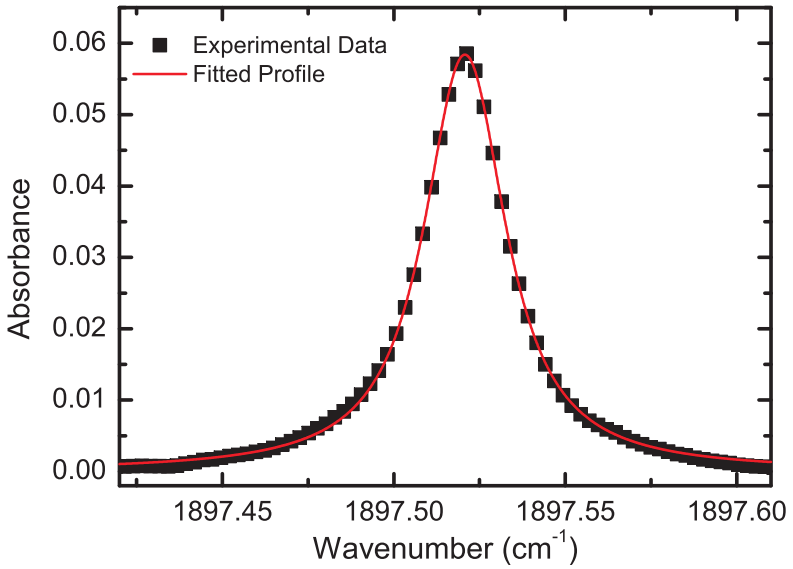

FIGURE 3.2: A typical spectrum of the (14,2,13) ← (13,1,12) transition of water recorded by scanning the PZT.

4.1.5). Instead this tuning method is very useful for the fast frequency change required in modulation spectroscopy as will be demonstrated in section 3.2.3.1. The use of this tuning methodology was further limited by the band pass filter applied internally to the injection current which meant that the transfer function of the modulation amplitude was not constant below c.a. 15 kHz.

In typical running modes, the EC-QCL output was attenuated immediately following the laser facet in order to both reduce saturation effects and make the laser beam eye-safe.

3.1.2 DFB QCLs

The DFB lasers used in the work presented in this chapter were acquired directly from the manufacturers, one 5 µm laser from Alpes Lasers SA operating between 10 and -30°C and producing up to 7 mW of laser light between 1818 and 1830 cm^{-1}, and a 10 µm laser from Hamamatsu operating between 1029.5 and 1032.3 cm^{-1} and producing up to 6 mW of power. The 5 µm laser was mounted in a prototype homemade device, as is shown in Figure 3.3, designed and built in order to allow the application of non-proprietary current and temperature drivers and thus permit a large degree of control and flexibility of operation.

The 10 µm laser by contrast was operated in an ILX Lightwave mount (LDM-4872), and both lasers were driven using an ILX Lightwave high compliance current driver (LDX-3232). For the most part low noise ILX temperature controllers (LDT-5545B) were utilised for both lasers, but where specified the 5 µm laser was utilised in tandem with

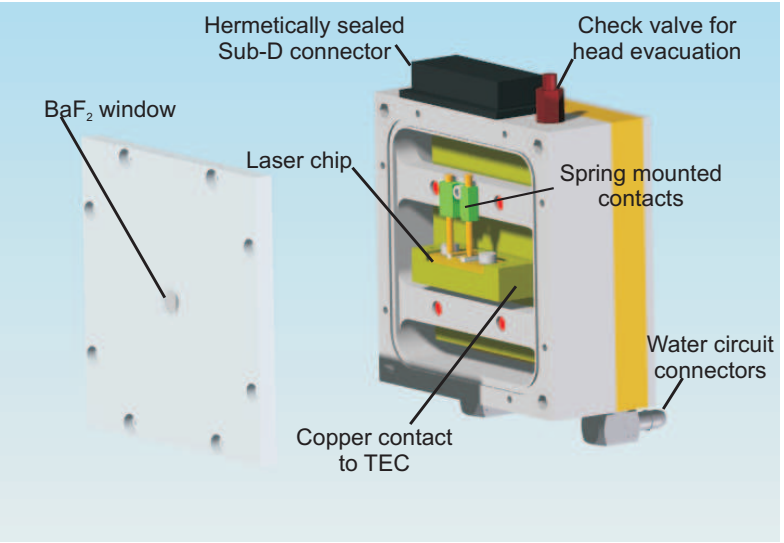

FIGURE 3.3: Exploded diagram showing design for prototype laser mount.

a homemade temperature control. As opposed to the Daylight system, direct control of the various laser operation parameters was available, and the laser output power and voltage as a function of applied current (LIV plot) is shown for the 5 µm laser in Figure 3.4 taken from the Alpes specification sheet.

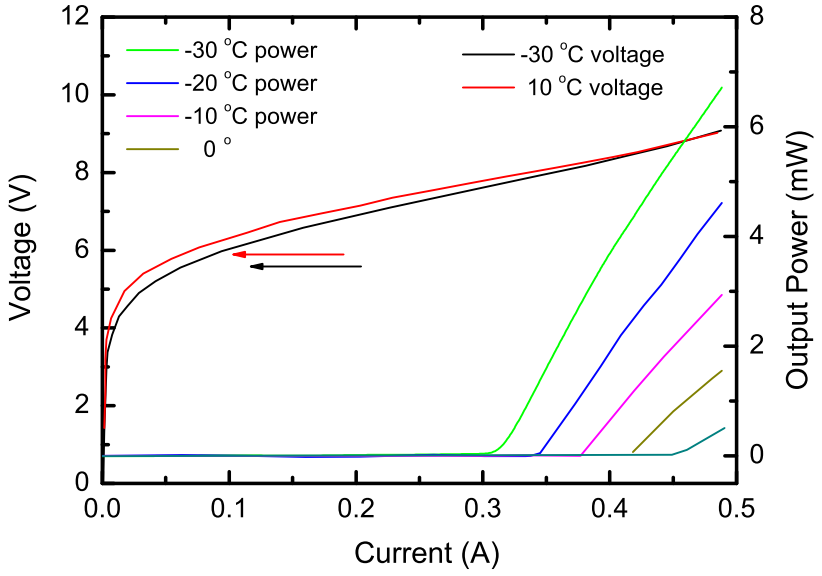

FIGURE 3.4: Output power and voltage as a function of applied current for the Alpes Laser 5 µm QCL at a range of temperatures. Voltage curves are only shown for the extreme temperature values for clarity.

Tuning of these lasers was performed through the simple application of an external function to the ILX controller, which effectively sums the two waveforms. QCLs are

particularly sensitive to noise in the injection current, and thus operation was performed in the high bandwidth mode, allowing modulation up to 250 kHz. In this arrangement, the laser could be tuned relatively quickly over a wide wavelength range, thereby shifting the timescale of data acquisition away from long term drift and the $1/f^n$ technical noise which has been shown by Bartalini et al [86] to be particularly limiting to laser bandwidth.

3.2 Spectroscopy

Much of the work presented here and in the following chapters is performed using nitric oxide, and as such a brief discussion of its spectroscopy, and real world importance is presented here first.

3.2.1 Nitric Oxide

Nitric oxide holds interest as both an atmospheric gas [87], as well as a human biomarker [53, 57, 88–92]. In the atmosphere NO acts as a source of tropospheric ozone during daylight through its reaction with partially oxidised organic species, and thus is a major contributor to photochemical smog. In terms of biological importance NO plays a part in all manner of processes, from immune reactions to neurotransmission [93, 94], and in 1998 the Nobel Prize in Physiology and Medicine was awarded to work recognising the role of NO in the cardiovascular system. In healthy human mouth breath there is typically 5-20 part per billion (ppb) of NO, 40-200 ppb in nasal breath, and levels of 200-500 ppb are reached whilst humming [95]. Variations from these parameters then signify an abnormality, with elevated concentrations largely associated with inflamed lower airways e.g. asthma, and reduced concentrations indicative of (amongst other things) cystic fibrosis - though it should be noted that there are better tests for the latter. Taking asthma as an example it is thus desired that a detection level of c.a. 1 ppb is achieved for accurate diagnostic use [95].

The ground state molecular orbital configuration of NO is:

$$X^2\Pi : (1\sigma)^2(2\sigma*)^2(3\sigma)^2(4\sigma*)^2(5\sigma)^2(1\pi)^4(2\pi*)^1 \tag{3.1}$$

As there is no strongly charged nucleus within the system, the resultant total orbital angular momentum, and electron spin, respectively L and S, are sufficiently weakly spin-orbit coupled that they instead couple to the electrostatic field produced by the 2 nuclear charges.

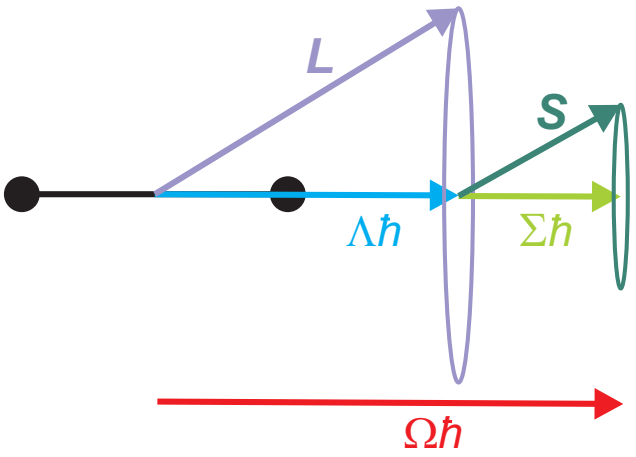

FIGURE 3.5: Schematic of the orbital and spin angular momenta in NO (Hund's case (a)).

The vector $\boldsymbol{L}$ is now strongly coupled to the field and the frequency of precession about the internuclear axis is so high that the magnitude of $\boldsymbol{L}$ is poorly defined, and it is no longer a good quantum number. Instead, only the component $\Lambda\hbar$ is defined. $\boldsymbol{S}$ is also coupled to the internuclear axis, but in this case due to the magnetic field caused by the motion of electrons and not the electrostatic field itself. S in fact remains a good quantum number with a projection onto the internuclear axis of $\Sigma\hbar$, with Σ analogous to M_s as $\Sigma = S, S-1, ... -S$, such that it has a multiplicity $2S+1$. The final quantum number of relevance here is $\Omega = |\Lambda + \Sigma|$, where $\Omega\hbar$ corresponds to the component of the total electronic angular momentum along the internuclear axis.

In the case of NO we have $\Lambda = 1$ and $\Sigma = \pm\frac{1}{2}$, and two closely spaced electronic states $^2\Pi_{\frac{1}{2}}$ and $^2\Pi_{\frac{3}{2}}$ as candidates for the ground state. The spin-orbit interaction shifts these levels by $\Delta E = A\Lambda\Sigma$, where A is the spin-orbit coupling constant. As A in this case is $+123$ cm^{-1} [96], $^2\Pi_{\frac{1}{2}}$ is the ground electronic state, but as the splitting between the two is significantly less than kT (208 cm^{-1}), there is appreciable population in both states and two sets of transitions are observed in the room temperature infrared spectrum. In Figure 3.6 both of the R(6.5) transitions in the $v = 1 \leftarrow 0$ fundamental vibrational band of NO are shown; the 'doublet' at c.a. 1900.07 cm^{-1} corresponding to the R(6.5)$_{\frac{1}{2}}$ and the 'singlet' at 1900.52 cm^{-1} to R(6.5)$_{\frac{3}{2}}$.

For all states with $\Lambda > 0$ a degeneracy is produced which, when perturbed by the rotation of the molecule, leads to two non-degenerate states, labelled e and f. It is this further splitting known as Λ-doubling that is apparent in R(6.5)$_{\frac{1}{2}}$, causing an observed doublet with a spacing of c.a. 330 MHz. This splitting also occurs in R(6.5)$_{\frac{3}{2}}$, but has a magnitude of only c.a. 26 MHz and so is not observable in Doppler broadened transitions with a width of c.a. 130 MHz.

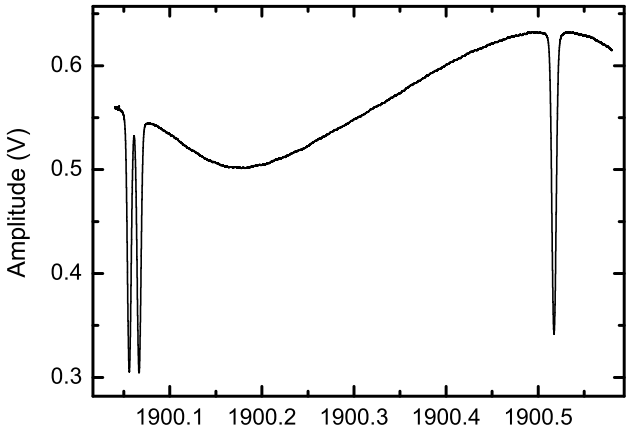

FIGURE 3.6: Spectrum showing the resolved and unresolved Λ-doublets due to the $R(6.5)_{\frac{1}{2}}$ and $R(6.5)_{\frac{3}{2}}$ transitions in the fundamental vibration band of NO respectively.

There is one more interaction of note here, though almost completely unobservable; the nuclear hyperfine interaction. As ^{14}N has a nuclear spin, I, of 1, each rotational level, J, is split into 3 hyperfine levels, characterised by $F = J, J \pm 1$ (excepting $J = 0.5$, which is split into $F = 0.5, 1.5$). This produces a shift in transition frequency of less than 1 MHz for the transitions observed here, and so can be disregarded for all but the most precise of work.

Finally, of importance when considering absorption spectroscopy are the selection rules in operation, the relevant ones being:

$$\Delta\Lambda = 0, \pm 1 \tag{3.2}$$

$$\Delta S = 0 \tag{3.3}$$

$$\Delta\Sigma = 0, \Delta\Omega = 0, \pm 1 \tag{3.4}$$

$$e \leftrightarrow e, f \leftrightarrow f, e \longleftrightarrow f \tag{3.5}$$

$$\Delta J = 0, \pm 1 \tag{3.6}$$

$$\Delta F = 0, \pm 1. \tag{3.7}$$

As the cases we will consider concern only ro-vibrational spectra we expect $\Delta\Lambda = 0$ and thus $\Delta\Omega = 0$. These rules are far from immutable, but Figure 3.7 shows the 3 strong transitions that make up one of the Λ-doublets of $R(6.5)_{\frac{1}{2}}$ in Figure 3.6.

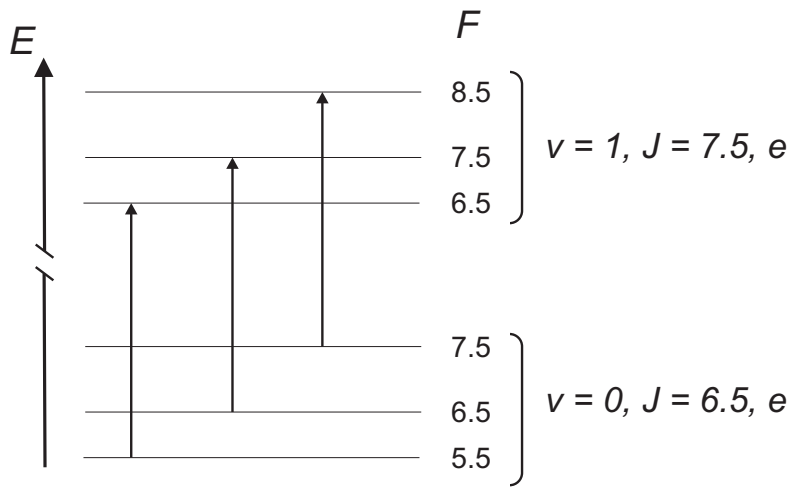

FIGURE 3.7: Schematic of the strong transitions between hyperfine split states making up one of the R(6.5)$_{\frac{1}{2}}$ doublets. All three of these transitions would appear within 1 MHz of each other in the centre of the lowest wavenumber doublet of R(6.5)$_{\frac{1}{2}}$ in Figure 3.6.

3.2.2 Direct spectroscopy

Direct absorption with a cw laser is one of the most obvious optical experiments. In this section similar experiments are performed with two lasers working around 5 µm (EC-QCL and Alpes). Considering the EC-QCL first, a 40 V signal was passed to the PZT at 97 Hz, and the laser radiation passed through a 70 cm cell and directed onto a detector (VIGO PVI-2TE-6). The cell was filled with 140 mTorr of NO, the laser tuned to 1906 cm^{-1}, and the resulting scan is shown in Figure 3.6. 100 averages were taken whilst acquiring this data, and the frequency scale was calibrated using a 500 MHz Ge etalon, giving line positions in agreement with literature to 0.005 cm^{-1} over the entire scan. The narrow absorptions (as has been discussed) correspond to the R(6.5) transitions, and the broad oscillation is in fact the same as the 'fast' oscillations seen in the wide scan in Figure 3.1. An oscillation of very small amplitude is also just perceptible upon the baseline in this spectrum which is due to optical feedback into the laser - an effect to which the external cavity laser is particularly susceptible, and one of the primary sensitivity limiting factors in all of our EC-QCL spectroscopy.

Figure 3.8 shows the $R(8.5)_{\frac{1}{2}}$ transition of 140 mTorr of NO in a 10 cm cell taken at 10 Hz. The 320 MHz Λ-doublet splitting for this absorption is clearly apparent, and by fitting Voigts to the individual hyperfine components with integrated area ratios determined by the HITRAN linestrengths, a measured Doppler width of 135 MHz was returned, in good agreement with the 130 MHz for a thermal sample at 298 K. Furthermore, the Lorentzian width component of the Voigt allows an estimate to be made of the laser bandwidth, which in this case is 18 MHz over the time taken for sample acquisition

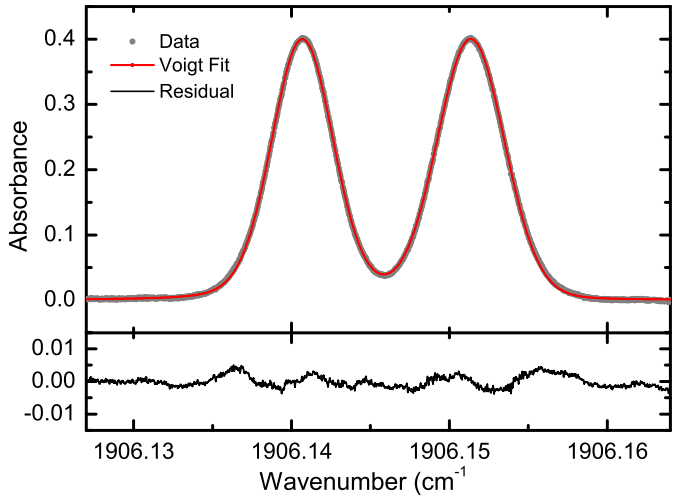

FIGURE 3.8: Spectrum showing the resolved Λ-doublets due to the R(8.5)$_{\frac{1}{2}}$ transition in the fundamental vibration band of NO taken with the Daylight Solutions EC-QCL alongside Voigt fit and residual.

(10 s). This is in reasonable agreement with other similar reported values of free running EC-QCLs [97–99], but is not the inherent linewidth, and this shall be further discussed in Chapter 4. The areas returned from these Voigt fits can further be used as a measure of the sample concentration, and from this a measure of the sensitivity of the detection method can be obtained. There are a number of ways of quantifying this sensitivity, and the choice is often largely arbitrary, but in this case, assuming a white noise dominated experiment we shall use the time normalised sensitivity, where

$$\alpha_{\min} = \frac{A}{(S/N)l}\sqrt{\pi\tau n}, \tag{3.8}$$

with A the absorbance at line centre, (S/N) the signal to noise ratio, l the path length, τ the time constant of detection, and n the number of averages. In this manner, typical sensitivities of $\alpha_{\min} = 4.8 \times 10^{-5}$ cm^{-1} Hz$^{-1/2}$ have been recorded for the wider tuning range EC-QCL.

Whilst running the Alpes laser it was possible to modulate at frequencies up to 250 kHz, and indeed, due to unisolable noise from the laboratory ground, it was desirable to operate at a frequency above the bulk of this noise. Figure 3.9 shows data taken with the laser tuning over the P(13.5)$_{\frac{1}{2}}$ transition at 1824 cm^{-1} at 150 kHz with 340 mTorr of NO in a 10 cm cell. Raw single sweep, and 6 MHz low pass filtered data are displayed, and time normalised sensitivities of $\alpha_{\min} = 2.5 \times 10^{-6}$ cm^{-1} Hz$^{-1/2}$ and $\alpha_{\min} = 9.2 \times 10^{-7}$ cm^{-1} Hz$^{-1/2}$ are achieved respectively. That this suggests a sensitivity at least an order of magnitude larger than that of the EC-QCL is determined largely by

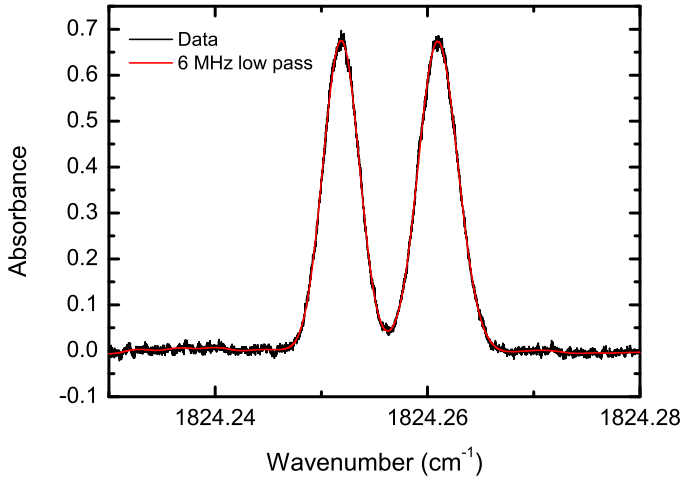

FIGURE 3.9: Spectrum showing the resolved Λ-doublets due to the $P(13.5)_{\frac{1}{2}}$ transition in the fundamental vibration band of NO, taken with the Alpes Laser QCL.

the fast acquisition permitted by the ILX current controller and measurements taken at 60 Hz returned a sensitivity of only 1.9×10^{-4} cm^{-1} Hz$^{-1/2}$. Thus, whilst a more sensitive measurement may be made in less time with the Alpes, this would not necessarily remain true were the Daylight capable of scanning over a transition at the same rate. Finally, Voigt fits of the fast scan data return a thermally anticipated Doppler width of c.a. 125 MHz and a Lorentzian component of 15 ± 2 MHz implying a time averaged laser bandwidth of that order.

3.2.3 Sensitive Detection Methods

Often, one wishes to detect a molecule that exists in small concentrations, or that has a weak absorption cross section - for example explosive detection, medical diagnosis or atmospheric analysis - and this remains one of the drivers of MIR spectroscopy. Therefore, higher sensitivity is desired than that which can be gained by pure direct absorption spectroscopy, and in these instances a number of techniques can be used, from modulation spectroscopies, to path length enhancement techniques, or even indirect detection methods such as photo-acoustic spectroscopy. This section discusses the relative merits, and compares the results of a few sensitive detection methods

3.2.3.1 Wavelength Modulation Spectroscopy

Wavelength modulation spectroscopy (WMS) is a detection method which removes random noise from a signal by encoding the incident radiation with a specific frequency

of modulation and then decoding the detected signal at that same frequency using a lock-in amplifier. Only the section of the detected signal which is encoded at the correct frequency and phase is then passed out from the lock-in for averaging. WMS was first demonstrated in 1978 [100, 101] and has found widespread use as the detection frequency is shifted away from the $1/f^n$ technical noise which peaks at low frequency. Unfortunately, the signals returned from the lock-in amplifier are not generally self-calibrated, as is the case for direct spectroscopy, but instead needs calibration by comparison with a direct technique. There are notable exceptions to this caveat in [102] and [103] though the first is applicable to only second harmonic detection of perfectly isolated lines and requires accurate knowledge of the frequency tuning, and the second whilst more widely applicable, requiring only collection of both in the signals in and out of phase with the applied sine wave (the x and y channels on an oscilloscope), is found to be difficult to implement in practice and requires significant absorption levels.

Theoretically, the application of WMS can be considered as follows: if we imagine a narrow band laser source, the overall angular frequency, ω, of the electric field associated with the emission frequency, ω_L, in the presence of an applied modulation frequency, ω_m, is,

$$\omega = \omega_L + a_m \cos(\omega_m t), \tag{3.9}$$

where a_m is the modulation amplitude. The overall time dependent intensity of the modulated radiation, $I(\omega_0, t)$ can be written as a cosine Fourier series,

$$I(\omega_0, t) = \sum_{n=0}^{\infty} H_n(\omega_0) \cos(n\omega_m t) \tag{3.10}$$

with each harmonic component, $H_n(\omega_0)$, capable of being extracted from the overall signal by the lock-in amplifier. At any one time, the lock-in can be set up to return a single harmonic component, and in the the presence of a frequency dependent absorption, $\sigma(\omega)$, the returned signal is given by

$$H_n(\omega_o) = \frac{2}{\pi} \int_0^{\pi} I_0(\omega_0 + a_m \cos(\theta)) e^{[-\sigma(\omega_0 + a_m \cos(\theta)]Cl} \cos(n\theta)\, \mathrm{d}(\theta) \tag{3.11}$$

$$= \frac{2I_0 Cl}{\pi} \int_0^{\pi} [-\sigma(\omega_0 + a_m \cos(\theta)] \cos(n\theta)\, \mathrm{d}(\theta). \tag{3.12}$$

Here, 3.11 becomes 3.12 based upon the assumptions that the transmitted intensity I is invariant with respect to frequency in the absence of an absorber, and that a small degree of absorption exists such that the Beer-Lambert Law becomes $I(\omega) = I_0[1 - \sigma(\omega)Cl]$. θ replaces the term $\omega_m t$.

When the amplitude modulation is much smaller than the absorption linewidth ($a_m <<$

$\Delta\omega$) a special case known as the derivative limit is found. In this case $H_n(\omega_0)$ is proportional to the n^{th} derivative of the lineshape $\sigma(\omega)$. The expression of this limit is derived using a Taylor expansion of $\sigma(\omega)$ and is given by the equation

$$H_n(\omega_0) \simeq \frac{I_0\, Cl\, 2^{1-n}}{n!}\, a_m^n \left(\frac{d^n\sigma}{d\omega^n}\right)_{\omega=\omega_0}. \tag{3.13}$$

The derivative limit provides simple analysis and interpretation of the recovered WMS signal, however this limit does not produces the largest WMS signals and as such is not ideal for sensitive detection. Instead, the dimensionless parameter, $b = 2a_m/\Delta\omega$, the modulation depth, is chosen such that the largest WMS signal is observed. There is also a further consideration here, as increasing the modulation amplitude, whilst increasing the size of H_n, also broadens the signal meaning that an optimum modulation depth is found at $a_m \sim \Delta\omega$, though exact optimum parameters are given in Table 3.1.

Harmonic	1	2	4	6
Gaussian b_{opt} =	1.6	2.1	3.6	5.2
Lorentzian b_{opt} =	2.0	2.2	3.9	7.4

TABLE 3.1: Optimum modulation indices for a selection of low harmonic WMS of Gaussian and Lorentzian lineshapes [104].

Figure 3.10 demonstrates the evolution of a Gaussian WMS signal as a function of harmonic. It is notable that at higher harmonics, the observed signal amplitude is decreased for a given modulation amplitude. It is however, also notable that whilst larger signals may be produced through the increase of b, this also introduces extra broadening which must be considered in any fitting routine, and can lead to more congested spectra. Furthermore, whilst the $1f$ harmonic has the highest maximum peak-to-peak amplitude, it is often preferable to use $2f$ detection instead, as the residual amplitude modulation (RAM) contribution to the noise is lower, and baselines are often smoother.

In order to show the congestion that can occur within WMS, Figure 3.11 shows the $1f$ signal for the $\mathrm{R}(8.5)_{\frac{1}{2}}$ transition at the same conditions as in Figure 3.8, with 1.5 mV ($\sim$ 60 kHz) modulation at 15 kHz on top of the 10 kHz PZT scanning. It is clear here, that even with modulation well within the derivative limit, $1f$ spectra of just two peaks are complicated by the applied modulation.

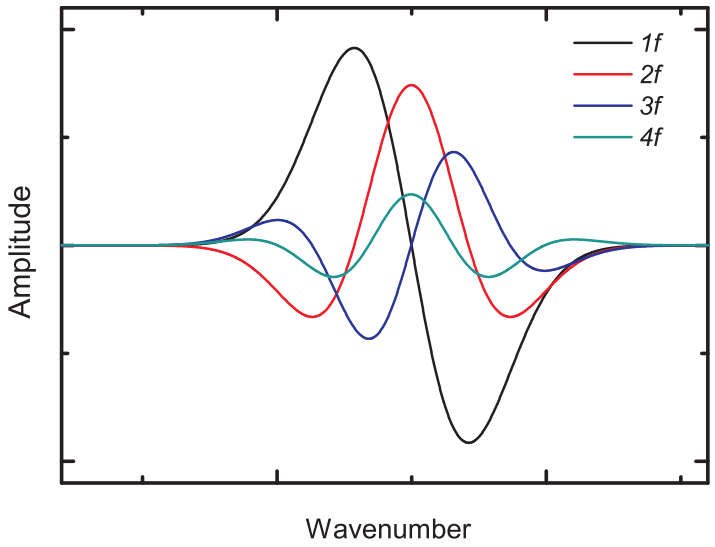

FIGURE 3.10: Schematics of WMS spectra of a Gaussian lineshape demodulated upon the first four harmonics.

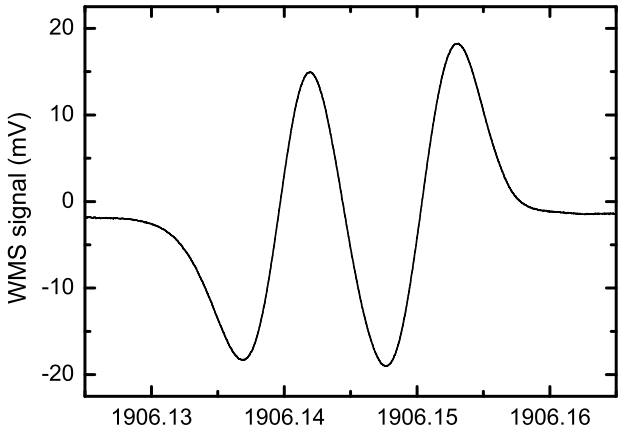

FIGURE 3.11: First harmonic WMS spectrum of the R(8.5)$_{\frac{1}{2}}$ transition of NO, demonstrating the congestion caused by neighbouring lines, even in the derivative limit.

The effect of harmonic changing upon a 'singlet' illustration is shown in Figure 3.12 for the Q(2.5)$_{\frac{3}{2}}$ transition in the NO Q-branch at 1875.72. 140 mTorr of NO were used in a 10 cm cell at a range of harmonics and the laser was ramped at 10 Hz and modulated at a frequency of 15 kHz.

Furthermore, Figure 3.13(a) shows the effect of increasing the modulation voltage upon the $2f$ signal of 140 mTorr of NO upon the Q(2.5)$_{\frac{3}{2}}$ transition. The magnitude of the signal, and hence the (S/N) ratio can be seen to initially increase with the modulation amplitude, but as we move further from the derivative limit, modulation broadening becomes apparent. In Figure 3.13(b) the measured signal amplitude is plotted as a function

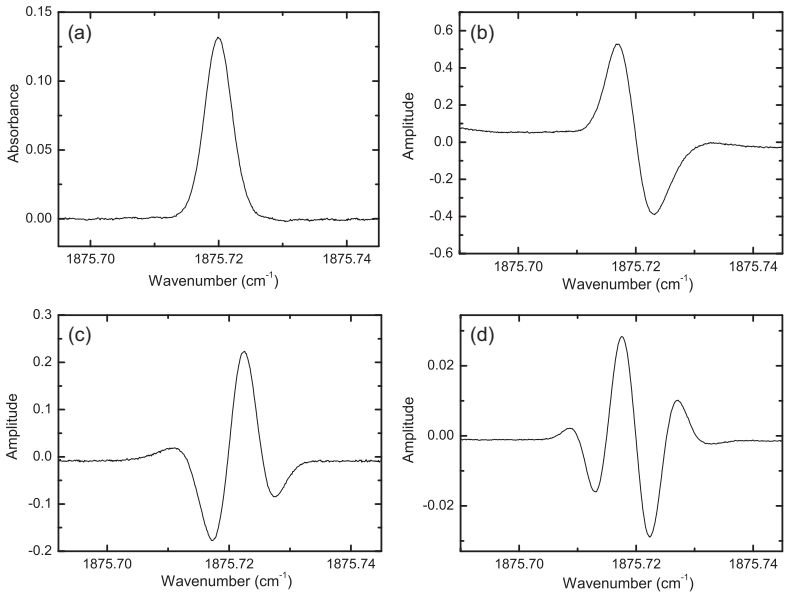

FIGURE 3.12: (a)Direct, (b)$1f$, (c)$3f$ and (d)$5f$ spectroscopy of the Q(2.5)$_{\frac{3}{2}}$ transition of 140 mTorr of NO.

of modulation voltage. Here, a maximum signal occurs at 700 mV, corresponding, as we have seen in Table 3.1, to a modulation index of 2.1, thus we can infer a modulation depth of 142 MHz.

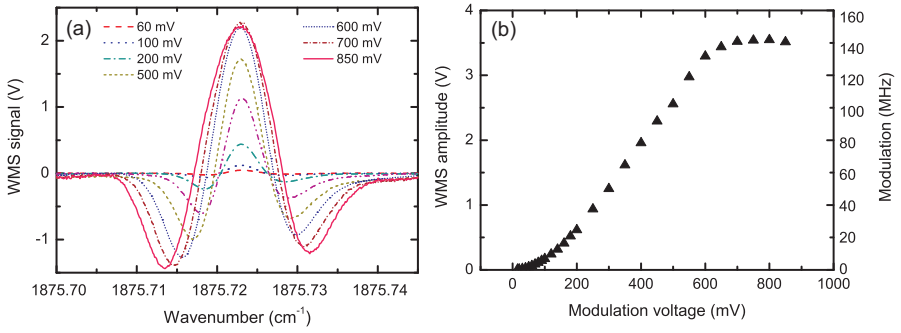

FIGURE 3.13: (a)Second harmonic WMS spectra of 140 mTorr of NO for the Q(2.5)$_{\frac{3}{2}}$ rovibrational transition centred at 1875.724 cm^{-1} as a function of modulation voltage. (b) The amplitude of the second harmonic WMS signal as a function of the applied modulation voltage.

Calculating the sensitivity of spectra obtained through WMS is a somewhat contentious issue, and typically sensitivities are given in so called bandwidth reduced form, whereby the time constant of detection utilised in the lock in is used in place of the time constant of detection in Equation 3.8. This time constant is often of the order of microseconds and using this methodology a maximum bandwidth reduced sensitivity, $\alpha_{\min}(BW_{\text{eff}})$, of 1.9×10^{-6} cm^{-1} Hz$^{-1/2}$ is recorded [46]. However, this methodology produces results which are not directly comparable to direct measurements as spectra could not, in reality, be recorded on such a short timescale. If we instead compare the time normalised

sensitivities then a value of 4.4×10^{-5} cm^{-1} Hz$^{-1/2}$ is returned, barely an improvement upon direct spectroscopy, due to residual modulations observed in the baseline.

3.2.3.2 Long Path Cell

Perhaps the simplest of techniques used to enhance the sensitivity of absorption spectroscopy is to pass a laser beam through a gas cell multiple times. This can be done manually for a small number of passes, but at larger multipliers it is often easier to utilise a pre-aligned multipass cell. There are two primary cell designs in operation for multipass spectroscopy: the White cell and the Herriott cell.

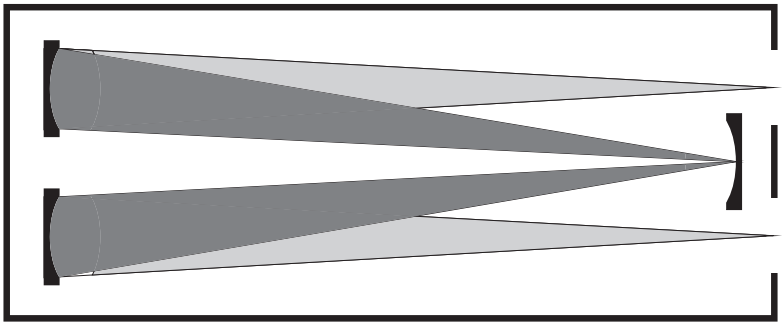

FIGURE 3.14: Schematic diagram showing a 4 pass path through a White cell.

The White cell was demonstrated by J White in 1942 [105], and a version of it has already been utilised in this thesis in Section 2.6. White cells are suitable for use with both lasers and incoherent light as light is refocused upon each pass. Typically, three spherical, concave mirrors with the same radius of curvature are employed in the manner shown in Figure 3.14, and whilst this diagram shows only 4 passes, the length can be extended by any multiple of 4 up to tens or occasionally hundreds of metres.

The Herriott cell by contrast was first demonstrated in 1965 [106] and can only be used with a coherent beam. It consists of two spherical or astigmatic mirrors placed facing each other with beam entry usually through a hole in one of the mirrors as is shown is Figure 3.15(a). In a spherical system, an off-axis alignment of the entrant laser is performed and an elliptical path is traced on the mirrors (Figure 3.15) before exiting through the first mirror, often after a hundred metres or so.

Furthermore, by replacing one or both of the mirrors with astigmatic mirrors then the paths traced can be far more complex, meaning that a larger proportion of the mirror surface can be utilised without beam spot overlap, and as such a longer pathlength achieved with limited fringing. Figure 3.16 shows a photograph of the Lissajous pattern

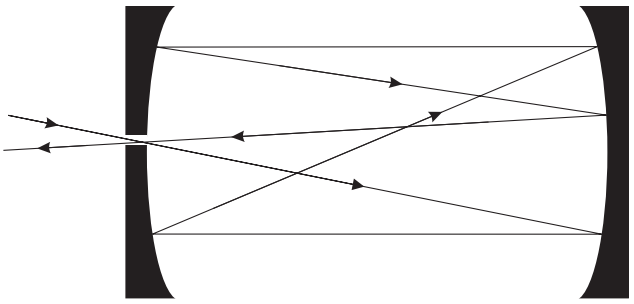

FIGURE 3.15: Schematic diagram showing a path through a Herriott cell.

traced by a red diode laser in our Aerodyne Research Inc 238 m pathlength astigmatic Herriott cell.

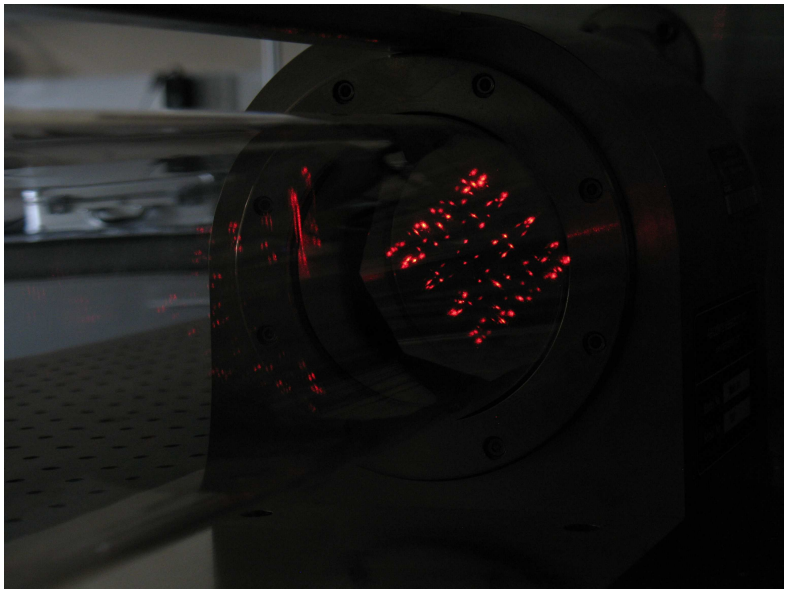

FIGURE 3.16: Lissajous pattern traced out by a red diode laser on an astigmatic mirror within a 238 m Herriott cell

As there are very specific exit conditions for Herriott cells, the spot pattern on the mirrors can be used to determine the path length in operation. As MIR radiation is not visible to the human eye we instead used a red diode laser spatially aligned with the 10 µm laser, and then verified the pathlength with a known quantity of gas. Figure 3.17 shows the spectrum of the P(42) transition of OCS at 1031.15 cm^{-1} taken at 30 kHz with 29 mTorr of gas within the cell. A Gaussian fit of the spectrum is shown with a linewidth of c.a. 40 MHz in reasonable agreement with a thermal sample at 298 K. No Lorentzian component is apparent and as such the laser linewidth cannot be estimated except to say that it is insignificant compared to the Doppler linewidth and as such $<$ 40 MHz. Furthermore, this data provides a time normalised sensitivity of

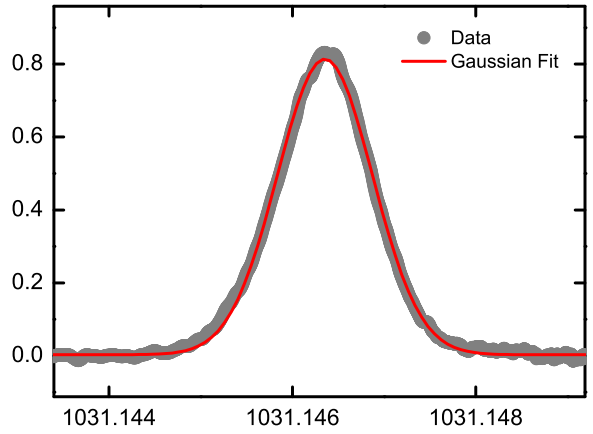

FIGURE 3.17: Spectrum of the P(42) transition of OCS at 1031.15 cm^{-1} in a 238 m pathlength Herriott cell. 29 mTorr of OCS were utilised, and this data is a result of 50 averages.

$8.67 \times 10^{-9} cm^{-1} Hz^{-1/2}$, meaning that - in combination with the strong transition at 1031.110 cm^{-1} - ppb levels of OCS could be detected.

3.2.3.3 Optical Cavities

Whilst the utilisation of a long path cell extends the path length in a very direct manner, passing a single beam between a series of mirrors, optical cavity techniques are designed to increase the path length by 'trapping' laser light between two highly reflective ($R > 99\%$) mirrors. These techniques have the advantage of providing an incredibly long path length in a very short base area, but in lower powered systems can be difficult to apply owing to low power levels exiting the cavities.

When setting up an optical cavity, there are two methodologies applied, either cavity ring down spectroscopy (CRDS), or cavity enhanced absorption spectroscopy (CEAS). In cw CRDS, laser light is injected into the optical cavity into the fundamental resonant mode (TEM_{00}), and allowed to build up. The light is then rapidly extinguished and the time taken for the intensity to leak out is recorded as is shown in Figure 3.18. If an absorber is placed between the two mirrors then on each round trip further absorption occurs and consequently the decay time is reduced. This ringdown time is then related to the absorption cross-section and the concentration of absorbing gas is thus determined. CRDS can be difficult to set up as it requires a very precise, on-axis alignment, however it has the advantage that the signal detected is mediated by the cavity and as

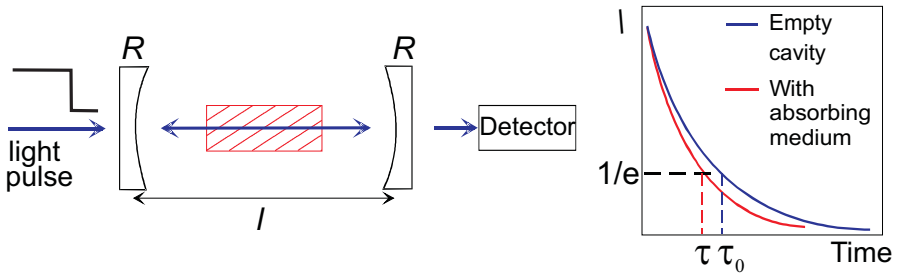

FIGURE 3.18: Schematic showing a CRDS experiment; as the incident radiation is extinguished, light leaks out from the cavity at a decaying rate, $1/\tau_0$. Introducing an absorber to the cavity changes this decay time by a characteristic, pressure dependent value allowing characterisation.

such measurements are insensitive to laser intensity fluctuations which plague amplitude domain methods.

CEAS in contrast is a much simpler, though generally lower sensitivity technique, without the need for fast switching electronics. For CEAS, in contrast to CRDS, a slightly off-axis alignment is employed such that many high-order cavity modes are excited simultaneously. By rapidly scanning the laser over a range of frequencies, these multiple modes result in a consistent, smooth baseline with which spectra may be acquired in a method analogous to that of direct absorption spectroscopy.

A thorough explanation of CEAS signals is given by Mazurenka et al [107], which is summarised here:

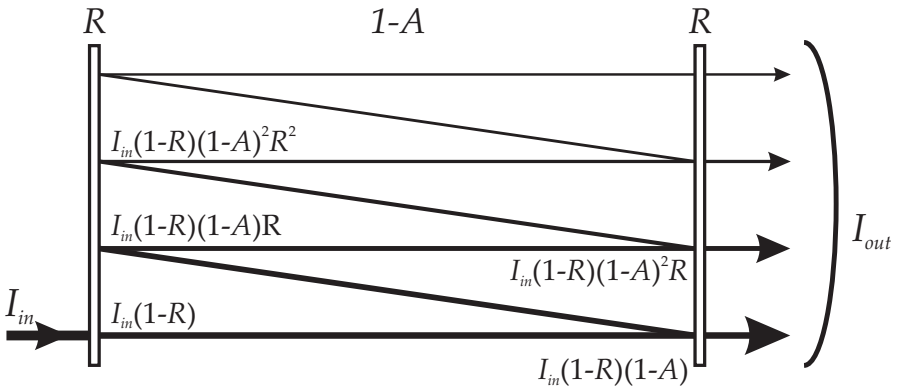

FIGURE 3.19: Schematic of a CEAS resonator, tracking the intensity variations with each pass of the cavity. Consecutive passes of the propagating beam have been displaced vertically for clarity.

As Figure 3.19 demonstrates, when radiation of intensity I_{in} is injected into a cavity, with mirrors of reflectivity, R, the initial mirror passes $I_{in}(1-R)$ radiation into the cavity. This then passes through the length, L, of the cavity with an intensity attenuated by the single pass absorption, A, such that the intensity at the end of a single pass is $I_{in}(1-$

$R)(1-A)$, and the consequent reflected intensity from that mirror is $I_{in}(1-R)(1-A)R$. This process continues ad infinitum such that the total output intensity is

$$I_{out} = I_{in}(1-R)^2(1-A)\sum_{n=0}^{\infty} R^{2n}(1-A)^{2n}. \tag{3.14}$$

For $R < 1$ and $A < 1$, this geometric progression can be rewritten as;

$$I_{out} = I_{in}\frac{(1-R)^2(1-A)}{1-R^2(1-A)^2} \tag{3.15}$$

If the cavity contains no absorbing media then the output intensity, and hence the baseline is:

$$I^0_{out} = I_{in}\frac{(1-R)}{(1+R)} \tag{3.16}$$

Thus, assuming a small degree of absorption, such that $(1-A) = e^{-\alpha L}$, where $\alpha = N\sigma$ as in Equation 1.1, the ratio of intensities with (I_{out}) and without (I^0_{out}) absorbance is given by:

$$\frac{I^0_{out}}{I_{out}} = \frac{1-(Re^{-\alpha L})^2}{(1-R^2)e^{-\alpha L}} \tag{3.17}$$

In the limit of highly reflective mirrors ($R \to 1$), Equation 3.17 can be expressed as

$$\frac{I^0_{out} - I_{out}}{I_{out}} = \frac{\alpha L}{1-R}, \tag{3.18}$$

with $1/(1-R)$ effectively the path length enhancement factor upon the observed absorption signal compared to an analogous single-pass experiment. With R values in excess of 99.9% path length enhancements greater than a factor of a 1000 are expected, thus an L of 1 m would lead to effective path lengths in excess of a km, demonstrating the power of this technique. The intensity dependent nature of Equation 3.18 means that CEAS is sensitive to laser fluctuations, and hence limits its sensitivity compared to CRDS. However, CEAS offers a much more robust, and straightforward setup, and in fact mechanical vibrations can often be of assistance with CEAS, dithering the length of the cavity and thus smoothing out mode noise when averaged.

Typical CEAS experiments are performed with a linear cavity, such that light is injected and leaked-out from the cavity upon the same axis, however as the EC-QCL is particularly sensitive to optical feedback the work presented here is based upon a V-shaped cavity. This was set up such that optical back-reflection from the first mirror was minimised. $R = 99.97\%$ mirrors over the wavelength region 5200 ± 100 nm(Los Gatos) were used in order to maximise the path length enhancement, and as the light exiting

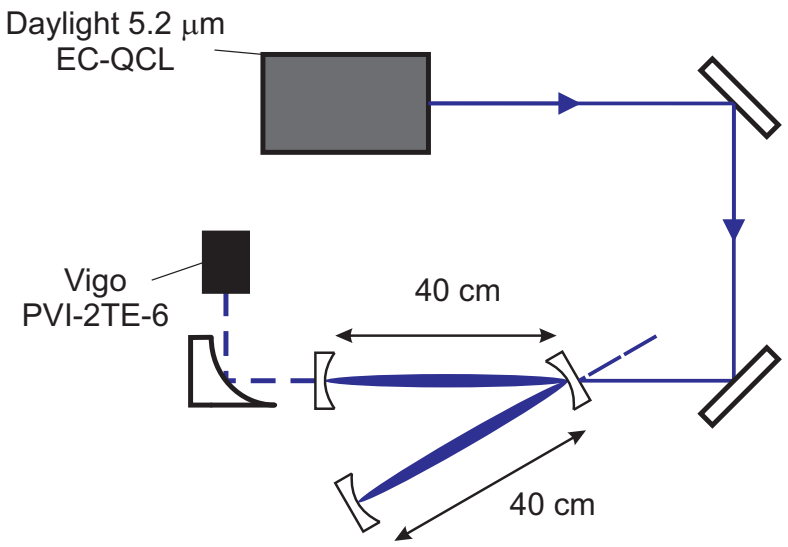

FIGURE 3.20: Schematic diagram demonstrating the experimental setup used for CEAS in a V-shaped optical cavity.

the cavity is divergent an off-axis parabolic mirror was used to focus the light onto the detector. The setup is demonstrated in Figure 3.20.

Initial tests found incredibly persistent mode structure within the cavity output, one of many sensitivity limiting symptoms endemic to mid-infrared cavities [108]. This structure is shown in Figure 3.21 for a 10 Hz scan, and suggests a non-optimal CEAS cavity alignment.

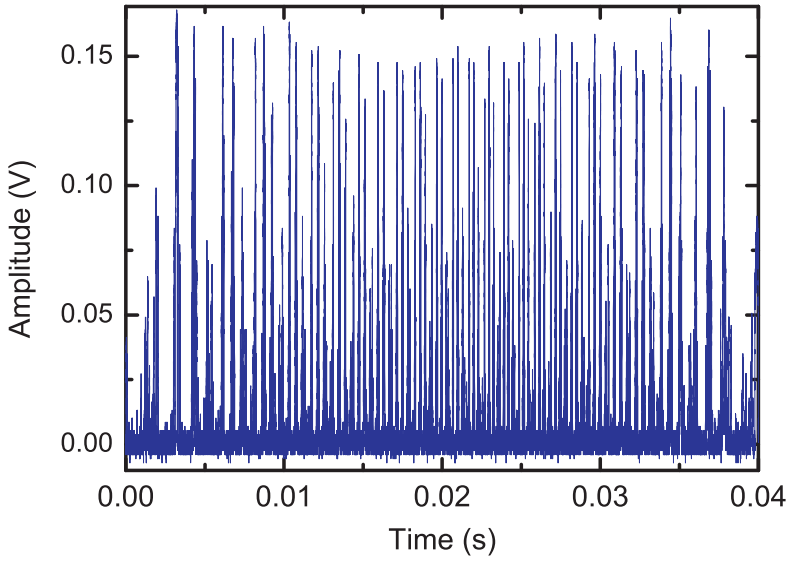

FIGURE 3.21: Transmitted light through the V-shaped cavity when scanning laser at 10 Hz over c.a. 0.7 cm^{-1} showing persistent mode structure.

Whilst this structure does not initially give a smooth baseline, mechanically dithering the cavity length whilst averaging does, and the spectrum of three transitions in the ν_2 fundamental band of aerial water around 1950 cm^{-1} are shown in Figure 3.22.

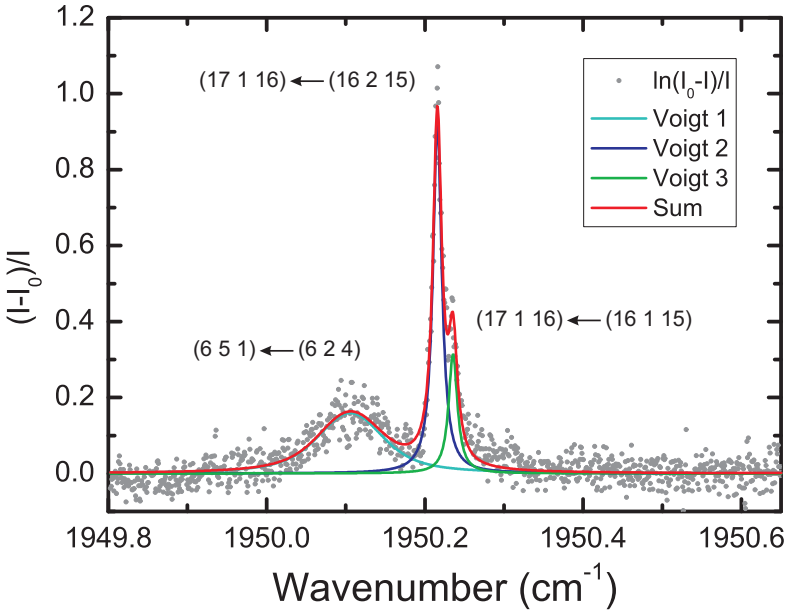

FIGURE 3.22: CEAS spectrum of water in laboratory air showing three transitions about 1950.22 cm^{-1}. This data corresponds to a reflectivity, R of 99.85%.

This data was taken at a repetition rate of 10 kHz, and is a result of 500 averages. Through comparison with the stronger water absorption in the direct spectra shown in Figure 3.2 (a water composition of 0.876%), a path length enhancement of 685 was determined, implying an R value of 99.85%. The widths of these transitions are notably different owing to an order of magnitude difference in air pressure broadening coefficients [1].

The cavity was then evacuated using a turbo pump, reaching a base pressure of 1.6×10^{-5} Torr, and a small amount of NO (5.8×10^{-5} Torr) leaked into the cell. The laser was tuned to the R(15.5)$_{\frac{3}{2}}$ transition and data recorded for 1000 averages whilst the cavity length was mechanically dithered. The resulting spectra is shown in Figure 3.23, and corresponds to a path length enhancement of c.a. 3000, and thus a mirror reflectivity of 99.97%. This extra enhancement was produced in part through improved alignment, but also in part to the removal of water and other unwanted gases from the cavity.

Due to residual mode structure, even after dithering and averaging for 1000 scans our signal to noise ratio is only 70 and a time normalised sensitivity of 5.2×10^{-7} cm^{-1} Hz$^{-1/2}$ has been achieved, 1-2 orders of magnitude smaller than that achieved in comparable experiments with NIR diode lasers [107], and significantly smaller than that for a long

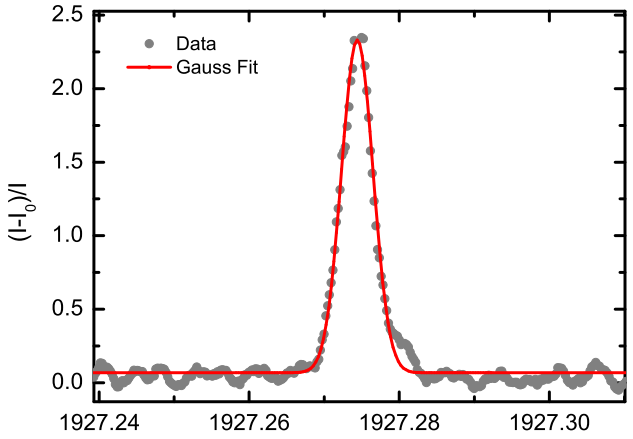

FIGURE 3.23: CEAS spectrum of NO showing the R(15.5)$_{\frac{3}{2}}$ transition at 1927.27 cm^{-1}. This data corresponds to a path length enhancement of c.a. 3000 and a reflectivity, R of 99.97%.

path cell. This situation is however not unique to this experiment, and a wide array of complications typically limit the sensitivity of MIR cavity techniques compared to their NIR analogues [108]. Regardless, in this situation the minimum detectable concentration of NO is 2 ppb, high enough to be useful for medical sensing techniques, and comparable with similar experiments in the literature [56, 88, 109].

3.3 High Resolution Spectroscopy of Deuterium Bromide

The work performed in this section is done to demonstrate the applicability of cw QCLs to high resolution spectroscopy, and with the narrow bandwidth being applied to the determination of previously unknown spectral constants.

The ro-vibrational spectra of the two most prevalent isotopologues of DBr ($D^{79}Br$ and $D^{81}Br$) are considered to be of particular interest largely due to their possible metrological application. Specifically, as DBr is a linear molecule, its spectra are relatively simple and the regular spacing and strengths of the transitions within its fundamental vibrational band lend it to the purpose of a secondary wavelength standard in the 1750 - 1900 cm^{-1} region.

At comparatively low resolution (< 0.02 cm^{-1}) the spectrum of the $v = 1 \leftarrow 0$ band of either isotopologue appears as a completely classical ro-vibrational spectrum as is shown in Figure 3.24, with a spectra simulated using PGOPHER [110] and constants from the literature.

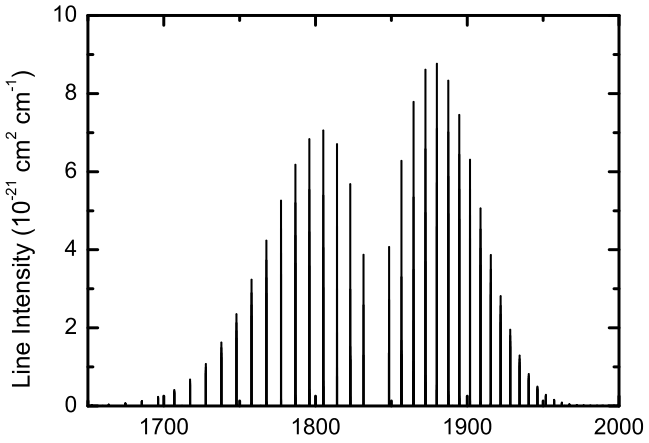

FIGURE 3.24: Fundamental vibrational band of $D^{79}Br$ as simulated using PGOPHER [110] and constants from the literature [111].

When one looks closer near the band centre however, hyperfine splitting caused by coupling of the nuclear spin of the Br isotope with the rotational energy of the molecule becomes apparent, and were one to look at a resolution far below Doppler, further splittings would be apparent due to the deuterium atom. Many studies have been performed upon DBr and the vast bulk of the relevant spectroscopic constants determined but the caché of constants has thus far not been completed. This is because, despite the application of FTIR, microwave spectroscopy, CO lasers, and heterodyne spectroscopy, the resolution of the MIR techniques is typically limited and the tunability of far-infrared radiation sources techniques usually minimal. Thus, to date the hyperfine coupling constant of the first excited state of $D^{81}Br$ has been undetermined, and only one measurement has been made of that for $D^{79}Br$.

In this section, work is performed to determine these spectroscopic constants with our widely tunable (1776-1958 cm^{-1}) Daylight EC-QCL. In particular, as the hyperfine splitting is most obviously manifest around band centre, we have observed the lines R(0), R(1), R(2), P(1) and P(2) for both isotopologues in a 10 cm long cell. These lines do not all lie within the mode-hop free range of this laser, but any mode-hops were suppressed in the region of interest by altering either the temperature or scan range. Relative frequency calibration was achieved with the use of the 500 MHz Ge etalon, and where possible absolute frequency verified using nearby water and NO spectral features. Figure 3.25 demonstrates this showing the spectrum of the R(2) transitions of both DBr isotopologues alongside the $P(3.5)_{\frac{1}{2}}$ Λ-doublet resolved transition of NO, and a composite H_2O spectral feature. Line positions were determined and compared with literature values [84], giving agreement to within 0.005 cm^{-1} over the entire scan range,

with most of this error due to greater uncertainties in the tuning range near the edge of the scan.

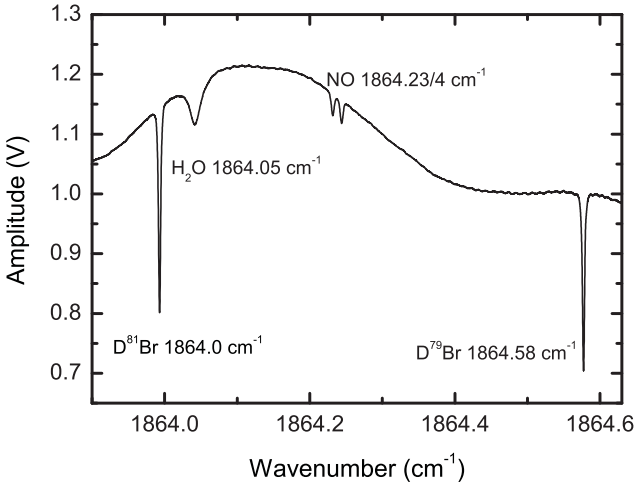

FIGURE 3.25: Absolute frequency calibration was performed, where possible using nearby NO and water lines, as exampled here for the R(2) transitions of both bromine isotopologues, the $P(3.5)_{\frac{1}{2}}$ Λ-doublet resolved transitions of NO, and a composite H_2O spectral feature. The shaped baseline and etalons are likely due to imperfections in the antireflection coating of the laser chip.

Figure 3.26 shows spectra of the isotopologues of DBr, specifically (a) $D^{79}Br$ P(1) (b) $D^{81}Br$ P(1), (c) $D^{79}Br$ R(1), (d) D^{81} P(2). As there were already a number of constants available in the literature, PGOPHER simulations have been performed for the $D^{79}Br$ transitions using literature values [111–113], and these are overlaid upon the data, showing good agreement.

As the splitting caused by the deuterium atom is very small (< MHz), and several orders of magnitude smaller than both the splitting caused by the bromine isotopes, and the Doppler broadening, we were able to neglect its effect, and treat both DBr isotopologues as diatomic molecules split by the hyperfine interaction from a single nucleus. As such the ro-vibrational energy levels are governed by the following relation:

$$\begin{aligned} G(v,F,J,I) &= \omega_e\left(v+\tfrac{1}{2}\right) - \omega_e x_e\left(v+\tfrac{1}{2}\right)^2 \\ &+ \left[B_e - \alpha_e\left(v+\tfrac{1}{2}\right)\right] J(J+1) \\ &- D_e J^2(J+1)^2 - f(F,J,I)e^2Qq \\ &+ \tfrac{1}{2}C[F(F+1) - J(J+1) - I(I+1)] \end{aligned} \tag{3.19}$$

where v is the vibrational quantum number, F, J and I are the total, rotational and nuclear spin quantum numbers, ω_e is the equilibrium oscillation frequency, $\omega_e x_e$ is the

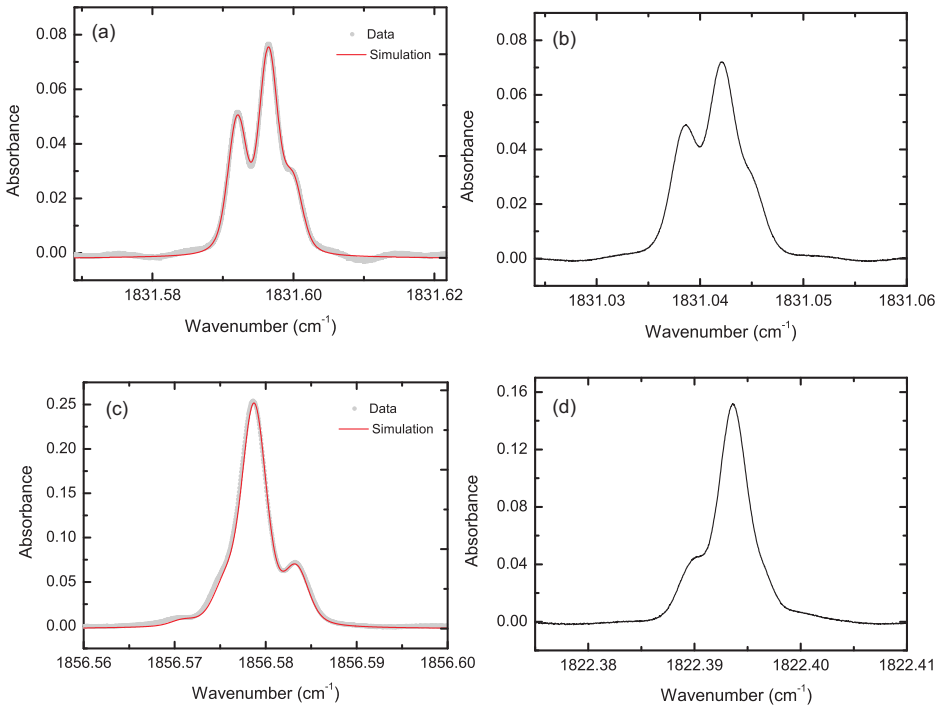

FIGURE 3.26: Spectra of the isotopologues of DBr, specifically (a) $D^{79}Br$ P(1) with simulation, (b) $D^{81}Br$ P(1), (c) $D^{79}Br$ R(1) with simulation, (d) D^{81} P(2).

anharmonicity constant, B_e is the rotational constant corresponding to the equilibrium separation, α_e is the vibration/rotation interaction constant, D_e is the centrifugal distortion constant, $f(F, J, I)$, is the Casimir function tabulated by Bardeen and Townes [114], eQ is the nuclear quadrupole moment, eq the electric field gradient, and $\frac{1}{2}C[F(F+1)-J(J+1)-I(I+1)]$ is the nuclear magnetic interaction whose importance in the spectra of hydrogen halides was pointed out by Burrus, Cowan, and Gordy[115, 116] with C a constant. As the electric field gradient, eq, is determined by all charges other than that of the nucleus in consideration, and the molecule is not rigid, it must vary with nuclear separation, R, like so:

$$eq(R) = eq^{(0)} + eq^{(1)}\xi + eq^{(2)}\xi^2 + ... \tag{3.20}$$

where $\xi = \frac{R-R_e}{R_e}$ and R_e is the equilibrium value at $v = 0$, $J = 0$, and the coefficients $eq^{(n)}$ are assumed to be of the same order of magnitude to ensure convergence. This equation can however, also be approximately expressed with respect to its average rotational and vibrational dependency:

$$eq(R) = eq^{(0)} + eq^{(J)}J(J+1) + eq^{(v)}\left(v + \tfrac{1}{2}\right) \tag{3.21}$$

which can be further expanded such that:

$$q^{(J)} = (2B_e/\omega_e)^2 q^{(1)} \tag{3.22}$$

$$q^{(v)} = (3B_e/\omega_e)(1 + \alpha_e\omega_e/6B_e^2)q^{(1)} + (2B_e/\omega_e)q^{(2)}. \tag{3.23}$$

Equation 3.22 is the rotational average considering that when a molecule rotates the internuclear distance assumes a distance such that the centrifugal force is balanced by the restoring force. It is also notable that Equation 3.23 is composed of two parts, with the first and second components an average of ξ and ξ^2 over the anharmonic and harmonic molecular vibration respectively.

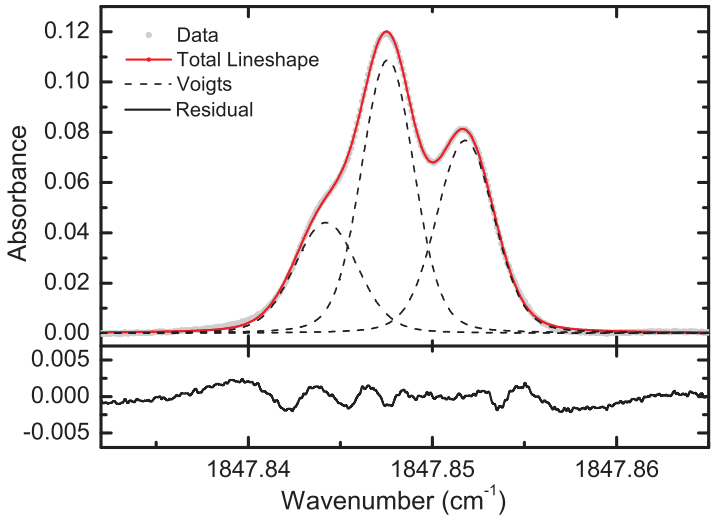

FIGURE 3.27: Individual fits to the R(0) transition of $D^{81}Br$ and their sum, with three Voigt profiles centred at 1847.845, 1847.848 and 1847.852 cm^{-1}.

As the equation for the Casimir function in Equation 3.19 is equal to zero when there is no rotational energy ($J = 0$), then these states are not split by hyperfine interactions, and as such the P(1) and R(0) lineshapes can be considered as pure triplets with splittings determined wholly by the hyperfine coupling constants in the lower, and upper vibrational states respectively. As such, the experimental spectra of these transitions was satisfactorily fit using three lineshape functions: specifically, Voigt profiles chosen to allow for both Gaussian and Lorentzian width contributions to the profile from Doppler and time averaged laser linewidth contributions respectively. In this case the anticipated Doppler width was set as determined by Equation 2.11, and the Lorentzian component to 18 MHz, the time averaged linewidth determined in Section 3.2.2. The result of this fitting routine is shown in Figure 3.27 for the R(0) transition of $D^{81}Br$, and the returned line centres were used to determine the hyperfine coupling constants from Equations

3.24–3.26.

$$\nu_1 = G'(v,F,J,I) + 0.2e^2Qq - C \quad (3.24)$$

$$\nu_2 = G'(v,F,J,I) - 0.05e^2Qq + \tfrac{3}{2}C \quad (3.25)$$

$$\nu_3 = G'(v,F,J,I) - 0.025e^2Qq - \tfrac{5}{2}C \quad (3.26)$$

where $G'(v,F,J,I)$ is the unsplit contribution to the ro-vibrational energy level, i.e. neglecting hyperfine and nuclear magnetic interactions. The magnetic interaction constants have previously been determined [113], and are considered to be unchanged by vibrational state [112]. The e^2Qq's were determined for the ground and first excited vibrational states of both isotopologues, and the results are presented in Table 3.2 and Figure 3.28 alongside measurements previously reported in the literature. Notably, our data shows good agreement with the literature, but with a generally larger error than that of these previously reported measurements. This is partially due to a difference of methodologies (i.e. pure rotational vs ro-vibrational spectroscopy), and partially due to an unavoidable contribution from uncertainties in the frequency scale, likely rooted in a combination of mechanical instability and optical feedback within our laser system.

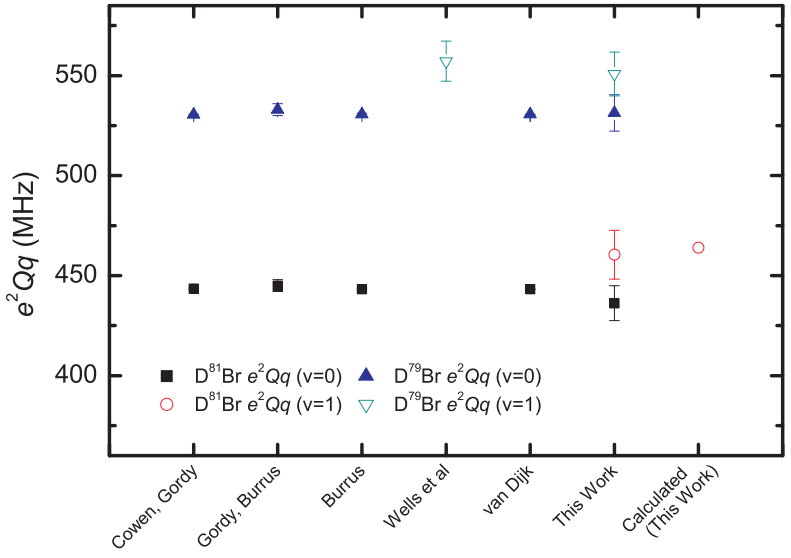

FIGURE 3.28: The hyperfine coupling constants determined in this study, and their comparison with previous measurements.

Furthermore, as the isotopic dependence of $eq^{(v)}$ and $eq^{(J)}$ is held largely in the constants ω_e, B_e and α_e, and these are well known for both isotopologues, analysis of literature values for the vibrational and rotational dependence of the electric field gradient for D^{79}Br in Tokuhiro [111] can be used to yield isotopic *independent* expansion coefficients $eq^{(0)}$, $eq^{(1)}$ and $eq^{(2)}$. These, when combined with the ratio of the nuclear quadrupole

TABLE 3.2: The hyperfine coupling constants determined in this study, and their comparison with previous measurements.

			$D^{79}Br$		$D^{81}Br$	
	Ref	Method	e^2Qq(v=0) (MHz)	e^2Qq(v=1) (MHz)	e^2Qq(v=0) (MHz)	e^2Qq(v=1) (MHz)
This Work	-	QCL	531.4 ± 9.1	550.8 ± 10.9	436.2 ± 8.7	460.5 ± 12.2
This Work	-	Calculated	-	-	-	464
van Dijk	[113]	Microwave	530.6315 ± 0.0021	-	443.2799 ± 0.0021	-
Gordy, Burrus	[117]	Microwave	533 ± 3	-	445 ± 3	-
Cowan, Gordy	[116]	Microwave	530.5 ± 0.3	-	443.5 ± 0.3	-
Wells et al	[112]	Heterodyne	-	557.2 ± 10	-	-
Burrus	[118]	Microwave	530.65 ± 0.5	-	443.29 ± 0.5	-

moments (eQ) of the bromine isotopes given by Hebert and Street [119], enable us to gain an estimate for the vibrational component of the hyperfine splitting of $D^{81}Br$, and consequently the hyperfine coupling constant for the first vibrationally excited state to be 464 MHz, again in good agreement with our observed value (460.5 ± 12.2 MHz).

3.4 Conclusions

In this chapter work has been performed examining the behaviour of both external cavity and DFB QCLs. Initial spectroscopic measurements have been made with both, and the wide tuning range of the EC-QCL demonstrated. Direct absorption spectroscopy has been performed upon nitric oxide with both a DFB and an EC-QCL and the optimal sensitivities compared (2.5×10^{-6} vs. 4.8×10^{-5} cm^{-1} $Hz^{-1/2}$). Wavelength modulation spectroscopy, long path cells, and optical cavities have been considered as sensitivity enhancing methods for use with QCLs and the resulting α_{min}'s compared, with achieved sensitivities high enough for medical sensing. The high resolution of cw QCLs has then been utilised in order to observe molecular transitions of both isotopologues of DBr about the centre of the fundamental ro-vibrational bands. The hyperfine coupling constants of both the upper, and lower vibrational state have been determined, in good agreement with values previously recorded in the literature. In addition, the first measurement of the hyperfine coupling constant for the first vibrationally excited state of $D^{81}Br$ was performed, returning a value of 460.5 ± 12 MHz, also in good agreement with predictions. In this manner the caché of constants required for the use of the DBr isotopologues as mid-infrared frequency calibration standards has been completed.

Chapter 4

Non-linear Spectroscopy with a cw EC-QCL

When the electromagnetic field incident upon a system becomes sufficiently strong, it perturbs the system, to the extent that the probability of photon absorption is modified. This can be analogously thought of as a speaker played at a volume above its capacity. As the driving voltage is increased there are audible distortions and these distortions create new sound frequencies at the sum and differences of the driving frequencies, as well as changing the amplitude. These effects have already been discussed in the case of difference and sum frequency generation (DFG and SFG) as methods of producing MIR radiation, but are equally present in spectroscopic measurements when considering a saturable absorber or a two photon absorption. The following two chapters discuss precisely these effects, investigating both the linewidth and the population transfer induced by a high powered QCL. Nitric oxide is utilised as a test case in this chapter as its transitions are large in this region and its spectrum is well known.

4.1 Lamb-dip Spectroscopy

The Doppler effect has already been discussed as a dephasing mechanism (Section 2.3), and at low pressures is often the limiting factor with respect to the resolution in cw spectroscopy. It is possible to reduce the Doppler width of a transition by reducing the number of velocities within the sample - in a molecular beam for instance - but in 1964 a method was predicted by Lamb [120] and then realised in 1969 by Costain [121] that allows the achievement of sub-Doppler resolution without complex apparatus. This methodology is referred to as Lamb-dip spectroscopy.

In order to understand Lamb-dip spectroscopy we will first step back and consider population transfer in the form of saturation. This derivation is based upon that by Demtröder [122]. Considering a system of two non-degenerate levels, coupled by a near-resonant electric field, then Figure 4.1 shows the processes determining the populations N_1 and N_2. Unperturbed, the system is in equilibrium with consistent relaxation between the two levels due to processes including the natural lifetime, determined by the Einstein coefficient, A, and collisional population transfer. Unless levels 1 and 2 are very closely spaced compared to kT then the population in the excited state at equilibrium will be fairly small and thus so will the rate of transfer from level 1 into level 2. When a coherent light source near resonance is applied to the system however, the system is perturbed from equilibrium as the light field couples the two states and excitation and de-excitation processes occur at a rate dependent upon the intensity of the radiation.

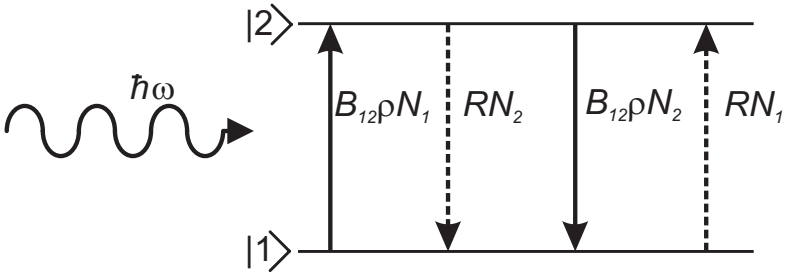

FIGURE 4.1: Schematic diagram demonstrating the population changing processes of a two level system in a resonant electromagnetic field (emitted photons are excluded for clarity).

The probability $P = B_{12}\rho(\omega)$ for a transition from level 1 to 2 by absorption of photons $\hbar\omega$ from a field of spectral density, $\rho(\omega)$ and the depopulation probability R_i for level $|i\rangle$ leads to the following rate equation:

$$\frac{\mathrm{d}N_1}{\mathrm{d}t} = -\frac{\mathrm{d}N_2}{\mathrm{d}t} = -PN_1 - R_1N_1 + PN_2 + R_2N_2. \tag{4.1}$$

Under stationary conditions ($\mathrm{d}N_i/\mathrm{d}t = 0$), and using the relation $N_1 + N_2 = N$ we can obtain:

$$N_1 = N\frac{P + R_2}{2P + R_1 + R_2}, \tag{4.2}$$

and thus see that as the pumping rate, P becomes much larger than relaxation rates, R_i, we tend towards the result of $N_1 = N_2 = N/2$ and the absorption coefficient, α, which is related to the absorption cross-section, σ and the population difference ($\alpha = \sigma(N_1 - N_2)$), tends to zero, and the system becomes transparent.

Comparing the notation used here with that in Chapter 2 the relaxation rate R_2 is the reciprocal of T_1, the deexcitation constant.

In the absence of radiation, i.e. $P = 0$ the population densities are:

$$N_{10} = \frac{R_2}{R_1 + R_2} N, \tag{4.3}$$

$$N_{20} = \frac{R_2}{R_1 + R_2} N. \tag{4.4}$$

If $\Delta N = N_1 - N_2$ and $\Delta N_0 = N_{10} - N_{20}$ are the population differences with and without the presence of radiation then

$$\Delta N = \frac{\Delta N_0}{1 + 2P/(R_1 + R_2)} = \frac{\Delta N_0}{1 + S}, \tag{4.5}$$

where S is the saturation parameter,

$$S = \frac{2P}{(R_1 + R_2)} = \frac{P}{\bar{R}} = \frac{B_{12}\rho(\omega)}{\bar{R}}. \tag{4.6}$$

Physically, S represents the ratio of the pumping rate, P, to the average relaxation rate, $\bar{R}$. Since the pump rate due to a monochromatic wave with intensity $I(\omega)$ is $P = \sigma_{12}(\omega)I(\omega)/\hbar\omega$, a saturation parameter of

$$S = \frac{2I_p\mu^2\tau^2}{\epsilon_0 c h^2}, \tag{4.7}$$

is obtained, where μ is the transition dipole moment, $I_p(\omega)$ is the incident 'pump' laser intensity and τ is the relaxation time of the system, $1/(R_1 + R_2)$. As transitions are not infinitely narrow, but instead homogeneously broadened by lifetime effects, Demotröder [122] explains the frequency dependent saturation parameter, S_ω, as an on resonance saturation parameter, S_0, spread over a Lorentzian distribution;

$$S_\omega = S_0 \frac{(\gamma/2)^2}{(\omega - \omega_0) + (\gamma/2)^2}. \tag{4.8}$$

where γ is the relaxation rate within the system (typically the reciprocal of τ) and ω_0 is the frequency at resonance.

It is now useful to consider our radiation as a monochromatic wave propagating in the z direction,

$$E = E_0 \cos(\omega t - kz), \tag{4.9}$$

with k, the wave vector in the z direction. Having defined the principle of saturation for an hypothetical stationary two level system we now consider our system as an array of gas molecules, moving with velocities determined by a Maxwell-Boltzmann distribution. Each molecule with a velocity component along the z axis, v_z, will see the radiation at a frequency Doppler shifted with respect to ω_0 and thus have a Doppler shifted resonance

frequency given by:

$$\omega_0' = \omega_0 \left(1 \pm \frac{v_z}{c}\right). \tag{4.10}$$

Were transitions to be infinitely narrow then this equation would be obeyed exactly, however, due to the homogeneous linewidth of a transition this condition becomes

$$\omega_0' = (\omega_0 \pm \gamma) \left(1 \pm \frac{v_z}{c}\right). \tag{4.11}$$

The absorption cross section for a molecule with this velocity component is then a Lorentzian:

$$\sigma_{12}(\omega, v_z) = \sigma_0 \frac{(\gamma/2)^2}{(\omega - \omega_0 - kv_z)^2 + (\gamma/2)^2}, \tag{4.12}$$

where σ_0 is the unperturbed cross section at line centre of the molecular transition. If the pump beam is strong enough that appreciable saturation occurs then population in the ground state $N_1(v_z)\mathrm{d}v_z$ is decreased within the interval $\mathrm{d}v_z = \gamma/k$, and population in the upper state N_2 is similarly increased. Equations 4.5 and 4.8 then lead to the following relations:

$$N_1(\omega, v_z) = N_{10}(v_z) - \frac{\Delta N_0}{\gamma_1 \tau} \left[\frac{S_0(\gamma/2)^2}{(\omega - \omega_0 - kv_z)^2 + (\gamma_s/2)^2}\right], \tag{4.13}$$

$$N_2(\omega, v_z) = N_{20}(v_z) + \frac{\Delta N_0}{\gamma_2 \tau} \left[\frac{S_0(\gamma/2)^2}{(\omega - \omega_0 - kv_z)^2 + (\gamma_s/2)^2}\right], \tag{4.14}$$

$$\Delta N(\omega, v_z) = \Delta N_0(v_z) \left[1 - \frac{S_0(\gamma/2)^2}{(\omega - \omega_0 - kv_z)^2 + (\gamma_s/2)^2}\right], \tag{4.15}$$

Figure 4.2 shows this effect for our case of a two-level system. Here the velocity selected minimum in the velocity distribution of $\Delta N(v_z)$ at $v_z = (\omega - \omega_0)/k$ is called a Bennett hole and has a homogenous width:

$$\gamma_s = \gamma\sqrt{1 + S_0}. \tag{4.16}$$

and a depth at hole centre ($\omega = \omega_0 + kv_z$)

$$\Delta N_0(v_z) - \Delta N(v_z) = \Delta N_0(v_z) \frac{S_0}{1 + S_0} \tag{4.17}$$

Whilst the population can thus be significantly changed, the $\alpha(\omega)$ profile is such that the Bennett holes burnt into the velocity distribution cannot be observed by tuning the saturating laser through the absorption profile. Instead, a congruous decrease in absorption is seen at all velocities reducing the absorption profile by a factor of $\sqrt{1 + S_0}$ such that:

$$\alpha(\omega) = \frac{\alpha^0(\omega)}{\sqrt{1 + S_0}}, \tag{4.18}$$

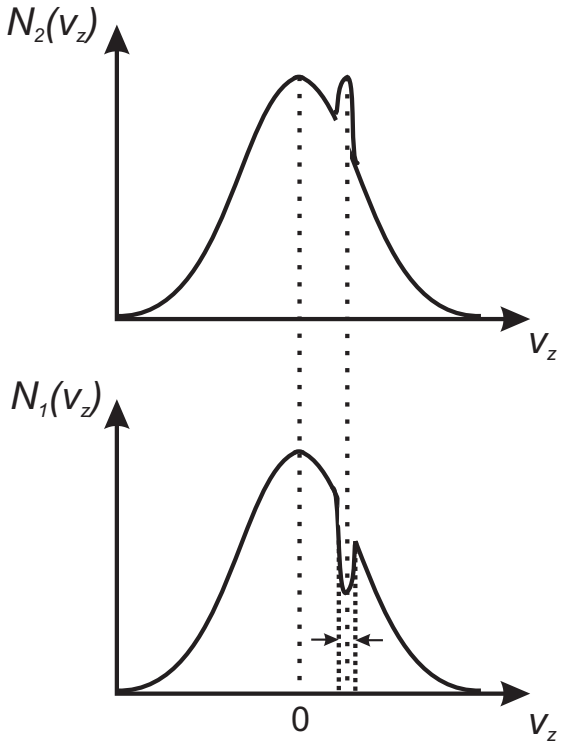

FIGURE 4.2: Velocity selective population transfer showing the Bennett hole and peak in the populations of the lower and upper states (adapted from [122]).

with $\alpha^0(\omega)$ the unsaturated absorption coefficient. It is however possible to detect the perturbed populations with a second 'probe' laser beam tunable over the transition lineshape. If the 'pump' beam has a wave vector $\boldsymbol{k}_1$ and a fixed frequency of ω_1, and the probe beam a wave vector of $\boldsymbol{k}_2$ and a frequency of ω_2 then the absorption coefficient for the probe laser is

$$\alpha_s(\omega_1, \omega_2) = \alpha^0(\omega) \left[1 - \frac{S_0}{\sqrt{1+S_0}} \frac{(\gamma/2)^2}{(\omega - \omega')^2 + (\Gamma_s/2)^2} \right]. \tag{4.19}$$

This absorption coefficent then corresponds to an unsaturated Doppler profile $\alpha^0(\omega)$ with a saturation dip at the probe frequency, ω_2 as is shown in Figure 4.3

$$\omega_2 = \omega' = \omega_0 \pm (\omega_1 - \omega_0) \frac{k_1}{k_2} \tag{4.20}$$

with + corresponding to co-propagating and − to counter-propagating beams.

The halfwidth $\Gamma_s = \gamma + \gamma_s = \gamma[1 + (1 + S_0)^{1/2}]$ of the observed dip then corresponds to the sum of the saturated dip and the unsaturated homogenous absorption width, γ, of the system probed by the weak probe wave.

The two beams, 'pump' and 'probe', may be generated by separate lasers, but in a special case a strong pump beam can be passed through a gas cell and retroreflected

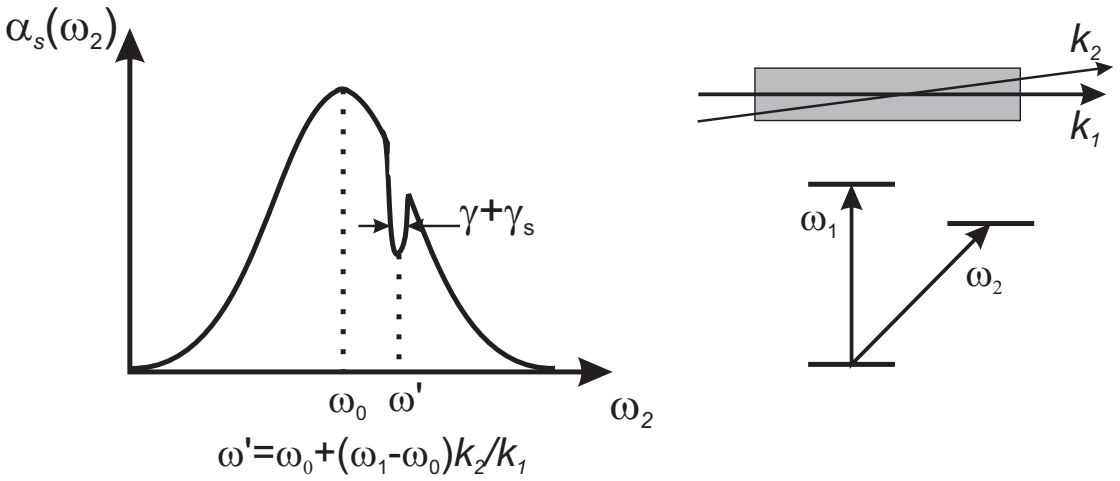

FIGURE 4.3: Observed dip in absorption coefficient of a Doppler broadened profile, burned by a strong laser at ω_1 and detected by a weak probe laser (From [122]).

such that it acts simultaneously as a probe beam. In this case both pump and probe lasers are tuned simultaneously and, as their beams are counter-propagating, typically interact with separate velocity subsets $\pm v_a$. When the incident laser radiation is at the central resonant frequency however, both the pump and probe beams will interact with the same subset of molecules with no component of velocity in the z direction (Figure 4.4).

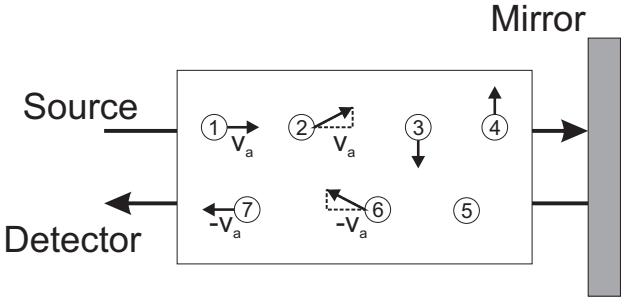

FIGURE 4.4: Schematic of a Lamb dip experiment. In this case molecules 1 and 2 will absorb at frequency, ω_a on the first pass, but are not in resonance on the return journey when 6 and 7 instead absorb at this frequency. Only molecules 3, 4 and 5 with no component of velocity in the direction of beam propagation will be in resonance in both passes at ω_0 (Adapted from [123]).

In this manner, the saturation is only probed at line centre and is observed as a Bennett-hole, ω_0, referred to here as a Lamb-dip. In the case of approximately equally powered beams the following absorption profile is observed:

$$\alpha(\omega) = \alpha^0(\omega)\frac{\Gamma}{B\left[1-\left(\frac{2(\omega-\omega_0)}{A+B}\right)^2\right]^{1/2}}, \tag{4.21}$$

with

$$A = \sqrt{(\omega - \omega_0)^2 + \Gamma^2} \tag{4.22}$$

$$B = \sqrt{(\omega - \omega_0)^2 + (1 + 2S_0)\Gamma^2} \tag{4.23}$$

and

$$\Gamma = \frac{\gamma}{2}. \tag{4.24}$$

This equation then yields a ratio of dip sizes of

$$\frac{\alpha_s(\omega_0)}{\alpha^0(\omega_0)} = \frac{1}{\sqrt{1 + 2S}}, \tag{4.25}$$

at line centre, and a Lamb dip width corresponding to γ_S. In the case of a weak beam ($I_{probe} << I_{pump}$) an equation similar to 4.19 is obtained but Γ_S is replaced with $\Gamma_S^* = (\gamma + \gamma_s)/2$ [122].

Were the linewidth of the incident radiation infinitely narrow then these equations would hold exactly true. However, this is not the case and instead the pump and probe fields exist as an array of frequencies. For transitions in the MIR with anticipated spontaneous emission lifetimes of the order of seconds it is this spread that will usually dominate the observable dip width.

4.1.1 Experimental

Initial experiments were performed in the following manner: the Daylight Solutions EC-QCL was passed through a 70 cm cell with BaF_2 windows and then retroreflected such that the 'probe' beam overlapped with the 'pump' beam through the cell in a counterpropagating manner but with an angle of separation large enough for the probe beam to be separately collected c.a. 1 m from the cell onto a detector (VIGO-PVI-2TE-6). This setup is in essence the schematic depicted in the previous section (Figure 4.4). Later experiments were performed with a complete realignment of the experiment such that a 'probe' beam of $\sim 5\%$ of the laser power was created with a CaF_2 beam splitter immediately following the laser and passed across a different path from the 'pump' before being overlapped through the cell as is shown in Figure 4.5.

A typical Lamb-dip experiment would have allowed complete overlap of the two beams, but the frequency instabilities caused by optical feedback into the EC-QCL made this operation mode unfeasible. Even with this alignment frequency instabilities during the scan caused by mechanical jitter in the cavity and low-frequency noise in the current

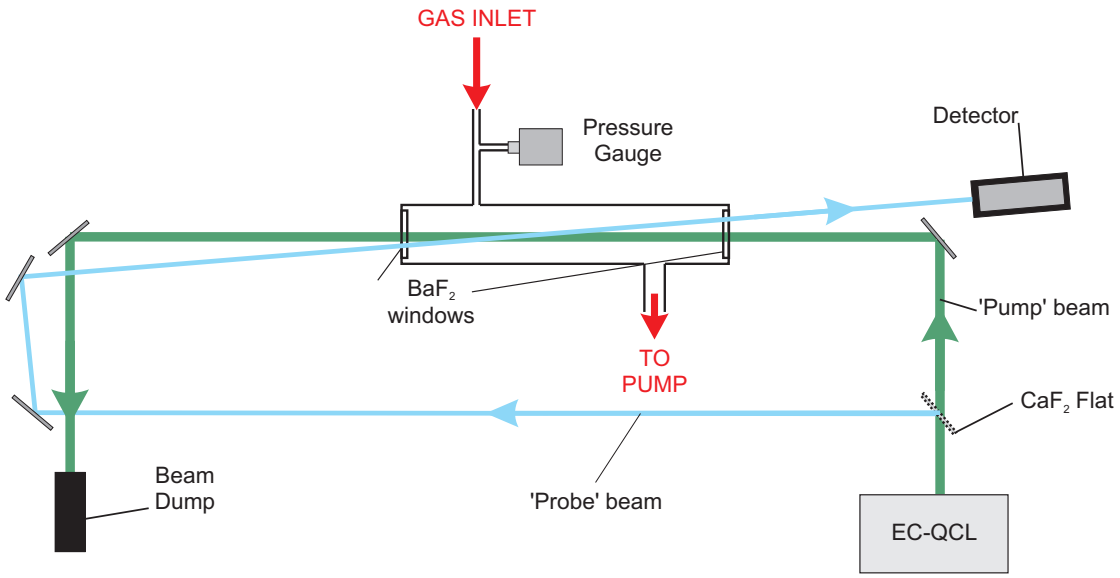

FIGURE 4.5: Lamb-dip experimental setup. A CaF_2 flat was used in order to split c.a. 5 % of the laser radiation from the main beam and this weak 'probe' beam then overlapped with the strong 'pump' beam in a counterpropagating manner.

controller meant that the narrow dips were unobservable following any scope-based averaging. As such, where mentioned a post-processing routine has been employed by which individual scans were recentred and then averaged using a routine in MATLAB.

4.1.2 Results

Initial experiments were performed using approximately equal parts NO and lab air (36 mTorr and 37 mTorr, respectively); the laser scanned over the $R(13.5)_{\frac{1}{2}}$ transition of NO at 1920.7 cm^{-1} at a rate of 40 Hz. The result of 80 individual scans post-processed and averaged is shown in Figure 4.6.

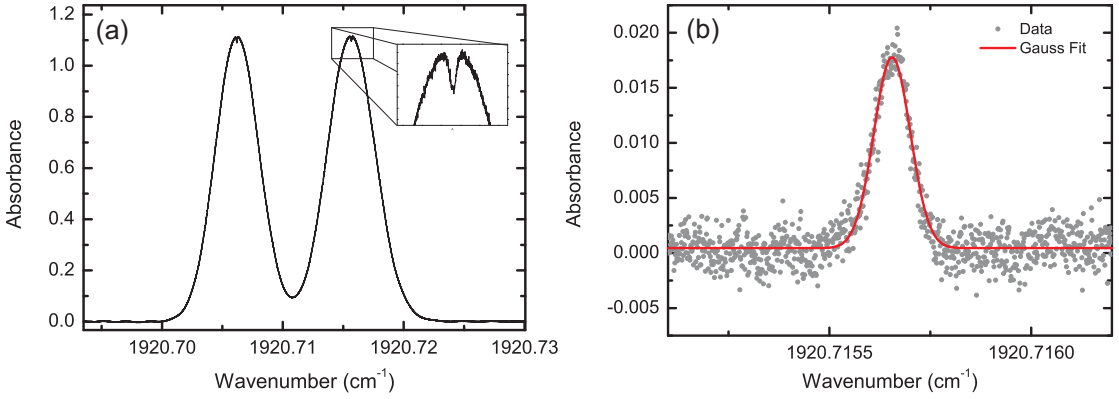

FIGURE 4.6: A Lamb dip spectrum taken using a retroreflected probe beam showing (a) the $R(13.5)_{\frac{1}{2}}$ transition with zoomed inset and (b) a Gaussian fit to the dip at 1920.7155 cm^{-1}. A FWHM of 2.7 ± 0.7 MHz, and a transition dipole moment of 2.3×10^{-3} D are returned from this data.

A global fit of the spectrum was performed by D Weidmann and returns a saturation parameter of 0.25 corresponding to a transition dipole moment of 2.3×10^{-3} D and a dip width of 2.7 ± 0.7 MHz. This value correllates to a direct measurement of the laser linewidth, and along with the transition dipole moment is in good agreement with previously measured values [86, 124–126]. The dip was found to be best fit with a Gaussian profile as is shown in Figure 4.6(b) rather than the typical Lorentzian profile of a laser, again mirroring findings in the literature [86, 125, 126], and most likely due to injection current fluctuations.

After these initial experiments had been performed the setup was dismantled and re-designed with the addition of a CaF_2 beam splitter to allow an improved degree of overlap between the pump and probe beams. Leaks within the pressure system were detected and removed such that data could be taken *without* lab air and at pressures of NO down to 2 mTorr. A selection of typical data recentred and averaged for 100 scans is shown in Figure 4.7 overlaid with a Lamb-dip global fit performed using Eqn 4.19 and the fitting routine is included in Appendix A.

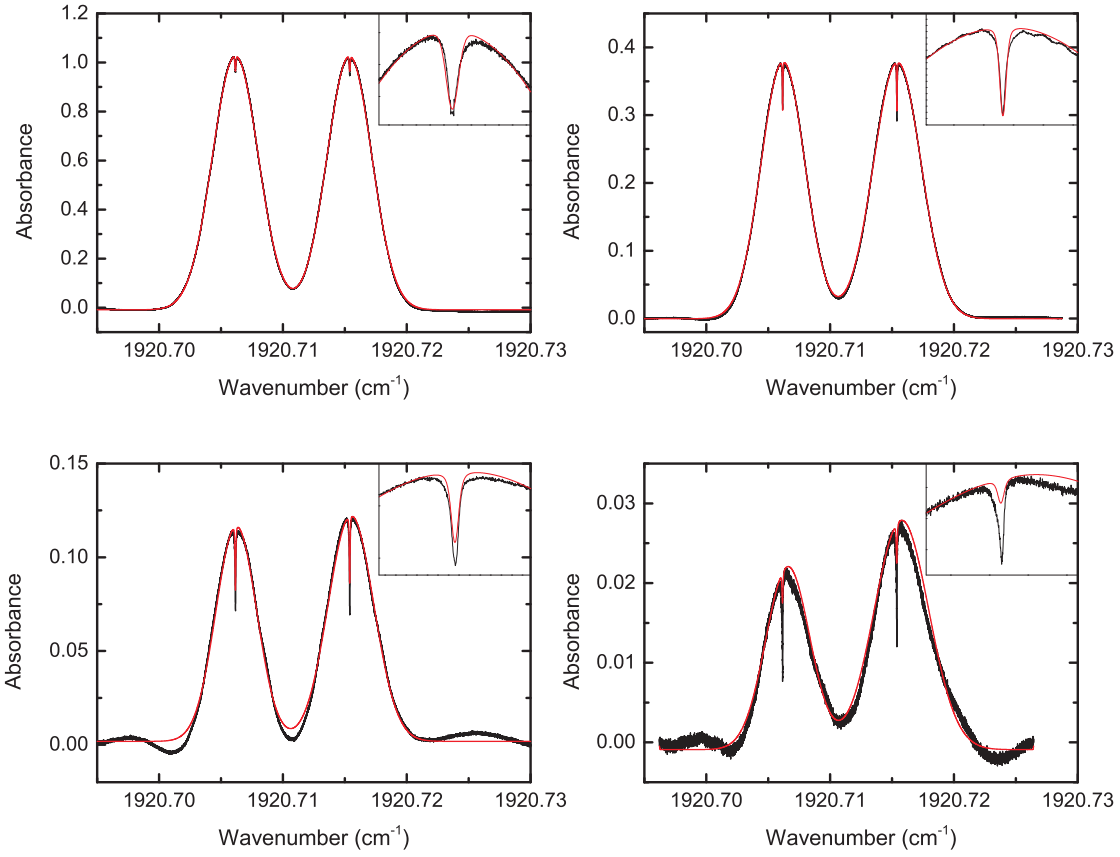

FIGURE 4.7: Lamb dip spectra of the R(13.5)$_{\frac{1}{2}}$ transition at (a) 65 mTorr, (b) 25 mTorr, (c) 10 mTorr and (d) 2 mTorr overlaid with a global fit and zoom upon the left hand dip. The Lamb-dip size can clearly be seen to increase as pressure is decreased, and at c.a. 10 mTorr the fitting routine can be seen to become unapplicable as it is no longer capable of reproducing the depth of Lamb-dip observed experimentally.

It is apparent that at high pressure we see Lamb dip spectra not unlike those observed in Figure 4.6, but as the pressure within the system decreases, the size of the Lamb dip drastically increases. This is a result that would be expected, as decreasing the pressure within the system should increase the saturation parameter, S. However, neither the standing wave model in Equation 4.21 nor the weak probe model in Equation 4.19 predict dips of quite the size observed at the lowest pressure. As our probe is much weaker than our pump then Equation 4.19 should hold, and as such we would expect a maximum dip of approximately 60% the size of the unsaturated peak before laser convolution. This is clearly not the case for our experimental data, and below c.a. 10 mTorr the Lamb-dips are not adequately fit by this model as is shown in Figures 4.7 (c) and (d).

It is also of note that the dip in the R(13.5)$_{\frac{1}{2}}$f transition at 1920.715 cm^{-1} is generally deeper than the the other Λ doublet which is not reflected in the fit. This is due to the assumption made here, and in the literature [124] that each of the doublets is a single transition with equal intensity, whilst they are in fact split by hyperfine interactions into three closely spaced transitions ($>$ 1 MHz) as is discussed in Chapter 3. The splitting in transition frequencies is in fact slightly different for the two doublets and in the transition at 1920.705 cm^{-1} the separation is approximately three times bigger than that in the transition at 1920.715 cm^{-1} (0.9 MHz vs 0.27 MHz). This extra splitting would thus provide additional convolution of the Lamb-dip, slightly altering its depth and width. However, post laser convolution the difference in widths is well within error and this, combined with a wish to not over-paramatise the fits, meant that a global fitting routine was chosen. Finally, a degree of asymmetry is seen in the dip shapes themselves, particularly at low pressure - an effect which may suggest that we are approaching a rapid passage like regime.

Figure 4.8 then shows the saturation parameters returned from global fits to a series of spectra taken at pressures above 10 mTorr, alongside parameters predicted from known quantities. It is here that an insight can be gained into the effect of changing the pressure upon the saturation parameter. In particular it was found that whilst both transit time and pressure broadening contributions were required to be added in quadrature in the γ in Equation 4.19 to produce reasonable fits to the global spectra, utilising the reciprocal of this parameter as the τ in S did not produce anywhere near the observed pressure dependence. Instead it was found that a τ consisting of only pressure broadening values from HITRAN [1] produced much closer agreement. This behaviour is in some manner intuitive, as whilst transit time broadening can be expected to broaden an observed spectrum, much like the Doppler effect, it should not have a direct effect upon the actual saturation produced within the system.

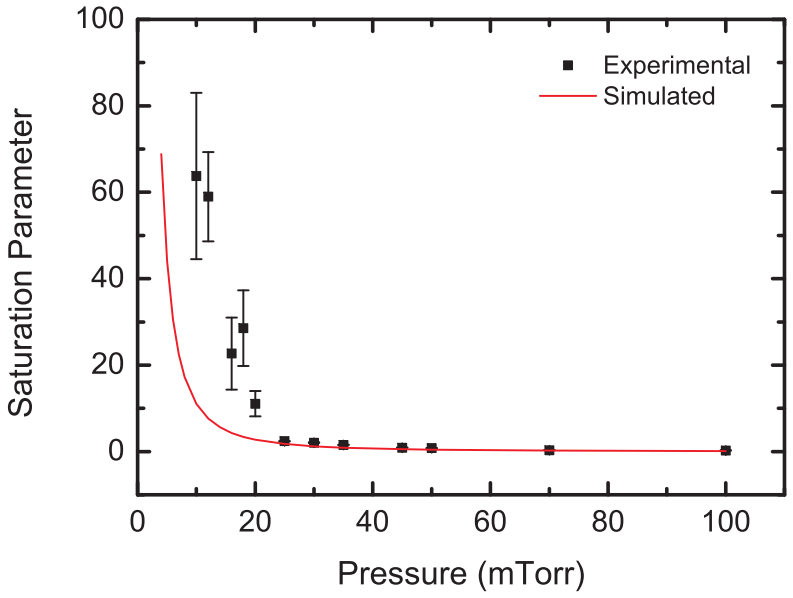

FIGURE 4.8: Saturation parameter as a function of pressure, showing both experimental (black) and simulated (red) values. Good agreement can be seen between simulated and experimental values, however at low pressure a significant deviation is seen.

This methodology produces a good degree of agreement between experiment and theory, and at 67 mTorr a transition dipole moment of 1.9×10^{-3} D is returned, in line with both literature values and those measured previously in this chapter. However, as the pressure of the system is reduced, the deviation between experiment and theory can be seen to drastically increase and at 12 mTorr (the lowest pressure profile adequately fit by 4.19) a saturation parameter approximately 8× larger than the anticipated value is returned, corresponding to a transition dipole moment of 4.5×10^{-3} D. This is far larger than literature values, and may in part be due to the fact that the collisional relaxation rates utilised here are taken from HITRAN [1] and are measured for a system in thermal equilibrium. In our case however, as the level of saturation within the system increases, the population in the first excited state will also increase, and relaxation rates between the states and in particular R_2 in Figure 4.1 may begin to play a part. This contribution is likely to be fairly limited however, and instead other more exotic forms of relaxation need to be considered. In particular the manifestation of extra dip depth is believed to be due to the production of coherence effects and so called cross-over resonances, which are neglected in Demtröder's derivation and are discussed in the following section.

4.1.3 Cross-Over Resonances

If two molecular transitions share either a common upper or lower state, and their observed transitions overlap within their Doppler widths then extra resonances are apparent in the Lamb-dip spectra. This effect was first observed by Uzgris et al [127] and is

in fact fairly common, largely due to the prevalence of hyperfine structure in molecular spectra.

In this case we shall consider a V-shaped resonance with a shared lower state and resonant frequencies ω_1 and ω_2, but a Λ-shaped system would produce similar results. When these two transitions are separated outside their Doppler widths then as the pump laser scans through the transitions from high negative to high positive velocity the probe laser simultaneously scans through the same transitions in the other direction as is shown in Figure 4.9.

In Figure 4.9(b) the two transitions are shown behaving as if they are completely independent, and we would expect to observe two separate transitions with Lamb-dips in their centres. However, once the Doppler widths of the two transitions overlap then this isolated picture is no longer true and at a mean frequency, $(\omega_1 + \omega_2)/2$, the pump laser is saturating a high velocity ω_1 group and a low velocity ω_2 group simultaneously as is shown in Figure 4.9(a). As both of these transitions share a common ground state this means that at the average velocity the subsets $v_0 \pm \mathrm{d}v_{avg}$ are pumped simultaneously, whilst at the same time being probed in the opposing transition. Thus, an extra dip is seen in the observed spectra with an intensity equal to the square root of the individual transition probabilities [122] (Figure 4.9(c)).

In the case of a shared ground state then a decreased population in this state means that an extra dip is seen, however in the case of a shared upper state then both waves contribute to an increase in that population and a peak should be observed at the central frequency. Although these extra transitions can complicate Lamb-dip spectra they can also assist in the assignment of spectra of a series of unknown transitions.

Figure 4.10 shows a spectrum of the $\mathrm{R}(1.5)_{\frac{1}{2}}$ transition of 8 mTorr of NO alongside the HITRAN positions and linestrengths (red) and the anticipated positions of cross-over transitions (cyan). It is apparent that in this case individual hyperfine components are easily observable as Lamb-dips, all with a FWHM of approximately 2 MHz. Further, extra cross-over resonances are clearly observable at the mid-points between transitions with shared upper or lower states as marked out by cyan lines. Figure 4.10(b) shows a Doppler subtracted spectrum of the $\mathrm{R}(1.5)_{\frac{1}{2}}\mathrm{e}$ transition, again with the HITRAN line positions and predicted cross-over resonances. The composite feature at 1884.2938 cm^{-1} is actually four cross-over resonances due to shared $F = 1.5$ and 2.5 components in either the ground and excited state.

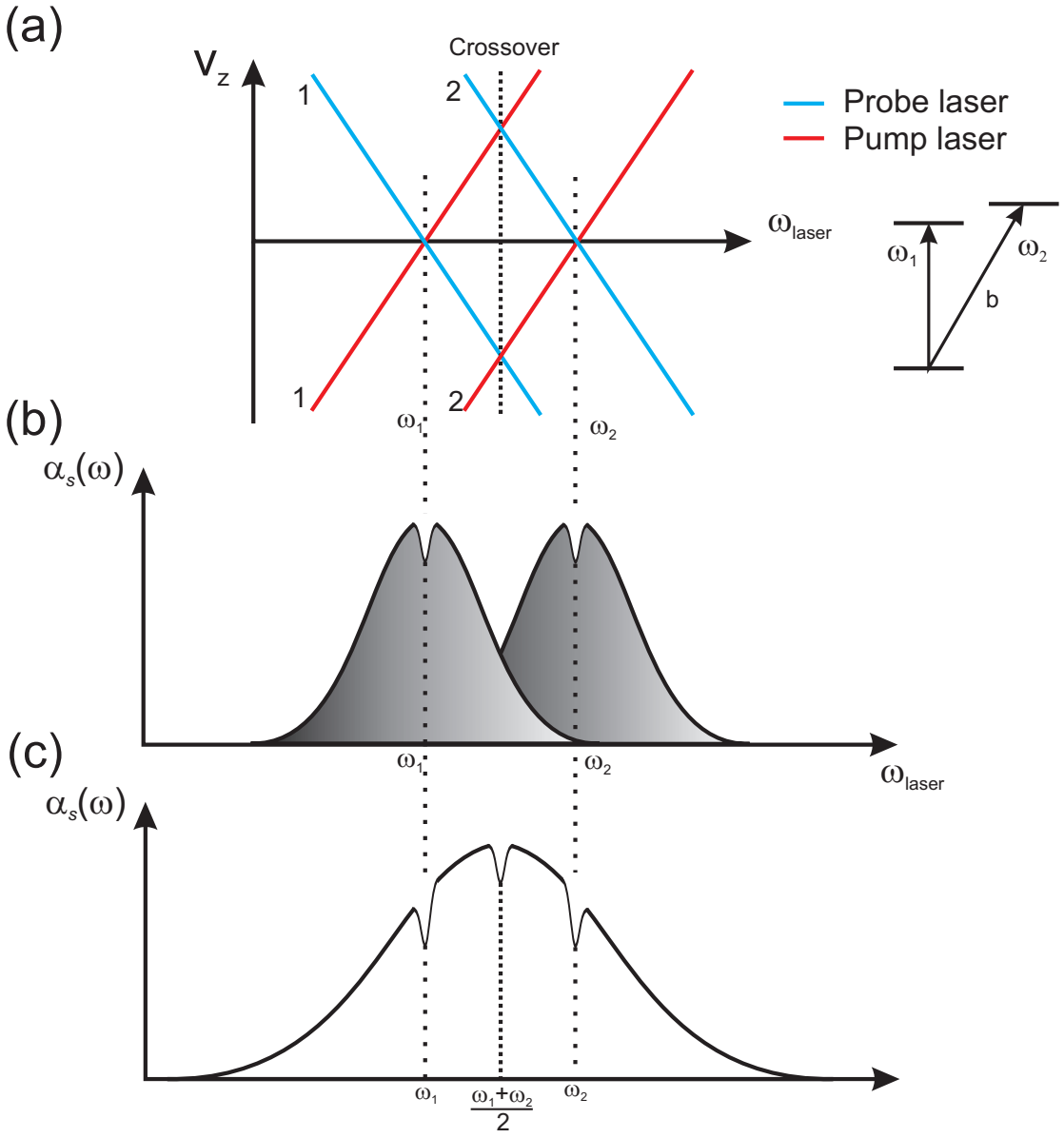

FIGURE 4.9: When two transitions are within each other's Doppler widths and share a lower state an extra resonance dip appears as is demonstrated here. As the pump laser scans from low velocity to high velocity (with respect to beam propagation) the probe laser scans through the same transition in the other direction and dips are only seen at the central frequency. When the transitions overlap however, an extra dip is observed in the probe spectrum at the mean frequency.

Returning now to a consideration of the increased size of the Lamb dip observed in our R(13.5)$_{\frac{1}{2}}$ NO spectra, it is noted that there are no directly shared states from which we could expect cross-over resonances at the central frequency. However, both the upper and lower states are hyperfine split by a magnitude < 1 MHz, so will simultaneously be excited within the linewidth of the laser. In such cases, cross-over type resonances should not occur but these resonances can become coupled [128–130] by angular momentum changing collisions, and as a result behave in a very similar manner to that of cross-over resonances. Specifically, as population is redistributed rapidly between these states then coupled resonance type behaviour is expected and additional dip intensity could be observed at the central wavelength frequency. Further evidence of a cross-over-type

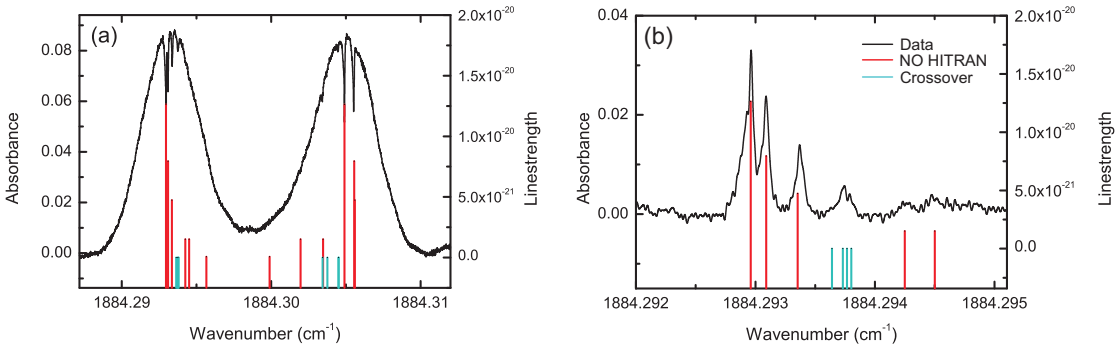

FIGURE 4.10: Lamb dip spectrum of R(1.5)$_{\frac{1}{2}}$ transition of 8 mTorr of NO. Showing (a) the entire transition and (b) a Doppler subtracted spectrum of the e peak at 1884.293 cm^{-1}. Also displayed are the HITRAN data for the positions and linestrengths of the hyperfine split transitions (red), and the positions of anticipated cross-over peaks (cyan) between the $\Delta F = +1$ around 1884.293 cm^{-1} and the weaker $\Delta F = 0$ transitions at 1884.2942/3 cm^{-1}.

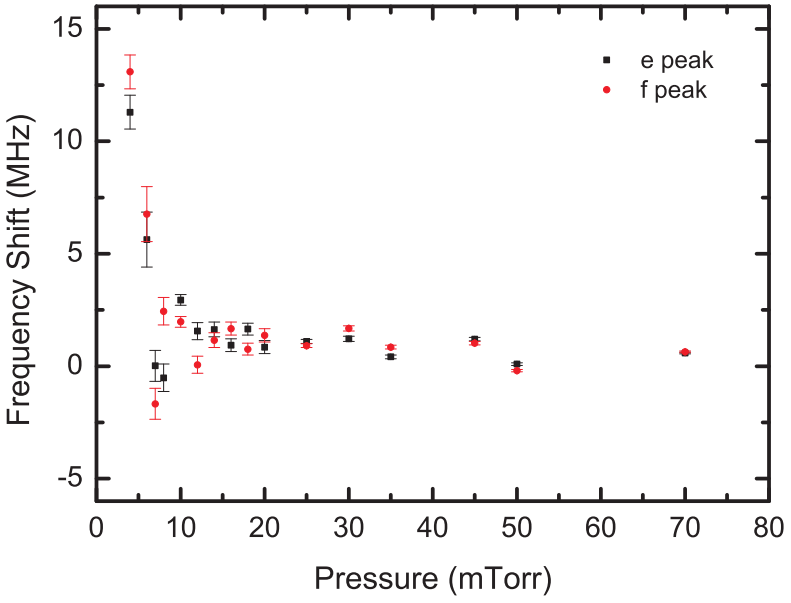

FIGURE 4.11: Displacement of R(13.5)$_{\frac{1}{2}}$ Lamb-dip from the broad absorption Gaussian centre.

effect in our $J = 13.5$ spectra is shown in Figure 4.11 where the position of the Lamb dips with respect to the broad underlying absorption can be seen to change as a function of pressure. This is an effect known to occur in cross over resonances and is explained in third order perturbation theory [131]. It is of note here also that the shift in position only becomes apparent below 10 mTorr, the point below which the fitting routine is no longer applicable.

4.1.4 Power Effects

The extra amplitude observed in the R(13.5)$_{\frac{1}{2}}$ dips at low pressures means that meaningful saturation parameters cannot be gained from low pressure data, however the widths of the dips remain consistent with the high pressure values. Thus, in order to investigate the linewidth of the laser as a function of power, low pressure data has been used due to the higher contrast especially for the lower pump powers.

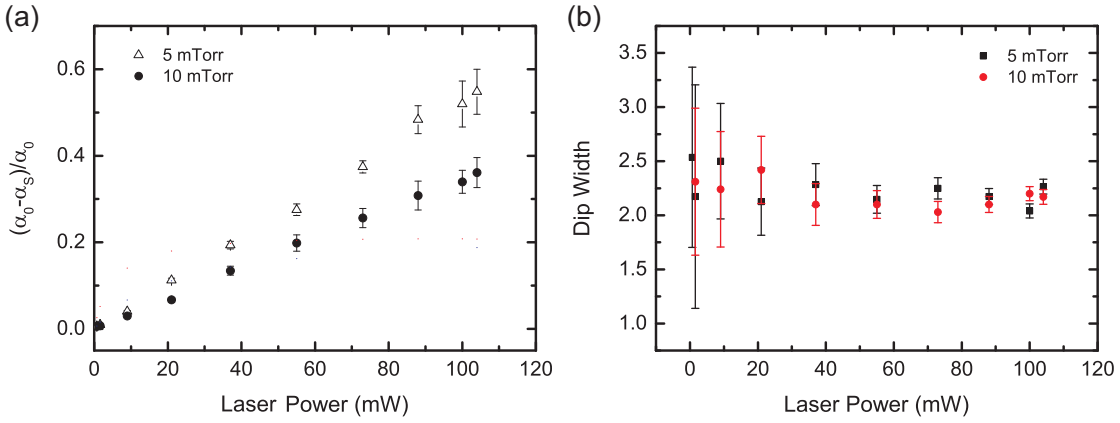

FIGURE 4.12: The effect of changing the saturating power upon (a) the dip height ratio given by $(\alpha_0 - \alpha_S)/\alpha_0$ and (b) the dip width. It is apparent here that changing the saturating power increases the size of the dip.

Two methods were used to attenuate the power of the pump beam. Firstly, a wire grid polariser was utilised immediately after the laser and measurements taken with both 5 and 10 mTorr of NO (Figure 4.12). It is clear from Figure 4.12(a) that as the saturating power increases so does the magnitude of the dip, as would be expected ($S \propto I_p$). However, as the model given by 4.19 does not appear to hold at these low pressures, simulations are unable to produce any meaningful information from these curves. It can also be seen in Figure 4.12(b) that the laser linewidth is invariant to the incident pump power within error, however the same is not true when we consider the Lamb-dips taken whilst the power is altered through the injection current to the laser (Figure 4.13).

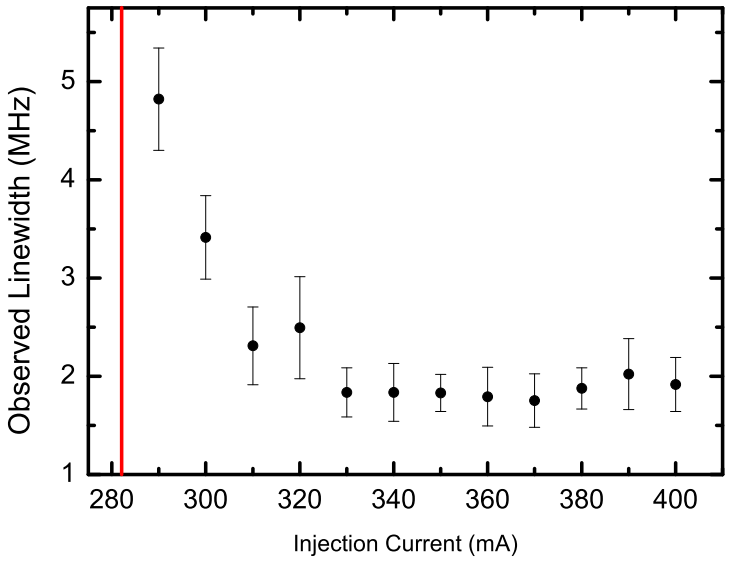

FIGURE 4.13: Observed laser linewidth as a function of applied current.

It is clear here that far from threshold current (I_{th}) the observed laser linewidth is constant at c.a. 2 MHz, but that as the current and thus power is reduced, the observed linewidth significantly increases. This is a well known effect and one which is described thoroughly by Yamanishi et al [16] in a paper discussing the intrinsic linewidth of QCLs. The following section describes their work and investigates the linewidth of our laser in more depth.

4.1.5 Linewidth

Before the first laser was experimentally demonstrated, Schawlow and Townes had produced their now famous formula describing the fundamental limit upon a laser's linewidth [132], but it was not until 1982 [133] that this formula was formally adapted to diode lasers with the Henry linewidth enhancement factor, α_e:

$$\delta\omega = \frac{v_g^2 h\omega\alpha\alpha_m n_{sp}}{4\pi P_o}(1+\alpha_e^2) \tag{4.26}$$

where v_g is the group velocity of the electrons, α the cavity losses, α_m the mirror losses, n_{sp} the spontaneous emission factor and P_o the output power. α_e accounts for refractive index variations caused by fluctuations in the electron density throughout the gain material, an effect which has typically widened traditional diode laser linewidths but which in QCLs is close to zero, as refractive index variations are negligible at the peak of the gain spectrum [11, 134, 135].

In a paper by Yamanishi et al [16] this equation was reformulated to become a function of the rate processes occurring within a three level QCL (Figure 4.14).

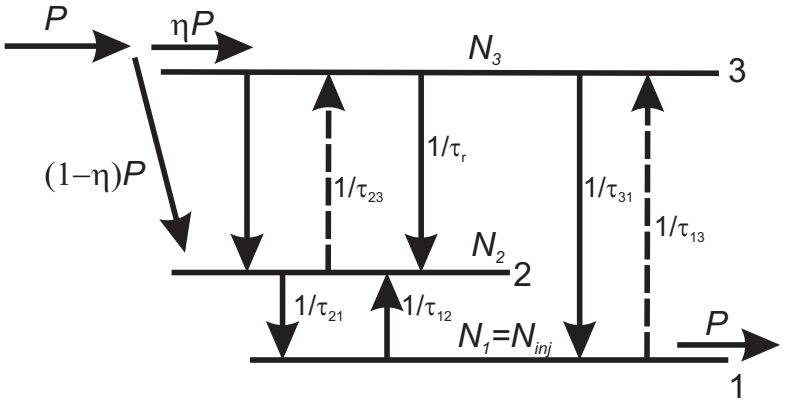

FIGURE 4.14: Three level model and rate processes utilised in this linewidth model. The assumption is made that all three level systems within the gain medium are equivalent. (From [16])

Here N_i corresponds to the electron population in each of the states, P corresponds to the rate of influx and outflow of photons from the laser system, η to the coupling into the level 3 and the τ's correspond to the time constants of relaxation. It should be noted that only τ_r corresponds to a radiative process and all other time constants τ_{ij} refer to phonon assisted relaxation between the levels i and j. The linewidth equation is then:

$$\delta\omega = (1/4\pi)F_R \frac{N_3}{(N_3 - N_2)_{th}} \frac{(\hbar\omega)\gamma_{photon}^2}{P_{int}}(1 + \alpha_e^2) \tag{4.27}$$

where F_R is a factor due to spontaneous emission enhancement caused by a single pass gain of spontaneous emission, and is assumed to be 1, γ_{photon} is the photon decay rate, $P_{int} = \gamma_{photon}(\hbar\omega)N_{photon}$ is the internal power and N_{photon} is the photon population. By considering only the case above threshold this then becomes:

$$\delta\omega = \frac{1}{4\pi} \frac{\beta_{\text{eff}}\ \gamma_{\text{photon}} n_{sp}}{1 - \epsilon} \left[\frac{1}{(I_o/I_{th} - 1)} + \epsilon \right] (1 + \alpha_e^2), \tag{4.28}$$

with:

$$\epsilon = \frac{\tau_{21}\tau_{31}}{\eta\tau_t(\tau_{21} + \tau_{31})}, \tag{4.29}$$

where τ_{ij} corresponds to the the reciprocal of γ_{ij}, the relaxation rate between two levels i and j, η is the upper level injection efficiency, I_o and I_{th} are the operating and threshold currents, and β_{eff} is the effective coupling of the spontaneous emission given by the ratio of the spontaneous emission rate coupled into the lasing mode, (β/τ_r), to the total relaxation rate, $(1/\tau_t)$, where β is the coupling efficiency of spontaneous emission into a single laser mode.

It is of note that this equation is not completely applicable to EC lasers, where the losses involved within the system [136] (and thus largely included within α and α_m) are also tempered by the mirror and grating reflectivities as well as the coupling of light from the diode into the cavity. As there is no information regarding the performance of the external cavity in the Daylight system we have presumed the losses to be equal to those of a bare diode.

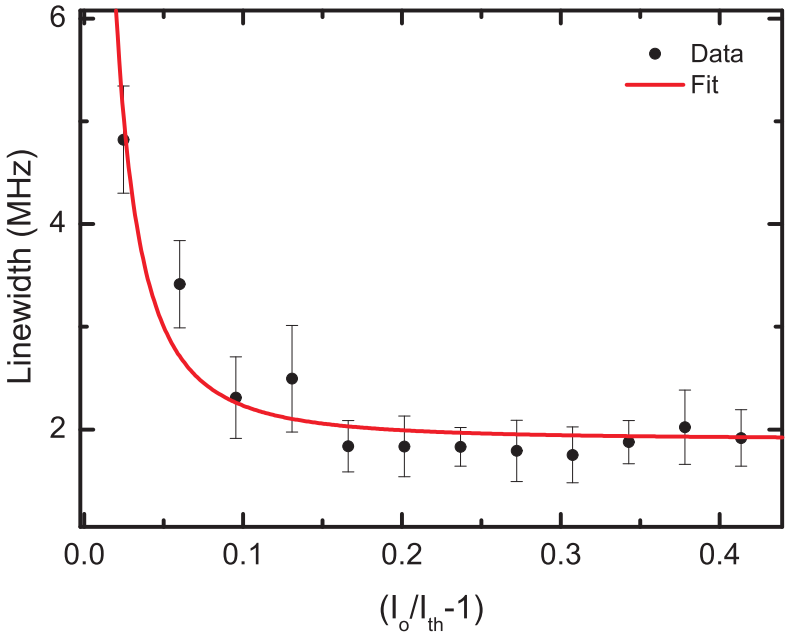

FIGURE 4.15: Width of the Lamb-dip as a function of injection current. The constants returned from the fit are $n_{sp} = 1.1781$, $\beta_{eff} = 1 \times 10^{-6}$, $\tau_{21} = 0.32$ ps, $\tau_{31} = 2.0$ ps, $\gamma = 1.0 \times 10^{12}$ Hz, τ_t=4.6 ps and $\eta = 0.612$.

In this manner, the laser linewidth can be related to the ratio of the operating current to the threshold current with all other parameters fixed and dependent only upon laser design. Unfortunately, as our laser system is commercially produced, we have little information about the exact constants for our specific laser, including the level of losses. However, a range of reasonable values for QCLs are given in the literature [16, 86] and using these as limiting values added in quadrature with a baseline noise level of c.a. 2 MHz allows the performance of a least-squares fit as is shown in Figure 4.15.

The constants returned from this fit are detailed above, and these imply an 'inherent' linewidth of 200 kHz were current noise not the dominating factor. These values are consistent with literature where theoretical calculations, and more recently experimental data [86] have shown that the inherent QCL linewidth can in fact be very narrow, and sub kHz values have been reported at optimal conditions.

TABLE 4.1: The constants returned from the fit shown in Figure 4.15 alongside the ranges of these constants as appeared have in the literature from [16, 86].

	n_{sp}	β_{eff}	τ_{21}	τ_{31}
Literature Range	1–1.2	1×10^{-8}–1×10^{-5}	0.15–0.35 ps	1.8–4.5 ps
Fitted Value	1.178	1×10^{-6}	0.32 ps	2.0 ps
	γ	τ_t	η	
Literature Range	1.2×10^{11}–2×10^{12} Hz	4.3–8.7 ps	0.6–0.8	
Fitted Value	1.0×10^{12} Hz	4.6 ps	0.612	

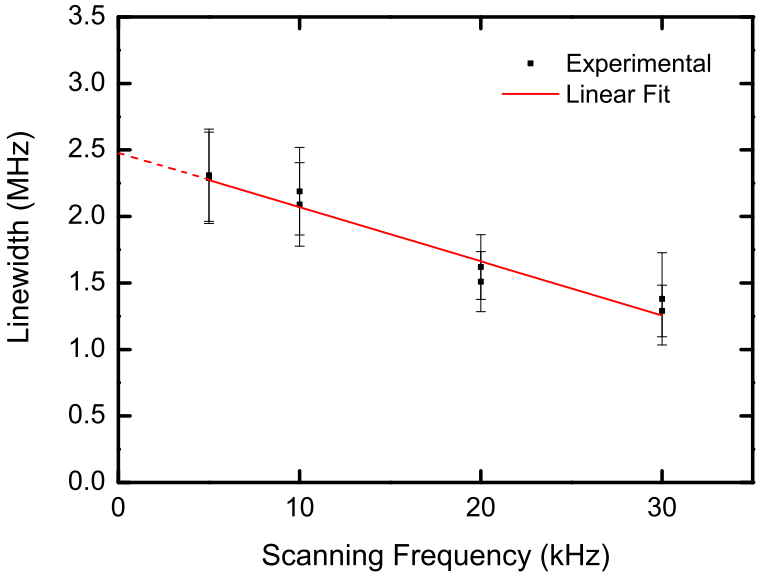

FIGURE 4.16: Width of Lamb-dip as a function of scanning frequency for fast scan rates. Interpolation of linear fit to baseline returns a y-axis crossing of 2.5 MHz in reasonable agreement with our slow scan data.

Evidence that 2 MHz is not the limiting linewidth of our laser is further shown in Figure 4.16, where the laser was scanned using direct modulation of the injection current with a 1 V sine wave at a range of frequencies. It can be seen that increasing the scan frequency decreases the width of the observed dip. This shows that the observed laser bandwidth is decreased as a function of interaction time, down to 1.3 MHz at 30 kHz scan rate when the bandwidth of the detector became the limiting factor. This behaviour implies a low frequency noise source causing additional broadening at long observation times. It should be noted that in this case the scanning range was limited such that our Ge etalon FSR was too large to provide useful frequency scale data, instead the frequency scan rate was calibrated using the width of a single Λ-doublet, explaining the larger than usual error bars. Also plotted in Figure 4.16 is a straight line through the observed data points. A linear fit is not theoretically implied in the literature but the data is well fit and when interpolated to the y-axis gives a crossing value of c.a. 2.5 MHz consistent

with our 'slow' data.

4.1.6 High-Resolution Spectroscopy

One final reason that Lamb-dip spectroscopy is performed is in order to obtain spectra of molecules with resolution smaller than the Doppler width. One example of such information has been shown for the $R(1.5)_{\frac{1}{2}}$ transition of NO in Section 4.9, demonstrating the ability to not only determine the position of the hyperfine transitions but also assign those transitions through the use of cross-over resonances. Further to this, the Lamb-dip spectrum of the unresolved $R(13.5)_{\frac{3}{2}}$ Λ-doublet of NO is shown in Figure 4.17(a) for 5 mTorr, and here a splitting of 80.0 ±7.2 MHz is clearly apparent in good agreement with literature [1].

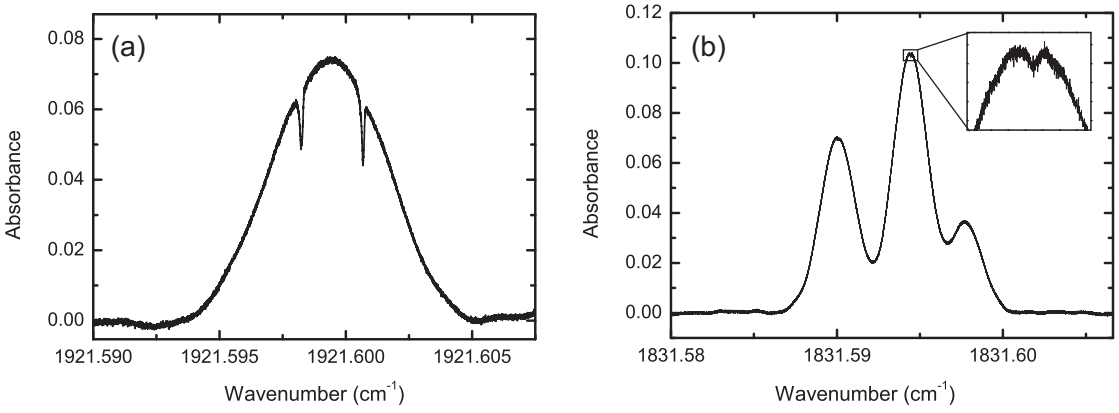

FIGURE 4.17: Lamb-dip spectra of (a) the $R(13.5)_{\frac{3}{2}}$ transition of 5 mTorr of NO and (b) the P(1) transition of c.a. 50 mTorr of $D^{79}Br$. Shown is the maximal dip size achieved, and as such there was insufficient contrast for hyperfine splitting determination in DBr.

It is notable that the extra resolution achieved using this methodology would have been useful for determining the DBr spectral constants measured in Chapter 3, however the absorption cross-sections for DBr are approximately 100 times smaller than those of NO, and as such, higher pressures were required for appreciable absorption. Higher pressure however lead to an increased collision rate, and as a result negligible contrast between dip and unsaturated absorption is observed as is shown in Figure 4.17(b) for 100 mTorr of DBr (isotope mixture c.a. 1:1).

4.2 Sub-Doppler Polarisation Spectroscopy

Whilst saturation spectroscopy, and in particular Lamb-dip spectroscopy, interrogates the change in absorption induced by a pump beam upon a probe beam, polarisation

spectroscopy detects a polarisation change induced in the probe beam by a polarised pump beam.

The principle of polarisation spectroscopy can be understood from Figure 4.18. When a beam of infrared radiation excites a ro-vibrational transition then along with the change of J there is also a change in the projection of J along the axis of electric field propagation, M. For a linearly polarised beam the selection rule is then $\Delta M = 0, \pm 1$, and in fact linearly polarised light can be thought of as a superposition of two circularly polarised light beams σ^+ and σ^- each of which has the specific selection rule $\Delta M = +1$ and $\Delta M = -1$ respectively. If a single circularly polarised beam is used to pump the system, say σ^+, then $\Delta M = +1$ and the spatial distribution of angular momentum will become anisotropic, as some M levels will not be populated (or not be depopulated depending upon the spectral branch). This behaviour is shown in Figure 4.18 for an R(1) transition.

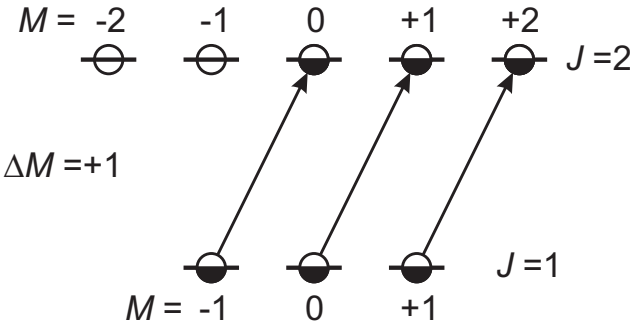

FIGURE 4.18: Schematic showing the effect of a σ^+ beam acting upon an R(1) transition. The imposed selection rule is $\Delta M = +1$ and it is apparent that in this case there will be a deficit of population in the $M < 0$ states and as such the system becomes partially oriented as the $\pm M$ states have different populations.

When this sample is then interrogated by a second, linearly polarised beam this spatial anisotropy is observed as a birefringence within the sample causing the plane of polarisation to rotate. If an experiment is set up in a similar manner to that used in Section 4.1, with a $\lambda/4$ waveplate in the the pump beam, then the pump beam becomes circularly polarised and the linearly polarised probe beam will detect any anisotropy only at line centre (Figure 4.19). In this setup, a polariser placed before the final detector allows selectivity of the the polarisation of light incident upon the detector, and thus allows the degree of birefringence to be measured.

More quantitatively, in a hybrid of Demtröder's formalism [122] and the work presented

by Bartalini et al. [137], when a linearly polarised probe wave $E = E_0 e^{i(\omega t - kz)}$ propagates along the z axis, its circularly polarised constituents can be described as:

$$E^+ = E_0^+ \, e^{\,i(\omega t - k^+ z)}; \quad E_0^+ = \frac{1}{2} E_0(\boldsymbol{x} + i\boldsymbol{y}) \tag{4.30}$$

$$E^- = E_0^- \, e^{\,i(\omega t - k^- z)}; \quad E_0^- = \frac{1}{2} E_0(\boldsymbol{x} - i\boldsymbol{y}), \tag{4.31}$$

where $\boldsymbol{x}$ and $\boldsymbol{y}$ are unit vectors in the x and y directions. When the probe beam passes through a sample within which anisotropy has been induced using a strong circularly polarised pump laser, then the two components of the probe will experience different absorption coefficients α^+ and α^-, and refractive index n^+ and n^- such that after a path length, L:

$$E^+ = E_0^+ \, e^{\,i(\omega t - k^+ L + i(\alpha^+/2)L)} \tag{4.32}$$

$$E^- = E_0^- \, e^{\,i(\omega t - k^- L + i(\alpha^-/2)L)}. \tag{4.33}$$

These two components sum to give an overall elliptically polarised beam, which when allowing for birefringence Δb_r and dichroism Δb_i within cell windows of thickness d is expressed as:

$$E(z = L) = E^+ + E^- \tag{4.34}$$

$$= \frac{1}{2} E_0 \, e^{i\omega t} \exp\left\{-i[\omega(nL + b_r)/c - i\alpha L/2 - \Delta b_i/2]\right\} \cdot \left[(\boldsymbol{x} + i\boldsymbol{y})e^{-i\Phi} + (\boldsymbol{x} - i\boldsymbol{y})e^{+i\Phi}\right]. \tag{4.35}$$

where n and α are the mean values of the respective properties for the σ^+ and σ^- waves, and Φ, is the phase factor:

$$\Phi = \frac{\omega}{2c}(L\Delta n + \Delta b_r) - i\left(\frac{L\Delta\alpha}{4} + \frac{\Delta\alpha_w}{2}\right). \tag{4.36}$$

with

$$\Delta n = n^+ - n^- \tag{4.37}$$

$$\Delta\alpha = \alpha^+ - \alpha^- \tag{4.38}$$

$$\Delta\alpha_w = \alpha_w^+ - \alpha_w^- \tag{4.39}$$

$$\Delta b_r = b_r^+ - b_r^-. \tag{4.40}$$

As was the case for saturation spectroscopy, there will be an array of molecules that interact with the pump and probe beams simultaneously around ω_0, and the change in

absorption will be a Lorentzian;

$$\Delta\alpha(\omega) = \Delta\alpha_0 \frac{\left(\frac{\gamma_s}{2}\right)^2}{\left(\frac{\gamma_s}{2}\right)^2 + (\omega - \omega_0)^2}. \tag{4.41}$$

The refractive indices and absorption coefficients are related by the Kramers-Krönig dispersion relation [138], which leads to

$$\Delta n = \frac{c}{\omega_0}\Delta\alpha_0 \frac{\gamma_s(\omega - \omega_0)}{\left(\frac{\gamma_s}{2}\right)^2 + (\omega - \omega_0)^2}, \tag{4.42}$$

and consequently a phase factor of:

$$\begin{aligned} \Phi \quad = \quad & \frac{1}{2}\left[\left(\Delta\alpha_0 L \frac{\frac{\gamma_s}{2}(\omega - \omega_0)}{\left(\frac{\gamma_s}{2}\right)^2 + (\omega - \omega_0)^2} + \Delta b_r'\right)\right. \\ & \left. + i\left(\frac{\Delta\alpha_0 L}{2} \frac{\left(\frac{\gamma_s}{2}\right)^2}{\left(\frac{\gamma_s}{2}\right)^2 + (\omega - \omega_0)^2} + \Delta b_i\right)\right]. \end{aligned} \tag{4.43}$$

If the polariser before the detector is uncrossed by an angle θ from the y axis then the transmitted electric field is given by:

$$E_t = E_x \sin\theta + E_y \cos\theta, \tag{4.44}$$

which is then used in $I_t = c\epsilon_0|E|^2$ to calculate the observed lineshape. Typically, this is considered for small angles of uncrossing ($\theta \ll 1$), however it is also solvable for the more general case as:

$$I_t = 2I_0 e^{-\alpha L}\left[\xi + |\sin\theta\cos\Phi + \cos\theta\sin\Phi|^2\right] \tag{4.45}$$

where ξ is equal to the transmission at $\theta = 0$, and is a function of the polarisers used, and the factor $I_0 e^{-\alpha L}$ represents the saturated absorption spectrum.

Polarisation spectroscopy has the potential to be significantly more sensitive than saturation spectroscopy as the crossing angles between the polarisers can be fairly small, and in this manner only light which has had its axis of polarisation rotated will be detected, as opposed to saturation spectroscopy, where the full intensity of the probe must be detected.

4.2.1 Experimental

The setup used in this experiment is shown in Figure 4.19 and is fairly similar to that used in the Lamb-dip experiment, except for the addition of a tunable $\lambda/4$ waveplate

(ALTECHNA PO-TWP-L4-25-UVIR) after the probe beam is separated from the pump, and crossed MgF_2 Rochon polarisers (ALPHALAS PO-RO-8-MGF) with an extinction coefficient of 10^{-5} placed both directly after the laser and immediately before the detector. The polarisation component of the beam rejected by the polariser was emitted at a separation angle of 1.8° from the main beam and was removed with the use of irises.

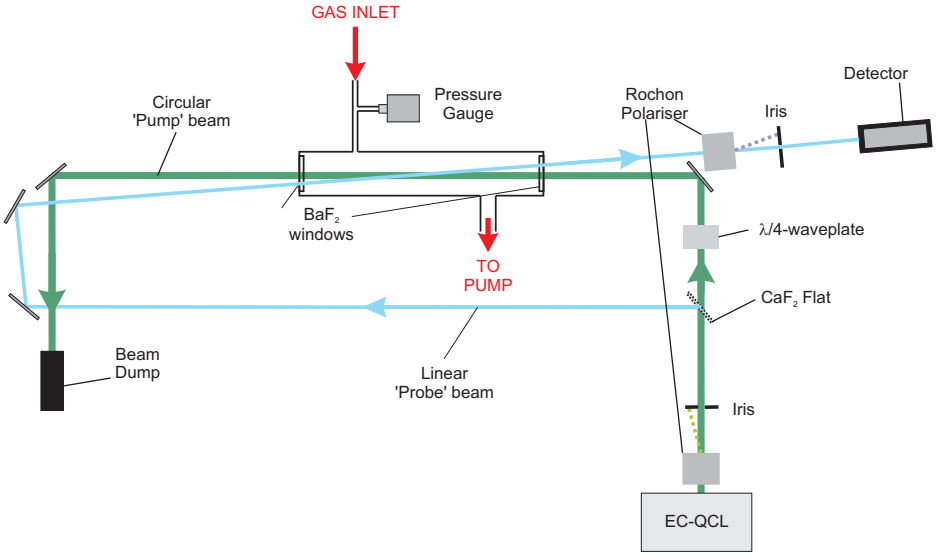

FIGURE 4.19: Experimental setup employed for polarisation spectroscopy.

The $\lambda/4$ waveplate required angle tuning for optimal operation at this wavelength, and this was performed by passing the beam through the waveplate and then returning it along the same path. A wire grid polariser was then set to allow only vertically polarised light through, and the angle of the waveplate tuned such that maximum signal was observed. In this manner, as the horizontally polarised light first passes through the waveplate it becomes circularly polarised. When the light is retroreflected the direction of polarisation rotation is reversed (σ^+ to σ^- or vice-versa), and the waveplate then further rotates the polarisation into the vertical plane. Thus, by minimising the signal incident upon the detector the degree of circular polarisation was optimised. This polarisation was again checked and readjusted in the far field at the position of the cell in order to correct for any depolarisation caused by the intervening mirrors.

4.2.2 Results

Initially experiments were performed analogous to Lamb-dip with the addition of a $\lambda/4$ waveplate and polarisers uncrossed, such that $\theta = 90°$, and it was through maximisation of the dip size that the optimal beam overlap was determined. Once again the $R(13.5)_{\frac{1}{2}}$

transition was chosen, and Figure 4.20 shows the effect of left and right circularly polarised probe beams with 12.5 mTorr of NO. The dispersion signal can be clearly seen to change sign as the selection rule of the transition is reversed and the system oriented with or against the direction of pump beam propagation.

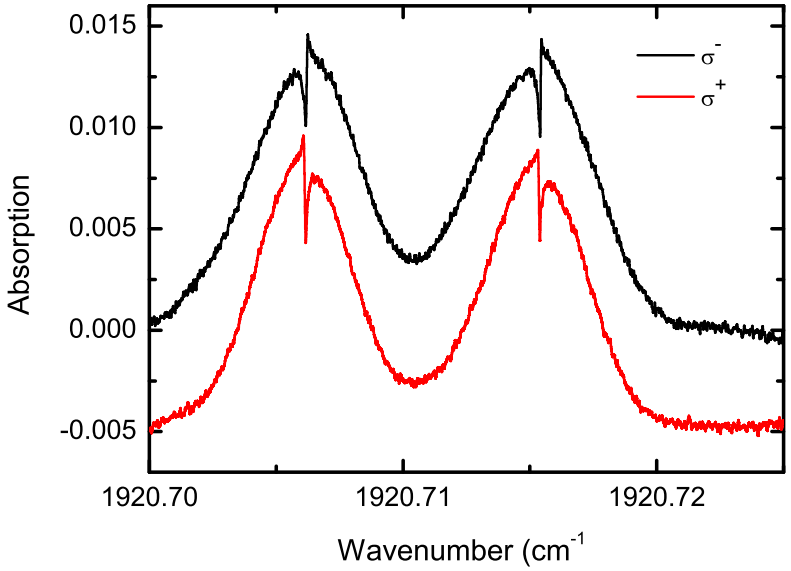

FIGURE 4.20: Polarisation spectrum of R(13.5)$\frac{1}{2}$ transition of NO with left and right circularly polarised pump beam detected by a linear probe with an uncrossing angle of 20°. σ^+ data is offset for clarity.

The polariser angle was then adjusted as is shown in Figure 4.21(a) for polarisation spectra of 15 mTorr of NO at a selection of crossing angles, with simulations overlaid in Figure 4.21(b). It should be noted that the data in Figure 4.21(b) is offset in the y-direction for clarity. As this simulation is performed for qualitative rather than quantitative agreement, the laser linewidth was accounted for by replacing γ_S with a value of 2 MHz [137]. A saturation parameter of 0.5 was also utilised, slightly lower than the measured value Lamb-dip value in order to account for losses from the waveplate.

A few things are apparent here - experiments with $\theta = 90°$ show a dip which is significantly smaller than equivalent Lamb-dip experiments, a result that is expected as not only is the power slightly decreased, the pump and probe beams are of different polarisations, and as such interact with slightly different subsets of molecules. Secondly, the expected polarisation spectroscopy behaviour can be observed as the angle of the polariser is changed towards crossing ($\theta = 0$). Here the dispersive profile at line centre becomes increasingly apparent whilst the 'normal' absorption signal decreases. As with

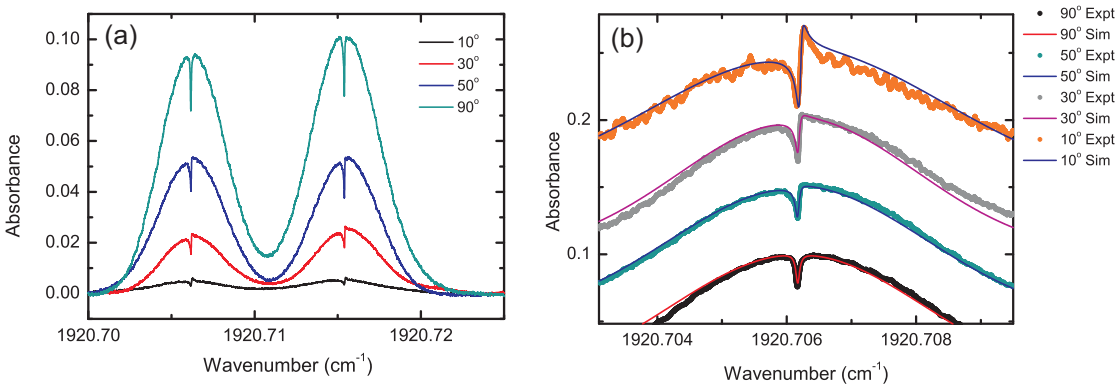

FIGURE 4.21: The polarisation signals of NO as a function of uncrossing angle, θ. As θ is decreased the dip become observably less symmetric as the dispersion signal become dominant.

the Lamb-dip data in Section 4.1, this data has once again been recentred and averaged for 100 scans. The dispersive signal apparent in the polarisation signals should in fact completely disappear at $\theta = 0$ [137] and a purely Lorentzian profile be returned. However, even realigning using the signal from the pump beam did not produce enough contrast for signal to be observed below $\theta = 10°$.

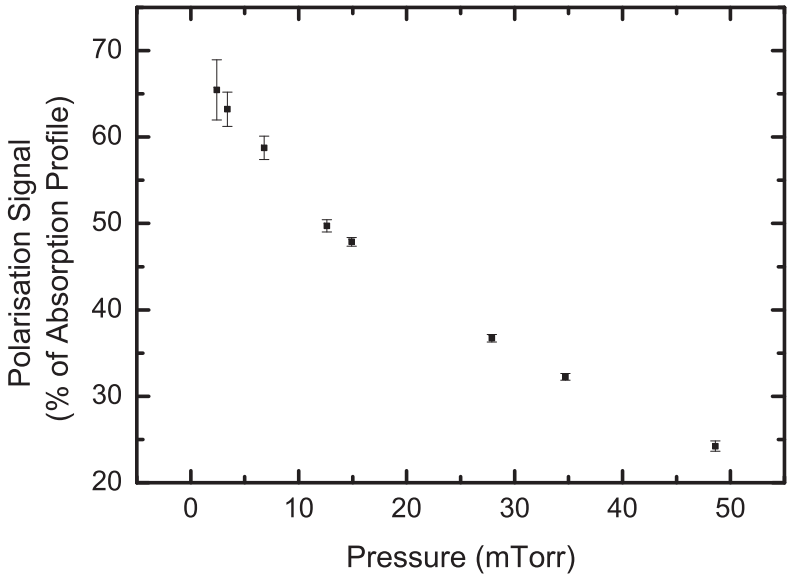

FIGURE 4.22: The percentage amplitude of polarisation signal as a function of pressure. As the pressure of the system was reduced, the degree of collisional dephasing decreases, increasing the degree of saturation. This in turn increases the degree of alignment within the system and thus the size of the observed signal.

Figure 4.22 shows the effect of pressure upon polarisation spectroscopy signal. The uncrossing angle was held at 20° and the results show increased polarisation signal percentage as the pressure is lowered as would be expected, up to a maximal value of 65 % at the lowest pressure (2.5 mTorr).

We desire to keep the uncrossing angle, θ small so that the dispersive signal is dominant, but these small signals produce a small overall signal size, and whilst increasing θ increases the dispersion signal, it further increases the size of the background saturated absorption which overrides the polarisation effects. It is possible to further increase the sensitivity of this technique by the addition of quadrature detection where both polarisation components are collected and both signals used to produce a background-free signal [139], but even this technique only provides a relatively small enhancement upon straight saturation spectroscopy [137].

A further use of polarisation spectroscopy is that the narrow lineshape and steep gradient at line centre provides an ideal frequency locking signal. That is, as the laser moves away from direct resonance a fast increase or decrease in amplitude is observed and this signal, conditioned for the specific laser, is an ideal correction signal to the injection current. In this manner a laser can be 'locked' to a particular frequency, and time averaged bandwidth reduced. The possibility of such a locking system for this laser was investigated, but the band pass electronics within the current modulation input make this untenable.

4.3 Conclusion

In this chapter work has been performed using sub-Doppler spectroscopic techniques. Lamb-dip spectroscopy has been performed, and dips greater than those expected from simple theory have been observed. The possible reasons for this behaviour have been discussed, and whilst determination of the saturation parameter is made impossible in the low pressure limit, at high pressure, coherent effects are minimised and a saturation parameter of 0.25 has been observed. This corresponds to approximately 20 % of population promoted to the excited state and is consistent with literature values of the transition dipole moment. The first direct measurement of the linewidth of an EC-QCL has been performed returning a value of c.a. 2.5 MHz in agreement with values found for DFB QCLs, and this value further investigated as a function of injection current and laser scan rate. Sub-Doppler polarisation spectroscopy has also been performed, independently confirming the observed laser linewidth. Collectively, these experiments have demonstrated the high-power and low-bandwidth nature of EC-QCLs and their applicability to high resolution spectroscopy, as well as hinting towards their use as an optical pump source, something which is further investigated in the next chapter.

Chapter 5

Pump-Probe Spectroscopy with cw QCLs

The desirability of preparing a sample such that an appreciable fraction of molecules are in an excited state has already been discussed. Population transfer mechanisms with a single laser were considered in Chapter 2, and Chapter 4 was concerned with saturation and polarisation spectroscopy, whereby population transfer was probed as a velocity selected Lamb-dip in the ground state, and a velocity selected anisotropy in the sample, respectively. This chapter presents work whereby the saturation induced by the high powered EC-QCL acting upon the fundamental rovibrational band of NO is probed in the first vibrationally excited state by a weak DFB QCL tuned to a transition in the first hot band.

5.1 Experimental

In this chapter a similar methodology is applied to that in Chapter 4, but whilst in Chapter 4 the strong pump beam and weak probe beam were produced by the same laser and tuned simultaneously, here these two beams are produced and tuned independently. Specifically, the EC-QCL is overlapped in a counterpropagating manner to the Alpes 5 µm DFB QCL. The pump beam was detected by a VIGO PVI-2TE-6 after attenuation to prevent saturation of the detector, whilst the probe beam was focused onto a VIGO PVMI-3TE-10.6 detector using an off-axis parabolic mirror with a focal length of 15 cm. Figure 5.1 shows the basis of the setup used, but omits extra mirrors used to extend the path length and thus allow improved overlap.

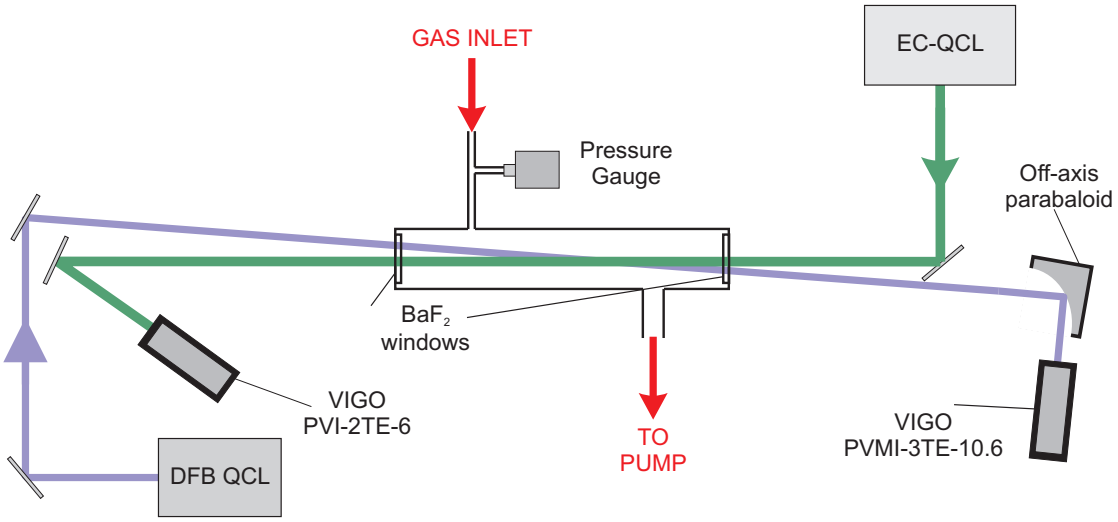

FIGURE 5.1: Schematic of the experimental setup used for pump-probe spectroscopy.

The pump laser was scanned primarily by using its piezo tuning at a rate between 5 and 100 Hz and over a range of approximately 1 GHz, and where mentioned by direct current modulation between 10 and 250 kHz over $\sim$ 500 MHz. The probe laser by contrast was scanned at rates of 1 kHz to 300 kHz over c.a. 3 GHz and ILX Lightwave temperature and current controllers (LDT-5545B and LDX-3232) were utilised for its operation. Whilst scanning, the scope was set to trigger with the EC-QCL scan and the multitude of DFB QCL scans over the course of the slow scan stored for later analysis.

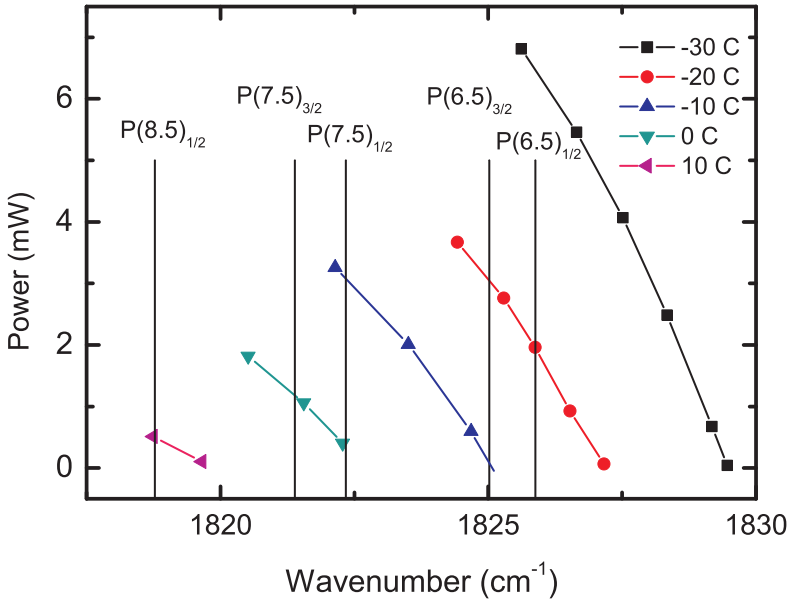

FIGURE 5.2: NO hot band transition line positions overlaid upon Alpes Laser specifications of power output as a function of wavenumber.

The lasers were initially tuned to transitions in a ladder configuration, with the pump laser upon a transition in the fundamental vibrational band of NO ($v = 1 \leftarrow 0$) and the

probe laser upon a transition in the first hot band ($v = 2 \leftarrow 1$). The tuning range of the probe laser was the primary limiting factor upon the exact transitions chosen, and Figure 5.2 shows the positions of NO hot band transitions overlaid upon the Alpes Laser specifications of its power as a function of wavenumber.

Ideally, a transition would be chosen at the highest power output so as to attempt to increase the sensitivity of our measurements. However, the cooling system in place in our mount is unable to reach temperatures below $-18°$C whilst the laser is running, which limits the choice to the P(7.5) and P(6.5) doublets. The $P(7.5)_{\frac{1}{2}}$ transition was thus chosen as the primary transition of interest as it would provide results at the highest possible power. The EC-QCL in turn behaves far better above $\sim$ 1875 cm^{-1} and as such the $R(6.5)_{\frac{1}{2}}$ transition was chosen as the bottom half of the ladder providing the configuration shown in Figure 5.3.

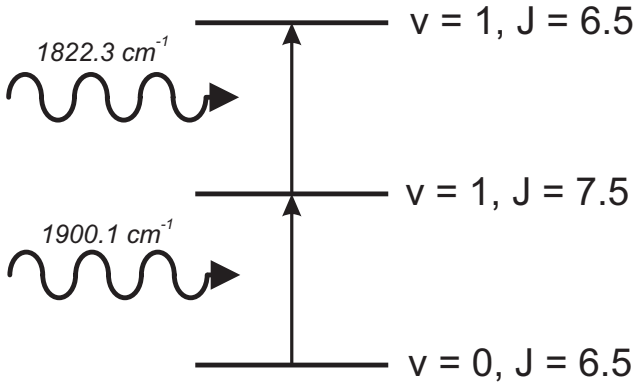

FIGURE 5.3: Schematic of the ladder configuration of NO states used in this pump-probe experiment. The EC-QCL first pumps the $R(6.5)_{\frac{1}{2}}$ transition in the fundamental vibration band at 1900.1 cm^{-1} and the probe DFB-QCL then probes the population in the excited state on the $P(7.5)_{\frac{1}{2}}$ transition in the first hot band at 1822.3 cm^{-1}.

5.2 Results

Having selected a set of transitions the pump and probe QCLs were set to tune over the relevant wavelength regions at 40 Hz and 50 kHz respectively. The cell was then filled with 100 mTorr of NO and the resulting signals are shown in Figure 5.4.

It can be clearly seen that when the pump laser is off resonance there is no observable signal in the probe scan (Figure 5.4(b)), but that when the pump laser is on resonance a somewhat complicated signal appears (Figure 5.4(c)), composed of two constituent parts and shown more clearly in Figure 5.5. A broad absorption is seen, similar to that which would be expected when interrogating a thermally equilibrated sample, and

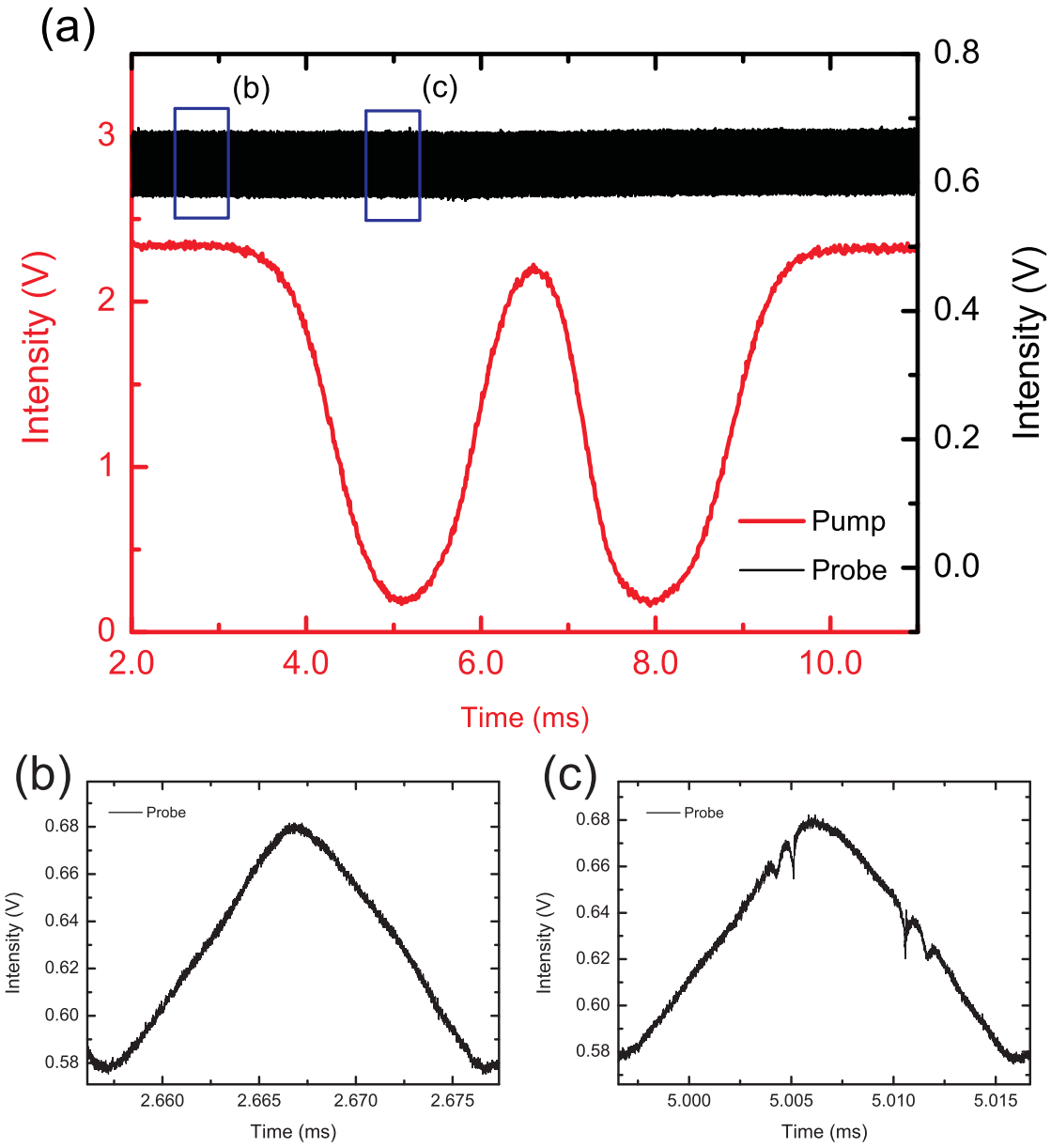

FIGURE 5.4: Example spectra taken from pump (red) and probe (black) beams as lasers are scanned over the $R(6.5)_{\frac{1}{2}}$ transition in the fundamental band and the $P(7.5)_{\frac{1}{2}}$ transition in the first hot band, respectively. (a) shows the signals recorded from both detectors simultaneously (the probe signal appears to be featureless due to the rapid repetition rate of the triangular scans), whilst (b) shows no visible absorption of the probe laser when the pump beam is off resonance and (c) shows the absorption apparent when the pump is on resonance.

overlaid upon that, a much narrower signal followed by a series of transient oscillations.

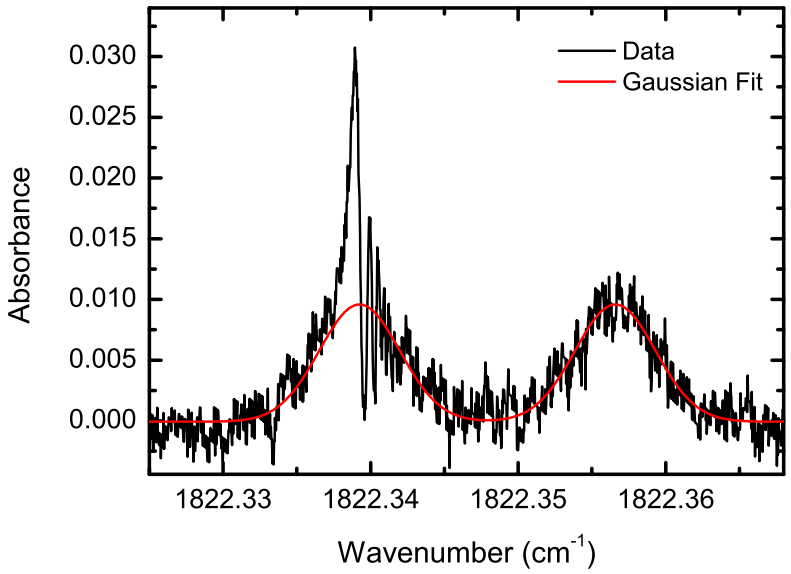

FIGURE 5.5: Absorption spectrum of the observed hot band P(7.5)$_{\frac{1}{2}}$ transition in Figure 5.4(c). The broad outline of a thermalised distribution is seen with a much narrower sharp peak observed followed by a series of transient oscillations.

The origin of these two effects is clearly optical pumping, but in order to gain a proper understanding of the processes occurring here it is useful to initially consider them separately.

5.2.1 Thermalised Signal

The broad absorption here corresponds not to an instantaneous population transfer but instead to an apparently equilibrated excited population produced cumulatively over the course of a pump laser scan. This population appears to be entirely thermalised as not only is the signal well fit by a Gaussian with a width of 126 ± 5 MHz in good agreement with the expected Doppler width at 300 K (124 MHz), but also that approximately equal population is seen in both Λ-doublets suggesting rapid equilibration between symmetry states.

This thermalisation is also apparent when transferring the pump laser from the R(6.5)$_{\frac{1}{2}}$ transition to an adjacent $\Omega = \frac{1}{2}$ state whilst still probing the R(7.5)$_{\frac{1}{2}}$ as is shown in Figure 5.6 for 100 mTorr of NO. As there is no longer a direct excitation into $v = 1$, $J = 7.5$ there is no sharp resonance in this state and instead only the broader Gaussian

resonance is observed with a width 121 ± 13 MHz and an amplitude approximately equivalent to that seen in Figure 5.4. This signal is also apparent when J states further afield are pumped, and perhaps more surprisingly even when molecules in the $\Omega = \frac{3}{2}$ spin-orbit state are interrogated by the pump laser.

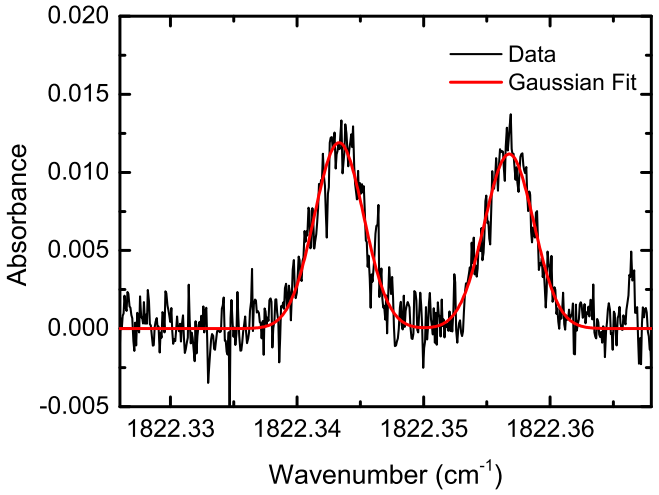

FIGURE 5.6: Absorption spectrum of the $P(7.5)_{\frac{1}{2}}$ hot band resonance observed when EC-QCL frequency is changed such that $R(7.5)_{\frac{1}{2}}$ in the fundamental vibration band is pumped.

J-J relaxation rates in the first vibrationally excited state of NO do not appear in the literature, however studies by Islam et al upon $v = 2$ [140] have shown that relaxation rates in that state are incredibly fast (lifetimes of the order of 1 µs at 100 mTorr) and there is little reason to expect them to differ substantially in $v = 1$. The relaxation of vibrational energy is anticipated to occur primarily through V-T collisional processes:

$$NO(v = 1) + NO \rightarrow NO(v = 0) + NO \tag{5.1}$$

and the rate constant for this at 300 K is 2.5×10^3 s^{-1} Torr^{-1} [141], corresponding to a vibrational lifetime of c.a. 4 ms at these pressures, much longer than the timescale of rotational transfer. It is thus anticipated that a thermal equilibrium would be reached within $v = 1$ before any significant collisional decay of the vibrational population occurs.

An attempt was made to measure the rate of relaxation into $v = 1$, $J = 7.5$ from other states. This was performed by fixing the current applied to the probe laser, such that it was providing fixed frequency radiation within the $P(7.5)_{\frac{1}{2}}$ transition, and scanning the pump laser over a ground state transition. This procedure is demonstrated in Figure 5.8 where the probe laser is at a fixed frequency within the $P(7.5)_{\frac{1}{2}}$ transition and the pump laser is tuned through the $R(7.5)_{\frac{1}{2}}$. Here there is no direct connection of the two

states but the excited population is still observed in the pump signal as the population is pumped into $v = 1$, $J = 8.5$ and then cascades into $J = 7.5$ (Figure 5.8).

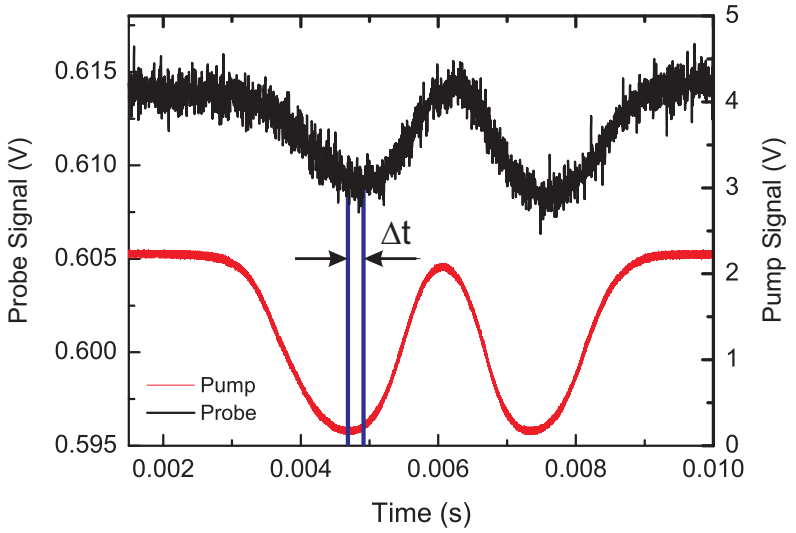

FIGURE 5.7: Delay between pump and probe signal whilst pumping the $R(7.5)_{\frac{1}{2}}$ state. and probing the $P(7.5)_{\frac{1}{2}}$ transition at a constant frequency.

Figure 5.6 shows the accumulated data for a number of transitions alongside the relaxation periods for the same J from reference [140]. In this paper individual $\Omega = \frac{1}{2} \leftarrow \frac{3}{2}$ relaxation rates were not measured, however a sum of relaxation rates into $\Omega = \frac{1}{2}$ was, and found to be at most a factor of 5 smaller than the sum of the $\frac{1}{2} \rightarrow \frac{1}{2}$ rates, and as such these inferred values are further displayed in the figure.

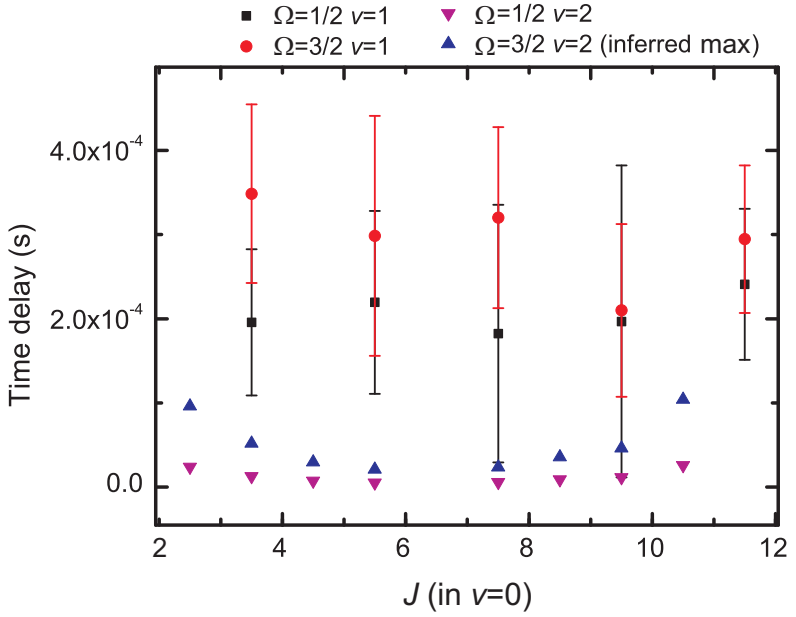

FIGURE 5.8: Measured values for the delay between pump and probe signals compared with relaxation periods from [140].

It is clear from Figure 5.8 that whilst a delay is consistently seen between these two signals, and whilst this delay is consistently longer for transfer from a $\Omega = \frac{3}{2}$ state versus transfer within $\Omega = \frac{1}{2}$, the noise due to long term drift in the current and temperature controllers of both lasers means that accurate measurements are not possible. It should be noted that this experiment measures the cumulative population in $v = 1$ and as such we would not expect the values to be precisely the same as those in [140], but similar trends would be expected. In theory, the addition of a fast radiation shut-off such as an acousto-optical modulator would allow a more accurate measurement of these values as the rising or falling population could then be directly measured. In our case however, no such fast amplitude switch was possible and therefore more accurate measurements could not be made.

Accurate measurement of the area of the broad absorptions produced when scanning was however possible and at 100 mTorr of NO an area was detected of c.a. 25× larger than would be anticipated in a room temperature sample without optical pumping, regardless of the transition used to excite population to the upper state. This fact, combined with both the Doppler width and the rotational relaxation rates suggest that complete thermalisation is occurring in $v = 1$. Thus, we consider a statistical spread of energy within the vibrational level, and from the absorption signal predict that 16% of the population from $v = 0$, $J = 6.5$ is transferred to the $v = 1$, $J = 7.5$. A value in good agreement with a saturation parameter of 0.5, of the order anticipated from the Lamb dip studies in Chapter 4.

5.2.2 Narrow Resonance

The narrow resonance here by contrast is a transient effect, appearing at very specific positions within the broad resonance, and is in fact a Bennett peak as seen in Section 4.1, due to the instantaneous population transfer into $v = 1$. The pump laser in this experiment is scanning at 40 Hz, and the probe laser at 50 kHz. The three orders of magnitude difference in scan rate means that on the timescale of a probe laser scan, the pump laser can be considered as essentially a fixed frequency radiation source. It is thus observed that when the probe laser comes into resonance with the specific velocity component simultaneously pumped by the EC-QCL a sharp peak is observed. This effect is further demonstrated in Figure 5.9.

Here we can see that as the pump laser sweeps from high to low wavenumber, different velocity components are excited into $v = 1$. Thus, probing velocity components in the ground state aligned with and against the direction of probe beam propagation leads to sharp features on either side of the broad hot band resonance. Whilst it may appear

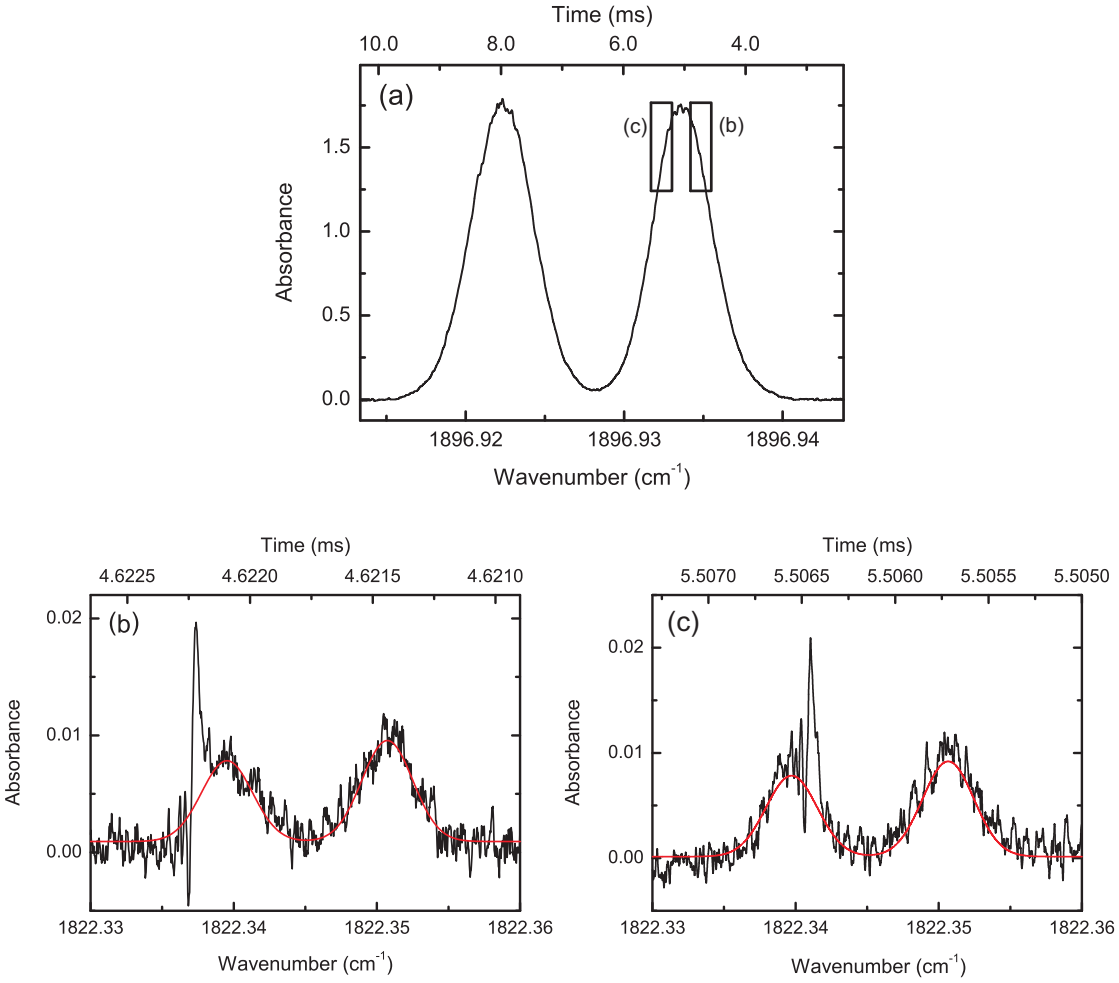

FIGURE 5.9: Observed off-resonance Pump-Probe resonances showing (a) Pump signal, (b) probe signal before line centre in time and (c) probe signal after line centre in time. The effect of pumping different velocity components is apparent.

that the population is transferred from one Λ-doublet to the other it is merely that the order of e and f components of the transition switches from the fundamental to the first hot band. It is further notable that the magnitude of absorption here is decreased slightly from that in Figure 5.5 as there is a decreased velocity resolved population in the ground state to be excited.

If the total pressure of NO in the sample is decreased, then the broad absorption diminishes whilst the sharp spike increases slightly in amplitude before decreasing also. This behaviour is shown in Figure 5.10 and is clearly understandable as decreasing the population decreases the number of population-scattering collisions thermalising the population in the excited state, as well as increasing the saturation parameter, S through its contribution to the relaxation within the system. Finally, as the population continues to decrease there are clearly fewer species to interact with leading to a decrease in the total number of molecules excited.

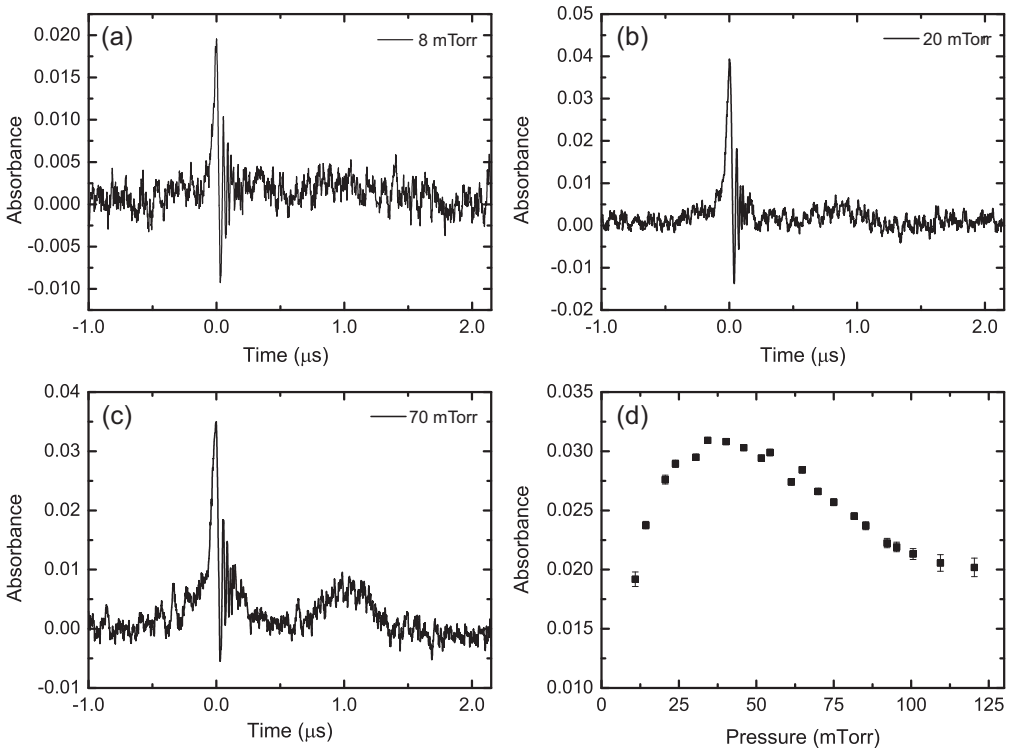

FIGURE 5.10: The evolution of the pump-probe signal as a function of pressure showing spectra of (a) 8 mTorr, (b) 20 mTorr, (c) 70 mTorr of NO and (d) the evolution of the size of the sharp peak (in absorbance).

The form of the observed Bennett peak is perhaps surprising. The oscillations observed here are not anticipated and in order to fully understand the processes occurring the effect of variables such as power and pressure needed to be explored. The oscillations were thus fit with the functional form:

$$A(t) = A_0 e^{-t/\tau_{damp}} \sin\left[(\alpha t + \beta)t\right], \tag{5.2}$$

as is shown in Figure 5.11, with A_0 the amplitude, τ_{damp} the decay period, and $(\alpha t + \beta)$ the frequency of oscillation.

Initially, it may be thought that the oscillations could correspond to Rabi cycling caused by the flux of population into and out of the first excited state at the Rabi frequency, Ω, due to the pump laser. This behaviour would be characterised by an oscillation frequency of $\Omega = \frac{\mu E}{\hbar}$, which would thus be expected to change as a function of applied power. However this was found to not be the case and instead the only variable which altered the oscillation frequency was the scan rate of the laser. In fact it was found that this oscillation frequency is equal to the laser scan rate divided by π, and the linear chirp of the frequency reflects the linear nature of the frequency change over the transition

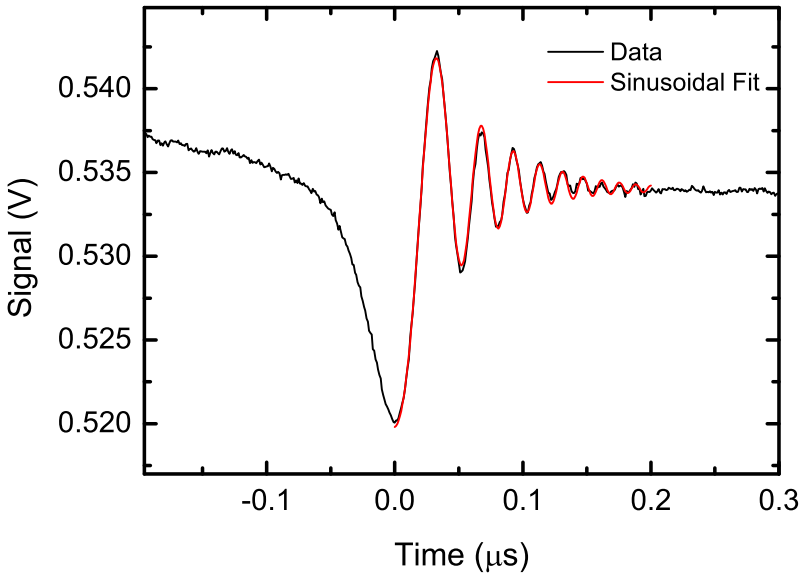

FIGURE 5.11: Fit of Equation 5.2 to the transient signal acquired with 20 mTorr of NO.

as is demonstrated in Figure 5.12. This result leads to the conclusion that the observed lineshape is due to a rapid passage effect was discussed in Chapter 2.

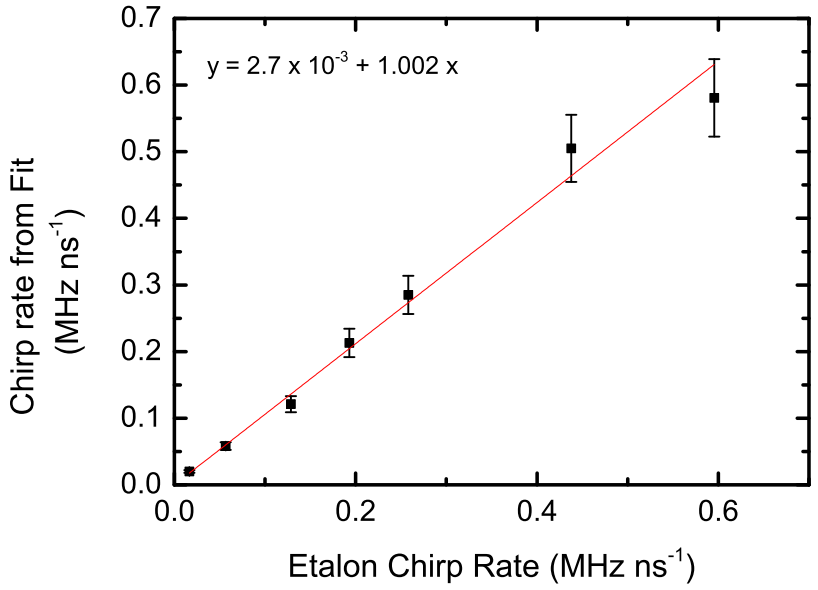

FIGURE 5.12: Tuning rate determined from the transient signal fit versus that determined using the Ge etalon. A linear fit is shown through the data with a gradient of 1.002 and an intercept of 2.7×10^{-3} MHz ns^{-1}.

The range of frequencies within which the laser could be tuned was limited at the low frequency end by the occurrence of noise in the injection current. This meant that when current ramp amplitudes became too small, noise fluctuations became an important factor in the tuning rate. This effect is shown in Figure 5.13 at the experimentally determined limiting point of 1 kHz repetition rate, as the noise introduced into the laser current is seen to alter the probe laser frequency such that it scans over the same sharp probe resonance three times in short succession. At the higher tuning rates the tuning rate was limited by the bandwidth of the ILX current controller which prevented laser tuning above c.a. 1 MHz ns^{-1}.

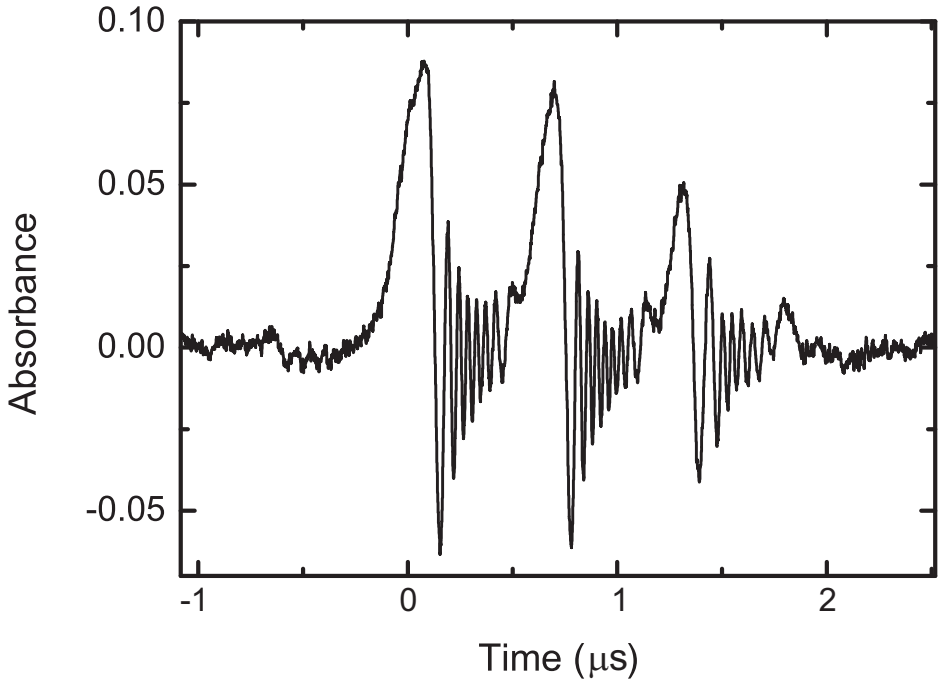

FIGURE 5.13: Multiple resonances observed as current noise causes jitter within the probe laser scan at 1 kHz and causes the smae transition to be probed three times in a single scan.

As the chirp rate determined from the fits of the experimental data appears to be accurate and is immediate i.e. not reliant upon signals recorded at a separate time, all chirp rates stated from this point onwards are determined from a fit of the experimental data.

The presence of rapid passage in these spectra is initially surprising as the chirp rates employed in these measurements are several orders of magnitude smaller than those in the intrapulse measurements of Chapter 2, and there is further no evidence of asymmetry in the Doppler broadened signals in Figure 5.6, nor in the ground state spectrum of the NO $P(13.5)_{\frac{1}{2}}$ seen in Figure 3.9. This signal also differs considerably from the standard rapid passage signal seen in Chapter 2, with perhaps the most marked difference being

the length of time over which the transient oscillations persist. These two disparities are however related, as in 'normal' rapid passage spectra, taken in the intrapulse mode of pulsed QCLs, the sample which is probed exists as an array of velocities, absorbing and oscillating at slightly different frequencies. This array of oscillations when summed over the sample destructively interfere, and as such the bulk polarisation is damped out much before the individual species have finished oscillating. In this case however, when the pump and probe frequencies are coincident upon the same velocity component only a very narrow range of species are excited and thus probed (c.a. 2 MHz). Hence the internal damping is minimised, and a rapid passage signal is observed at chirp rates much below what would typically be expected. Figure 5.14 shows the signal produced when the probe laser is tuned at 0.13 MHz ns^{-1} with 30 mTorr of NO in the cell overlaid with a simulation which is the work of E. McCormack and is performed using the same program as is utilised in Chapter 2. To summarise again, the results of the optical Bloch equations are propagated over the path length by the analytical expressions for a driven two-level system with relaxation, given by Torrey [78]. Good agreement is seen between experiment and theory, though a little extra damping is apparent in the experimental data than would be anticipated from pure collisional relaxation and velocity-group dephasing. This is expected however as the Maxwell-Bloch equations remain designed for a two-level system, which this is clearly not. In this simulation the range of velocity components detected was set by using the laser linewidth determined in Chapter 4, and inputting this into Equation 2.11 which results in a presumed temperature range of c.a. 1 K

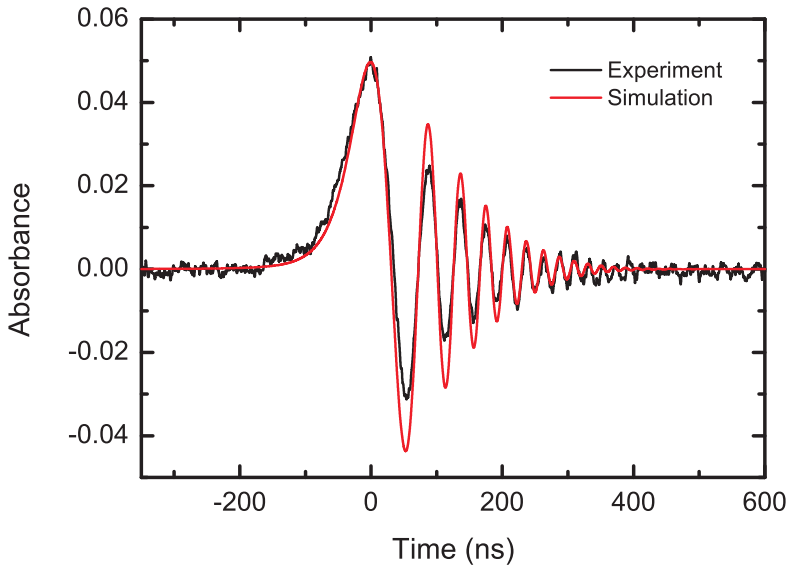

FIGURE 5.14: A simulation performed by E McCormack alongside experimental data of the pump-probe transient signal observed at 30 mTorr of NO, probed at 0.13 MHz ns^{-1}. Good agreement is seen between experiment and theory, though a little extra damping is apparent in the experimental data than would be anticipated from pure collisional relaxation and velocity-group dephasing.

As we thus know that the frequency of oscillation returned in the observed spectra is determined purely by the tuning rate of the laser, the figures of interest here are thus the amplitude, A_0 and the decay period of the oscillations τ. The amplitude of the observed pump-probe signal has already been shown to be function of pressure, but we would further expect it to vary as a function of applied pump power. Figure 5.15(a) shows the maximum absorbance of the transients observed whilst varying the pump power by placing a wire grid polariser in the beam path.

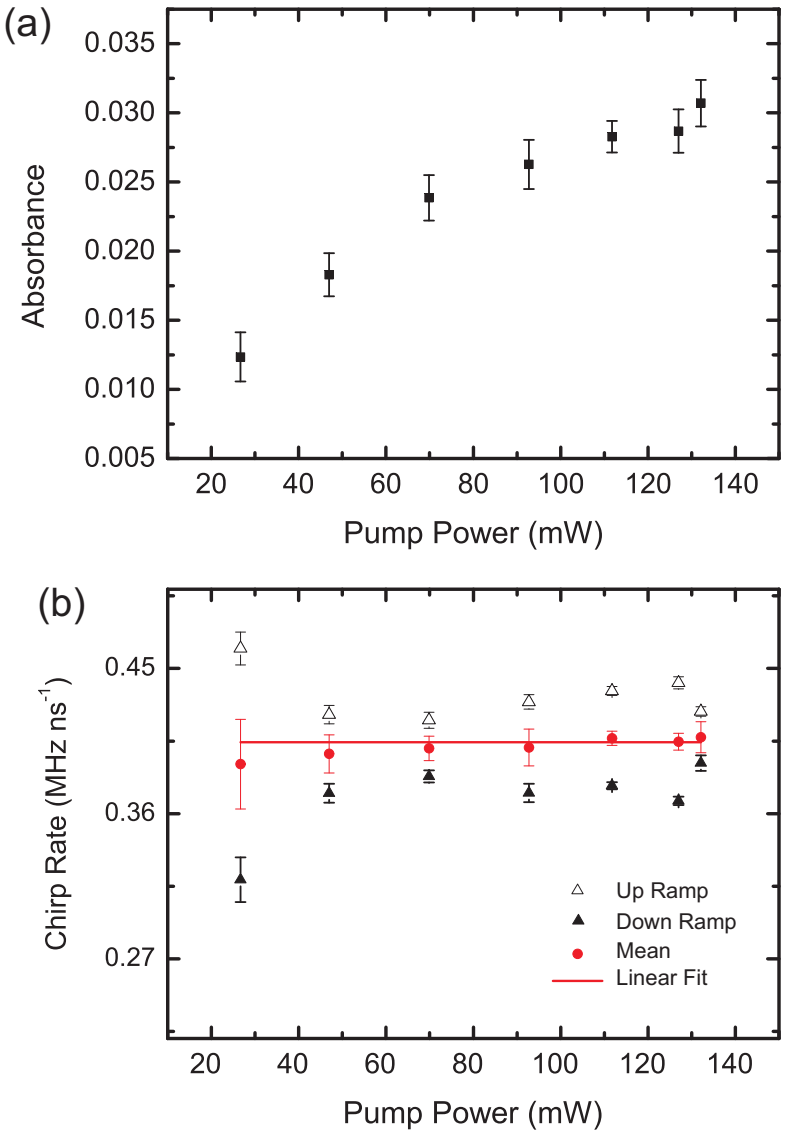

FIGURE 5.15: The effect of pump power upon (a) amplitude (in absorbance) and (b) chirp rate of the sharp pump-probe feature for 30 mTorr of NO gas. (b) shows the chirp rate returned for both up and down sweeps (open and closed triangles respectively) as well as the average values and constrained linear fit (gradient =0) well within error.

Figure 5.15(b) further shows the variation of chirp rate returned from the fits over these powers. Notably, there is a clear scatter of results beyond error, which would initially

appear to contradict the earlier determined invariance of chirp rate with variables other than the probe laser scan rate. However, the mirrored up and down sweep rates lend a clue to the true origin of this effect, as in this measurement we are sensitive enough to the chirp rate that we are measuring the asymmetry of the applied triangular waves used to scan the laser. It is thus clear that for these measurements the 'up ramp' chirp rate is typically c.a. 7% faster than the 'down ramp' but that the mean tuning rate remains constant within error, with an average value of 0.404 MHz ns^{-1}.

As the pump and probe beams are initially at opposite polarisations with the pump laser horizontally and the probe laser vertically polarised, a further increase in the signal amplitude was found by changing the axis of polarisation of the pump laser to that of the probe using a $\lambda/2$ waveplate (Figure 5.16). The amplitude of the transient increases by a factor of 1.5× when both lasers are vertically polarised, an effect which would be expected as the lasers thus interact with exactly the same subsection of molecules, whereas while the polarisations are crossed the subset of molecules interacting with both lasers is decreased [142].

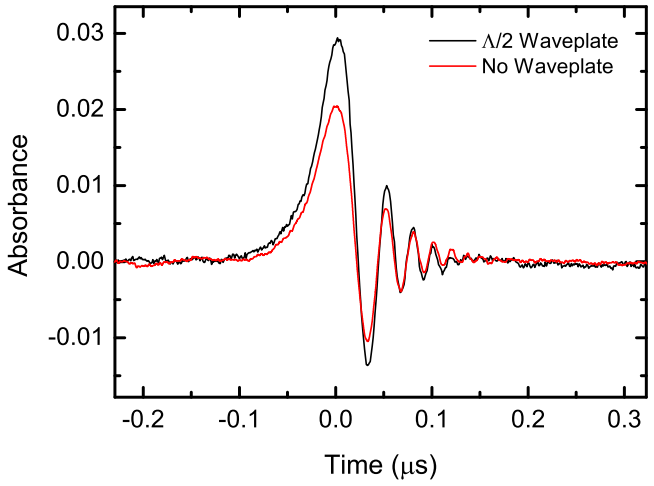

FIGURE 5.16: The transient signal both for 30 mTorr of NO with (red) and without (black) the addition of a $\lambda/2$ waveplate into the pump beam path.

The effect of pumping other ladder conformations was also investigated for both the $v = 0, J = 5.5, \Omega = \frac{1}{2}$ and the $v = 0, J = 6.5, \Omega = \frac{3}{2}$ states pumped in the R branch and detected upon their correspond hot-band P-branches. Figure 5.17 shows the resulting absorption signals for 30 mTorr of NO. It is notable that the size of absorption spike here is approximately the same as it is when the $R(6.5)_{\frac{1}{2}}$ transition is pumped, reflecting the fact that the percentage of NO population in each of the ground states is approximately equal over this narrow range. It is also notable here however that the

transient oscillations are much less prominent in these cases. This effect is not due to the transition pumped, but instead a function of the probe laser noise levels at these wavelengths.

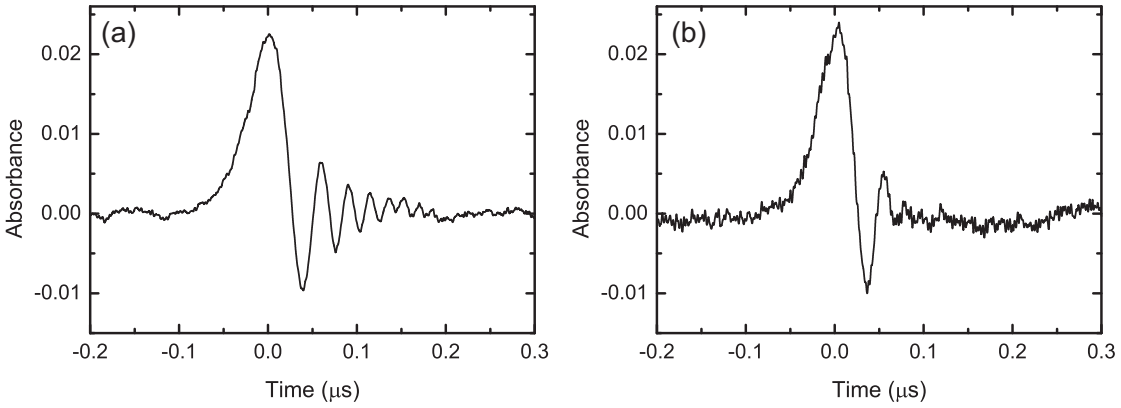

FIGURE 5.17: Pump-probe signals from 30 mTorr of NO (a) when the $R(5.5)_{\frac{1}{2}}$ $v = 1 \leftarrow 0$ transition is pumped and the $P(6.5)_{\frac{1}{2}}$ $v = 2 \leftarrow 1$ is probed, and (b) when the $R(6.5)_{\frac{3}{2}}$ $v = 1 \leftarrow 0$ transition is pumped and the $P(7.5)_{\frac{3}{2}}$ $v = 2 \leftarrow 1$ is probed.

The origin of decay processes within a rapid passage are discussed in Section 2.3, and it is thus unsurprising that the oscillations show damping as a function of pressure, as is shown in Figure 5.18.

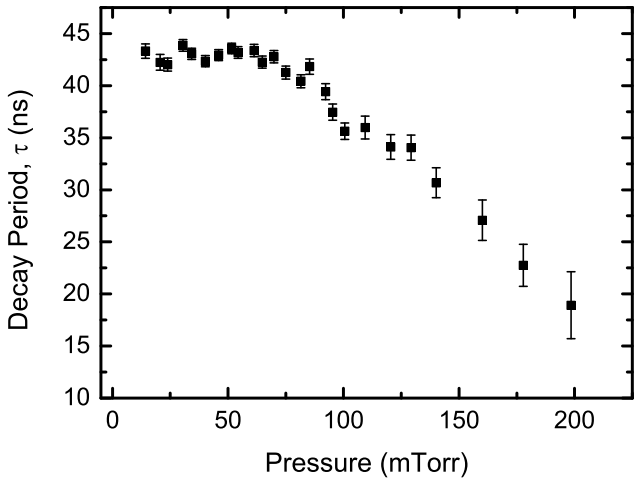

FIGURE 5.18: The decay period, τ_{damp} returned from fits of pump probe data displayed as a function of NO pressure.

This decrease in decay period is expected as the chromophore pressure is increased and thus collisions become more effective at removing the coherence. It should be noted that the dephasing rate that is observed is two orders of magnitude higher than HITRAN

would predict for pressure broadening. The HITRAN values however are determined for a bulk of velocity components and as such are not as sensitive to the effect of velocity changing collisions as the measurement here. Interestingly, the decay period reaches a plateau at low pressures indicating in this case that the dephasing of the induced polarisation with respect to the probe laser field pumped system becomes limited by the spread in molecular velocity components being sampled rather than by collisional effects.

Further, it can be observed that as the scan rate of the probe laser increases, the decay period decreases. This is likely in part due to the increased effective laser linewidth as the scan rate is increased, but also to the fact that as the laser is tuned faster the features begin to approach the 50 MHz estimated bandwidth of the detection system and the rapid passage signals are no longer completely resolved. This effect is particularly noticeable in the levelling off of the decay period at $\tau = 20$ ns $= 1/50$ MHz shown in Figure 5.19, and is an effect that would need to be considered if this technique were to be used to gain dynamical data.

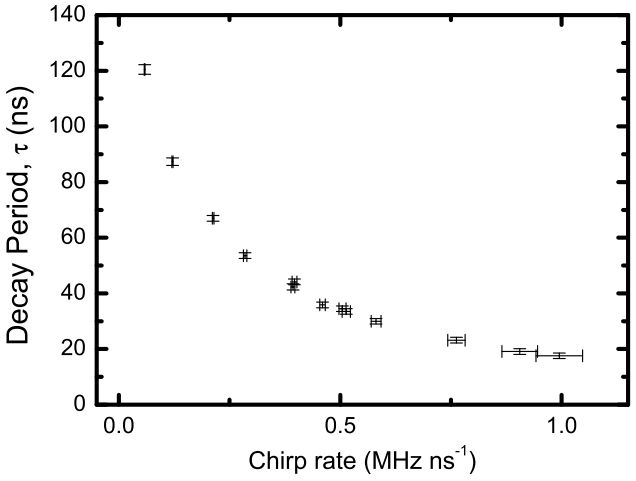

FIGURE 5.19: The decay period, τ, returned from fits of observed transients displayed as a function of probe laser chirp rate.

Finally, the rate at which the pump laser was tuned is also variable. Tuning the laser with the PZT between 1 - 100 Hz (c.a. 5 Hz ns^{-1} - 500 Hz ns^{-1}) over the pump transition had no observable effect upon the hot band signal, however tuning the laser instead over the pump transition by directly modulating the injection current at 10 kHz and above (17.5 kHz ns^{-1}) has a very clear effect. In this case the observed signal rapidly diminishes in amplitude such that negligible transient absorbtion is seen above even 10 kHz. Figure 5.20(a) shows the optimum pump-probe signal detected at 10 kHz for 30 mTorr of signal

with the probe laser kept at 50 kHz tuning as before, and it is clear that it is both much wider and that the oscillations decay much more rapidly than the signal observed for the slower pump tuning rates. This behaviour occurs as when the pump laser tunes more rapidly it can no longer be considered as a fixed frequency source with respect to the probe scan. Thus, several velocity components are excited and probed simultaneously and these multiple components will oscillate together and lead to a damped signal much like that which occurs for intrapulse spectra. As the pump laser now tunes much more rapidly there are no longer multiple probe laser scans over the course of a pump laser transition and as such not every scan contains a sharp resonance. Figure 5.20(b) shows the detected signal on one of these ramps, and a clear broad resonance is still observable as for the slowly scanned pump data. In this case, whilst the lasers do not simultaneously hit the ladder resonances the probe hits the transition a short period of time ($< 1\mu s$) after the pump and as such detects the population once it has been scattered into a range of states. In this case, an absorbance is seen of a magnitude in agreement with those taken in Figure 5.10, and Gaussian widths of 124 ± 3 MHz are recorded.

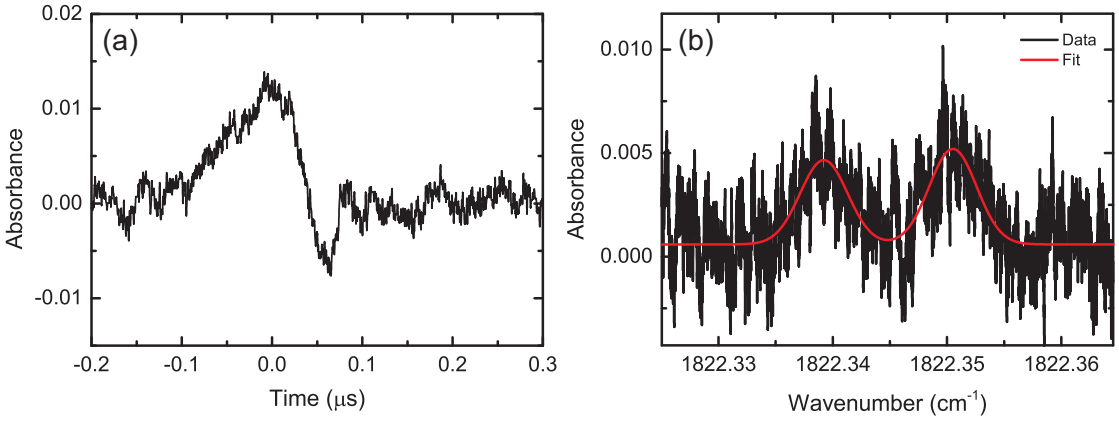

FIGURE 5.20: Pump-Probe signals shown with the pump laser tuning at 10 kHz (17.5 kHz ns^{-1} showing (a) the transient spike when the ladder resonances are stimulated simultaneously and (b) the broad absorption detected on the probe scan immediately after optical pumping.

At these fast pump laser scan rates we would anticipate beginning to move towards the adiabatic rapid passage regime, and may expect a larger degree of population transfer. However the chirp rate is still more than an order magnitude larger than would be required for the adiabatic condition ($\alpha/\Omega^2 = 1$) at these Rabi frequencies. It would in theory be possible to achieve this condition by drastically reducing the amplitude of the applied current modulation, however, this would mean that only a portion of the line was covered during a pump scan. Perhaps more importantly in this case, in order to maintain a 'rapid' regime the pressure would also have to be drastically reduced such that collisional relaxation occurred on a timescale longer than the scan. This was not

possible with our setup, and would likely require the addition of both a turbo pump for the low pressure and a long path cell such that appreciable absorption could be maintained.

Despite the inability to reach adiabatic passage in this case, directly observing the population transferred to the excited state here whets the appetite for secondary applications. Here insufficient population has been transferred to likely be of use in many investigations, however were we to replace the weak probe laser utilised here with a high powered-narrow linewidth laser it would open up the prospect of midinfrared stimulated Raman adiabatic rapid passage (STIRAP), with which population may be transferred from the ground state to an excited level with 100 % efficiency and which requires limited population transfer efficiency in each individual step.

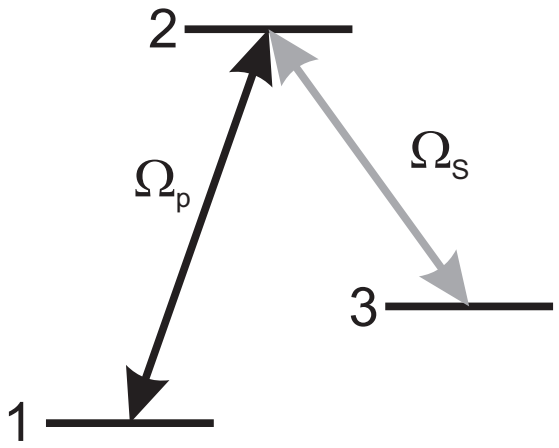

FIGURE 5.21: Schematic of a Λ arrangement of levels, in resonance with pump, Ω_P and Stokes, Ω_S radiation. Note that levels 1 and 3 are not directly connected.

STIRAP is a methodology first proposed in 1989 [72] and is described by Vitanov et al [79] for the case of a so called Λ-system as is shown in Figure 5.21. The three states are labelled 1, 2 and 3 and the transitions referred to with respect to their Rabi frequencies as the pump and Stokes pulses, $\Omega_P(t)$ and Ω_S(t), for historic reasons with a required condition of the single photon detunings $\Delta = \Delta_P = \Delta_S$ from the respective resonances. The three eigenstates of the Hamiltonian are then:

$$\Phi_+(t) = \psi_1 \sin\theta(t) \sin\phi(t) + \psi_2 \cos\phi(t) + \psi_3 \cos\theta(t) \sin\phi(t), \tag{5.3}$$

$$\Phi_0(t) = \psi_1 \cos\theta(t) - \psi_3 \sin\theta(t), \tag{5.4}$$

$$\Phi_-(t) = \psi_1 \sin\theta(t) \cos\psi(t) - \psi_2 \sin\phi(t) + \psi_3 \cos\theta(t) \cos\phi(t), \tag{5.5}$$

where the mixing angles θ and ϕ are

$$\theta(t) = \arctan\left(\frac{\Omega_P(t)}{\Omega_S(t)}\right) \tag{5.6}$$

and

$$\phi(t) = \frac{1}{2}\arctan\left[\frac{\sqrt{\Omega_P^2 + \Omega_S^2}}{\Delta}\right]. \tag{5.7}$$

STIRAP then works by utilising this Φ_0 which is an admixture of just the first and third states in the Λ system. For a system of counterinutitive pulses as is shown in Figure 5.22 $\Omega_p(t)/\Omega_S(t) \xrightarrow{t\to-\infty} 0$ and $\Omega_p(t)/\Omega_S(t) \xrightarrow{t\to+\infty} \infty$ hence as time progresses θ goes from an initial value of 0 to a final value of $\frac{\pi}{2}$. Therefore Φ_0 goes from a bare state of ψ_1 to an admixture of ψ_1 and ψ_3 and eventually a pure ψ_3 state with no population resting in ψ_2 at any time. ψ_2 is clearly directly connected to both ψ_1 and ψ_3 but if there is no relaxation mechanism from ψ_3 to ψ_1 then this process creates what is referred to as a 'trapped state' and complete population transfer is theoretically possible as is shown in Figure 5.22

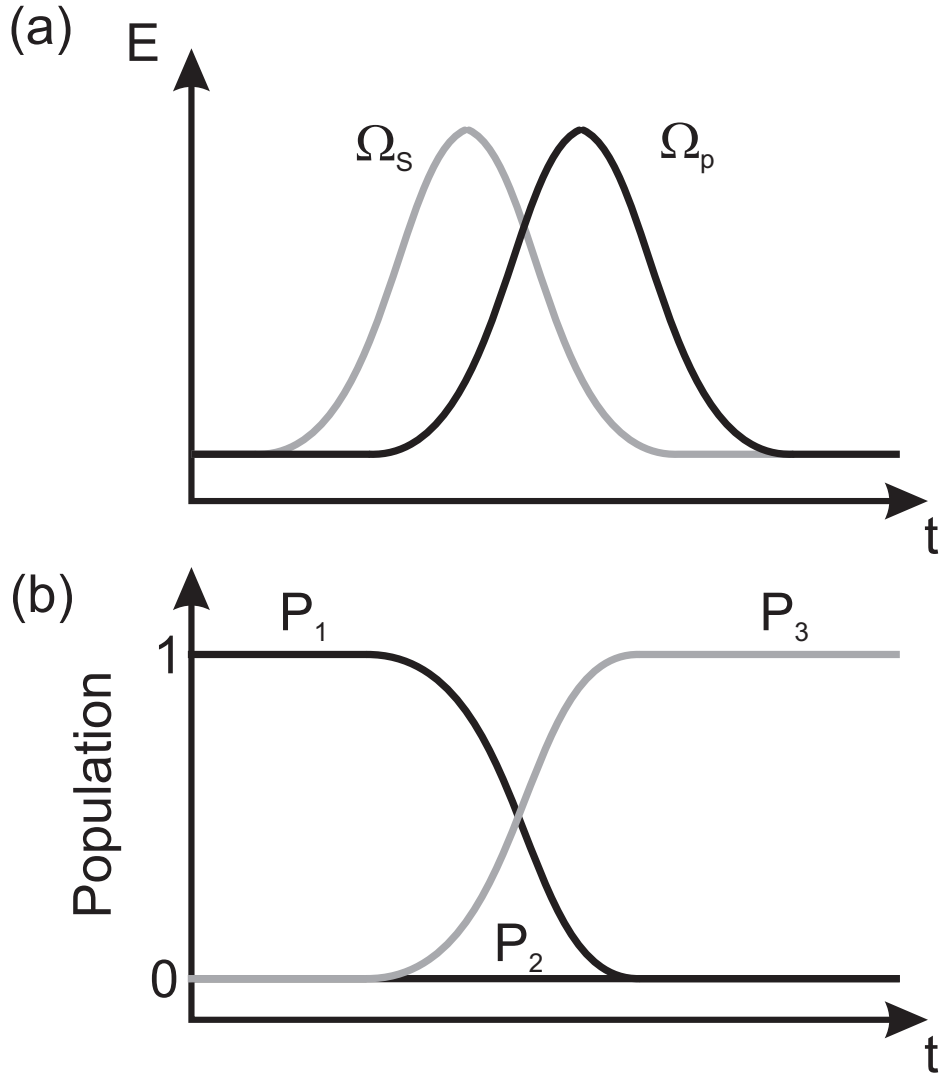

FIGURE 5.22: Schematic of a STIRAP experiment showing (a) the counter-intuitive pulse order and (b) the theoretical population transfer. It should be noted here that at no time does population rest in level 2 as can be seen in (b). From [79]

Putting this theory into practice can be difficult, but Bergmann *et al.* achieved successful results with cw lasers intercepting a molecular beam of Na dimers at right angles [143], and similar results have been seen with metastable Ne [144–146].

Mukherjee and Zare [147] have proposed a mid-infrared STIRAP experiment involving the population and polarisation of HCl at 3 µm, and calculated that complete population transfer could be achieved with 1 µs pulses of 10 kHz linewidth laser radiation with a 1 mm beam waist and a laser intensity of 30 mW mm^{-2}. This frequency range is currently outside of the range of commercially available QCLs, however similarly strong transitions pervade further into the mid-infrared. Imagining an equivalent system within our laser's tuning ranges, the primary limiting factor is the laser linewidths which are c.a. 100× larger than Mukherjee and Zare indicated. However, with stabilisation, experimental linewidths of 12 kHz have been recorded directly [148] by servo-locking to the side of an absorption resonance, and effective single Hz linewidths whilst locking to a cavity mode in heterodyne beat spectroscopy [149]. Further calculations performed within our group have shown that even were this degree of stabilisation not achieved, linewidths of the order of 1 MHz could be used to produce 70 % population transfer in this frequency displaced system.

5.3 Conclusions

This chapter has shown the first measurement of excited state population produced and probed with quantum cascade lasers. Approximately 16% of the population in the $v = 0, J = 6.5$ state has been pumped with an commercially available EC-QCL upon the $\mathrm{R}(6.5)_{\frac{1}{2}}$ transition, and the excited population detected in the $v = 1$, $J = 7.5$ state using a weaker DFB QCL tuned to selected transitions within the hot band. Rapid scattering of the excited population amongst the rotational states in $v = 1$ has been observed such that pumping upon any one of a range of transitions in the fundamental vibrational band leads to the same broad level of population in $v = 1$, $J = 7.5$.

When population is pumped from $v = 0$, $J = 6.5$ on the $\mathrm{R}(6.5)_{\frac{1}{2}}$ transition and the probe laser scanned over $\mathrm{P}(7.5)_{\frac{3}{2}}$ in the first hot band, then as well as the broad thermalised signal there is also a sharp spike caused by the instantaneous, velocity-selected, Bennett peak excited by the pump laser. This signal is however not detected as a pure absorption signal, but instead as a rapid passage signal caused by the fast scan of the probe laser. This is the first measurement to our knowledge of a velocity selected rapid passage signal, and the effect of pump power, gas pressure, pump and probe scan rate and polarisation have been investigated upon it.

This work shows significant population transfer to the first excited vibrational state of NO, and suggests - with the addition of a second high powered laser - the possibility of operating a STIRAP style population transfer experiment with the prospect of high levels of population transfer for utilisation in a secondary application.

Chapter 6

Frontiers in Quantum Cascade Lasers

In Chapter 1, advancements in QCL gain material design were discussed, pushing towards the production of short wavelength devices. This chapter shows some initial measurements performed using two prototype 3 µm devices acquired through collaboration with Prof. John Cockburn from Sheffield University. Access to the 3 µm region is particularly desired due to the presence of strong C-H, O-H and N-H stretch transitions of a great many molecules of both fundamental and applied interest, as well as the fundamental vibrational bands of HCl which is a standard system for studies of photodissociation dynamics.

6.1 Fabry-Pérot Device

6.1.1 Experimental

In this section a Fabry-Pérot pulsed QCL is utilised, operating between 2980 and 3065 cm^{-1} at room temperature and similar to one which has appeared previously in the literature [28]. The full design and physical characteristics of this laser are described there and it is beyond the purview of this chapter to list the exact conditions of manufacture. In brief it is a strain compensated InGaAs/AlAsSb/InP device based upon the bound-to-continuum design producing pulsed powers in the order of Watts.

The laser was mounted in a Cascade Technologies LS-03-D laser head and run at temperatures above 290 K in order to prevent condensation on the chip from aerial water. Light emitted from the QCL was divergent at $\sim 60^{\circ}$ and so was collimated using an off-axis paraboloid mirror which produced a beam of approximately 3 mm radius.

As the FP device has no wavelength selective device and is multi-mode, its spectral output was determined by coupling the radiation into a Perkin Elmer Spectrum 100 scanning Fourier transform infrared spectrometer (FTIR). Whilst these devices are typically operated with continuous wave sources, if the pulse repetition rate is significantly faster than the rate of mirror scanning then the FTIR detects the signal as essentially a weak continuous signal [150]. In this case pulses of between 25 and 100 ns were produced by the laser at rates in the range 2.5-10 kHz whilst the FTIR samples at rates up to 500 Hz.

6.1.2 Results

The FP device was initially uncharacterised and as such an LIV curve was initially measured at three temperatures as is shown in Figure 6.1. The peak powers shown here were recorded continuously using a Gentec-EO power meter and then calculated taking into account the operating conditions. It is of note here that the threshold is very high (~ 3 A), reflecting the high levels of losses within the system that make short wavelength QCLs so difficult to produce.

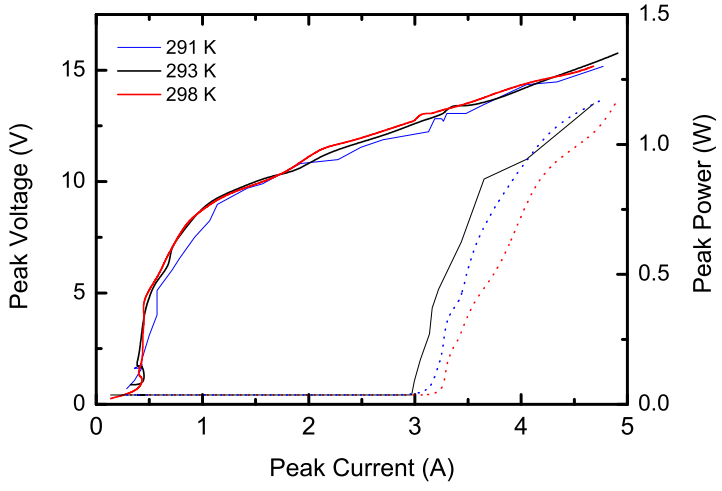

FIGURE 6.1: The LIV curve of the FP device showing data taken at 291, 293 and 298 K in blue red and black respectively.

The collimated light from the laser was then directed into the FTIR and spectra taken at a pulse amplitude of 4.5 mA (corresponding to 28 V) and 298 K at a spectrometer resolution of 2 cm^{-1} for 4 minutes as is shown in Figure 6.2. Here the Fabry-Pérot structure is clearly apparent, with a spectral range between 2960 and 3070 cm^{-1}, centred at 3036 cm^{-1}. An average mode spacing of 7.84 ± 0.01 cm^{-1} was found, corresponding to

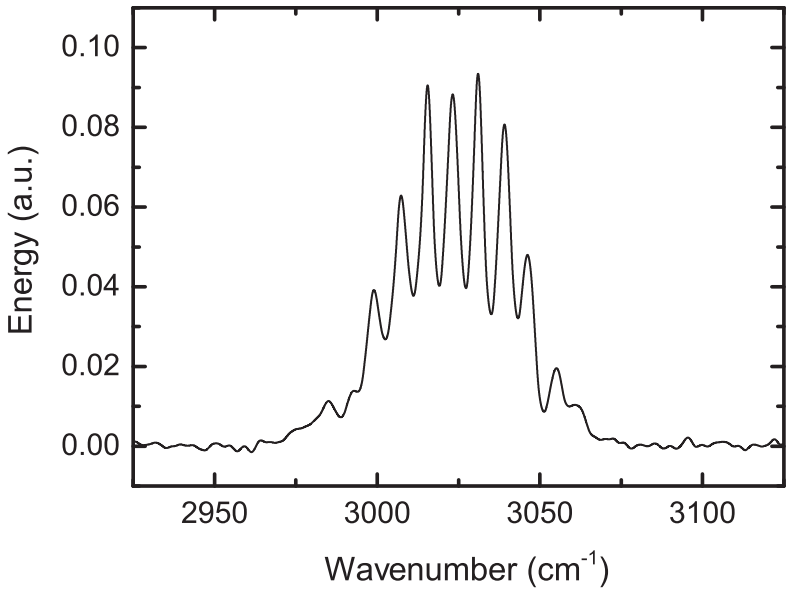

FIGURE 6.2: FTIR spectrum of the output from the FP device with an 4.5 mA pulse applied to the laser at 298 K.

a resonator length of 1.9 mm as calculated from the free spectral range (FSR) equation 1.4 presuming a refractive index of 3.3 [18, 151]. This resonator length is in good agreement with the expected chip length. The data appears to show that the QCL chip is a low finesse resonator (c.a. 2) and in order to demonstrate that this is not an effect due to the resolution of the spectrometer Figure 6.3 shows the same data taken at the two highest resolutions achievable with our spectrometer.

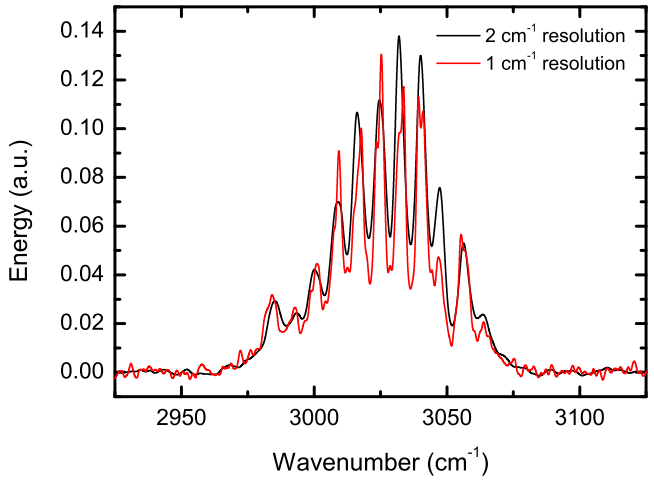

FIGURE 6.3: FTIR spectra of the FP device output at 1 cm^{-1} and 2 cm^{-1}. There is a slight narrowing of modes as the resolution is changed to 1 cm^{-1} however, this difference is not very significant whilst a definite decrease in S/N is seen for the same change.

As the resolution is increased, the S/N in the spectra decreases as would be expected, but it is important to note that the shape of the signal does not change significantly. As this is the case, all spectra in this section are taken with 2 cm^{-1}.

As this is a pulsed laser, it was of interest to investigate whether or not the output demonstrated a frequency chirp during operation. Therefore the laser output was recorded whilst changing the amplitude (Figure 6.4(a)) and length of the current pulse (Figure 6.4(b)). Within these operating ranges the modes do not change position with either variable - perhaps as we are limited by the resolution of the spectrometer, and the only notable effects are seen when changing the pulse amplitude, leading to an increase in output energy as would be expected, along with as a shift in central operating frequency.

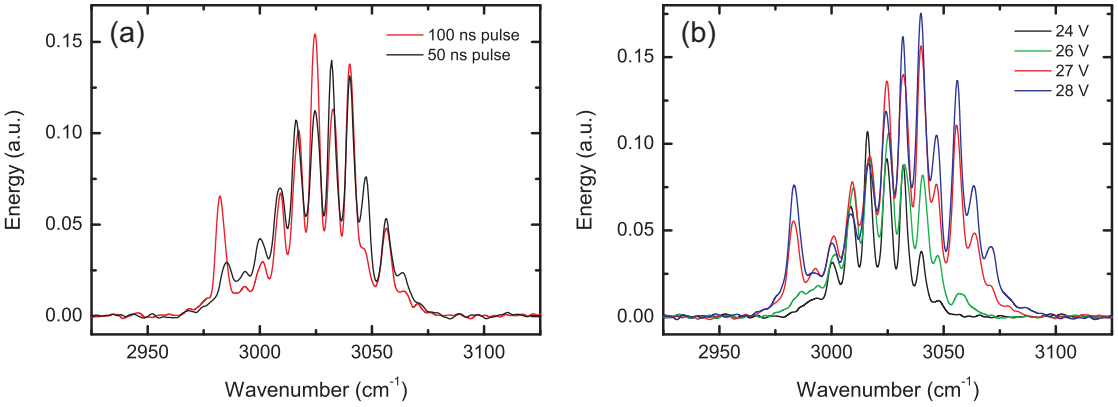

FIGURE 6.4: Spectra taken investigating the effect of pulse length and applied current. (a) Shows the effect of changing the applied current pulse amplitude with an observed spread of observed spectral modes as well as a shift in central frequency, but individual modes remain unmoved. (b) Shows 27 V pulses of 50 ns applied at 5 kHz (black) and 100 ns applied at 2.5 kHz (red). The frequency was adjusted to normalise for power and little difference is seen between the two sets of spectra, with only slight changes in the powers of individual modes.

Changing the temperature of the laser whilst running however, did have an effect upon the positions of the FP modes as is shown in Figure 6.5 returning a mode tuning rate of ~ 0.5 cm^{-1} K^{-1}, approximately double that observed for a typical single mode DFB QCL [18]. The two modes that appear upon the edges of the output at c.a. 2970 and 3060 cm^{-1} do not obey this behaviour however, barely changing frequency with temperature, and it is thought that they may be due to lasing through non-standard pathways, for example from continuum to continuum, or from top states in neighbouring wells.

This temperature tuning means that by changing the temperature by 12 K the entire frequency range could be covered by the modes of the laser, and a LabView routine was

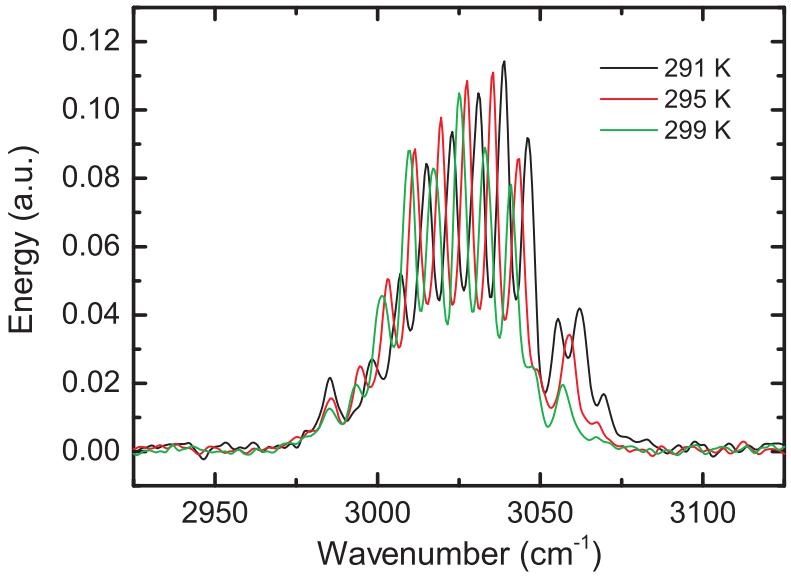

FIGURE 6.5: FTIR spectra taken as a function of chip temperature. A clear red shift of the modes can be seen as a function of temperature corresponding to a tuning rate of 0.5 cm^{-1} K^{-1}.

set up as follows. 50 ns pulses of 4 A were applied to the laser and the FTIR set to average for 26 minutes whilst the temperature was set to step 1 K each minute from 291 - 303 K and back again. This methodology produced a reasonably smooth, and most importantly, reproducible spectral output which was then used in order to perform some simple spectroscopy. A 20 cm cell with CaF_2 windows was filled with 2.6 Torr of CH_4 and placed in the sample chamber of the FTIR and a 26 minute spectrum taken followed by a spectrum with an empty sample chamber. The results of these two scans are shown in Figure 6.6(a) with the baseline adjusted by a factor of 0.81 (0.9*0.9) for the CaF_2 windows of the cell. Figure 6.6(b) then shows the absorbance spectra determined from these measurements overlaid with both a spectrum taken with the black body source of the FTIR, and a HITRAN simulation of the $v = 1 \leftarrow 0$ rovibrational spectrum of the Q-branch of the ν_3 band of CH_4, apodised with the 2 cm^{-1} resolution of the FTIR.

Despite the residual mode structure present in this data, the QCL resultant spectrum is in surprisingly good agreement with literature values. These results show the promise of these devices for the production of short wavelength radiation, but the next step towards the production of a commercial device must be the production of single mode radiation as can be achieved with a DFB QCL. Such a laser is characterised in the next section.

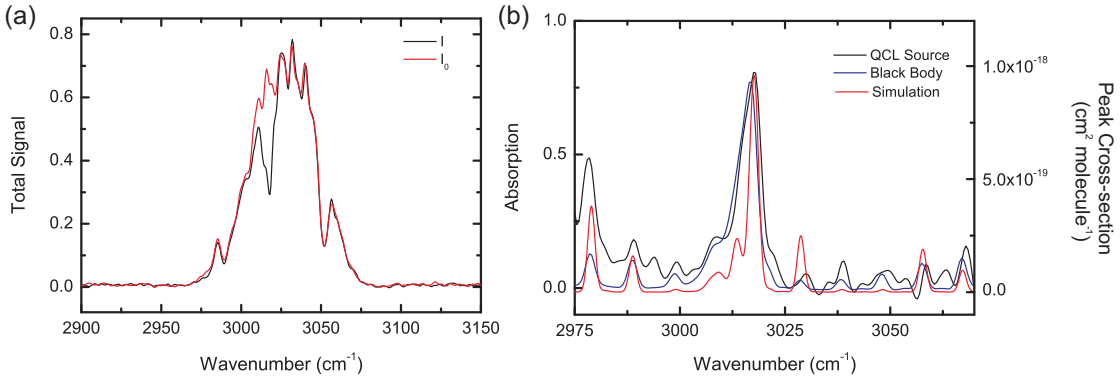

FIGURE 6.6: Temperature tuned spectrum of the Q branch of the ν_3 band of CH_4 showing (a) signal with and without a 20 cm cell containing 2.6 Torr of CH_4 and (b) the resultant absorbance spectrum (black) compared with both a spectrum taken with the FTIR's internal black body source (blue) and a HITRAN simulation apodised for the 2 cm^{-1} resolution.

6.2 3 µm DFB-QCL

In this section a DFB laser is operated which is in essence an extension of the previous laser design: a InGaAs/AlAsSb/InP bound-to-continuum device with the addition of a buried third order Bragg grating, similar to one which has appeared previously in the literature [152]. The wavelength selected by a Bragg grating is given by:

$$\lambda_0 = \frac{2\Lambda n_{eff}}{m}, \tag{6.1}$$

where Λ is the grating period, m is the grating order and n_{eff} is the effective refractive index of the optical mode. In order to achieve single mode tuning with a first order grating ($m = 1$) in the 3 micron range then grating features become too small ($\sim$ 250 nm) to be fabricated using usual methods (UV-photolithography) and instead have to be manufactured by e-beam or holographic lithography [152]. These processes add extra complication to the fabrication process which is undesirable. With higher order gratings Λ can be greatly increased, but grating shape must be carefully considered in order to maximise coupling. For second order gratings ($m = 2$) at 3 µm these shape considerations mean that some grating features will be small enough that UV-lithography is unapplicable. For third order (m=3) gratings however this is not a problem and grating features of c.a. 800 nm are required for $\lambda \sim 3.35$µm operation, fully achievable with standard methodology.

6.2.1 Experimental

The DFB QCL was operated with a stated central wavelength of at 3.365 µm ($\sim$ 2970 cm^{-1}) and in practice single mode light was seen to be produced in the range 2966 – 2970 cm^{-1}

at room temperature. 100 ns pulses were sent to the laser at a repetition rate of 5 kHz and as the collimated light from the laser was single mode, detection was performed using a VIGO PVI-2TE detector coupled with a LeCroy Wavefurfer 350 MHz scope.

6.2.2 Results

As little was known about the laser beyond its central output wavelength, initial experiments involved observing a bare pulse at a chip temperature of 290 K after propagation through 1 m of lab air as is shown in Figure 6.7. The most apparent feature here is that unlike the QCL pulses shown in Chapter 1 there is no 'flat' area within the pulse, and after an initial strong increase in detected signal at the start of the pulse there is a relatively steep slope back towards the baseline. This effect is caused by rapid heating of the gain medium by the applied current, which in turn reduces the output power. In this case a 100 ns pulse has been applied to the laser but rapid Joule heating means that the laser pushes below its threshold after approximately 85 ns.

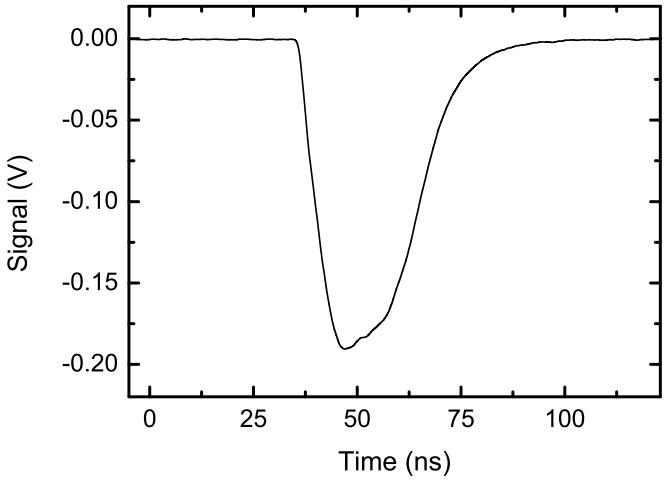

FIGURE 6.7: Bare pulse from the DFB QCL at 290 K incident upon the detector after propagating through 1 m of lab air.

A 20 cm cell containing c.a. 10 Torr of CH_4 was placed between the laser and detector and the signal observed at temperatures between 290 and 324 K as is shown in Figure 6.8. Within these spectra two absorptions corresponding to R(7) transitions in the (0 1 0 1) $\leftarrow$ (0 0 0 0) band at 2971 cm^{-1} are apparent, spaced by 6.2 GHz [1]. By tracing the spacing between these two transitions as they move across the pulse with changing temperature, we can gain an idea of the frequency tuning rate of the laser as is shown in Figure 6.9(a), and put the pulse on an absolute frequency scale (Figure 6.9(b)). A

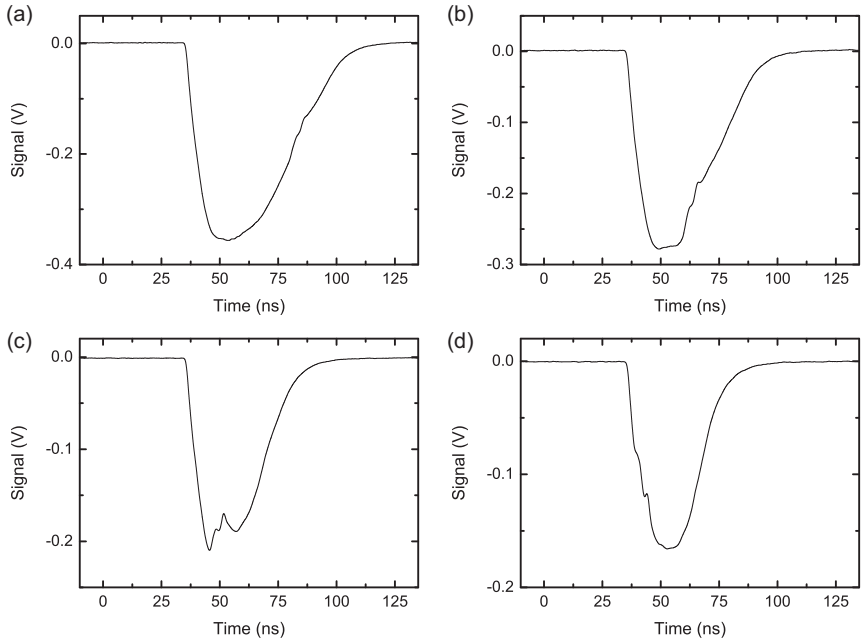

FIGURE 6.8: Pulses from the DFB QCL with a 20 cm cell containing 10 Torr of CH_4 in the beam path. Data is taken with the laser at (a)300 K (b) 310 K (c) 317 K and (d) 320 K and the CH_4 feature can be seen to move across the pulse as the frequency range is changed indicating a frequency shift with temperature.

second order polynomial was chosen in order to fit the frequency change as this is the behaviour that we have observed for a typical DFB QCL like those demonstrated in Chapter 2.

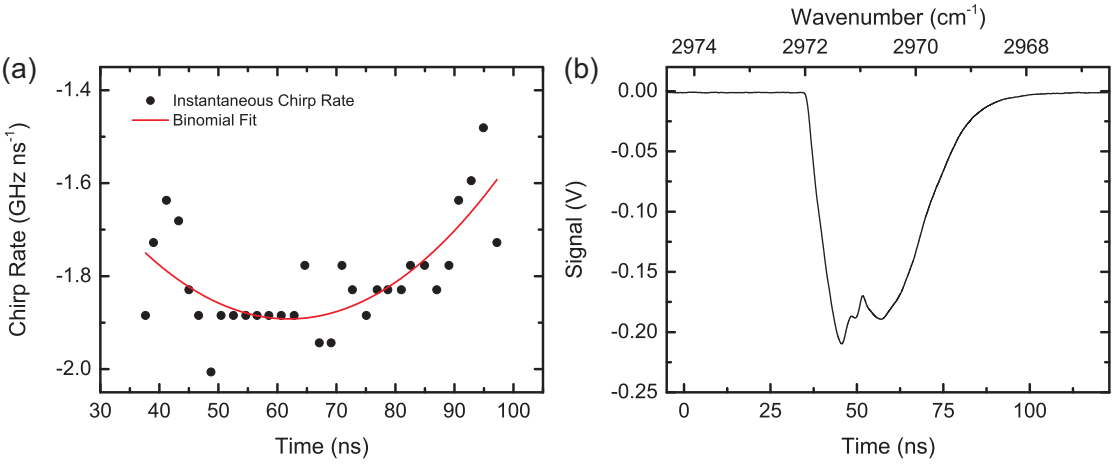

FIGURE 6.9: (a) The chirp rate determined from the spacing of the CH_4 doublet, and (b) a spectrum where this chirp rate is used to determine a frequency scale for a pulse.

From this data we can estimate an average laser chirp rate of 1.8 GHz ns^{-1}, at least an order of magnitude higher than the chirp rate measured for commercial DFB QCLs in Chapter 2. This chirp rate is again a measure of the poor heat dissipation over short timescales (ns-µs) within the system and has a further impact upon the observed spectra.

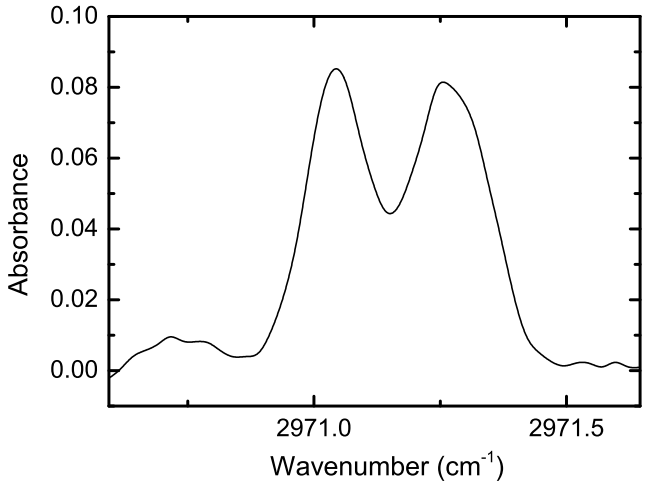

FIGURE 6.10: Absorption spectrum obtained of 10 Torr of CH_4 in a 20 cm cell. The spectrum is clearly assymmetrical and is not well fit with two peak functions. .

Further to this, if we presume that the frequency tuning range stays approximately static for all temperatures then these scans also give us a tuning rate of 0.127 cm^{-1} K^{-1} in reasonable agreement with similar lasers in the literature. Figure 6.10 shows the absorption spectrum after correcting for an empty cell taken at 310 K. These transitions show absorption in relatively good agreement with the literature, but it is anticipated that the very high chirp rate would be causing fast distortion to these lineshapes which is not visible with the current detector. Further studies with higher bandwidth detection systems are currently being pursued.

6.3 Conclusion

These initial experiments give us important information about the state of InGaAs/AlAsSb/InP QCLs at short wavelengths. These prototype devices act as a successful proof of principle, showing that short wavelength devices such as these are applicable to spectroscopy. However, at present, the combination of very high threshold current as is seen in Figure 6.1 and poor thermal management as is shown in Figure 6.7 mean that robust single mode continuous wave operation is a way off yet. Further, the lifetime of these devices at present is very short, and after only tens of hours of use the single mode device was no longer behaving as single mode.

Whether short wavelength QCLs or ICLs (as mentioned in Chapter 1) will be forthcoming as the device to fulfil the desire for a high powered single mode device around 3 µm is unknown. Devices such as those demonstrated in this chapter show some promise

but are still in their infancy and a number of improvements have yet to be tested (e.g. epi-down mounting). Single mode ICLs are beginning to come to market, though they too are not without their problems, and testing of an EC-ICL with an eye to inclusion in this thesis showed a drop-off of power of c.a. $\times 100$ over the course of 2 days of operation showing that they are also far from mature devices.

Rapid advancements are however being made in both devices, and whichever succeeds, the ability to access (or indeed pump) the strong X-H bonds around 3 µm or the HCl transitions proposed for STIRAP by Mukherjee and Zare [147] would prove incredibly useful in the fields of dynamics and kinetics.

Chapter 7

General Conclusions and Future Work

This thesis has examined quantum cascade lasers (QCLs) as a spectroscopic tool, and in particular their application to population transfer.

Chapter 2 contains work examining the spectra of pulsed QCLs operated in the intrapulse mode, where the fast chirp rate (100s MHz ns^{-1}) leads to an asymmetrical absorption signal with rapid oscillations following the maximum absorption in time. These signals are indicative of the nonlinear process termed 'rapid passage' by which the chirped laser radiation produces changes in the real and imaginary parts of the refractive index of the system as well inducing a (very small) degree of population transfer. The rapid passage signals produced by two different QCLs have been considered as a function of a number of different parameters, and a pressure shift in the oscillations measured in comparatively short path lengths contradicting previous suggestions which highlighted the importance of self-focusing in driving this phenomena. The requirements for increasing the degree of population transfer using this methodology were further discussed. The level of control, and specifically, the low chirp rates required for adiabatic rapid passage however are not achievable using intrapulse operated QCLs.

Continuous wave (cw) QCLs do not suffer from an observable fast frequency chirp and as such, spectra taken with them are not complicated by this rapid passage effect. Chapters 3 and 4 then demonstrated the applicability of continuous wave (cw) QCLs to a range of spectroscopies, utilising their narrow bandwidth, high power and (for the EC-QCL) wide tunability in tandem with the large absorption cross-sections in the midinfrared. In this manner time-normalised sensitivities as high as 8.7×10^{-9} cm^{-1} $Hz^{-1/2}$ have been achieved using a 10 µm DFB with a 238 m asymmetric Herriott cell, and minimum detectabilities high enough for medical sensing achieved with an optical cavity. The

hyperfine coupling constants of both isotopologues of DBr have been measured, including the previously unknown value for the hyperfine coupling constant of $D^{81}Br$ in the first excited vibrational state. Sub-Doppler resolution has been achieved in both Lamb-dip and polarisation spectroscopy using an EC-QCL acting upon NO, and the laser linewidth determined as c.a. 2.5 MHz on a millisecond timescale. The evolution of this linewidth with injection current has been measured and from this an estimate of the fundamental linewidth of this laser system is made at 200 kHz. This sub-Doppler resolution is further utilised in order to perform high resolution spectroscopic measurements upon both the $R(13.5)_{\frac{3}{2}}$ and the $R(1.5)_{\frac{1}{2}}$ transitions. The latter of which spectra displays not only the hyperfine split transitions, but also extra cross-over resonances due to shared levels and possible coherent effects.

In Chapter 5 a pump-probe experiment was performed using saturation created with the EC-QCL whilst scanning over a transition in the fundamental vibrational band of NO, which was simultaneously probed by a weak DFB QCL acting upon a transition in the first vibrational hot band. The $P(7.5)_{\frac{1}{2}}$ signal was observed in the first excited state as a function of power, pressure and chirp rates, and its lineshape was found to be a combination of both a broad, thermalised transition produced by rapid collisionally induced population transfer within $v = 1$, and a sharp Bennett peak-like feature exhibiting rapid passage. The observed rapid passage would not normally be expected in a Doppler broadened signal, but in this case the velocity-selected signal oscillating at a very narrow range of frequencies leads to little destructive interference and the oscillations are seen to persist much longer than those seen in Chapter 2 with pulsed systems. The broad signal further allows us to estimate population transfer at 16% of the population in $v = 0, J = 6.5$ pumped into the first excited state, a value consistent with a saturation parameter of c.a. 0.5 in line with expectations from our Lamb-dip measurements. This population is however still relatively small and methods of increasing it are considered. Increasing the scan rate of the pump laser such that adiabatic rapid passage occurs is not possible due to limitations of both the laser system and the vacuum system, however the possibility of replacing the weak pump laser with a higher powered system and performing a STIRAP experiment is considered, and current experimental realities compared to those of a theoretical HCl experiment proposed by Mukherjee and Zare [147].

Chapter 6 presented work with prototype short wavelength QCLs working around 3.3 µm. A Fabry-Pérot (FP) device and a DFB device are used to record spectra of CH_4 transitions in the region and their prospects for widespread use are considered. Spectra obtained with the FP laser required the use of a Fourier transform spectrometer (FTIR) and the production of a smooth baseline was at best challenging. The wide tuning range of such devices does suggest the prospect of monitoring the spectra of molecules

with broad absorption features (e.g. acetone) but in practice this can currently be more successfully achieved with a black body source coupled to the FTIR. The DFB device was single mode and as such, spectra could be obtained of two CH_4 transitions without the use of an FTIR. These two transitions were used in order to determine the chirp rate of the laser system and it was found that the laser frequency was changing at a rate of c.a. 1.8 MHz ns^{-1}. This frequency change is 1–2 orders of magnitude faster than that achieved in a typical pulsed DFB QCL and is due to poor thermal management within the system suggesting that there is some way to go before these devices are suitable for widespread use.

Appendix A

Lamb-dip Fitting Routine

```
cd(uigetdir);
files = dir('*.txt');

for i=1:length(files)

    data = importdata(files(i).name);

    t=data(:,2)-1920.7;

    y1=data(1,3);
    y2=data(end,3);
    x1=data(1,2);
    x2=data(end,2);
    m=((y2-y1)/(x2-x1));
    b= 0.5* ((y1+y2)-m*(x1+x2));
    base=m*data(:,2)+b;
    absorb=-log(data(:,3)./base);
    sm=smooth(absorb,200);

    rm=sm-absorb;
    [~,lcs(:,1)]=findpeaks(smooth(rm,10),'minpeakheight'...
        ,0.004,'minpeakdistance',0.5e3);


    f0=[t(lcs(1)),t(lcs(2)),0.06*(data(end,2)-data(1,2)),...
       (max(absorb)-min(absorb)),(max(absorb)-min(absorb)),1,0];
    doub=@(x,xdata) x(7)+x(4)*gaussian(xdata,x(1),x(3))...
    +x(5)*gaussian(xdata,x(2),(x(6)*x(3)));
    f=nlinfit(t,absorb,doub,f0);

    p1=p(i);
    m=max(absorb); % evaluates max value of absorb for nomalisation in fit.
    x0=[0,0.25*(100/p1)^2,t(lcs(1)),t(lcs(2)),2e6];
    lb=[min(absorb),0,min(t),min(t),1.2e6];
    ub=[mean(absorb),700,max(t),max(t),3e6];
    x=x0;
    options=optimset('TolFun',1e-8);
```

```
    x=lsqcurvefit(@Leqn,x0,t,absorb,lb,ub,options);

    l=Leqn(x,t);
    clf

    subplot(2,1,1);hold on
    plot(t,absorb)
    plot(t,l,'r')
    subplot(2,1,2);plot(t,absorb-l)
    hold off
    fitty(:,i)=x;
    S(i)=x(2)
    beep

end


%% The function which evaluates the Lamb-dip model and performs
%% the laser convolution

function integral=Leqn(x,t)%,dat,f)
k=1.38e-23;
T=300;
ma=30;
v=sqrt(2*k*T/(ma*1.660e-27));
wid=2e-3;
Dw=sqrt(2*log(2)) * v/wid; %transit time broadening
p=evalin('base', 'p1');
gamma=(sqrt((Dw)^2+ ((2.5e3*p))^2)) /30e9;

f = evalin('base', 'f');
a01=f(4)*gaussian(t,f(1),f(3));
a02=f(5)*gaussian(t,f(2),f(3)*f(6));

a=f(7)+x(1)+ a01.*(1-(x(2)/sqrt(1+x(2))).*(gamma/2)^2./((t-x(3)).^2 ...
+((0.5*gamma*(1+sqrt(1+x(2)))/2)^2)))...
+ a02.*(1-(x(2)/sqrt(1+x(2))).*(gamma/2)^2./((t-x(4)).^2...
+((0.5*gamma*(1+sqrt(1+x(2)))/2)^2)));

integral=zeros(length(t),1);
for u=1:length(t)
    laser=gaussian(t,t(u),x(5)/30e9);
    integral(u)=laser'*a;
end

m = evalin('base', 'm');
integral=(integral*m)/max(integral);
```

References

[1] L. S. Rothman, I. E. Gordon, A. Barbe, D. C. Benner, P. F. Bernath, M. Birk, V. Boudon, L. R. Brown, A. Campargue and J.-P. Champion. "The HITRAN 2008 molecular spectroscopic database". *Journal of Quantitative Spectroscopy and Radiative Transfer*, **110**, 533–572 (2009).
http://dx.doi.org/10.1016/j.jqsrt.2009.02.013

[2] C. Brown, J. J. Orlando, J. Reid and D. R. Smith. "Diode laser detection of transient CF_3 radicals formed by CO_2 laser multiphoton induced dissociation of halocarbons". *Chemical Physics Letters*, **142**, 213–216 (1987).
http://dx.doi.org/10.1016/0009-2614(87)80925-9

[3] S. Stry, P. Hering and M. Mürtz. "Portable difference-frequency laser-based cavity leak-out spectrometer for trace-gas analysis". *Applied Physics B: Lasers and Optics*, **75**, 297–303 (2002).
http://dx.doi.org/10.1007/s00340-002-0966-9

[4] O. Tadanaga, Y. Nishida, T. Yanagawa, H. Miyazawa, K. Magari, T. Umeki, K. Yoshino, M. Asobe and H. Suzuki. "Diode-laser based 3 mW DFG at 3.4 μm from wavelength conversion module using direct-bonded QPM-LN ridge waveguide". *Electronics Letters*, **42**, 988 (2006).
http://dx.doi.org/10.1049/el:20061751

[5] L. E. Myers, R. C. Eckardt, M. M. Fejer, R. L. Byer, W. R. Bosenberg and J. W. Pierce. "Quasi-phase-matched optical parametric oscillators in bulk periodically poled $LiNbO_3$". *Journal of the Optical Society of America B*, **12**, 2102 (1995).
http://dx.doi.org/10.1364/JOSAB.12.002102

[6] W. R. Bosenberg, A. Drobshoff, J. I. Alexander, L. E. Myers and R. L. Byer. "93% pump depletion, 35-W continuous-wave, singly resonant optical parametric oscillator". *Optics Letters*, **21**, 1336 (1996).
http://dx.doi.org/10.1364/OL.21.001336

[7] M. Tacke. "New developments and applications of tunable IR lead salt lasers". *Infrared Physics & Technology*, **36**, 447–463 (1995). http://dx.doi.org/10.1016/1350-4495(94)00101-P

[8] A. Hugi, R. Maulini and J. Faist. "External cavity quantum cascade laser". *Semiconductor Science and Technology*, **25**, 083001 (2010). http://dx.doi.org/10.1088/0268-1242/25/8/083001

[9] L. Esaki and R. Tsu. "Superlattice and Negative Differential Conductivity in Semiconductors". *IBM Journal of Research and Development*, **14**, 61–65 (1970). http://dx.doi.org/10.1147/rd.141.0061

[10] R. A. Kazarinov, R F Suris. "Possible amplification of electromagnetic waves in a semiconductor with a superlattice". *Fizika i Tekhnika Poluprovodnikov*, **5**, 797–800 (1971).

[11] J. Faist, F. Capasso, D. L. Sivco, C. Sirtori, A. L. Hutchinson and A. Y. Cho. "Quantum Cascade Laser". *Science*, **264**, 553–556 (1994). http://dx.doi.org/10.1126/science.264.5158.553

[12] O. Malis, C. Gmachl, D. L. Sivco, L. N. Pfeiffer, A. M. Sergent and K. W. West. "The quantum cascade laser: A versatile high-power semiconductor laser for mid-infrared applications". *Bell Labs Technical Journal*, **10**, 199–214 (2005). http://dx.doi.org/10.1002/bltj.20114

[13] Y. Bai, S. Slivken, S. Kuboya, S. R. Darvish and M. Razeghi. "Quantum cascade lasers that emit more light than heat". *Electrical Engineering*, **4**, 99–102 (2010). http://dx.doi.org/10.1038/NPHOTON.2009.263

[14] A. Lyakh, R. Maulini, A. Tsekoun, R. Go, C. Pflugl, L. Diehl, Q. J. Wang, F. Capasso and K. P. C N. "3 W continuous-wave room temperature single-facet emission from quantum cascade lasers based on nonresonant extraction design approach". *Applied Physics Letters*, **95**, 141113 (2009). http://dx.doi.org/10.1063/1.3238263

[15] F. Capasso. "High-performance midinfrared quantum cascade lasers". *Optical Engineering*, **49**, 111102 (2010). http://dx.doi.org/10.1117/1.3505844

[16] M. Yamanishi, T. Edamura, K. Fujita, N. Akikusa and H. Kan. "Theory of the Intrinsic Linewidth of Quantum-Cascade Lasers: Hidden Reason for the Narrow Linewidth and Line-Broadening by Thermal Photons". *IEEE Journal of Quantum Electronics*, **44**, 12–29 (2008). http://dx.doi.org/10.1109/JQE.2007.907563

[17] J. Faist, M. Beck, T. Aellen and E. Gini. "Quantum-cascade lasers based on a bound-to-continuum transition". *Applied Physics Letters*, **78**, 147 (2001).
http://dx.doi.org/10.1063/1.1339843

[18] C. Gmachl, F. Capasso, D. L. Sivco and A. Y. Cho. "Recent progress in quantum cascade lasers and applications". *Reports on Progress in Physics*, **64**, 1533–1601 (2001).
http://dx.doi.org/10.1088/0034-4885/64/11/204

[19] J. Faist, F. Capasso, C. Sirtori, D. L. Sivco, A. L. Hutchinson and A. Y. Cho. "Continuous wave operation of a vertical transition quantum cascade laser above T=80 K". *Applied Physics Letters*, **67**, 3057 (1995).
http://dx.doi.org/10.1063/1.114863

[20] R. Maulini, M. Beck, J. Faist and E. Gini. "Broadband tuning of external cavity bound-to-continuum quantum-cascade lasers". *Applied Physics Letters*, **84**, 1659–1661 (2004).
http://dx.doi.org/10.1063/1.1667609

[21] A. Hugi, R. Terazzi, Y. Bonetti, A. Wittmann, M. Fischer, M. Beck, J. Faist and E. Gini. "External cavity quantum cascade laser tunable from 7.6 to 11.4 μm". *Applied Physics Letters*, **95**, 061103 (2009).
http://dx.doi.org/10.1063/1.3193539

[22] R. Köhler, A. Tredicucci, F. Beltram, H. E. Beere, E. H. Linfield, A. G. Davies, D. A. Ritchie, R. C. Iotti and F. Rossi. "Terahertz semiconductor-heterostructure laser." *Nature*, **417**, 156–9 (2002).
http://dx.doi.org/10.1038/417156a

[23] R. Paiella. "Terahertz quantum cascade lasers: Going ultrafast". *Nature Photonics*, **5**, 253–255 (2011).
http://dx.doi.org/10.1038/nphoton.2011.73

[24] A. Tredicucci, R. Köhler, L. Mahler, H. E. Beere, E. H. Linfield and D. A. Ritchie. "Terahertz quantum cascade lasersfirst demonstration and novel concepts". *Semiconductor Science and Technology*, **20**, S222–S227 (2005).
http://dx.doi.org/10.1088/0268-1242/20/7/012

[25] J. P. Commin, D. G. Revin, S. Y. Zhang, A. B. Krysa and J. W. Cockburn. "High performance, high temperature λ
*sim*3.7 μm InGaAs/AlAs(Sb) quantum cascade lasers". *Applied Physics Letters*, **95**, 111113 (2009).
http://dx.doi.org/10.1063/1.3232219

[26] J. Faist, F. Capasso, D. L. Sivco, A. L. Hutchinson, S.-N. G. Chu and A. Y. Cho. "Short wavelength (λ3.4 μm) quantum cascade laser based on strained compensated InGaAs/AlInAs". *Applied Physics Letters*, **72**, 680 (1998).
http://dx.doi.org/10.1063/1.120843

[27] D. G. Revin, J. W. Cockburn, M. J. Steer, R. J. Airey, M. Hopkinson, A. B. Krysa, L. R. Wilson and S. Menzel. "InGaAs/AlAsSb/InP quantum cascade lasers operating at wavelengths close to 3 μm". *Applied Physics Letters*, **90**, 021108 (2007).
http://dx.doi.org/10.1063/1.2431035

[28] S. Y. Zhang, D. G. Revin, J. W. Cockburn, K. Kennedy, A. B. Krysa and M. Hopkinson. "$\lambda\sim$3.1μm room temperature InGaAs/AlAsSb/InP quantum cascade lasers". *Applied Physics Letters*, **94**, 031106 (2009).
http://dx.doi.org/10.1063/1.3073865

[29] O. Cathabard, R. Teissier, J. Devenson, J. C. Moreno and A. N. Baranov. "Quantum cascade lasers emitting near 2.6 μm". *Applied Physics Letters*, **96**, 141110 (2010).
http://dx.doi.org/10.1063/1.3385778

[30] J. D. Wu, Y. S. Huang, B. S. Li, A. Shen, M. C. Tamargo and K. K. Tiong. "Photoluminescence and photoreflectance characterization of $Zn_xCd_{1-x}Se$/MgSe multiple quantum wells". *Journal of Applied Physics*, **108**, 123105 (2010).
http://dx.doi.org/10.1063/1.3520477

[31] Y. Yao, A. Alfaro-Martinez, K. J. Franz, W. O. Charles, A. Shen, M. C. Tamargo and C. F. Gmachl. "Room temperature and narrow intersubband electroluminescence from ZnCdSe/ZnCdMgSe quantum cascade laser structures". *Applied Physics Letters*, **99**, 041113 (2011).
http://dx.doi.org/10.1063/1.3614561

[32] W. O. Charles, Y. Yao, K. J. Franz, Q. Zhang, A. Shen, C. Gmachl and M. C. Tamargo. "Growth of Zn_x,$Cd_{(1-x')}SeZn_xCd_yMg_{(1-x-y)}Se$–InP quantum cascade structures for emission in the 3–5 μm range". *Journal of Vacuum Science & Technology B: Microelectronics and Nanometer Structures*, **28**, C3G24 (2010).
http://dx.doi.org/10.1116/1.3276438

[33] B. A. Ikyo, I. P. Marko, A. R. Adams, S. J. Sweeney, C. L. Canedy, I. Vurgaftman, C. S. Kim, M. Kim, W. W. Bewley and J. R. Meyer. "Temperature dependence of 4.1 μm mid-infrared type II W interband cascade lasers". *Applied Physics Letters*, **99**, 021102 (2011).
http://dx.doi.org/10.1063/1.3606533

[34] R. Q. Yang, C. J. Hill, B. Yang and J. K. Liu. "Room-temperature type-II interband cascade lasers near 4.1 μm". *Applied Physics Letters*, **83**, 2109 (2003). http://dx.doi.org/10.1063/1.1611260

[35] M. Kim, C. L. Canedy, W. W. Bewley, C. S. Kim, J. R. Lindle, J. Abell and I. Vurgaftman. "Interband cascade laser emitting at λ=3.75 μm in continuous wave above room temperature". *Applied Physics Letters*, **92**, 191110 (2008). http://dx.doi.org/10.1063/1.2930685

[36] J. Y.-T. Huang, D. P. Xu, L. J. Mawst, T. F. Kuech, I. Vurgaftman and J. R. Meyer. "GaAsSbN-GaAsSb-InP Type-II W Quantum Wells for Mid-IR Emission". *IEEE Journal of Selected Topics in Quantum Electronics*, **13**, 1065–1073 (2007). http://dx.doi.org/10.1109/JSTQE.2007.902831

[37] A. Bauer, M. Dallner, M. Kamp, S. Hofling, L. Worschech and A. Forchel. "Shortened injector interband cascade lasers for 3.3 to 3.6 μm emission". *Optical Engineering*, **49**, 111117 (2010). http://dx.doi.org/10.1117/1.3505831

[38] D. Caffey, T. Day, C. S. Kim, M. Kim, I. Vurgaftman, W. W. Bewley, J. R. Lindle, C. L. Canedy, J. Abell and J. R. Meyer. "Performance characteristics of a continuous-wave compact widely tunable external cavity interband cascade lasers." *Optics express*, **18**, 15691–6 (2010). http://www.ncbi.nlm.nih.gov/pubmed/20720951

[39] D. M. Sonnenfroh, R. T. Wainner, M. G. Allen and R. K. Varner. "Interband cascade laser-based sensor for ambient CH_4". *Optical Engineering*, **49**, 111118 (2010). http://dx.doi.org/10.1117/1.3498769

[40] H. Kogelnik and C. V. Shank. "Stimulated Emission in a Periodic Structure". *Applied Physics Letters*, **18**, 152 (1971). http://dx.doi.org/10.1063/1.1653605

[41] M. G. Littman and H. J. Metcalf. "Spectrally narrow pulsed dye laser without beam expander". *Applied Optics*, **17**, 2224 (1978). http://dx.doi.org/10.1364/AO.17.002224

[42] J. Faist, C. Gmachl, F. Capasso, C. Sirtori, D. L. Sivco, J. N. Baillargeon and A. Y. Cho. "Distributed feedback quantum cascade lasers". *Applied Physics Letters*, **70**, 2670 (1997). http://dx.doi.org/10.1063/1.119208

[43] C. Gmachl, J. Faist, J. N. Baillargeon, F. Capasso, C. Sirtori, D. L. Sivco, S. N. G. Chu and A. Y. Cho. "Complex-coupled quantum cascade distributed-feedback laser". *IEEE Photonics Technology Letters*, **9**, 1090–1092 (1997). http://dx.doi.org/10.1109/68.605510

[44] G. P. Luo, C. Peng, H. Q. Le, S. S. Pei, W.-Y. Hwang, B. Ishaug, J. Um, J. N. Baillargeon and C.-H. Lin. "Grating-tuned external-cavity quantum-cascade semiconductor lasers". *Applied Physics Letters*, **78**, 2834 (2001). http://dx.doi.org/10.1063/1.1371524

[45] R. F. Curl, F. Capasso, C. Gmachl, A. A. Kosterev, B. McManus, R. Lewicki, M. Pusharsky, G. Wysocki and F. K. Tittel. "Quantum cascade lasers in chemical physics". *Chemical Physics Letters*, **487**, 1–18 (2010). http://dx.doi.org/10.1016/j.cplett.2009.12.073

[46] R. J. Walker, J. H. van Helden and G. A. D. Ritchie. "Quantum cascade laser absorption spectroscopy of the 1←0 band of deuterium bromide at 5 μm". *Chemical Physics Letters*, **501**, 20–24 (2010). http://dx.doi.org/10.1016/j.cplett.2010.10.060

[47] S. Schilt, L. Thévenaz, E. Courtois and P. A. Robert. "Ethylene spectroscopy using a quasi-room-temperature quantum cascade laser". *Spectrochimica Acta Part A*, **58**, 2533–2539 (2002). http://dx.doi.org/10.1016/S1386-1425(02)00070-7

[48] M. Taslakov, V. Simeonov and H. van Den Bergh. "Open path atmospheric spectroscopy using room temperature operated pulsed quantum cascade laser". *Spectrochimica acta. Part A*, **63**, 1002–1008 (2006). http://dx.doi.org/10.1016/j.saa.2005.11.007

[49] S. Wright, G. Duxbury and N. Langford. "A compact quantum-cascade laser based spectrometer for monitoring the concentrations of methane and nitrous oxide in the troposphere". *Applied Physics B*, **85**, 243–249 (2006). http://dx.doi.org/10.1007/s00340-006-2384-x

[50] F. Hempel, V. Artyushenko, F. Weichbrodt and J. Röpcke. "Application of quantum cascade lasers and infrared-fibres for the monitoring and control of industrial plasma processes". *Journal of Physics: Conference Series*, **157**, 012003 (2009). http://dx.doi.org/10.1088/1742-6596/157/1/012003

[51] S. Welzel, L. Gatilova, J. Röpcke and A. Rousseau. "Time-resolved study of a pulsed dc discharge using quantum cascade laser absorption spectroscopy: NO

and gas temperature kinetics". *Plasma Sources Science and Technology*, **16**, 822–831 (2007).
http://dx.doi.org/10.1088/0963-0252/16/4/018

[52] G. Hancock, S. J. Horrocks, G. A. D. Ritchie, J. H. van Helden and R. J. Walker. "Time-resolved detection of the CF_3 photofragment using chirped QCL radiation". *The Journal of Physical Chemistry A*, **112**, 9751–9757 (2008).
http://dx.doi.org/10.1021/jp804849m

[53] K. Namjou, C. B. Roller and G. McMillen. "Breath-Analysis Using Mid-Infrared Tunable Laser Spectroscopy". In "2007 IEEE Sensors", pp. 1337–1340. Sensors, 2007 IEEE, Atlanta, GA (2007).
http://dx.doi.org/10.1109/ICSENS.2007.4388658

[54] J. Manne, A. Lim, W. Jäger and J. Tulip. "Off-axis cavity enhanced spectroscopy based on a pulsed quantum cascade laser for sensitive detection of ammonia and ethylene." *Applied optics*, **49**, 5302–8 (2010).
http://www.ncbi.nlm.nih.gov/pubmed/20885466

[55] B. W. M. Moeskops, H. Naus, S. M. Cristescu and F. J. M. Harren. "Quantum cascade laser-based carbon monoxide detection on a second time scale from human breath". *Applied Physics B*, **82**, 649–654 (2006).
http://dx.doi.org/10.1007/s00340-005-2124-7

[56] M. R. McCurdy, Y. A. Bakhirkin and F. K. Tittel. "Quantum cascade laser-based integrated cavity output spectroscopy of exhaled nitric oxide". *Applied Physics B*, **85**, 445–452 (2006).
http://dx.doi.org/10.1007/s00340-006-2365-0

[57] M. L. Silva, D. M. Sonnenfroh, D. I. Rosen, M. G. Allen and A. O'Keefe. "Integrated cavity output spectroscopy measurements of NO levels in breath with a pulsed room-temperature QCL". *Applied Physics B*, **81**, 705–710 (2005).
http://dx.doi.org/10.1007/s00340-005-1922-2

[58] M. Pushkarsky, A. Tsekoun, I. G. Dunayevskiy, R. Go and C. K. N. Patel. "Sub-parts-per-billion level detection of NO_2 using room-temperature quantum cascade lasers." *PNAS*, **103**, 10846–10849 (2006).
http://dx.doi.org/10.1073/pnas.0604238103

[59] F. Fuchs, S. Hugger, M. Kinzer, R. Aidam, W. Bronner, R. Losch, Q. Yang, K. Degreif and F. Schnurer. "Imaging standoff detection of explosives using widely tunable midinfrared quantum cascade lasers". *Optical Engineering*, **49**, 111127

(2010).
http://dx.doi.org/10.1117/1.3506195

[60] R. G. Brewer and R. L. Shoemaker. "Photo Echo and Optical Nutation in Molecules". *Physical Review Letters*, **27**, 631–634 (1971).
http://dx.doi.org/10.1103/PhysRevLett.27.631

[61] R. G. Brewer and R. L. Shoemaker. "Optical Free Induction Decay". *Physical Review A*, **6**, 2001–2007 (1972).
http://dx.doi.org/10.1103/PhysRevA.6.2001

[62] M. Loy. "Observation of Population Inversion by Optical Adiabatic Rapid Passage". *Physical Review Letters*, **32**, 814–817 (1974).
http://dx.doi.org/10.1103/PhysRevLett.32.814

[63] J. C. McGurk, T. G. Schmalz and W. H. Flygare. "Fast passage in rotational spectroscopy: Theory and experiment". *The Journal of Chemical Physics*, **60**, 4181 (1974).
http://dx.doi.org/10.1063/1.1680886

[64] N. Bloembergen, E. Purcell and R. Pound. "Relaxation Effects in Nuclear Magnetic Resonance Absorption". *Physical Review*, **73**, 679–712 (1948).
http://dx.doi.org/10.1103/PhysRev.73.679

[65] E. Hahn. "Nuclear Induction Due to Free Larmor Precession". *Physical Review*, **77**, 297–298 (1950).
http://dx.doi.org/10.1103/PhysRev.77.297.2

[66] J. H. van Helden, S. J. Horrocks and G. A. D. Ritchie. "Application of quantum cascade lasers in studies of low-pressure plasmas: Characterization of rapid passage effects on density and temperature measurements". *Applied Physics Letters*, **92**, 081506 (2008).
http://dx.doi.org/10.1063/1.2885725

[67] G. Duxbury, N. Langford, M. T. Mcculloch and S. Wright. "Rapid passage induced population transfer and coherences in the 8 micron spectrum of nitrous oxide". *Molecular Physics*, **105**, 741–754 (2007).
http://dx.doi.org/10.1080/00268970601181549

[68] M. T. McCulloch, G. Duxbury and N. Langford. "Observation of saturation and rapid passage signals in the 10.25 micron spectrum of ethylene using a frequency chirped quantum cascade laser". *Molecular Physics*, **104**, 2767–2779 (2006).
http://dx.doi.org/10.1080/00268970600857651

[69] J. H. Northern, G. a. D. Ritchie, E. P. Smakman, J. H. van Helden, J. Cockburn and G. Duxbury. "Rapid passage signals induced by chirped quantum cascade laser radiation: K state dependent-delay effects in the ν_2 band of NH_3". *Optics Letters*, **35**, 2750 (2010).
http://dx.doi.org/10.1364/OL.35.002750

[70] G. Duxbury, N. Langford and K. Hay. "Delayed rapid passage and transient gain signals generated using a chirped 8 μm quantum cascade laser". *Journal of Modern Optics*, **55**, 3293–3303 (2008).
http://dx.doi.org/10.1080/09500340802315321

[71] L. Allen and J. H. Eberly. *Optical Resonance and Two-Level Atoms*. Dover Publications, New York, reprint edition (1987).

[72] J. R. Kuklinski, U. Gaubatz, F. T. Hioe and K. Bergmann. "Adiabatic population transfer in a three-level system driven by delayed laser pulses". *Physical Review A*, **40**, 6741–6744 (1989).
http://dx.doi.org/10.1103/PhysRevA.40.6741

[73] J. C. McGurk, R. T. Hofmann and W. H. Flygare. "Transient absorption and emission and the measurement of T_1 and T_2 in the J O→1 rotational transition in OCS". *The Journal of Chemical Physics*, **60**, 2922 (1974).
http://dx.doi.org/10.1063/1.1681462

[74] S. M. Kim, F. Hatami, J. S. Harris, A. W. Kurian, J. Ford, D. King, G. Scalari, M. Giovannini, N. Hoyler, J. Faist and G. Harris. "Biomedical terahertz imaging with a quantum cascade laser". *Applied Physics Letters*, **88**, 153903 (2006).
http://dx.doi.org/10.1063/1.2194229

[75] M. T. McCulloch, E. L. Normand, N. Langford, G. Duxbury and D. A. Newnham. "Highly sensitive detection of trace gases using the time-resolved frequency downchirp from pulsed quantum-cascade lasers". *Journal of the Optical Society of America B*, **20**, 1761 (2003).
http://dx.doi.org/10.1364/JOSAB.20.001761

[76] J. Bösenberg. "Measurements of the pressure shift of water vapor absorption lines by simultaneous photoacoustic spectroscopy." *Applied Optics*, **24**, 3531 (1985).
http://www.ncbi.nlm.nih.gov/pubmed/18224082

[77] A. Z. Genack, R. O. Brickman and A. Schenzle. "Pulse formation and amplification in an absorbing medium by optical-phase switching". *Applied Physics B Photophysics and Laser Chemistry*, **28**, 276–277 (1982).
http://dx.doi.org/10.1007/BF00697856

[78] H. Torrey. "Transient Nutations in Nuclear Magnetic Resonance". *Physical Review*, **76**, 1059–1068 (1949).
http://dx.doi.org/10.1103/PhysRev.76.1059

[79] N. V. Vitanov, T. Halfmann, B. W. Shore and K. Bergmann. "Laser-induced population transfer by adiabatic passage techniques." *Annual review of physical chemistry*, **52**, 763–809 (2001).
http://dx.doi.org/10.1146/annurev.physchem.52.1.763

[80] R. R. Ernst. *Sensitivity Enhancement in Magnetic Resonance vol 2.* Academic Press (1966).

[81] F. Bloch. "Nuclear Induction". *Physical Review*, **70**, 460–474 (1946).
http://dx.doi.org/10.1103/PhysRev.70.460

[82] S. M. Hamadani, A. T. Mattick, N. A. Kurnit and A. Javan. "Observation of adiabatic rapid passage utilizing narrow infrared saturation resonances". *Applied Physics Letters*, **27**, 21 (1975).
http://dx.doi.org/10.1063/1.88273

[83] M. Beck, D. Hofstetter, T. Aellen, J. Faist, U. Oesterle, M. Ilegems, E. Gini and H. Melchior. "Continuous wave operation of a mid-infrared semiconductor laser at room temperature." *Science (New York, N.Y.)*, **295**, 301–5 (2002).
http://dx.doi.org/10.1126/science.1066408

[84] L. S. Rothman, D. Jacquemart, A. Barbe, D. Chris Benner, M. Birk, L. R. Brown, M. R. Carleer, C. Chackerian Jr, K. Chance, L. H. Coudert, W. Dana, V. M. Devi, J. M. Flaud, R. R. Gamache, A. Goldman, J. M. Hartman, K. W. Jucks, A. G. Maki, J. Y. Mandin, S. T. Massie, J. Orphal, A. Perrin, C. P. Rinsland, M. A. H. Smith, K. Tennyson, R. N. Tolchenov, R. A. Toth, J. Vander Auwera, P. Varanasi and G. Wagner. "The 2004 molecular spectroscopic database". *Journal of Quantitative Spectroscopy and Radiative Transfer*, **96**, 139–204 (2005).
http://dx.doi.org/10.1016/j.jqsrt.2004.10.008

[85] G. Wysocki, A. A. Kosterev and F. K. Tittel. "Spectroscopic trace-gas sensor with rapidly scanned wavelengths of a pulsed quantum cascade laser for in situ NO monitoring of industrial exhaust systems". *Applied Physics B*, **80**, 617–625 (2005).
http://dx.doi.org/10.1007/s00340-005-1764-y

[86] S. Bartalini, S. Borri, P. Cancio, A. Castrillo, I. Galli, G. Giusfredi, D. Mazzotti, L. Gianfrani and P. De Natale. "Observing the Intrinsic Linewidth of a Quantum-Cascade Laser: Beyond the Schawlow-Townes Limit". *Physical Review Letters*,

104, 4 (2010).
http://dx.doi.org/10.1103/PhysRevLett.104.083904

[87] T. C. Degges. "Vibrationally Excited Nitric Oxide in the Upper Atmosphere". *Applied Optics*, **10**, 1856 (1971).
http://dx.doi.org/10.1364/AO.10.001856

[88] M. R. McCurdy, Y. Bakhirkin, G. Wysocki and F. K. Tittel. "Performance of an exhaled nitric oxide and carbon dioxide sensor using quantum cascade laser-based integrated cavity output spectroscopy." *Journal of biomedical optics*, **12**, 034034 (2007).
http://dx.doi.org/10.1117/1.2747608

[89] F. N. Schleich, L. Seidel, J. Sele, M. Manise, V. Quaedvlieg, A. Michils and R. Louis. "Exhaled nitric oxide thresholds associated with a sputum eosinophil count >=3% in a cohort of unselected patients with asthma." *Thorax*, pp. 1039–1044 (2010).
http://dx.doi.org/10.1136/thx.2009.124925

[90] B. Buszewski, M. Kesy, T. Ligor and A. Amann. "Human exhaled air analytics: biomarkers of diseases." *Biomedical chromatography : BMC*, **21**, 553–66 (2007).
http://dx.doi.org/10.1002/bmc.835

[91] L. Prieto. "Measurement of exhaled nitric oxide concentrations in asthma. Technical aspects and clinical usefulness". *Alergologia e Inmunologia Clinica*, **17**, 72–89 (2002).
http://revista.seaic.es/abril2002e/72-87.PDF

[92] H.-w. Shin, C. M. Rose-gottron, R. S. Sufi, F. Perez, D. A. N. M. Cooper, A. F. Wilson and S. C. George. "Flow-independent Nitric Oxide Exchange Parameters in Cystic Fibrosis". *Critical Care Medicine* (2002).
http://dx.doi.org/10.1164/rccm2105098

[93] B. Gaston, J. M. Drazen, J. Loscalzo and J. S. Stamler. "The biology of nitrogen oxides in the airways." *American journal of respiratory and critical care medicine*, **149**, 538–51 (1994).
http://www.ncbi.nlm.nih.gov/pubmed/7508323

[94] K. Bhagat and P. Vallance. "Nitric oxide 9 years on." *Journal of the Royal Society of Medicine*, **89**, 667–73 (1996).
http://www.pubmedcentral.nih.gov/articlerender.fcgi?artid=1296027&tool=pmcentrez&rendertype=abstract

[95] Y. A. Bakhirkin, A. A. Kosterev, C. Roller, R. F. Curl and F. K. Tittel. "Mid-Infrared Quantum Cascade Laser Based Off-Axis Integrated Cavity Output Spectroscopy for Biogenic Nitric Oxide Detection". *Applied Optics*, **43**, 2257 (2004). http://dx.doi.org/10.1364/AO.43.002257

[96] J. M. Brown and A. Carrington. *Rotational Spectroscopy of Diatomic Molecules*. University Press, Cambridge, Cambridge, first edition (2003).

[97] D. Weidmann and G. Wysocki. "High-resolution broadband (¿100 cm⁻1) infrared heterodyne spectro-radiometry using an external cavity quantum cascade laser". *Optics Express*, **17**, 248–259 (2008). http://dx.doi.org/10.1364/OE.17.000248

[98] G. Wysocki, R. Lewicki, R. F. Curl, F. K. Tittel, L. Diehl, F. Capasso, M. Troccoli, G. Hofler, D. Bour, S. Corzine, R. Maulini, M. Giovannini and J. Faist. "Widely tunable mode-hop free external cavity quantum cascade lasers for high resolution spectroscopy and chemical sensing". *Applied Physics B*, **92**, 305–311 (2008). http://dx.doi.org/10.1007/s00340-008-3047-x

[99] A. Karpf and G. N. Rao. "Absorption and wavelength modulation spectroscopy of NO_2 using a tunable, external cavity continuous wave quantum cascade laser". *Applied Optics*, **48**, 408–413 (2009). http://dx.doi.org/10.1364/AO.48.000408

[100] J. Reid, B. K. Garside, J. Shewchun, M. El-Sherbiny and E. A. Ballik. "High sensitivity point monitoring of atmospheric gases employing tunable diode lasers". *Applied Optics*, **17**, 1806 (1978). http://dx.doi.org/10.1364/AO.17.001806

[101] J. Reid, J. Shewchun, B. K. Garside and E. A. Ballik. "High sensitivity pollution detection employing tunable diode lasers". *Applied Optics*, **17**, 300 (1978). http://dx.doi.org/10.1364/AO.17.000300

[102] J. Henningsen and H. Simonsen. "Quantitative wavelength-modulation spectroscopy without certified gas mixtures". *Applied Physics B: Lasers and Optics*, **70**, 627–633 (2000). http://dx.doi.org/10.1007/s003400050871

[103] K. Duffin, A. McGettrick, W. Johnstone, G. Stewart and D. Moodie. "Tunable diode-laser spectroscopy with wavelength modulation: a calibration-free approach to the recovery of absolute gas absorption line shapes". *Journal of Lightwave Technology*, **25**, 3114–3125 (2007). http://ieeexplore.ieee.org/xpls/abs_all.jsp?arnumber=4346610

[104] J. A. Silver. "Frequency-modulation spectroscopy for trace species detection: theory and comparison among experimental methods". *Applied Optics*, **31**, 707 (1992).
http://dx.doi.org/10.1364/AO.31.000707

[105] J. U. White. "Long Optical Paths of Large Aperture". *Journal of the Optical Society of America*, **32**, 285 (1942).
http://dx.doi.org/10.1364/JOSA.32.000285

[106] D. R. Herriott and H. J. Schulte. "Folded Optical Delay Lines". *Applied Optics*, **4**, 883 (1965).
http://dx.doi.org/10.1364/AO.4.000883

[107] M. Mazurenka, A. J. Orr-Ewing, R. Peverall and G. A. D. Ritchie. "Cavity ring-down and cavity enhanced spectroscopy using diode lasers". *Annual Reports Section "C" (Physical Chemistry)*, **101**, 100 (2005).
http://dx.doi.org/10.1039/b408909j

[108] E. J. Moyer, D. S. Sayres, G. S. Engel, J. M. St. Clair, F. N. Keutsch, N. T. Allen, J. H. Kroll and J. G. Anderson. "Design considerations in high-sensitivity off-axis integrated cavity output spectroscopy". *Applied Physics B*, **92**, 467–474 (2008).
http://dx.doi.org/10.1007/s00340-008-3137-9

[109] Y. A. Bakhirkin, A. A. Kosterev, C. Roller, R. F. Curl and F. K. Tittel. "Mid-infrared quantum cascade laser based off-axis integrated cavity output spectroscopy for biogenic nitric oxide detection." *Applied Optics*, **43**, 2257–2266 (2004).
http://www.ncbi.nlm.nih.gov/pubmed/15098827

[110] C. M. Western. "PGOPHER, a Program for Simulating Rotational Structure". *University of Bristol* (2009).
http://pgopher.chm.bris.ac.uk

[111] T. Tokuhiro. "Vibrational and Rotational Effects on the Nuclear Quadrupole Coupling Constants in Hydrogen, Deuterium, and Tritium Halides". *Journal of Chemical Physics*, **47**, 109–113 (1967).
http://dx.doi.org/10.1063/1.1711832

[112] J. S. Wells, D. A. Jennings and A. G. Maki. "Improved deuterium bromide 1-0 band molecular constants from heterodyne frequency measurements". *Journal of Molecular Spectroscopy*, **107**, 48–61 (1984).
http://dx.doi.org/10.1016/0022-2852(84)90264-9

[113] F. A. van Dijk and A. Dymanus. "Hyperfine and Stark spectrum of DBr in the millimeter-wave region". *Chemical Physics*, **6**, 474–478 (1974).
http://dx.doi.org/10.1016/0301-0104(74)85032-9

[114] J. Bardeen and C. Townes. "Calculation of Nuclear Quadrupole Effects in Molecules". *Physical Review*, **73**, 97–105 (1948).
http://dx.doi.org/10.1103/PhysRev.73.97

[115] C. A. Burrus and W. Gordy. "One-to-Two Millimeter Wave Spectroscopy. III. NO and DI". *Physical Review*, **92**, 1437–1439 (1953).
http://dx.doi.org/10.1103/PhysRev.92.1437

[116] M. Cowan and W. Gordy. "Precision Measurements of Millimeter and Submillimeter Wave Spectra: DCl, DBr, and DI". *Physical Review*, **111**, 209–211 (1958).
http://dx.doi.org/10.1103/PhysRev.111.209

[117] W. Gordy and C. A. Burrus. "Spectrum of DBr in the One-Millimeter Wave Region". *Physical Review*, **93**, 419–420 (1954).
http://dx.doi.org/10.1103/PhysRev.93.419

[118] C. A. Burrus. "Stark Effect at 0.93, 1.18, and 1.5 Millimeters Wavelength: DCl, DBr, and DI". *Journal of Chemical Physics*, **31**, 1270–1272 (1959).
http://dx.doi.org/10.1063/1.1730582

[119] A. Hebert and K. Street. "Nuclear-Quadrupole Ratio of Bromine Isotopes in Molecular LiBr". *Physical Review*, **178**, 205–206 (1969).
http://dx.doi.org/10.1103/PhysRev.178.205

[120] W. Lamb. "Theory of an Optical Maser". *Physical Review*, **134**, A1429–A1450 (1964).
http://dx.doi.org/10.1103/PhysRev.134.A1429

[121] C. C. Costain. "The use of saturation dip absorption in microwave spectroscopy and in microwave frequency stabilization". *Canadian Journal of Physics*, **47**, 2431–2433 (1969).
http://dx.doi.org/10.1139/p69-299

[122] W. Demtröder. *Laser Spectroscopy: Basic Concepts and Instrumentation.* Springer-Verlag, Berlin Heidelberg New York, third edition (2003).

[123] J. M. Hollas. *High Resolution Spectroscopy.* Butterworths, London, first edition (1982).

[124] J. T. Remillard, D. Uy, W. H. Weber, F. Capasso, C. Gmachl, A. L. Hutchinson, D. L. Sivco, J. N. Baillargeon and A. Y. Cho. "Sub-Doppler resolution limited Lamb-dip spectroscopy of NO with a quantum cascade distributed feedback laser". *Optics Express*, **7**, 243–248 (2000).
http://dx.doi.org/10.1364/OE.7.000243

[125] N. Mukherjee and C. K. N. Patel. "Molecular fine structure and transition dipole moment of NO_2 using an external cavity quantum cascade laser". *Chemical Physics Letters*, **462**, 10–13 (2008).
http://dx.doi.org/10.1016/j.cplett.2008.07.050

[126] S. Borri, S. Bartalini, I. Galli, P. Cancio, G. Giusfredi, D. Mazzotti, A. Castrillo, L. Gianfrani and P. De Natale. "Lamb-dip-locked quantum cascade laser for comb-referenced IR absolute frequency measurements". *Optics Express*, **16**, 11637 (2008).
http://dx.doi.org/10.1364/OE.16.011637

[127] E. Uzgiris, J. Hall and R. Barger. "Precision Infrared Zeeman Spectra of CH_4 Studied by Laser-Saturated Absorption". *Physical Review Letters*, **26**, 289–293 (1971).
http://dx.doi.org/10.1103/PhysRevLett.26.289

[128] J. W. C. Johns, A. R. W. McKellar, T. Oka and M. Römheld. "Collision-induced Lamb dips in laser Stark spectroscopy". *The Journal of Chemical Physics*, **62**, 1488 (1975).
http://dx.doi.org/10.1063/1.430610

[129] E. V. Baklanov, V. P. Chebotayev and M. P. Staroselsky. "New nonlinear resonances in a gas in the presence of a strong optical field". *Applied Physics B Photophysics and Laser Chemistry*, **49**, 163–167 (1989).
http://dx.doi.org/10.1007/BF00332277

[130] R. L. Shoemaker, S. Stenholm and R. G. Brewer. "Collision-induced optical double resonance". *Physical Review*, **10**, 2037–2050 (1974).
http://dx.doi.org/http://link.aps.org/doi/10.1103/PhysRevA.10.2037

[131] V. P. Chebotayev. "Coherence in High Resolution Spectroscopy". In M. S. Feld and V. S. Letokhov, editors, "Coherent Nonlinear Optics", chapter 3, pp. 59–109. Springer-Verlag, Berlin Heidelberg New York (1980).

[132] A. Schawlow and C. Townes. "Infrared and Optical Masers". *Physical Review*, **112**, 1940–1949 (1958).
http://dx.doi.org/10.1103/PhysRev.112.1940

[133] C. Henry. "Theory of the linewidth of semiconductor lasers". *IEEE Journal of Quantum Electronics*, **18**, 259–264 (1982).
http://dx.doi.org/10.1109/JQE.1982.1071522

[134] J. von Staden, T. Gensty, W. Elsässer, G. Giuliani and C. Mann. "Measurements of the alpha factor of a distributed-feedback quantum cascade laser by an optical feedback self-mixing technique." *Optics letters*, **31**, 2574–6 (2006).
http://www.ncbi.nlm.nih.gov/pubmed/16902623

[135] T. Aellen, R. Maulini, R. Terazzi, N. Hoyler, M. Giovannini, J. Faist, S. Blaser and L. Hvozdara. "Direct measurement of the linewidth enhancement factor by optical heterodyning of an amplitude-modulated quantum cascade laser". *Applied Physics Letters*, **89**, 091121 (2006).
http://dx.doi.org/10.1063/1.2345035

[136] S. D. Saliba and R. E. Scholten. "Linewidths below 100 kHz with external cavity diode lasers". *Applied Optics*, **48**, 6961 (2009).
http://dx.doi.org/10.1364/AO.48.006961

[137] S. Bartalini, S. Borri and P. De Natale. "Doppler-free polarization spectroscopy with a quantum cascade laser at 4.3 µm". *Optics Express*, **17**, 7440–7449 (2009).
http://dx.doi.org/10.1364/OE.17.007440

[138] P. L. Christensen and E. S. Yeung. "Improvements in polarization spectroscopy based on high-frequency modulation". *Talanta*, **36**, 179–184 (1989).
http://dx.doi.org/10.1016/0039-9140(89)80093-1

[139] Y. Yoshikawa, T. Umeki, T. Mukae, Y. Torii and T. Kuga. "Frequency Stabilization of a Laser Diode with Use of Light-Induced Birefringence in an Atomic Vapor". *Applied Optics*, **42**, 6645 (2003).
http://dx.doi.org/10.1364/AO.42.006645

[140] M. Islam, I. W. M. Smith and M. H. Alexander. "State-to-state rate coefficients for transfer from the rotational levels $J = 7.5$, 20.5, 31.5 and 40.5 in NO(X $^2\Pi_{1/2}$, $v = 2$) in collisions with He, Ar and N_2 and for J=7.5, 20.5 and 31.5 in collisions with NO: comparisons between experim". *Physical Chemistry Chemical Physics*, **2**, 473–479 (2000).
http://dx.doi.org/10.1039/a906693d

[141] G. Hancock, M. Morrison and M. Saunders. "Vibrational relaxation of NO ($v =$ 1-16) with NO, N_2O, NO_2, He and Ar studied by time-resolved Fourier transform infrared emission." *Physical chemistry chemical physics : PCCP*, **11**, 8507–15

(2009).
http://dx.doi.org/10.1039/b909195e

[142] U. Shin and R. H. Schwendeman. "Polarization effects in infraredinfrared double resonance in methyl fluoride". *The Journal of Chemical Physics*, **96**, 8699 (1992).
http://dx.doi.org/10.1063/1.462277

[143] K. Bergmann and B. W. Shore. "Coherent Population Transfer". In H. L. Dai and R. W. Field, editors, "Molecular Dynamics, Spectroscopy by Stimulate Emission Pumping", pp. 315–373. World Scientific, Singapore (1995).

[144] T. A. Laine and S. Stenholm. "Adiabatic processes in three-level systems". *Physical Review A*, **53**, 2501–2512 (1996).
http://dx.doi.org/10.1103/PhysRevA.53.2501

[145] H. G. Rubahn, E. Konz, S. Schiemann and K. Bergmann. "Alignment of electronic angular momentum by stimulated Raman scattering with delayed pulses". *Zeitschrift für Physik D - Atoms, Molecules and Clusters*, **22**, 401–406 (1991).
http://dx.doi.org/10.1007/BF01438564

[146] A. Lindinger, M. Verbeek and H. G. Rubahn. "Adiabatic population transfer by acoustooptically modulated laser beams". *Zeitschrift für Physik D Atoms, Molecules and Clusters*, **39**, 93–100 (1997).
http://dx.doi.org/10.1007/s004600050114

[147] N. Mukherjee and R. N. Zare. "Preparation of polarized molecules using coherent infrared multicolor ladder excitation". *Journal of Chemical Physics*, **132**, 154302 (2010).
http://dx.doi.org/10.1063/1.3352553

[148] R. M. Williams, J. F. Kelly, J. S. Hartman, S. W. Sharpe, M. S. Taubman, J. L. Hall, F. Capasso, C. Gmachl, D. L. Sivco, J. N. Baillargeon and A. Y. Cho. "Kilohertz linewidth from frequency-stabilized mid-infrared quantum cascade lasers". *Optics Letters*, **24**, 1844 (1999).
http://dx.doi.org/10.1364/OL.24.001844

[149] M. S. Taubman, T. L. Myers, B. D. Cannon, R. M. Williams, F. Capasso, C. Gmachl, D. L. Sivco and A. Y. Cho. "Frequency stabilization of quantum-cascade lasers by use of optical cavities." *Optics letters*, **27**, 2164–6 (2002).
http://dx.doi.org/10.1364/OL.27.002164

[150] E. Normand, G. Duxbury and N. Langford. "Characterisation of the spectral behaviour of pulsed quantum cascade lasers using a high resolution Fourier transform

infrared spectrometer". *Optics Communications*, **197**, 115–120 (2001).
http://dx.doi.org/10.1016/S0030-4018(01)01402-X

[151] T. Mozume. "Indices of refraction of InGaAs/Alas/AlAsSb multiple-quantum-wells measured by an optical waveguide technique". *Physica E: Low-dimensional Systems and Nanostructures*, **40**, 2031–2033 (2008).
http://dx.doi.org/10.1016/j.physe.2007.09.125

[152] J. P. Commin, K. Kennedy, D. G. Revin, S. Y. Zhang, A. B. Krysa and J. W. Cockburn. "$\lambda\sim$3.36 μm room temperature InGaAs/AlAs(Sb) quantum cascade lasers with third order distributed feedback grating". *Applied Physics Letters*, **97**, 111113 (2010).
http://dx.doi.org/10.1063/1.3487781

List of Publications

G. Hancock, S. J. Horrocks, G. A. D. Ritchie, J. H. van Helden and R. J. Walker. "Time-resolved detection of the CF_3 photofragment using chirped QCL radiation". *The Journal of Physical Chemistry. A*, **112**, 9751–9757 (2008).
http://dx.doi.org/10.1021/jp804849m

J. H. van Helden, R. Peverall, G. A. D. Ritchie and R. J. Walker. "Rapid passage effects in nitrous oxide induced by a chirped external cavity quantum cascade laser". *Applied Physics Letters*, **94**, 051116 (2009).
http://dx.doi.org/10.1063/1.307940

J. H. Northern, G. A. D. Ritchie, E. P. Smakman, J. H. van Helden, R. J. Walker and G. Duxbury. "Chirped quantum cascade laser induced rapid passage signatures in an optically thick gas". *Applied Physics B*, **102**, 37–42 (2010).
http://dx.doi.org/10.1016/j.cplett.2010.10.060

G. Hancock, J. H. van Helden, R. Peverall, G. A. D. Ritchie and R. J. Walker. "Direct and wavelength modulation spectroscopy using a cw external cavity quantum cascade laser". *Applied Physics Letters*, **94**, 201110 (2009).
http://dx.doi.org/10.1063/1.3141521

R. J. Walker, J. H. van Helden and G. A. D. Ritchie. "Quantum cascade laser absorption spectroscopy of the 1←0 band of deuterium bromide at 5 μm". *Chemical Physics Letters*, **501**, 20–24 (2010).
http://dx.doi.org/10.1016/j.cplett.2010.10.060

G. Hancock, G. A. D. Ritchie, J. H. van Helden, R. J. Walker and D. Weidmann. "Applications of midinfrared quantum cascade lasers to spectroscopy". *Optical Engineering*, **49**, 111121 (2010).
http://dx.doi.org/10.1117/1.3498770

R. J. Walker, J. H. van Helden, J. Kirkbride, E. A. McCormack, M. T. Bell, D. Weidmann and G. A. D. Ritchie. "Rapid passage signals from a vibrationally excited target:

a pump and probe experiment with continuous wave quantum cascade lasers". *Optics Letters*, **36**, 24, 4725–4727 (2011).
http:dx.doi.org/10.1364/OL.36.004725